An Examination of the Transition Region between the Troposphere and Stratosphere using Tracer Space

A thesis
submitted in partial fulfilment
of the requirements for the Degree
of
Doctor of Philosophy in Physics
in the
University of Canterbury

by

Kathleen Patricia Monahan

University of Canterbury
2008

Abstract

Stratosphere Troposphere exchange (STE) is important to study as it controls the chemical composition of the upper troposphere/lower stratosphere (UTLS) and thus the radiative balance of this region. STE also controls the transport of chemicals into the stratosphere which are vital to ozone depletion. The troposphere and the stratosphere have specific chemical characteristics and the transition region between these regions displays characteristics of both. Ozone and water vapour concentrations can be used as tracers for the characteristics of the troposphere and stratosphere. This thesis develops measures in tracer space, which allow the determination of the strength and depth of atmospheric mixing between the troposphere and the stratosphere in extratropical regions.

The application of entropy as a measure of atmospheric mixing as introduced by *Patmore and Toumi* [2006], is improved in this study. This is a measure of how the ozone and water vapour mixing ratios vary as a result of mixing. An additional metric to give further information on the form of the mixing line in tracer space is also developed. This measure uses the ozone and water vapour mixing ratios at the boundaries of the transition region (BO3 and BH2O). This study uses data from ozonesondes and hygrometers, along with satellite data from the Atmospheric Infrared Sounder (AIRS). The ozone product from AIRS is also validated as part of this study.

The entropy, BO3 and BH2O measures from this study, are successfully shown to detect regions of enhanced mixing in comparison studies. A key comparison shows that the measures developed in this study are able to produce comparable conclusions to higher resolution aircraft data, with regards to mixing. The separation of entropy, BO3 and BH2O, into different categories allows mixing processes to be assigned to some of the categories. Mixing is shown to have geographic preference, with some regions having significantly more mixing. Some categories have preference with regards to their location either poleward or equatorward of the jet stream. In addition, some information as to the direction of the vertical transport, whether stratosphere to troposphere or vice versa, is obtained.

Acknowledgements

Firstly I must thank my supervisor, Dr Adrian McDonald. He has spent countless hours working with me and teaching me many skills. He has also spent many hours reading my work and thesis drafts and has provided much useful feedback. I have been very blessed to have such a great supervisor.

Thanks also go to my co-supervisor, Dr Greg Bodeker, for providing a different perspective on this thesis work. To Dr Steve George, for reading through several of the thesis chapters, and for generally providing new ideas and methods for confirming my results. His assistance has been very valuable to me.

Thanks to those who have provided the financial support to enable me to complete this thesis. To the Physics and Astronomy Department at the University of Canterbury, for providing me with a scholarship and teaching opportunities. To NIWA, for providing me with additional funding. Many thanks to COST 723 for funding me to attend the UTLS international summer school in Cargèse, Corsica, France. Thanks also to NCAR for funding me to visit Boulder, Colorado in the USA as a visiting researcher and Dr Laura Pan who supervised this visit. And thanks to the ACD group at NCAR and Jo Ann Joselyn who made the trip to Boulder very enjoyable.

Thanks to those who provided data sets for use in this thesis. Holger Vömel for the Boulder Ozonesonde and hygrometer data. Andrew Gettelman and Garth D'Attilo, for the AIRS level 3 data. Hamish Chisholm and NIWA, for the Lauder ozonesonde and hygrometer data.

Thanks to the Physics and Astronomy department for the logistical support, along with the helpful and friendly people. Thanks also to the Atmospheric Physics group, for the presentation opportunities, helpful feedback and general companionship.

To my many office mates over the years. Thank you for all the laughs we have shared, brainstorming sessions, and the many many batches of brownies as we each tried to perfect the recipes. Special thanks to Dr Petra Huck who has mentored me through many aspects of being a PhD student, has provided the voice of reason and has been a great friend.

Many thanks to all my friends who have supported me, cheered from the sidelines, and provided me with lots of encouragement. Without my friends, this process

would have been much more difficult. Also thanks to all those who have offered me prayer support and have helped keep me balanced and centered. Special thanks to those of my friends that proof read my thesis - Paul, Megan, Trudy and Mike. Your input has helped make this a better thesis.

To my wonderful flatmates over the last few years - Megan, David and Sarah. Thank you for making our flat a home and for providing me with so much of the support that I have needed during this time.

To my family, Janet, Peter and Shaun. For the love and understanding you have given me on this journey. For offering me encouragement when I needed it. And for allowing me to talk each of you into proofing some of my thesis. Your support over the course of this thesis has been very valuable to me.

To my Heavenly Father. For the gifts and talents that I have been given that have enabled me to carry out this course of study. For the blessings in my life. For carrying me through this period in my life.

"I can do all things through Christ who strengthens me." Phil 4:13

Contents

List of Figures

List of Tables

Chapter 1

Introduction

The troposphere (the region of the atmosphere between the Earth's surface and approximately 15 km altitude) and the stratosphere (the region of the atmosphere between approximately 15 km and 50 km altitude) have distinctly different chemical composition. For example, tropospheric air has a high water vapour mixing ratio and a low ozone mixing ratio, whereas stratospheric air has a low water vapour mixing ratio and a high ozone mixing ratio. These contrasting properties can be used as a signature to determine the origin of air parcels and to identify mixing between these regions. The boundary between these two regions is called the tropopause.

The tropopause acts as a pseudo-barrier to transport between the troposphere and the stratosphere. The barrier is observed by the strong gradients in a number of different substances, such as ozone, water vapour, methane and hydrogen fluoride. However, it is only a pseudo-barrier as the effects of exchange through this "barrier" are observed in the atmosphere. The primary characteristic of this barrier is the change in the temperature structure, where the troposphere has decreasing temperature with height and the stratosphere has increasing temperature with height. This creates a strong difference in stability and potential vorticity.

Transport and mixing of air between the troposphere and stratosphere is important for the chemical balance of the atmosphere. This is called stratosphere troposphere exchange, or STE. This exchange can occur in both directions, with different strengths, at different locations around the world, with different seasonal patterns, and by a number of different mechanisms. As the stratosphere and troposphere have very different characteristics, movement of air between these two layers can have a large effect on the atmosphere by changing the characteristics of the mixed air. This can result in a transitional layer with both tropospheric and stratospheric chemical compositions.

The two recent ozone assessments [*World Meteorological Organization*, 2003, 2007] highlight that transport is an important step in ozone depletion, as it allows the movement of ozone destroying species and their precursors from the surface to the stratosphere. This transport is particularly important because it influences the effects that substances, particularly halogen gases, which are produced at the surface or at altitude, have on stratospheric ozone. The fraction of these substances in the stratosphere depends on the local chemical lifetime relative to the local transport scales, that is, the rate at which the chemicals break down versus the time taken for the chemicals to arrive in the stratosphere.

Downwards transport from the stratosphere to the troposphere can significantly influence the composition of some species in the troposphere [*Levy et al.*, 1980]. The chemical effects from STE can influence the radiative flux balance in the troposphere and lower stratosphere, thereby affecting the radiative forcing which may have an impact on the climate.

STE has been studied from a number of different angles using a variety of methodologies and data sets, with either local or global focus. Some studies are concerned with quantifying the amount of exchange by looking at the movement of substances across the tropopause. Others are interested in the relative occurrence of STE mechanisms. Using high resolution data to study the exchange within a single event is also common.

This thesis aims to develop a set of measures that can identify STE on a global scale with the highest spatial resolution available. Previous global scale studies of STE generally either use only model or reanalysis data, focus on a single hemisphere, or only focus on a particular type of exchange event. This thesis aims to provide a broader scope and a data driven, rather than a model driven, method. This means that a minimal number of parameters are used in the method, with parameters adjusting to the data set. Any parameters used should also be robust, with small variations to the values having a minimal effect. In comparison, models tend to be highly sensitive to the parameters used.

Chapter 2 contains the background required to discuss transport and mixing between the stratosphere and troposphere. It is important to establish the definitions and boundaries required to understand STE. Mainly this involves understanding the different definitions used for the tropopause as this is key for studying transport across the tropopause. Furthermore, a description of tracer space and the different regions of the atmosphere are included. From

the literature, there are a number of different mechanisms established for STE. These mechanisms include convection, isentropic transport and tropopause folds.

Chapter 3 contains a detailed description of the data sets that are used in this thesis. There are four key data sets. Ozonesondes are released from Lauder, located in Central Otago, New Zealand, and Boulder, Colorado in the United States. These records provide high resolution, location specific ozone data, along with temperature and several other parameters. Some of the ozonesondes are accompanied by hygrometers, which provide high resolution water vapour data. For the larger scale global studies, the Atmospheric Infrared Sounder, or AIRS, which is a instrument on NASA's Aqua satellite, is utilised. This provides low vertical resolution ozone and water vapour mixing ratio measurements with excellent temporal and spatial coverage. The final data set utilised is NCEP/NCAR reanalysis data which is a model that assimilates a variety of measurements from different instruments. The NCEP/NCAR reanalysis data set provides a comprehensive set of parameters, however, this thesis uses mainly the temperature and wind data.

Tropopause folds are an important mechanism for STE. A method of tropopause fold identification is explored in Chapter 4, based on the method detailed in *Van Haver et al.* [1996]. This method looks for regions of stratospheric air in the troposphere using high vertical resolution ozonesonde records from Lauder and Boulder. Exchange events are identified using a number of adjustable parameters and the quality/utility of this algorithm is examined.

In order to expand the region of study from two locations (Lauder and Boulder) to globally, a second data set is required. The Atmospheric Infrared Sounder (AIRS) provides a global daily data set, however, the lower vertical resolution for this instrument compared to the ozonesondes requires a different methodology for identifying transport and mixing between the troposphere and stratosphere. Tracer space, which requires a tropospheric and stratospheric tracer, is used to analyse the transport and mixing. Tracer space is defined by two chemicals or species (known as tracers) plotted with respect to one another, with one on the x-axis and the other on the y-axis. This allows the relationship between the two tracers to be clearly and easily identified. AIRS data includes both water vapour, a tropospheric tracer, and ozone, a stratospheric tracer. The water vapour mixing ratios have been previously validated. Chapter 5 covers the validation of the AIRS ozone profile product to show that the measurements are sufficiently accurate to use in the UTLS region.

Using tracer space coordinates, the amount of mixing can be measured using the entropy calculation method outlined in *Patmore and Toumi* [2006]. This method looks at the transition region between the troposphere and stratosphere where the ozone and water vapour mixing ratios change from their tropospheric to stratospheric values. By examining the distribution of observations in tracer space, an entropy value describing the amount of mixing between these regions can be calculated. The application of this method to the AIRS and ozonesonde/-hygrometer data is discussed in Chapter 6.

Analysis detailed in Chapter 6, shows that entropy does not fully describe tracer space. An additional measure is needed to define the scale of the mixing. Such a measure is proposed in Chapter 7 that uses the ozone and water vapour values at the transition layer boundaries, called BO3 and BH2O. This allows the gradient of the transport and mixing to be determined. The ability of these measures in separating out different processes is detailed in Chapter 8.

Entropy, BO3 and BH2O are then used in conjunction to identify regions of mixing and transport in Chapter 8. Results are shown on both a small, daily scale, including a comparison to aircraft measurements, along with larger scale and longer time periods to examine mixing and transport on global and climatological scales. These measures are demonstrated to be useful in identifying regions of STE on a global scale.

Finally, Chapter 9 contains a summary of the methodology and key results from this thesis. A number of possibilities for furthering this work are also included.

Chapter 2

Background

Stratosphere Troposphere exchange (STE) describes the movement of air between the two lowest atmospheric layers. The stratosphere and troposphere have different physical and chemical properties, hence exchange between the two can be very significant due to the large potential for change in composition. The troposphere has high water vapour number densities and low ozone number densities and is unstable. Whereas, the stratosphere has low water vapour number densities and high ozone number densities and is relatively stable due to temperature increasing with height. Any movement of air between these regions carries the signature of its sphere of origin and can be tracked until the signature becomes blended or well mixed with the air in the new sphere. The convention of *Stohl et al.* [2003] is that air movement in both directions is described as STE, whereas movement in a single direction is transport, denoted by STT for stratosphere to troposphere transport, and TST for troposphere to stratosphere transport.

STE is important for ozone depletion [*Butchart and Scaife*, 2001; *World Meteorological Organization*, 2007] and climate predictions [*Collins et al.*, 2003; *Sudo et al.*, 2003] as the residence times and exchange rates between the troposphere and stratosphere can have a great effect. An increase or a decrease in STE can significantly change the composition of the stratosphere, which could result in more, or less ozone depleting chemicals in the stratosphere, changes in radiative forcing or circulation.

James et al. [2003a] showed that more than 95% of the mass of the troposphere has been in the stratosphere in the previous year. Furthermore, most exchange is shallow with exchange particles returning to their original sphere in 6 hours to 2 days [*James et al.*, 2003b; *Wernli and Bourqui*, 2002]. As STE is frequent, it has the potential to have a large impact on the atmosphere. However, shallow reversible events are unlikely to change the composition of either the stratosphere

or the troposphere, therefore it is deep exchange that will have the largest impact on the atmosphere.

2.1 Tropopause Definitions

To be able to measure STE we first need to define what constitutes transport from one region to the other. Typically the boundary between the stratosphere and troposphere is called the tropopause and is determined based on changes in temperature with altitude (see Section 2.1.1). However, there are a number of other definitions for the tropopause which are not defined based on the temperature structure of the atmosphere. There is also discussion as to whether the tropopause is a level or a layer [*Hoinka*, 1997; *Pan et al.*, 2004]. This section will summarise the different tropopause definitions. These tropopauses are not necessarily at the same altitude and the choice of which tropopause to use is dependent on the question to be addressed [*Wirth*, 2001].

There is an additional tropopause definition that is not outlined in the following sections called the tropical tropopause layer. While this region is important for STE studies [*Gettelman and Forster*, 2002], due to limitations in the data sets used in this thesis, this region is not discussed.

2.1.1 Thermal Tropopause

The most common tropopause definition is the thermal tropopause with the standard definition being given by the *World Meteorological Organization* [1957]. This definition states that the tropopause is the lowest level at which the lapse rate decreases to at least $2\,\mathrm{Kkm^{-1}}$ and the averaged lapse rate for the next 2 km is less than $2\,\mathrm{Kkm^{-1}}$ [*Stohl et al.*, 2003]. The lapse rate, Γ, is the change in temperature with respect to altitude,

$$\Gamma = -\frac{dT}{dz} \tag{2.1}$$

where T is the parcel temperature and z is the altitude above the surface of the Earth [*Salby*, 1996].

The height of the thermal tropopause varies depending on latitude and season. In the tropics, due to strong surface heating, the thermal tropopause has an altitude of 16-17 km. In contrast, areas with less surface heating, such as the

extratropics* have lower tropopause heights 7-8 km, with higher altitudes during the summer [*Shepherd*, 2003]. During polar winter the thermal tropopause is an inappropriate definition, as under cyclonic conditions the low static stability of the lower stratosphere does not yield a sensible height [*Zängl and Hoinka*, 2001]. It is also possible to have multiple thermal tropopauses defined in a single profile [*Bischoff et al.*, 2007; *Wirth*, 2001; *Randel et al.*, 2007].

2.1.2 Static Stability

It is possible to use the static stability to define the tropopause. The Brunt Väisälä frequency at level i is calculated as follows:

$$N_i^2 = \frac{g}{\theta_i}\left(\frac{\theta_{i+1} - \theta_i}{z_{i+1} - z_i}\right) \tag{2.2}$$

Potential temperature, θ, is given by:

$$\theta = T\left(\frac{1000\,hPa}{P}\right)^{\kappa} \tag{2.3}$$

where T is temperature, P is pressure, $\kappa = 0.286$ and the resultant units of θ are in Kelvin, K [*Salby*, 1996]. Height, z, is given by:

$$z_i = -H_i \ln\left(\frac{P_i}{1000\,hPa}\right) \tag{2.4}$$

where P_i is the pressure at level i and H_i is the scale height at level i and is given by:

$$H_i = \frac{RT_i}{g} \tag{2.5}$$

where R=287.05 $\mathrm{Jkg^{-1}K^{-1}}$, g=9.8 $\mathrm{ms^{-2}}$ and T is the temperature at level i [*Salby*, 1996].

Wirth [2003] showed that there is a discontinuity in N^2 at the thermal tropopause with a sharp peak just above the thermal tropopause as shown in Figure 2.1. Outside of the tropopause regions, the tropospheric and stratospheric values of N^2 are clearly different as is shown in Figure 2.1. It should be noted that in practice the stratospheric and tropospheric values are not as smooth as suggested

*There are a range of terms used to describe different parts of the globe. Some of the more obscure ones are: Midlatitudes 30-60°; subtropical ∼30°; subpolar ∼60°; extratropical poleward of 30° [*Stull*, 2000].

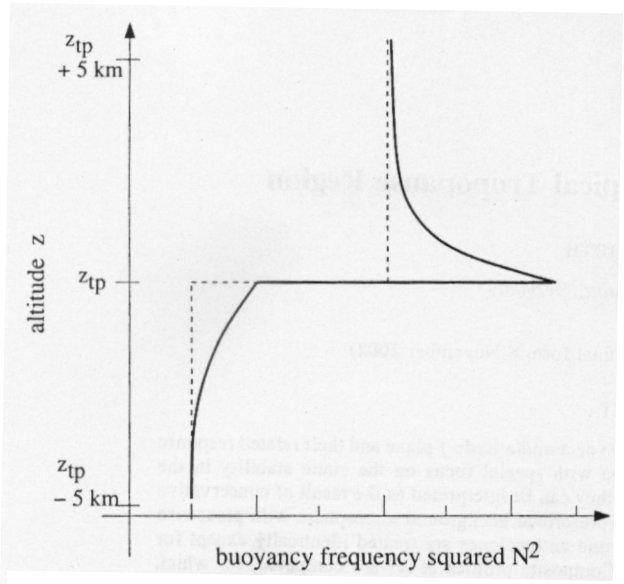

Figure 2.1: Schematic representation of the climatological profile of Brunt Väisälä frequency over Southern Germany from radiosondes. Figure from *Wirth* [2003].

in Figure 2.1. The peak is a result of the rapid change in the temperature gradient and is an indicator of the increased stability above the tropopause.

2.1.3 Dynamic Tropopause

The dynamic tropopause is based on the stability differences caused by different thermal gradients between the troposphere and the stratosphere using Potential Vorticity (PV). The dynamic tropopause is a material surface under conservative conditions [*Wirth*, 2001]. PV is given by

$$PV = -g\eta\frac{\partial\theta}{\partial p} \tag{2.6}$$

where η is absolute isentropic vorticity, g is the gravitational constant, θ is potential temperature from Equation 2.3, $\frac{\partial\theta}{\partial p}$ is the static stability and a potential vorticity unit (PVU) is $1\,\mathrm{PVU}{=}10^{-6}\mathrm{m}^2\mathrm{K\ kg}^{-1}\mathrm{s}^{-1}$ [*Goering et al.*, 2001]. η is given by $\eta = (\zeta_\theta + f)$, where ζ_θ is the relative vorticity and f is the Coriolis parameter [*Hoinka et al.*, 1993]. Under adiabatic and frictionless conditions, PV has been shown to be conserved and emphasizes the material surface nature of the tropopause [*Stohl et al.*, 2003].

The stratosphere is statically stable due to its temperature gradient, this pro-

duces large PV values [*Goering et al.*, 2001]. Hence the PV tropopause would be expected to show a sharp change in PV values. However, there is some debate in the literature as to which value best describes the dynamic tropopause.

The *World Meteorological Organization* [1986] defines the dynamic tropopause to be 1.6 PVU. *Zängl and Hoinka* [2001] state that tropospheric air has a PV of $\lesssim$1 PVU and stratospheric air of >5 PVU, and these values agree with most studies. However, the values between 1-5 PVU give the possible range for the dynamic tropopause.

Some studies use the 1.6 PVU limit for their dynamic tropopause [*Hoinka et al.*, 1993; *Van Haver et al.*, 1996], with one using a lower limit of 1 PVU [*Bithell et al.*, 2000] although it was stated that the value was conservative and may still be located within the troposphere. Many locate the dynamic tropopause at 2 PVU [*Seo and Bowman*, 2002; *Sprenger et al.*, 2003; *Stohl et al.*, 2003; *Wernli and Bourqui*, 2002], particularly those that use the Holton style model displayed in Figures 2.5 and 2.6. A higher value of 3.5 PVU is also very common [*Birner et al.*, 2002; *Hoerling et al.*, 1991; *Jing et al.*, 2004; *Zängl and Hoinka*, 2001].

2.1.4 Chemical Tropopause

The tropopause can also be defined using the distributions of ozone and water vapour to form the ozonopause and hygropause, respectively. It should be noted that these definitions are rarely used. The ozonopause and hygropause are based on the fact that there are significant cross-tropopause gradients for ozone and water vapour between potential temperatures of 300-340 K [*Esler et al.*, 2001].

The ozonopause is defined as the region where there is a sharp transition from low concentrations of ozone in the troposphere to higher concentrations of ozone in the stratosphere [*Stohl et al.*, 2003]. More specifically, a definition is given in *Baray et al.* [1999] as "the height where the vertical ozone gradients goes up from the tropospheric value of 5 ppbv km^{-1} to the stratospheric value of 50 ppbv km^{-1}"

The hygropause is able to be calculated as the water vapor mixing ratio decreases sharply in the upper troposphere. A minimum of a few ppmv is reached at the point called the hygropause. Water vapor increases above the hygropause as a result of the oxidation of methane. In the tropics it is possible to have the hygropause up to 18 km high. [*Salby*, 1996]

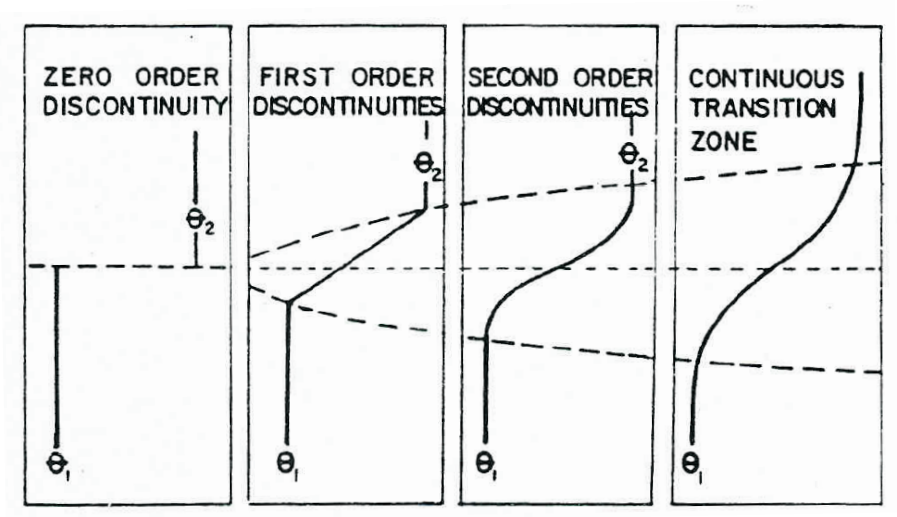

Figure 2.2: Transition types between the troposphere and stratosphere. The thickness of the transition layer is the region between the dashed lines. Figure from *Hoinka* [1997].

A further use of a chemical tropopause is discussed in Section 2.1.5, where the chemical tropopause is defined in relation to the mixing layer [*Zahn and Brenninkmeijer*, 2003], or the mixing line [*Pan et al.*, 2004].

2.1.5 Layer Tropopause and Tracer Space

The above definitions treat the tropopause as a level or surface in the atmosphere, however, recent studies such as *Pan et al.* [2004] and *Fischer et al.* [2000] indicated that this region may more accurately be defined as a layer. Figure 2.2 shows several different mathematical forms that can approximate the tropopause. The thickness of the tropopause layer is the region between the dashed lines. The previous definitions for the tropopause (eg. thermal, dynamic) view the tropopause as a zero order discontinuity.

The utility of the tropopause definition as a layer becomes evident when examining the distribution of tracers with respect to one another. A tracer is a chemical or property present in a parcel of air which allows the movement of the air to be tracked. In particular, tracers which are representative of the troposphere (eg. H_2O) and the stratosphere (eg. O_3) can be examined with respect to one another to allow atmospheric properties and processes to be studied.

Each tracers is measured as a mixing ratio with respect to height. Tracer space is then created by plotting the two tracers with respect to one another, that is

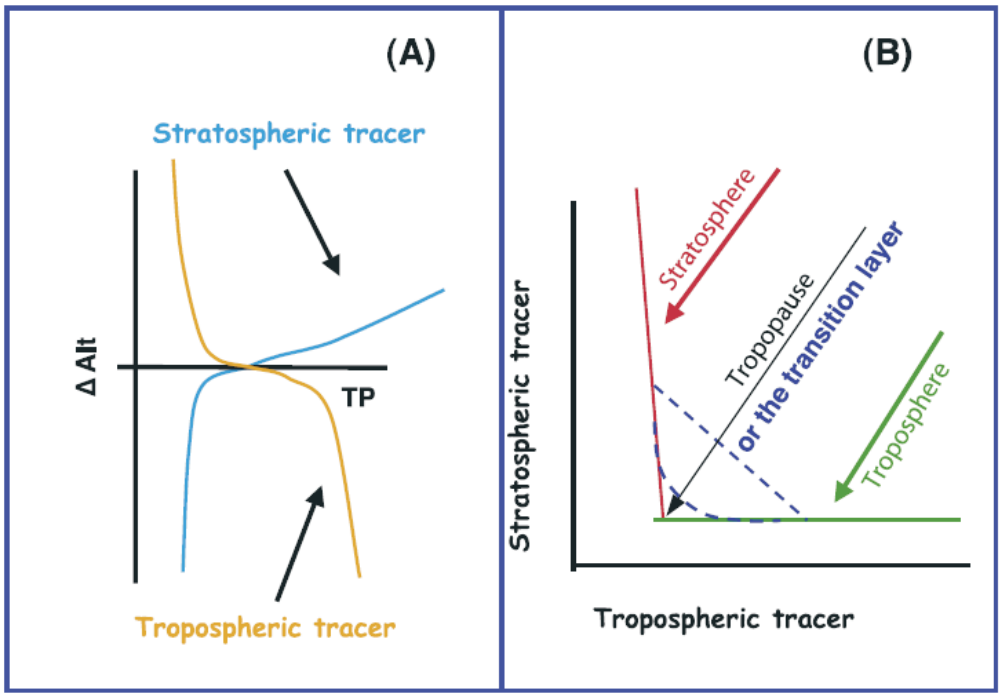

Figure 2.3: Relationship between stratospheric and tropospheric tracers and tracer space. Dashed lines in (b) show mixing lines, which can be curved or straight. Note that the convention as to which tracer is displayed on which axes varies between papers. Figure from *Pan et al.* [2004].

with one on the x-axis and the other on the y-axis. This situation is illustrated in Figure 2.3a using tropopause relative vertical coordinates. The easiest way to view the tropopause layer is using tracer space as shown in Figure 2.3b. Mixing lines are indicated in Figure 2.3b by the dashed lines and describe the relationship and mixing processes between the tracers. By studying the shape of the line, and how far it deviates from the origin, some information can be obtained as to the mixing process involved. Different points along a mixing line can be though of as having different proportions of stratospheric and tropospheric air. Mixing lines can be curved, indicating different strengths of mixing at different distances from the stratosphere or troposphere. Or mixing lines can be straight, indicating constant mixing throughout the region. The origin and a more detailed discussion of how mixing lines, tracer space and mixing process are related can be found in Chapter 6, as mixing lines and tracer space are key to the work from Chapter 6 onwards.

Tracer space allows us to define the relationship between two chemicals that have different sources or distributions in the atmosphere. In this study, a tracer which

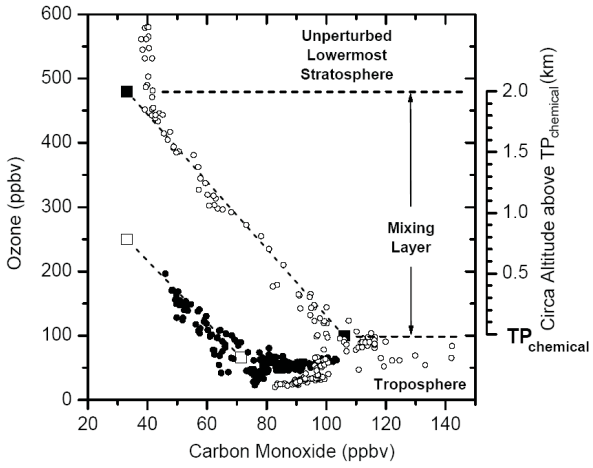

Figure 2.4: Mixing layer is indicated in an ozone/carbon monoxide tracer space. Mixing lines are shown by the dashed lines between the box markers. Figure is from *Zahn and Brenninkmeijer* [2003], where the chemical tropopause is defined as the top of the troposphere before the mixing layer begins.

represents stratospheric origin and one which represents tropospheric origin are utilised. Figure 2.3a shows the relationship of these two tracers with respect to the tropopause. This shows that there is a narrow region where both stratospheric and tropospheric tracers are both present at significant concentrations. Tracer space can be used to highlight air with anomalous properties and potentially the presence of mixing [*Hegglin et al.*, 2004].

The layer which defines the tropopause is commonly called the transition or mixing layer. An illustration of this mixing layer is shown in Figure 2.4, where the mixing layer is defined as the altitude difference between the measurements at either end of the mixing line. The mixing line that is further from the origin shows mixing over a deeper region than the other mixing line. The position of an air parcel along the mixing line indicates the quantity of mixing, as is discussed at the beginning of Chapter 6.

Figure 2.4 uses a definition of the chemical tropopause, where the chemical tropopause is the lower altitude limit of the mixing layer. This varies from the chemical tropopause defined by *Pan et al.* [2004] which is defined as the mid-point of the mixing line as shown in Figure 2.3. The ability to use tracer space as a means to determine layer depth is discussed in Section 6.2.

2.1.6 Over-, Middle- and Under- world

An alternative method to viewing STE as transport across a boundary or a layer is to view it as transport between regions in the atmosphere. These regions are typically defined using potential vorticity (PV) surfaces and isentropic (constant potential temperature) surfaces [*Hoskins*, 1991; *Holton et al.*, 1995; *Stohl et al.*, 2003; *Yang and Tung*, 1996]. A common definition for dividing the atmosphere into regions from *Stohl et al.* [2003] is as follows:

Overworld The region which is above the 380 K isentropic surface and lies entirely in the stratosphere.

Middleworld The region between the 380 K isentropic surface and the dynamic tropopause. Isentropic surfaces in the middleworld lie partially in the troposphere, and partially in the stratosphere. The middleworld is important for STE as transport can occur adiabatically along the isentropes between the middle- and under- world.

Underworld The region below the dynamic tropopause and is entirely within the troposphere.

The division between the middle- and under- world is the dynamic tropopause (see Section 2.1.3). The division between the middle- and upper- world occurs at the 380 K isentrope, which is usually equivalent to the thermal tropopause at the tropics. This is shown diagrammatically in Figure 2.5. PV cannot be used in the tropics as the calculation requires the Coriolis parameter which is latitude dependant. Often the dynamic definition is used up to the midlatitudes, the thermal definition for the tropics, and the region in between is extrapolated.

Horizontal mixing can occur either along isentropes (adiabatic) or across isentropes (diabatic). As isentropes are surfaces of constant potential temperature, adiabatic process require no heat exchange and are hence easier to occur. In comparison, diabatic process require either heating or cooling, and are therefore more difficult than adiabatic processes. Hence, mixing between the underworld and the middleworld, where there are common isentropic surfaces, can be significantly faster than between the middleworld and overworld, where all transport processes must be diabatic.

However, there are some barriers to adiabatic transport. While no heat exchange is required, *Holton et al.* [1995] mentions that there must be some resistance

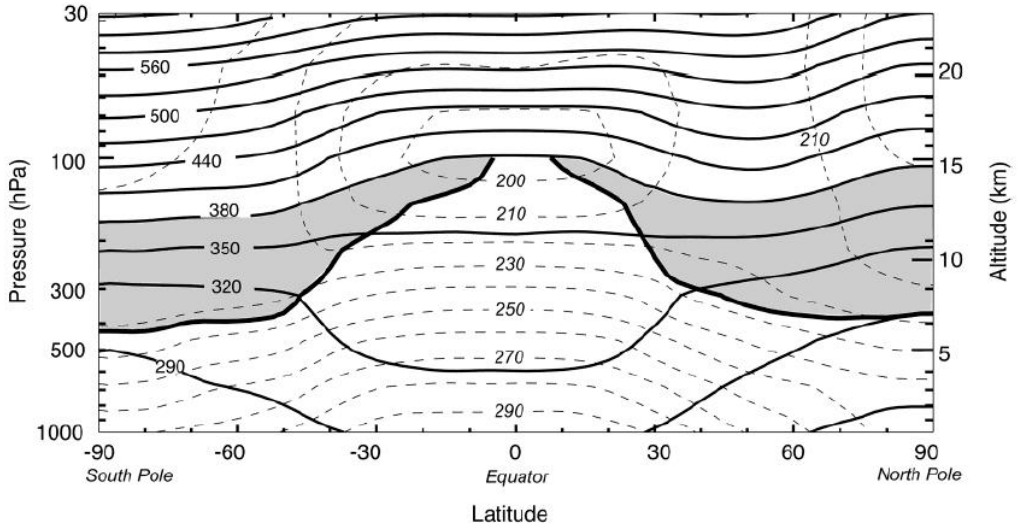

Figure 2.5: Division of atmosphere into different worlds based on the dynamic tropopause (2PV, thick solid line) and isentropes (solid lines). Also marked are temperature contours (dashed lines). The overworld is the region above the 380 K isentrope. The middleworld is shaded grey, with the remaining region the underworld. Figure from *Shepherd* [2003] after *Holton et al.* [1995].

against isentropic transport as there is a band of strong gradients in PV, ozone, water vapour and a number of other species, on isentropic surfaces at midlatitudes. These create barriers along isentropic transport surfaces and reduce the occurrence of adiabatic mixing. Resistance to adiabatic transport is provided by the Rossby-wave restoring mechanism, which creates a band of strong PV gradients.

General processes for exchange are discussed in more depth in the following section. Figure 2.5 shows the form of the isentropes in the atmosphere, thereby indicating the preferred paths for isentropic/adiabatic transport.

The mixing region in the atmosphere between the stratosphere and troposphere can also be described by the terms upper troposphere (UT) and lower stratosphere (LS). Generally these are vague definitions to describe the region around the tropopause. One definition of the LS found in *Holton et al.* [1995] makes it the equivalent of the middleworld, however, in practice this definition is not used. The UTLS region can be identified as the region where the properties of the atmosphere transit from tropospheric to stratospheric, and is closely related to the idea of the "tropopause" as a layer.

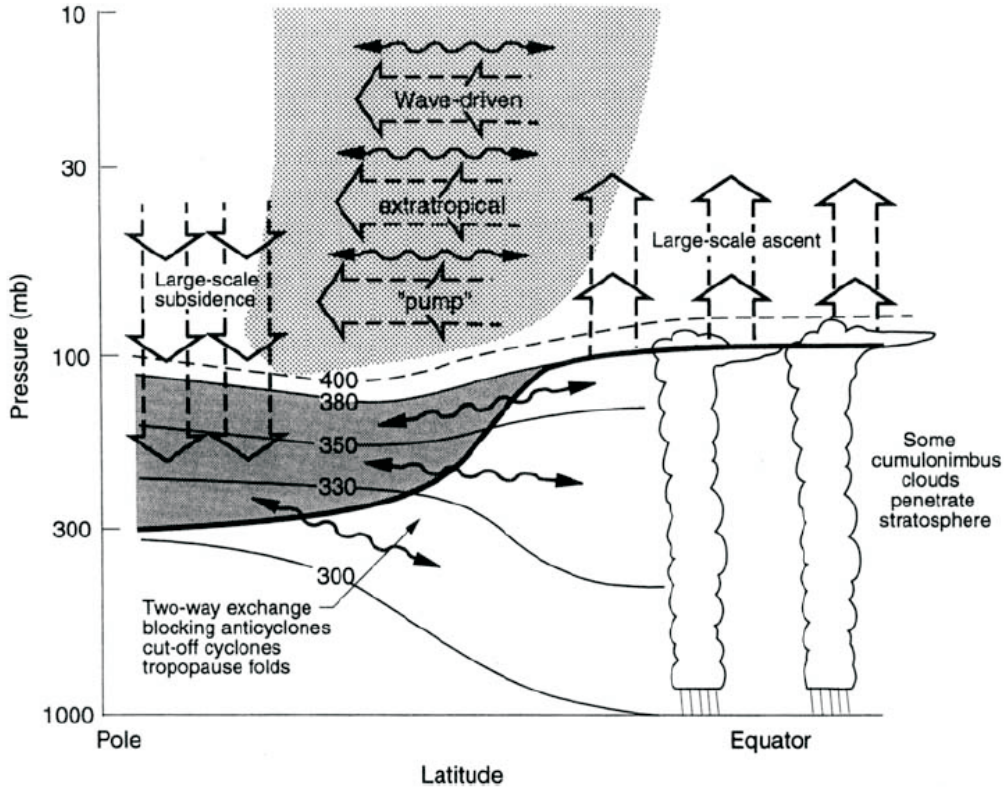

Figure 2.6: Transport mechanisms between the stratosphere and the troposphere. Tropopause is shown as the thick dark line, with isentropes as thin solid lines. Large scale processes are indicated by the large arrows, with small processes by the smaller wavy arrows. Figure from *Stohl et al.* [2003] after *Holton et al.* [1995].

2.2 Mechanisms for Transport/Mixing between the Troposphere and Stratosphere

A clear picture of the boundary between the troposphere and stratosphere, along with an overview of how the different parts of the atmosphere are related isentropically, has been established. It is now possible to look at the mechanisms that cause exchange between the troposphere and the stratosphere.

The main meridional circulation in the stratosphere is the Brewer-Dobson circulation. Transport in the lower stratosphere is a two-cell system where air rises in the tropics and descends at mid and high latitudes. At higher altitudes there is a single cell that rises in the tropics and descends in the winter hemisphere. Transport in the troposphere is overturning at the equator with larger cells from the equator to the poles [*Plumb*, 2002]. Figure 2.6 shows this large scale meridional circulation in the stratosphere indicated by the large arrows.

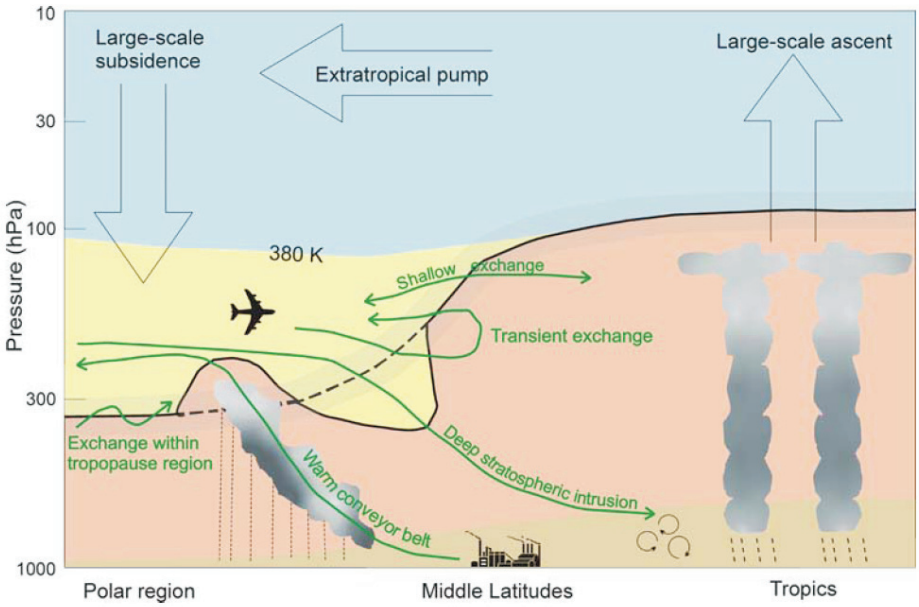

Figure 2.7: A more complete view of transport mechanisms between the stratosphere and the troposphere showing smaller and transient exchange. Tropopause is indicated by the solid line, large scale processes by the large arrows, and small scale processes by the thin arrows. The overworld is shaded blue, the middleworld is shaded yellow and the underworld is shaded pink. Figure from [*Stohl et al.*, 2003].

In Figure 2.6, the smaller scale transport is indicated by the smaller wavy arrows. Note that the arrows being double headed does not indicate that the exchange is equal in both directions, rather that exchange can occur in both directions. The processes represented by the wavy arrows include tropospheric troughs, cutoff lows (COLs) and tropopause folds (TPFs) and isentropic transport. COLs and TPFs are discussed in more detail in Sections 2.2.1 and 2.2.2, respectively.

While Figure 2.6 is useful for visualising transport, it fails to take into account short time scale processes and small spatial scale processes. It also fails to show deformations in the tropopause layer. As mentioned earlier, most exchange is thought to be only temporary, hence it is important to include these effects in the understanding of exchange to assess their impact. This leads to the development of Figure 2.7, where a number of smaller processes are included, such as transient exchange and exchange within the tropopause region. These processes are shown by the green arrows. Of note in Figure 2.7, with regards to large scale transport, is that the cumulonimbus clouds in the tropics no longer reach the stratosphere, as newer studies have shown this to be the case [*Stohl et al.*, 2003].

Leclair De Bellevue et al. [2006] found from observations that cyclones and deep

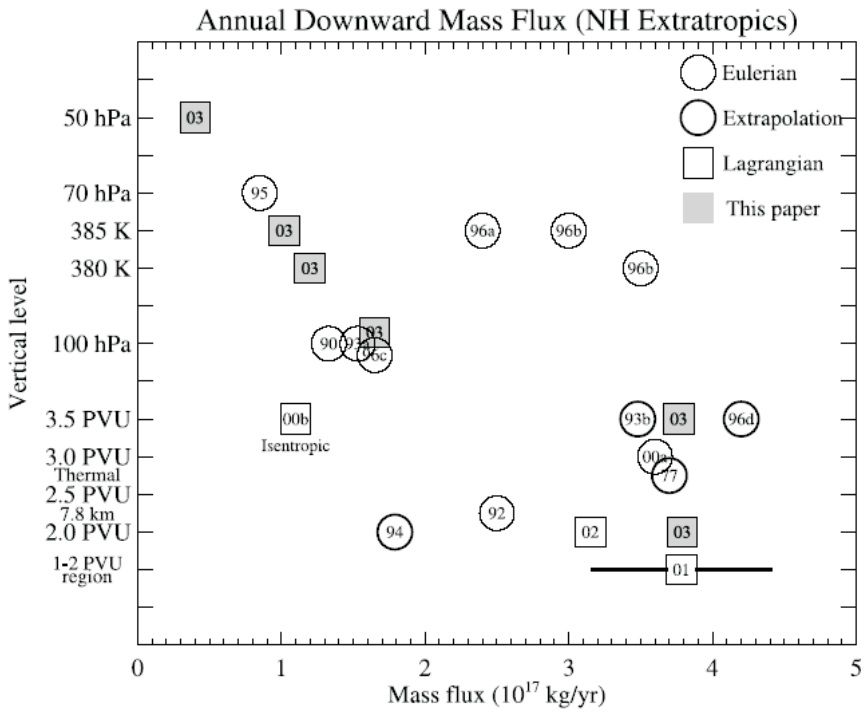

Figure 2.8: Annual total northern extratropical net STT in units of 10^{17} kg yr^{-1}. Comparisons from 17 different papers using different calculation methods. Note that the numbers on the points refer to the year the paper the value came from was published, for further details see *Seo and Bowman* [2002]. Figure from *Seo and Bowman* [2002].

convection are likely to produce exchange between the LS and UT, especially when there are interactions with the jet stream. From *Stohl et al.* [2003], TPFs and COLs are associated with large latitudinal displacements of the tropopause on isentropic surfaces which facilitate the exchange of air.

A common way to quantify STE is to use models to measure the amount of exchange between the troposphere and stratosphere. There are a number of different types of models that can be used, such as general circulation models, or trajectory models using Lagrangian or Eulerian transport schemes. Each model type has a different method of tracking exchange, along with different input data driving the model and different definitions as to what counts as exchange, such as what PV value to use for the dynamic tropopause. As a result of the different model frameworks and definitions of exchange, studies often provide very different estimates of the amount of exchange. This is summarised in a study by *Seo and Bowman* [2002] where a number of different results are shown in Figure 2.8. This shows that while there is some agreement between the different methods, in general there are too many different methods and parameters. The impact of

model differences is further confirmed by *Cristofanelli et al.* [2003], where they compare seven different models using the same input data to generate STT events. This showed that while they all capture the same general behaviour, there are differences in the intensity and spatial development of STT events.

One of the methods indicated in Figure 2.8 is extrapolation. This method calculates the mass exchange by extrapolating the exchange from a single event, such as a tropopause fold or baroclinic disturbance. *Lamarque and Hess* [1994] made an estimate of the number of tropopause fold events in the Northern Hemisphere, and an estimate of the amount of exchange in a single tropopause fold event from a model. Using these estimates, a value is calculated for the total mass exchange in the Northern Hemisphere for a year. Note that this assumes that all tropopause folds are the same as the one modelled.

While an exact numerical value for mass exchange cannot be identified, there are some useful outcomes of these types of studies. In general the proportions of flux are similar between studies, along with the key regions for exchange. Therefore, while the numerical values lack meaning due to the range between studies, the processes they describe are still of use. One example from *Yang and Tung* [1996] is shown in Figure 2.9, where the exchange in different regions of the atmosphere can be observed using a radiative transfer model and three years of UKMO[†] and UARS[‡] data. In general there is upward flux in the tropics and downward flux in the extratropics. Roughly 40% of the mass passing over the 385 K surface never passes over the 444 K surface. There is asymmetry between the hemispheres, and much of this is accounted for by larger poleward movement in the Northern Hemisphere (NH).

A similar pattern is observed by *Rosenlof and Holton* [1993], where the dominant movement across the 100 hPa surface (approximately 380 K) is upwards in the tropics and downwards at midlatitudes. The upwelling in the tropics is stronger during December to February than June to August, along with the mean downwards flux across the 100 hPa surface being stronger in the Northern Hemisphere extratropics.

Olsen et al. [2003] show, using PV and ozone flux, that the greater flux in the NH, compared to the Southern Hemisphere (SH), is mostly due to the larger amounts of ozone available for exchange in the NH, rather than differences in

[†]UKMO: United Kingdom Meteorological Office
[‡]UARS: Upper Atmosphere Research Satellite

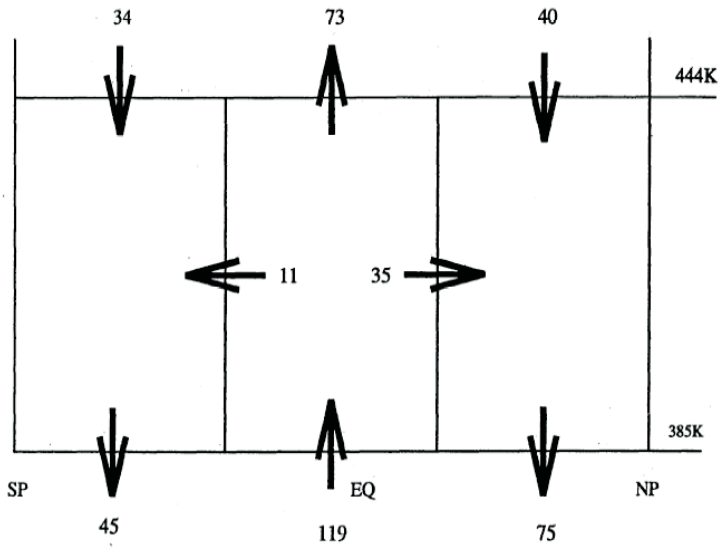

Figure 2.9: Transport across isentropic surfaces for different portions of the atmosphere. All values are $\times 10^8 kgs^{-1}$. Note that the lower surface (385 K) is approximately the middle/overworld boundary. The upper surface (440 K) is located in the overworld. Figure from *Yang and Tung* [1996].

the dynamical structure. 80-100% of the STT of ozone occurs at latitudes less than 60°, with the net transport mainly downwards in the midlatitude region and upwards in the tropics. The changeover from upwards to downwards motion occurs roughly at the subtropic jet, between 30° in winter to 45° in summer. The hemispheric asymmetry is also effected by the Brewer-Dobson circulation which is 2-3 times stronger in the Boreal winter than in the Austral winter [*Holton et al.*, 1995].

Other studies examine flux or exchange across a given surface (eg. thermal tropopause or 380 K) as a function of location rather than a single global value for exchange. An example is *Sprenger et al.* [2003], where the locational mass flux across the dynamic tropopause is calculated globally using ECMWF data and a Lagrangian trajectory model. The mass flux is then presented as values on a world map. Using a similar method, *Wernli and Bourqui* [2002] show the locational mass flux for the Northern Hemisphere only. *Olsen et al.* [2004] examines the flux across the 380 K surface and *Seo and Bowman* [2001] examines the flux across the dynamic tropopause on several isentropic surfaces. Each of the studies highlight regions where STE has a greater preference, that is, the mass flux is higher in some locations than others. Some of these studies also display differences in the flux between seasons. A number of these studies are discussed in later sections.

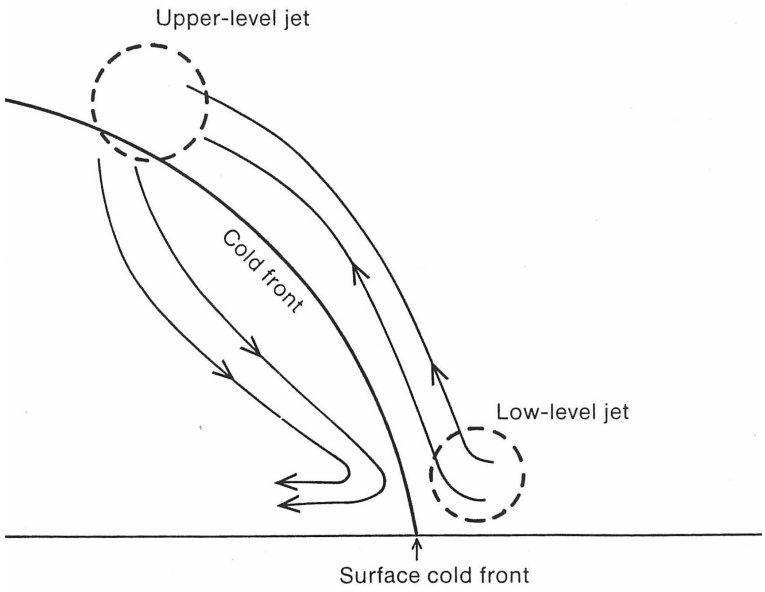

Figure 2.10: Cross frontal geostrophic motion. Figure from *Bennetts et al.* [1988].

2.2.1 Tropopause Folds - TPFs

Tropopause folds (TPFs) are regions where a tongue of stratospheric air has intruded into the troposphere. These are generally associated with regions where there is a horizontal boundary between air masses, such as in a frontal region. In a frontal region there are two main types of flow, those along the front and those across the front. Ageostrophic motion in a frontal region is driven through changes in the air motion along the front. This creates a cross frontal movement of closed circular loops. The addition of an upper level jet to the frontal region eliminates the necessity of cross frontal movement. As a result, this allows dry stratospheric air to be brought down into the troposphere behind the frontal region [*Bennetts et al.*, 1988], as is shown in Figure 2.10. This is essentially the key movement in TPFs.

In frontal regions there are several types of air streams or conveyor belts. *Cooper et al.* [2002] list these as warm conveyor belt, cold conveyor belt, dry air stream and post cold front air stream. The warm conveyor belt contains warm moist air, which rises just ahead of the surface of the front. This movement is further responsible for the downward air movement to balance the air movement in the frontal region [*Bennetts et al.*, 1988].

Note that while the airstreams move as coherent features, there will also be

smaller scale mixing occurring at the extremities. This will act to blur the signatures of the different air streams [*Cooper et al.*, 2002]. As a result, TPF regions may have characteristics of both the troposphere and the stratosphere [*Shapiro*, 1980], particularly along the "edges" of the TPF.

Typically TPFs are identified by looking for regions of air in the troposphere that have a stratospheric signature. There are several different data types used for identifying TPFs, including ozonesondes [*Van Haver et al.*, 1996; *Blonsky and Speth*, 1998], satellite imagery [*Wimmers et al.*, 2003], reanalysis data [*Sprenger et al.*, 2003; *Elbern et al.*, 1998], lidar [*Eisele et al.*, 1999], radar [*Rao and Kirkwood*, 2005] and aircraft [*Gouget*, 2000; *Pan et al.*, 2007b; *Danielsen et al.*, 1987].

Price and Vaughan [1993] suggest that for TPFs the sharpness of the tropopause can indicate whether transfer occurred. For example, an indistinct tropopause could show a mixing of two different air masses causing the stability of the region to gradually change. Whereas, a distinct tropopause would suggest little mixing and hence no transfer. In light of the idea of thinking about the tropopause as a layer rather than a level, we would interpret that an indistinct tropopause is possibly related to a thicker tropopause layer and representative of more mixing.

A study by *Van Haver et al.* [1996] uses ozonesondes from Uccle in Belgium ($50°48'$N $4°21'E$) and Observatorie de Haute Provence (OHP) in South France ($43°54'$N $5°45'E$) to investigate TPFs. An algorithm for identifying TPFs from ozonesondes is developed in their paper, then the results compared to a 1.6PVU surface from the ECMWF[§] analysis. The 25 year data set from Uccle showed TPFs in 4.8% of the soundings, whereas the 8 year data set from OHP only displayed 2% of observations where a TPFs could be identified. There was little seasonal variation in the occurrence of TPFs, however, the soundings showed a higher ozone content in the folds during the spring and early summer. The algorithm from *Van Haver et al.* [1996] is the basis of the work detailed in Chapter 4.

Olsen et al. [2002] show that not all baroclinc[††] systems and TPFs transport the same amount of ozone to the the troposphere which can be spatially or seasonally dependent. The most extensive TPFs are associated with very strong jets [*Holton et al.*, 1995; *Price and Vaughan*, 1993; *Shapiro*, 1980].

[§]European Centre for Medium-Range Weather Forecasts

[††]Baroclinic: Isotherms and isobars cross each other which may result in warm or cold advection. [*Sturman and Tapper*, 1996]

Intrusions of stratospheric air into the troposphere always occur on the cyclonic (poleward) side of the jet stream [*Danielsen et al.*, 1987]. This is observed both in frontal regions and in regions on cyclogenesis.

2.2.2 Cutoff Lows - COLs

Price and Vaughan [1993] describe cutoff lows (COLs) as isolated cyclonic vortices in the upper level flow and can be identified by isolated regions of high PV. COLs are often treated as separate types of events from TPFs, however, *Ancellet et al.* [1994] state the following:

> "Although the transport of ozone by tropopause folding and the one by cutoff low evolution are often described as two separate processes; they are in fact strongly linked since a tropopause fold will generally form on the flank of a cutoff low, where an intense upper level frontogenesis is present."

Transfer mechanisms in a COL include convective erosion, turbulence near jet streams, tropopause folding, re-intensification of COL systems and radiative effects[*Price and Vaughan*, 1993].

COLs are more often found in the NH during summer and their geographical location is determined by the location of the jet streams as they either form equatorward of the jet or as an extension of the jet stream [*Price and Vaughan*, 1992]. *Fuenzalida et al.* [2005] found that in the SH COLs are more frequent in the winter, opposite to the maxima in the NH. In the NH this is related to the weakening of the mid level westerlies during the summer, whereas there is only a weak seasonality in the SH, which would suggest other factors are more important. A climatology of the occurrence of COLs in the SH from NCEP/NCAR reanalysis (NNR) is shown in Figure 2.11. This figure shows that COLs are more frequent equatorward of high wind speeds. Note that this figure shows the wind speed at 500 hPa, whereas the jet stream tends to be at approximately 200 hPa. For the jet stream location, refer to Figure 3.3 where the occurrence of the jet stream from the NNR is shown.

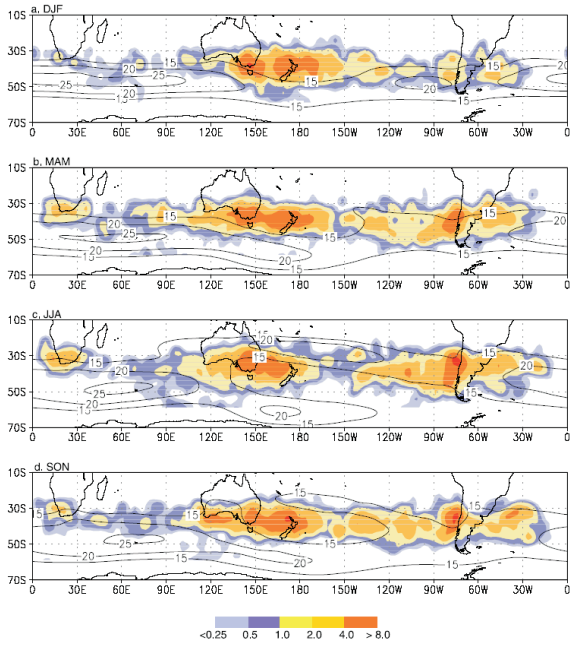

Figure 2.11: Seasonal average of the number of COLs in a $2.5° \times 2.5°$ box normalised by area. Contours show the climatological mean at 500 hPa for zonal wind in ms^{-1}. Figure from *Fuenzalida et al.* [2005].

2.3 Conclusion

This chapter has detailed many of the definitions used for the boundary between the troposphere and stratosphere. It is crucial to have an understanding of the boundary between the stratosphere and the troposphere as this can greatly affect the outcome of any exchange studies. Small variations in the definition can create a large difference in the amount of exchange measured. For this thesis, the tropopause layer definition and the use of tracer space are used intensively and are further described in Chapter 6.

There are a number of different processes that contribute to STE. These processes have varying levels of impact based on their size, location and frequency. STE has been studied using both global and location specific methods and a range of different data sets.

Chapter 3

Data sets

Stratosphere troposphere exchange (STE) can be studied using a number of different types of data from different instruments. The most common measurement methods used are instruments located on aircraft, balloon sondes and satellites. Alternatively, STE can be studied using reanalysis data from modelling. Often there is a trade off between vertical resolution, spatial coverage and the temporal range of the data. Generally, data can have high vertical resolution observations but be location specific such as data from aircraft measurements, or can have good spatial coverage but poor vertical resolution as with some satellites measurements.

The work presented in this thesis uses four different data sets - ozonesondes, hygrometers,[§] reanalysis data and satellite data from the Atmospheric Infrared Sounder (AIRS) onboard the Aqua satellite. These different data sets provide a range of different vertical resolutions, spatial and temporal coverage. A detailed description of each of the data sets is presented in this chapter.

3.1 Ozonesondes

Ozonesondes are balloon based instruments that measure ozone, temperature, pressure and humidity.* An example of a typical ozonesonde profile is shown in Figure 3.1, where the ozone mixing ratio, temperature and humidity vary with height. This study utilises ozonesondes launched from Lauder (45.0°S, 169.7°E) and Boulder (39.9°N, 105.3°W) at approximately weekly intervals, however, during measurement campaigns this frequency may be higher. There are 1337

[§]Note that some of the ozonesondes and hygrometers are flown on the same balloon and are used in conjunction with one another.

*Some also measure the location of the ozonesonde in latitude and longitude, along with wind speed.

ozonesondes available for study at Lauder from August 1986 to May 2007, and 111 lower vertical resolution sondes at Boulder from August 2002 to September 2005.[†] Frost point hygrometers are also flown on occasion with the ozonesondes and are discussed in further detail in Section 3.2. There are 15 valid hygrometer flights at Lauder (included in the 1337) and an additional 45[‡] at Boulder with coincident higher resolution ozonesondes. The lower resolution Boulder ozonesondes are pre-processed prior to obtaining the data to a vertical resolution of 250 m. The higher resolution Boulder ozonesondes have a mean vertical resolution of 6.8 m. Approximately 0.3% of the data had height differences >30 m, and 1.7% with ≥20 m. For the AIRS validation in Chapter 5, the 250 m resolution for the Boulder ozonesondes is sufficient as the AIRS vertical resolution is sufficiently low and a larger number of ozonesondes is preferable for better statistical confidence. For the tropopause fold studies in Chapter 4 and the entropy work in Chapters 6 and 8, the higher vertical resolution Boulder ozonesondes are used as the resolution of the ozonesondes can affect the outcome of the analysis.

There have been several instrument changes in the 21 year record at Lauder, which mainly affects the vertical resolution of the measurements as a consequence of faster measurement times. The height resolution in relation to the instruments is shown in Table 3.1. From August 1986 to October 1989, type 4A ECC (electrochemical concentration cell) ozonesondes were used. From August 1989 to June 1994, the ozonesonde type was changed to 5A ECC ozonesondes. Since July 1994, mainly type 1Z ECC ozonesondes have been used, although a number of 2Z have also been used. The type 4A ozonesondes are not used for some of the analysis due to their low vertical resolution. The Boulder measurements, both high and low resolution, are type 2Z ECC ozonesondes.

ECC ozonesondes contain a pump and a sensor made up of a KI (potassium iodide) cathode-anode cell. An ozone molecule entering the sensor causes the formation of iodide resulting in a current flowing in the cell. The ozone concentration is calculated based on the sensor current and the pump airflow rate [*Boyd et al.*, 1998].

The seasonal distribution for the release of ozonesondes is important as it determines whether results are biased by the measurement times. At Lauder, from

[†]Ozonesondes are an ongoing data set at both Lauder and Boulder.

[‡]Some of these 45 are included in the 111, some are not. These data sets were provide by two different sources, hence the differences in resolution and temporal coverage.

For the AIRS validation, only the lower resolution ozonesondes are used. For later work requiring the hygrometers, only the 45 ozonesonde/hygrometers are used.

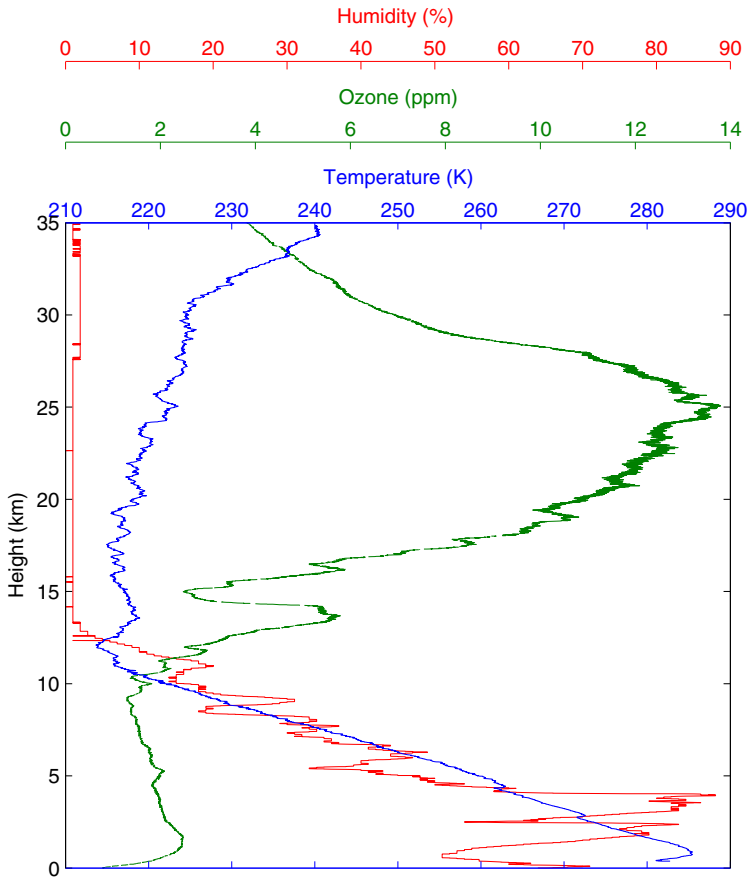

Figure 3.1: An example of a typical ozonesonde profile, showing temperature in blue, ozone mixing ratio in green and humidity in red. Ozonesonde is from Lauder, NZ on 18th April 2001.

Table 3.1: Lauder ozonesonde height resolution.

	mean (m)	median (m)	sigma (m)	% of differences* >40 m	>30 m	>20 m
1986 to 1990	234.19	255	85.45	-	98.2	99.7
1990 to 1998	32.26	32	15.46	17.2	58.6	90.4
1998 to 2007	7.61	7	8.91	0.6	1.8	3.1

* The final three columns give the percentage of the altitude differences that are smaller than the given value.

1990 to 2007, the number of ozonesondes launched per season are as follows: DJF-260, MAM-256, JJA-248, SON-334. More ozonesondes are released during the spring months due to the interest in the break up of the ozone hole during this period. At Boulder the release of ozonesondes is roughly even as a function of season.

The ECC 1Z-series ozonesondes operate with a 0.5% buffered KI cathode solution [*Boyd et al.*, 1998]. Corrections are also applied to the ozonesonde values above 200 hPa to account for pump efficiency degradation [*Bodeker et al.*, 1998]. The response time of ozonesondes results in an overestimation of the altitude by about 150m [*Brinksma et al.*, 2000].

The ozone profile uncertainty at Lauder, as determined by Monte Carlo simulation, is less than 5% in the troposphere, 2-4% in the stratosphere up to about 30 km, and 4-7.5% between 30-35 km. The maximum error below 30 km occurs around the tropopause [*Bodeker et al.*, 1998]. The downwind drift of the Lauder ozonesondes causes very small differences in ozone measurements when compared to a directly vertical ozone profile from lidar.

Boulder ozonesondes are EN-SCI 2Z-type ozonesondes operating with a 2% unbuffered KI cathode solution. They have an accuracy of about 10% for tropospheric mixing ratios, except for very low mixing ratios (i.e.<10 ppb) when accuracy is 15% [*Newchurch et al.*, 2003]. Comparisons of the column ozone from these ozonesonde measurements and those from Total Ozone Mapping Spectrometer (TOMS) overpasses indicate agreement to within 2%.

3.2 Hygrometers

The hygrometers flown coincidentally with ozonesondes have been discussed briefly in Section 3.1 with regards to the number flown and the location. The hygrometer data used is from Cryogenic Frostpoint Hygrometers (CFH) built at the University of Colorado. *Vömel et al.* [2007] describe how the CFH operates to make measurements of water vapour. The CFH is based on the chilled mirror principle where a constant layer of condensate is maintained on a temperature controlled mirror. Changes in the frost or dew coverage on the mirror are measured by a photodiode using reflected LED light off the mirror, allowing measurements of water vapour to be determined. CFH can be used both for day and night measurements and are a very accurate research quality instrument. Pairing the hygrometer with the ozonesonde allows coincident measurements of ozone, temperature and water vapour.

At Lauder CFH are operated using balloons with a valve which allows the balloon to descend before the balloon pops. Water vapour measurements are then only used on the descent leg of the flight to ensure correct functioning of the CFH and to avoid contamination from the rising balloon. However, some contamination from condensation forming on the balloon is often detected around the turning point of the flight (ie. when the direction changes from ascent to descent). This contamination manifests itself as unusually high water vapour measurements which can be easily removed from the data set.

As water vapour and relative humidity are closely related, the CFH can be compared to instruments that measure water vapour or humidity. *Vömel et al.* [2007] showed that the CFH measurements have good agreement with older NOAA/CMDL[§] frostpoint hygrometer and with Aura Microwave Limb Sounder (MLS) measurements. A large disagreement was observed between the CFH and the Harvard Lyman-α hygrometer, which is an aircraft-based instrument. However, this is commonly seen whenever the Harvard instrument has been compared with balloon based instruments.

Humidity is usually measured by radiosondes, which are released with high frequency over the whole globe. Two thirds of the global radiosonde stations fly RS80 radiosondes, which have a correctable time lag error and have problems when the flight path passes through clouds. The remainder of the stations fly

[§]NOAA: National Oceanic and Atmospheric Administration, CMDL: Climate Monitoring and Diagnostics Laboratory.

Sippican radiosondes, which have poor water vapour measurements in the upper troposphere when compared to other instruments. This is due to limitations in the design where humidity measurements essentially cannot be made below -40° C [*Miloshevich et al.*, 2006]. RS90 or RS92 are considered the most accurate radiosondes for humidity measurements, as they are less variable and are capable of measurements above cloud layers. The mean difference in relative humidity between RS92 radiosondes and CFH measurements is less than 3% through the entire troposphere [*Vömel et al.*, 2007].

3.3 NCEP/NCAR Reanalysis - NNR

The National Center for Environmental Prediction (NCEP) and the National Center for Atmospheric Research (NCAR) have a joint reanalysis project known as the NCEP/NCAR reanalyses (NNR). A number of data sets, including land surface, ship, radiosonde, pibal (pilot weather balloon), aircraft, satellite and others, are used as inputs into a data assimilation model to produce global fields of a number of different products, from 1948 to the present [*Kistler et al.*, 2001].

The data assimilation has 3 different phases based on the amount and types of data used in the reanalyses. Prior to 1958 there is a very limited amount of data available, particularly from upper air observations. The observation coverage from 1946 to 1998 is shown in Figure 3.2. Between 1958-1978, the modern radiosonde network has a large impact on the number of observations used in the reanalyses, although there were very few observations in the Southern Hemisphere. A lack of observational input into the reanalyses results in the output parameters being mainly model based and hence less reliable. Note that radiosondes are much more important for reanalyses than surface measurements. Post 1979, satellite data was available for assimilation, resulting in a much larger number of observations and a greater global coverage, with only the extreme polar regions still having low observation numbers. Due to the large changes in the data assimilation, NNR should not be used for analysing trends, and pre and post 1979 data should be calculated separately [*Kistler et al.*, 2001].

There are three different categories for the products derived from the NNR, based on how strongly they are influenced by the input data and the model. Type A variables are the most reliable products as they are strongly influenced by the

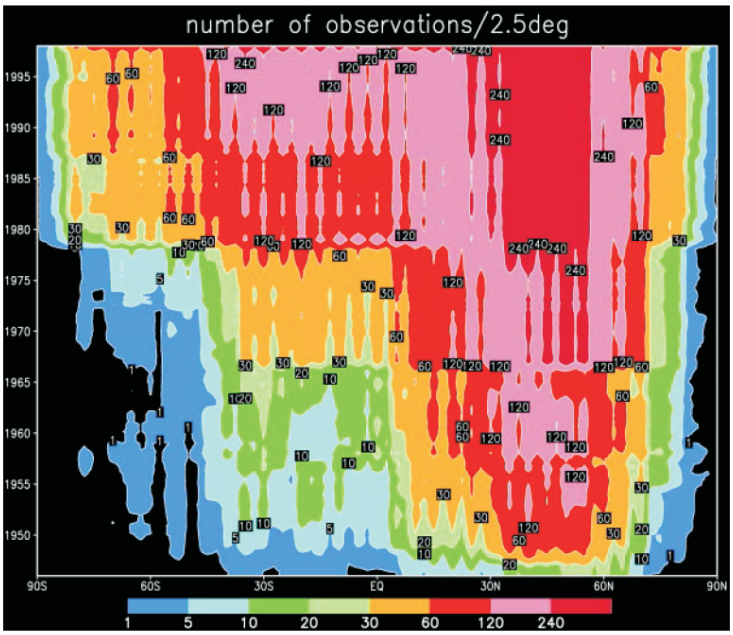

Figure 3.2: Zonal mean number of observations used in the NCEP/NCAR reanalysis data per 2.5° lat-long box per month from 1946 to 1998 (y-axis). A 12-month running mean has been applied. Latitude is given on the x axis, from 90°S to 90°N. Figure from *Kistler et al.* [2001].

input data. These variables include upper air temperature, wind* and geopotential height. Type B variables are influenced more by the model and hence are less reliable. Some examples of type B variables include moisture variables and surface parameters. Type C variables are entirely from the model and are the least reliable. These include surface fluxes and heating rates [*Kistler et al.*, 2001].

The NNR data has 6 hour (00UT, 06UT, 12UT, 18UT) or 24 hour (00UT) temporal resolution and 2.5° × 2.5° spatial resolution. The closest grid point to Lauder is located at 45°S 170°E, and the closest to Boulder at 40°N 105°W. The NNR data used in this thesis is either on 17 pressure levels or 11 isentropic levels. These levels are listed in Appendix B.2. The NNR products used in this thesis are zonal (u) and meridional (v) winds on pressure levels; air temperature on pressure levels which are used to derive potential temperatures (see Equation 2.3), height (see Equation 2.4) and tropopause heights; and potential vorticity on isentropic levels (see Equation 2.6). Note that potential vorticity is a more highly derived quantity than air temperature and winds.

*Zonal (u) wind is a type A variable, except in the tropics where the model influence is larger and hence is a type B variable.

In future sections, the jet stream speed as calculated from NNR is utilised. A jet stream is typically described as a wind speed ($\sqrt{u^2 + v^2}$) greater than 60 knots, which is equivalent to 30.9 ms^{-1}. In general, the jet stream level used is 200 hPa at 30 ms^{-1} (for examples see *Yang et al.* [2002] and *Ding* [2006]). Figure 3.3 shows the fraction of the year where a given wind speed occurs in a 2.5° × 2.5° grid box at a specific pressure level from NNR. A strong jet (>30 ms^{-1}) is shown at approximately 30°N in *Ding* [2006] in March-April and a weaker ($\leq$30 ms^{-1}), more northerly jet across the Eurasian region (∼40°N) in June-July. The highest occurrence of jet stream winds occurs at 200 hPa for all three speeds. By examining the wind speeds at different thresholds at three pressure levels, it is possible to build up a picture of the jet stream location. The location of more frequent higher wind speeds indicates the location of the centre of the jet. Figure 3.3 clearly shows that the jet streams have preferred locations as in previous studies.

There are a number of different studies that compare the NNR to other reanalysis, such as the European Centre for Medium-Range Weather Forecasts (ECMWF) 15 year reanalysis (ERA-15) and 40 year reanalysis (ERA-40).[‡] *Pawson and Fiorino* [1998] examined the differences between ECMWF and NNR. A major difference is that the clouds are predicted in ECMWF, but are diagnosed in NNR. This could result in differences in the thermodynamic structure. The two reanalyses also have differences in the initialisation of the model. NNR is biased towards the input satellite values and should be superior at lower pressures as the model is more tightly constrained to observations. ECMWF resolves the cold temperatures in the tropics better.

Trigo [2006] found that both ERA-40 and NNR agree on the main cyclone activity regions, although there is some differences in the number that they detect. Some of these differences may be a result of the different spatial resolutions of the models. However, this would not fully account for all the differences. *Bromwich and Wang* [2005] compared NNR, ERA-15 and ERA-40 with two short term Arctic radiosonde campaigns. All three reanalyses showed close agreement to the radiosonde for wind, wind variability, geopotential height, temperature and moisture. Overall *Bromwich and Wang* [2005] found that ERA-40 performs best for the measurement period and area.

[‡]Some studies state specifically which ECMWF reanalysis is used, others are more vague. If it is known whether ERA-15 or ERA-40 is used, it will be stated. Otherwise, it will be referred to generally as ECMWF reanalysis. Note that ECMWF reanalyses are generally on a smaller grid size than NNR and hence have to be adjusted (usually via interpolation) to the NNR grid size or 2.5° × 2.5°.

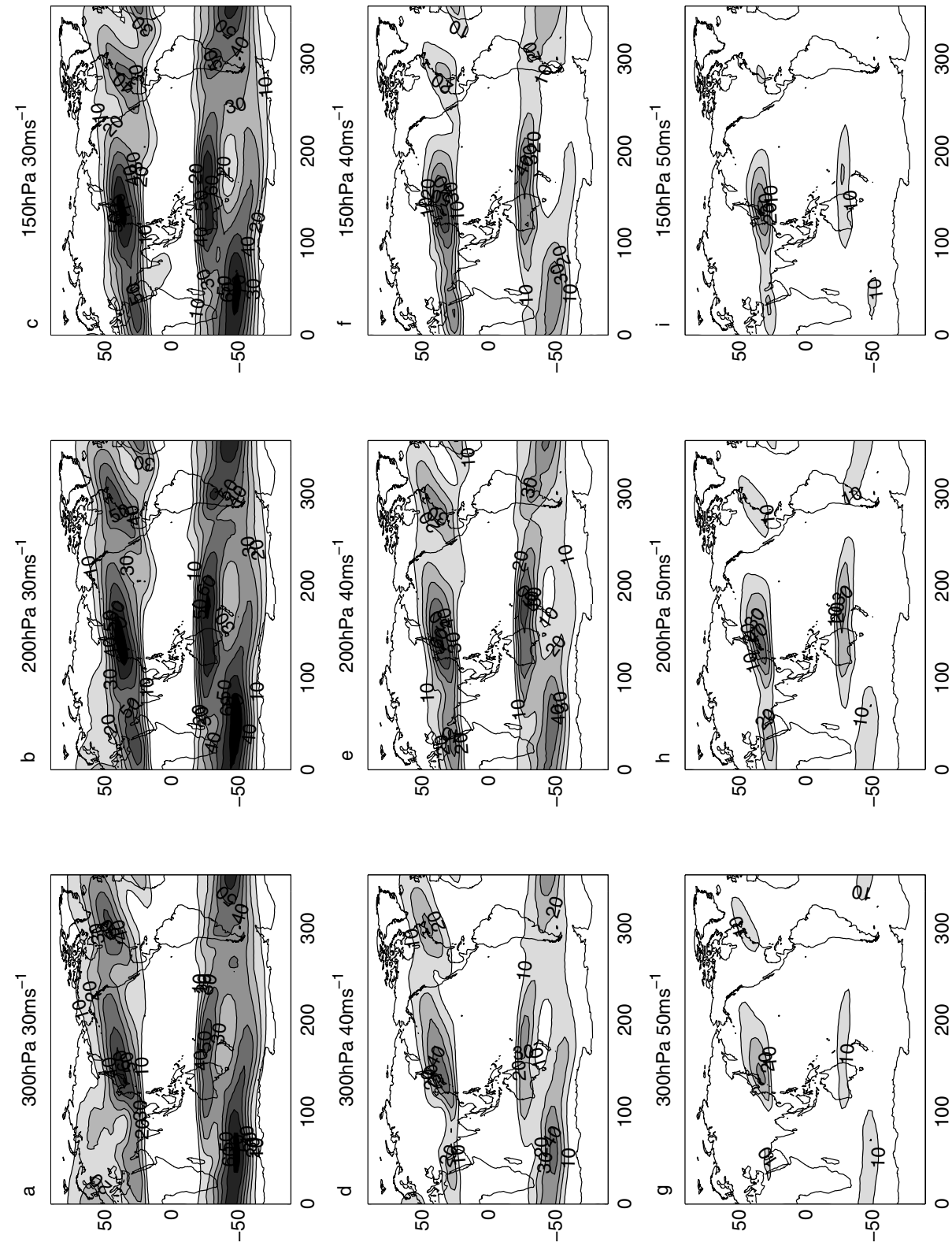

Figure 3.3: Occurrence percentage of wind speed ($\sqrt{u^2 + v^2}$) at different pressure levels from 17 years of NCEP/NCAR reanalyses 24hr data 2.5°×2.5° from 1990 to 2006. a-c) have a minimum wind speed of 30/,ms^{-1}, d-f) have a minimum wind speed of 40/,ms^{-1}, and g-i) have a minimum wind speed of 50/,ms^{-1}. Panels a,d and g are on the 300/,hPa pressure surface. Panels b,e and h are on the 200/,hPa pressure surface. Panels c, f and i are on the 150 hPa pressure surface.

In the Southern Hemisphere midlatitudes and over Antarctica, *Bromwich and Fogt* [2004] found in a comparison between ERA-40 and NNR that the NNR captures greater variability than ERA-40 but has larger biases. This is particularly true during the early part of the data set (pre-1979) and in data sparse regions. In a comparison between radiosondes and NNR over Antarctica, *Marshall* [2002] show that there are seasonal variations in the differences between the temperature of two data sets, which are stronger at lower altitudes. However, the mean temperature difference between NNR and the radiosondes is small.

3.4 Atmospheric Infrared Sounder - AIRS

The Atmospheric Infrared Sounder (AIRS) is located on NASA's Earth Observing System (EOS) Aqua satellite. AIRS was launched on 4th May 2002 and has produced twice daily global data sets since late 2002. AIRS is a medium resolution infrared grating spectroradiometer, which takes 2378 spectral samples with a spectral resolution of 0.5cm^{-1} at long wavelengths to 2cm^{-1} at shorter wavelengths [*Hagan et al.*, 2004]. The infrared spectral range is 3.74-4.61 μm, 6.20-8.22 μm and 8.80-15.4 μm.* The infrared measurements through a retrieval process produce measurements of temperature, water vapour, ozone, carbon monoxide, methane and sulfur dioxide,† along with a number of other products. The AIRS retrieval is discussed in more detail in Chapter 5. Of particular interest for studies in the upper troposphere/lower stratosphere (UTLS) are the profile products of ozone and water vapour, as these both change rapidly in this region. In the context of this thesis, the AIRS data set provides the potential to study Stratosphere Troposphere exchange (STE) on a global scale with daily resolution.

While AIRS has an expected lifetime of five years, it has already exceeded this expectation and currently remains operational [*Hagan et al.*, 2004]. AIRS was the first launched of a series of satellites collectively known as the "A train", which currently consists of five satellites with plans to increase this number to seven. Known as formation flying, these satellites orbit in the same path so that over a brief span of time, less than an hour, they make measurements over the same portion of the Earth. This allows a wider range of science to be achieved.‡ AIRS has a 16 day orbital repeat cycle, in a polar sun-synchronous orbit of height

*http://www-airs.jpl.nasa.gov/technology/specifications
†Methane and sulfur dioxide are new products in version 5.
‡http://aqua.nasa.gov/index.php

705 km. The orbit crosses the equator at 1:30 pm (±15min) on the ascending node and at approximately 1:30 am on the descending node. Each swath has a width of approximately 1650 km.[§]

AIRS data is available in three different formats: the level 1 spectral measurements, along with the level 2 and level 3 products. The level 2 data is broken up into 240 six minute sections per day, called swaths, each made up of 1350 profiles and an associated time of measurement. The level 2 data are available from the Goddard Earth Sciences Distributed Archive Center.[¶] The level 3 data are daily averages on a $1^\circ \times 1^\circ$ degree grid. The processing for the level 3 data involves a basic quality check. The level 3 data used in this thesis was obtained from Andrew Gettelman at the National Center for Atmospheric Research in Boulder, Colorado. A level 3 product is available through the official channels, however, it does not include ozone profile information. For validation purposes the level 2 data is used, as more restrictive conditions on the quality flags are applied than for the level 3 data (see Chapter 5 for more information). For other purposes the level 3 data is used as the files are significantly smaller and easier to use. Level 2 profiles of ozone and water vapour are available on 28 pressure levels from 1100 hPa to 0.1 hPa. Level 3 profiles are available on 14 (or 20) pressure levels, from 1000 hPa to 50 hPa (or 5 hPa). Further details on the pressure levels are indicated in Appendix B.1. Ozone and water vapour are provided as layer quantities. Therefore, they are the mean value of the layer bounded by two pressure levels, with the value reported at the pressure value at the bottom of the layer [*Olsen et al.*, 2005]. The vertical resolution with respect to the geopotential height is uneven as it varies with increasing altitude, as shown in Figure 3.4. It can be observed here that the AIRS data is of a significantly lower vertical resolution than the ozonesondes, but is comparable to NNR.

Previous studies have detailed the AIRS retrieval methodology [*Goldberg et al.*, 2003; *Susskind et al.*, 2003, 2006; *Tobin et al.*, 2006] and have examined the quality of the temperature, water vapour and ozone profile retrievals [*Divakarla et al.*, 2006; *Fetzer et al.*, 2006; *Gettelman et al.*, 2004; *Strow et al.*, 2006; *Susskind et al.*, 2003, 2006]. A detailed discussion of the retrieval method is covered in Chapter 5. *Fetzer et al.* [2003] and *Fetzer et al.* [2005] review the AIRS validation efforts in detail. In general, validation efforts have focused on the quality of the temperature and water vapour retrievals, while the ozone product has received

[§]http://www-airs.jpl.nasa.gov/Technology/AIRScoverageaccuracy
[¶]http://disc.sci.gsfc.nasa.gov/data/dataset/AIRS

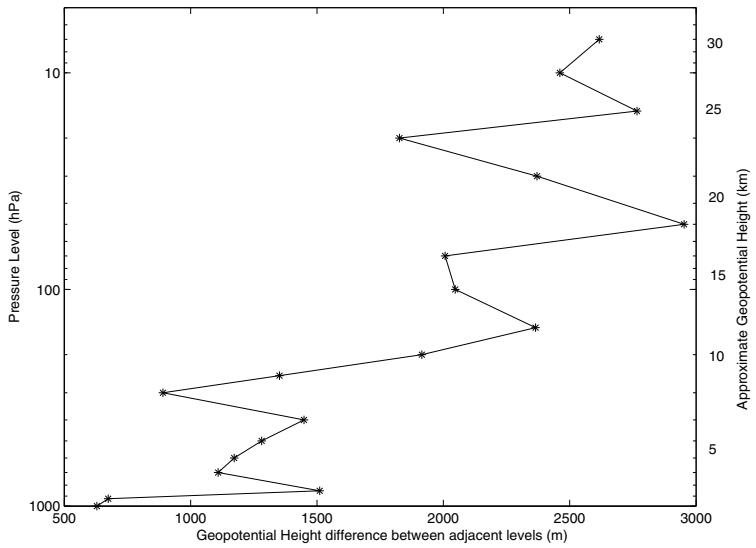

Figure 3.4: An example of the vertical resolution for AIRS data at midlatitudes. The geopotential height difference between two pressure levels is reported at the lower pressure level. Note that the use of a global mean geopotential height does not alter the general pattern of the resolution.

less attention. For studies in the UTLS region we are interested in both the ozone and water vapour retrievals, hence a validation of the ozone product is detailed in Chapter 5. The results of previous water vapour validation efforts are detailed in the following paragraph.

Water vapour is only retrieved up to 100 hPa and the measurements have a sensitivity limit of 10 ppmv [*Gettelman et al.*, 2004]. *Hagan et al.* [2004] show AIRS water vapour has an agreement of 25% or better between 100-500 hPa using aircraft and radiosondes at San José, Costa Rica. Further measurements in *Gettelman et al.* [2004] from the WB57 aircraft starting at San José, Costa Rica and Houston, Texas, with a latitude range of 0 to 40°N between 100-150 hPa, show AIRS measurements have a wet bias, and up to 200 hPa there is a better than 25% agreement. The same study also showed that there is no bias in the temperature measurements between 50-500 hPa where measurements are within ±1.5 K. These results are shown in Figure 3.5. In addition, *Fetzer et al.* [2005] using RS90 and RS80 radiosondes at four locations showed that they have an agreement of between -10 to 20% from 800-150 hPa.

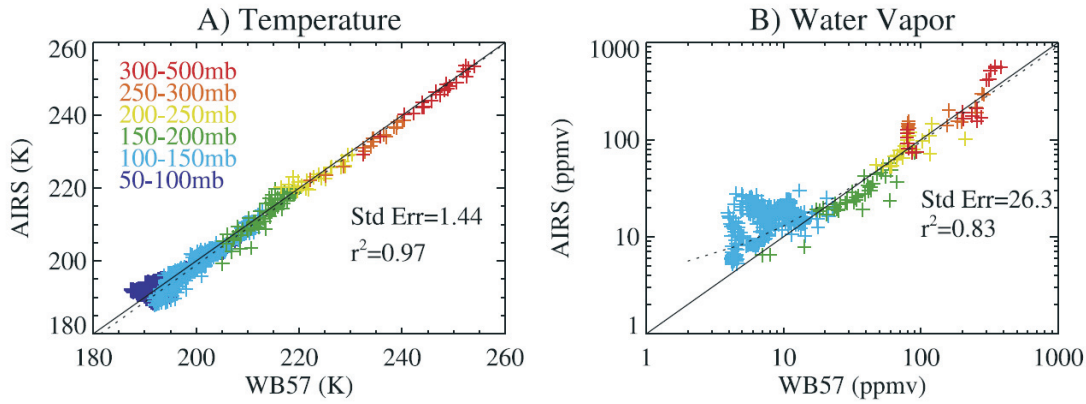

Figure 3.5: Comparison between WB57 aircraft observations and AIRS satellite observations. Colour of data points refers to pressure range of measurements as indicated by the key in panel A. Figure from *Gettelman et al.* [2004].

Chapter 4

Tropopause Folds

Tropopause folds (TPFs) are regions where a tongue of stratospheric air has intruded into the troposphere. These events are important for exchange between the troposphere and stratosphere and are likely to be responsible for the majority of the ozone transport from the stratosphere to the troposphere [*Holton et al.*, 1995]. TPFs feature both vertical and horizontal movement, as there is both altitudinal and latitudinal displacement of air [*Stohl et al.*, 2003].

There are a number of different methods for identifying TPFs, some of which were outlined briefly in Section 2.2.1. These methods involve detecting the various signatures of TPFs. The troposphere and the stratosphere have different characteristics in terms of ozone and water vapour mixing ratios, stability and a number of other parameters. Hence a TPF can be identified by examining the troposphere for air parcels that have properties characteristic of the stratosphere. This can be achieved either by looking at vertical profiles, such as obtained by ozonesondes [*Blonsky and Speth*, 1998; *Van Haver et al.*, 1996], or at the bulk properties, such as total column ozone [*Wimmers and Moody*, 2004].

This chapter focuses on the identification of TPFs using high resolution ozonesondes at Lauder, NZ (45.0°S, 169.7°E) and Boulder, USA (39.9°N, 105.3°W) using the method developed in *Van Haver et al.* [1996]. The ozonesonde data sets are discussed in depth in Section 3.1. By examining the ozonesonde profiles for regions of air with high ozone content, low water vapour content or low humidity and high stability, within the troposphere, possible TPFs can be identified.

Figure 4.1 shows a cross section of a TPF and the intersection of an ozonesonde flight through the tongue of stratospheric air. The ozonesonde profile will observe the tongue as a layer with stratospheric properties, with the layers of air above and below displaying tropospheric properties. An example of an ozonesonde profile

through a TPF from *Van Haver et al.* [1996] is shown in Figure 4.2. For this example, there is a layer at approximately 400 hPa of increased ozone, decreased humidity and a variation in the temperature profile indicating increased stability in the layer. These properties indicate the presence of a TPF in the region that the ozonesonde measured.

This chapter investigates the identification of TPFs using ozonesondes. Section 4.1 covers the development of a TPF identification algorithm based on the method described in *Van Haver et al.* [1996]. A sensitivity study is described in Section 4.4, followed by the application to ozonesonde data sets from Lauder and Boulder. This algorithm is then compared to the cross sectional stability from the NCEP/NCAR reanalyses (NNR) in Section 4.2. To conclude the limitations of this method of TPF identification are discussed in Section 4.5.

4.1 Tropopause Fold Identification Algorithm

The TPF identification algorithm discussed by *Van Haver et al.* [1996] requires high resolution profile data of ozone, humidity, temperature and upper level wind speed. Hence the use of ozonesonde observations is ideal for TPF identification. The main adjustment to the algorithm is with regards to the wind speed. The majority of the ozonesondes at Lauder and Boulder do not measure wind speed. The wind speed condition for TPFs is therefore based on the NNR wind data (see Section 3.3 for details), with the final results presented both with and without the application of the wind speed condition. The vertical resolution of the data is crucial as it limits the magnitude of the TPFs identified. Only the higher resolution ozonesondes from Lauder and Boulder are used in the algorithm (see Section 3.1 for details). All ozonesondes are then interpolated to the same resolution over the whole profile to remove variations caused by the measurement method. The vertical interpolated resolution used is 30 m based on the average vertical resolutions presented in Table 3.1.

The algorithm is designed to detect well developed TPFs which have the greatest potential for large amounts of ozone transport. Ozone peaks are identified within the profiles and then tested against a number of conditions to test whether they are well developed folds. For a positively identified TPF, Conditions 1 through 3 must be passed, with Condition 4 applied as an optional condition. These conditions are summarised in Table 4.1 and are outlined in more detail in this

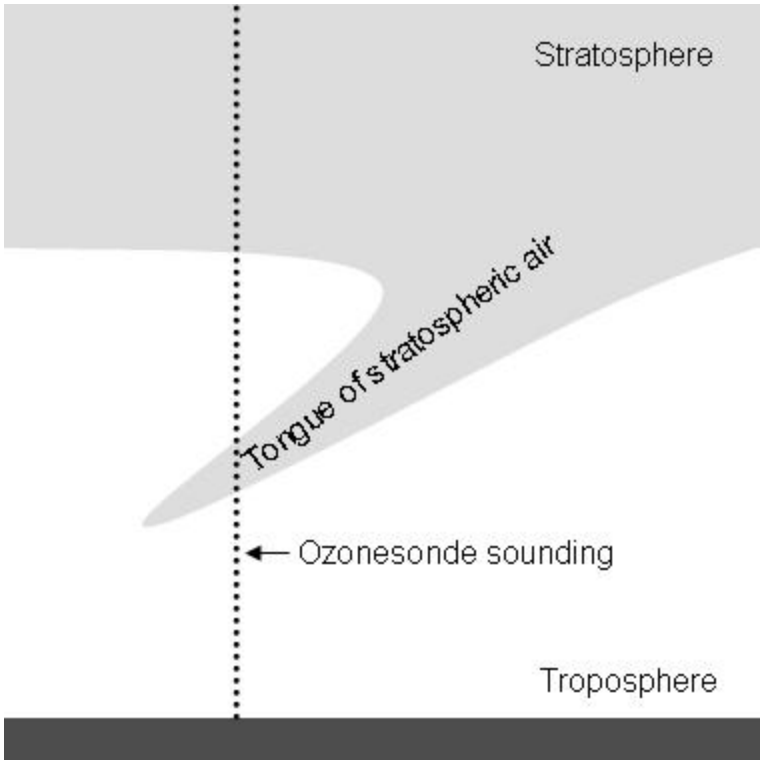

Figure 4.1: A cross section of the atmosphere showing the intersection of a ozonesonde with a tropopause fold. The light grey shading shows air with stratospheric characteristics, while the unshaded region shows air with tropospheric characteristics. The path of the ozonesonde is indicated by the dotted line.

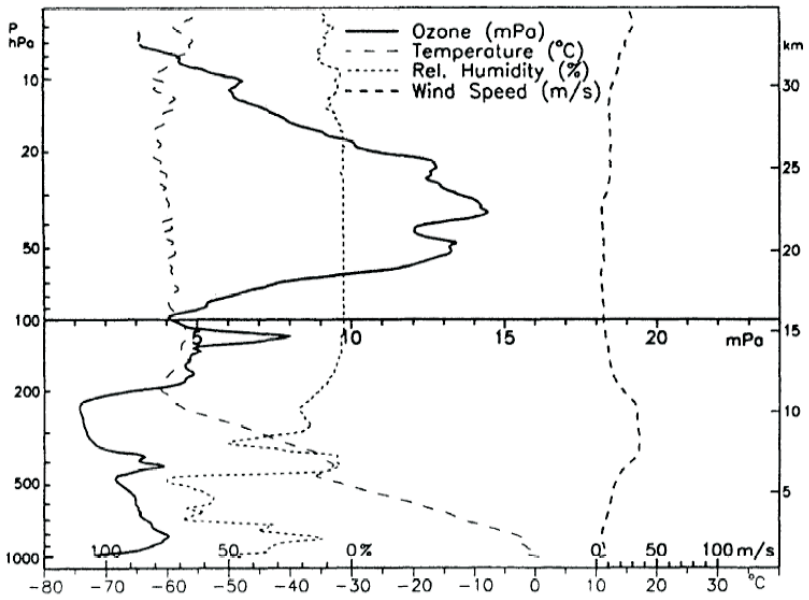

Figure 4.2: Ozonesonde sounding of a tropopause fold. The tropopause fold is located at approximately 400 hPa. Note that the scale on the humidity measurements is reversed. Figure from *Van Haver et al.* [1996].

Table 4.1: Summary of the tropopause fold conditions used in the identification algorithm.

Condition #	Parameter	Application to peak
1a	O_3	Greater than climatology
1b	O_3	Magnitude greater than surroundings
1c	O_3	Detached from stratosphere
2	Humidity	Dry Air
3	Stability	Stable layer using Brunt Väisälä frequency
4	Wind Speed	Location of the jet stream from NNR

section. Briefly, these conditions test that the ozone peak is sufficiently large with respect to its surroundings and the local climatology, along with confirming that a tongue rather than a deformation has been sampled. In addition the layer must have humidity and stability properties indicative of stratospheric air, that is dry and stable. The location of the jet stream is also tested to examine the impact that wind speeds have on the formation of TPFs. It has been shown previously [*Holton et al.*, 1995; *Price and Vaughan*, 1993; *Shapiro*, 1980] that jet streams and TPFs are likely to be related. The numerical values for these conditions are indicated in *Van Haver et al.* [1996], with the impact of variations to these parameters presented in Section 4.4. Testing a range of variations is important, as while the parameters used are based on characteristic values, different choices could be made.

The first condition is broken into three parts and is based on the ozone profile. A pronounced ozone peak must be identified between 3 km in altitude, to 1 km below the thermal tropopause. For example, if the tropopause is located at 11 km, then ozone peaks can be between 3 to 10 km. Each peak is then tested against conditions 1a, 1b and 1c, of which either 1a and 1b or 1a and 1c must be true. Each of these criteria are detailed below. The tropopause heights are calculated from the temperature profile recorded by the ozonesonde, using the method detailed in *Reichler et al.* [2003].

The ozone peaks are firstly identified by looking for local maxima, where the range for the local maxima (R) is ± 150 m. This dictates that ozone peaks must be a minimum of 150 m from any adjacent peaks. There can be multiple peaks identified from a single ozonesonde, where each peak is tested individually against the remaining conditions.

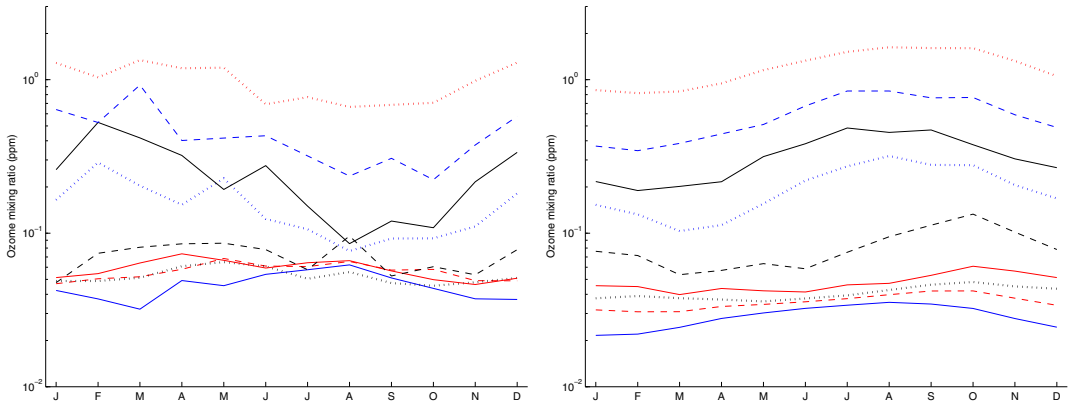

(a) Boulder from Oct 2002 to Nov 2006 (b) Lauder from 1990 to 2006

Figure 4.3: Ozonesonde climatologies from a) Boulder and b) Lauder. The ozone mixing ratio in ppm are given at each height level as a function of season. The altitude levels are marked as follows: – 2 km, - - 4 km, ··· 6 km, – 8 km, - - 10 km, ··· 12 km, – 14 km, - - 16 km, ··· 18 km.

Condition 1a states that the peaks in the ozone profile must be at least 25% greater than the mean ozone mixing ratio at the same altitude in the free atmosphere. The climatologies of the ozone mixing ratio for Boulder and Lauder from the ozonesondes are shown in Figure 4.3. Both locations show an increase in ozone at lower altitudes during the late winter, and at higher altitudes during the summer. Boulder has more small scale variations than Lauder, although some of those may be a result of a smaller data pool used for the Boulder climatology. The ozone level at the surface and at higher altitudes is lower for Lauder than for Boulder. This agrees with other studies, such as *Olsen et al.* [2003] and *Wang et al.* [1998], that show that the ozone levels are higher in the Northern Hemisphere than in the Southern Hemisphere.

Conditions 1b and 1c originate from the desire that the layer of increased ozone be clearly separated from the stratosphere to ensure that a deep TPF is being measured. This requires that the air above and below the ozone peak have tropospheric characteristics with respect to ozone. Only one of these two conditions is required to be true. These two conditions both place limitations on the width of the ozone peak. However, 1b has a much wider range than 1c which should reduce the impact of this limitation.

Condition 1b examines the ozone in layers 1-3 km above and below the peak and compares them to the ozone value at the peak. The peak must be 30% larger than the ozone values in the layers above and below. This ensures that the peak

has a significant magnitude with respect to its surroundings.

Alternatively, condition 1c ensures that the ozone peak is sufficiently separated from the stratosphere by examining the ozone in layers 300 m thick above and below the peak. The ozone values in these layers must be less than 80% of the ozone value at the peak.

After the distinctness of the ozone peak from its surroundings has been established by condition 1, it is then required to check the water content of the peak. As previously stated, stratospheric air is dry along with being ozone rich. Condition 2 requires that the ozone peak has a relative humidity of less than 25%. This further confirms that the layer of air has likely origins in the stratosphere.

Stratospheric air is very stable relative to tropospheric air due to the increasing temperature with altitude. TPFs will carry this signature of stability into the troposphere. Condition 3 tests the stability of the air associated with the ozone peak. *Van Haver et al.* [1996] sets a stability limit where the change in potential temperature with pressure must be less than 11.5 K per 100 hPa around the ozone peak with a range of ±250 m. As this condition has mixed units it is more difficult to apply and lacks an intuitive feel as to how it selects regions of increased stability. As an alternative measure for stability the Brunt Väisälä frequency squared (N^2) is used. This measure is based on $\frac{d\theta}{dz}$ rather than $\frac{d\theta}{dP}$ as in *Van Haver et al.* [1996] and sets different limits for the troposphere and stratosphere. In the troposphere the value of N^2 is lower than in the stratosphere, as was shown in Figure 2.1. The Brunt Väisälä frequency is calculated using:

$$N^2 = \frac{g}{\theta}\frac{d\theta}{dz} \tag{4.1}$$

where θ is the potential temperature, z is the altitude and g is the gravitational acceleration. To find ozone peaks with stratospheric stability qualities, the N^2 value for the ozone peak is compared to a stratospheric mean N^2 value. If the N^2 at the peak is greater than the stratospheric mean, then it has stratospheric stability qualities.

The data must be filtered to create a reliable stratospheric mean value. The temperature and height are smoothed using a 4th order Savitzky-Golay Filter. This filter fits a 4th order polynomial to a moving window of 13 data points to find the value of the data point at the centre of the window. With the default ozonesonde vertical resolution this is equivalent to a range of about 400 m. This

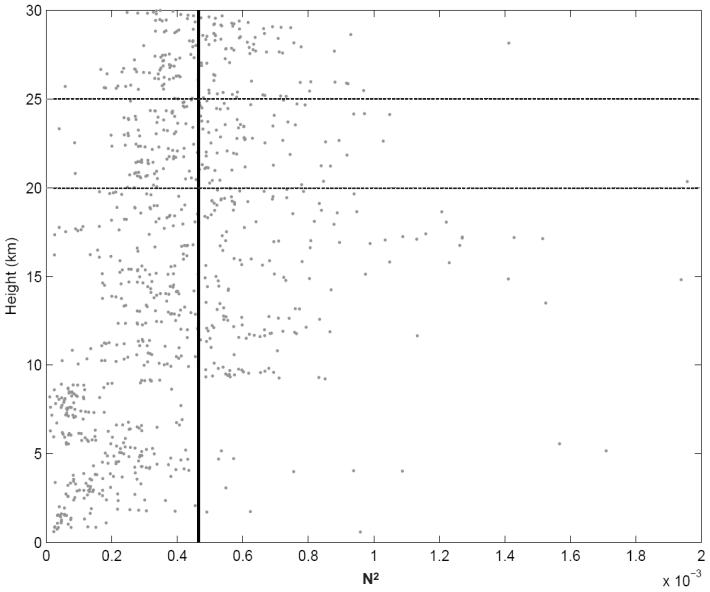

Figure 4.4: Brunt Väisälä frequency (N^2) for a sample ozonesonde from Lauder, showing the calculation of Condition 3. The N^2 is averaged between 20 to 25 km as indicated by the horizontal dashed lines. The stratospheric mean is shown by the solid vertical line.

type of filter is good for filtering noisy data while still retaining small scale structure [*Savitzky and Golay*, 1964]. It is necessary to filter the data before calculating a stratospheric mean to remove the noise in the profile and give a more robust mean. Note that while the mean has been used, the median may be more appropriate for the nature of this data set.

To obtain a stratospheric mean value, the N^2 values are averaged between 20-25 km (Or from 20 km to the top of the file if ozonesonde doesn't reach 25 km). Prior to averaging, the values smoothed by the Savitzky-Golay filter are screened to remove values less than zero as we are only interested in N^2 greater than zero as these represent stable air. Values greater than 0.002 are also removed as these values are outliers and adversely affect the average. The Brunt Väisälä frequency for a sample ozonesonde with the stratospheric mean value marked is given in Figure 4.4. Values of N^2 in the troposphere greater than the stratospheric mean are likely to be associated TPFs. They could also be temperature inversions, however, the coincidence of this criteria with the conditions suggests this is unlikely. Through the testing of previously identified ozone peaks against N^2, a further confirmation of stratospheric origin can be confirmed for the identification of TPFs.

Van Haver et al. [1996] uses a fourth condition based on wind speed to ensure that the layer is located in a frontal region as this is important to the formation of TPFs. This condition requires that the vertical gradient of the horizontal wind speed be greater than or equal to 5 m/s/km averaged over a 2 km region adjacent to the ozone peak. However, most of the ozonesondes used in this study do not measure wind speed making this condition unsuitable for this study. This condition can be modified to examine the wind speeds from the NNR data (see Section 3.3 for more information). Frontal regions are associated with jet streams, therefore by determining the presence of a jet stream near the ozonesonde launch, the importance of these events on TPFs can be determined. The numbers of TPFs positively identified by the TPF algorithm are presented both with and without the application of Condition 4.

For condition 4, the NNR data is examined at 300 hPa for wind speeds greater than 30 ms^{-1}. Jet streams were discussed in more detail in Section 3.3. In Figure 3.3a it is shown at Lauder that the jet streams are present approximately 30% of the time, with the jet tending to be slightly to the south of Lauder. At Boulder, the jet stream is present about 30-40% of the time. Note that later in this thesis a different level has been used for the jet stream location (ie. 200 hPa rather than 300 hPa. The jet stream is observed at multiple pressure levels.

4.2 Case Studies

In order to confirm that the TPF identification algorithm works correctly and to give a more solid understanding of the results, some ozonesonde profiles are presented with their associated TPFs. To confirm that the algorithm correctly identifies TPFs, some of the ozonesondes are also viewed in the NNR data using a method for viewing TPFs from *Pan et al.* [2007b].

Three examples of TPFs identified at Lauder are presented in Figures 4.5, 4.6 and 4.7, showing both the ozone and humidity profile, along with the ozone climatology that is utilised in condition 1a. Each TPF can be seen as an ozone spike in a region of low humidity below the tropopause level, as indicated by the arrows. These three figures indicate how different positively identified folds can appear. Two TPFs are indicated in Figure 4.5 just below 5 km and are part of a broader vertical structure. These two TPFs may actually be a single fold structure, however, due to the nature of the identification calculations, the

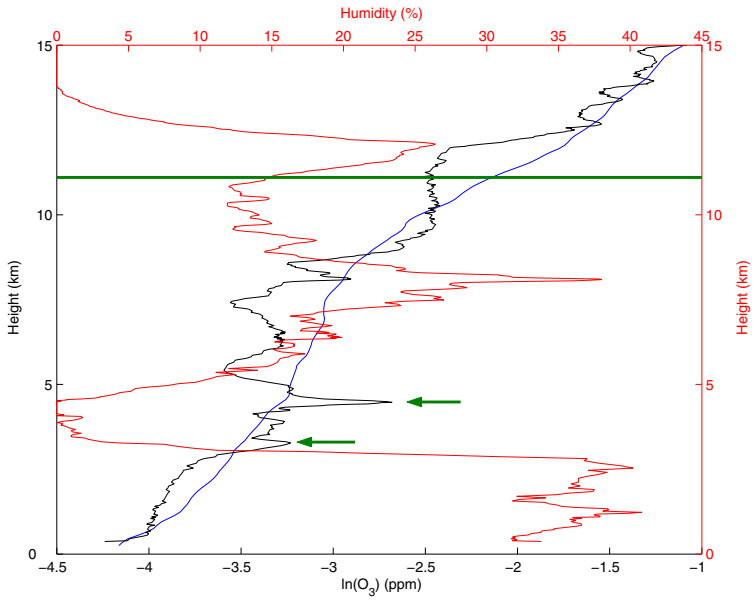

Figure 4.5: Ozonesonde profile from Lauder for 1820UT 18th Dec 1997, with the black line giving the ozone profile, the blue line the climatological ozone mean at Lauder for December and the red line the humidity profile. The thermal tropopause height for this flight was 11.1 km which is marked by the horizontal green line. Two TPF peaks are identified by the green arrows.

algorithm has identified them separately. This is a limitation of the algorithm as it is unable to identify very broad structures. It should be noted that if this whole region between the two peaks was to be tested as a single fold, it would fail the majority of the conditions in the identification algorithm.

In comparison, the TPF in Figure 4.6 is very narrow although it has a similar altitude. There is what may look to be a second TPF in this profile, however, this second peak is approximately at the tropopause level therefore it does not qualify as a TPF. Similarly in Figure 4.7 there is also an enhancement of ozone at the tropopause level along with the TPF at approximately 5 km. This TPF is also part of a broader structure as in the first example.

Pan et al. [2007b] identified a TPF from flight data from HIAPER,[†] where measurements were made by flying through the feature. To back up this identification, data from NCEP (National Centers for Environmental Prediction) Global Forecast System (GFS) and NCEP Final Global Data Assimilation System (FNL) was used to look at the stability, potential vorticity (PV) and the thermal tropopause, which is shown in Figure 4.8a. This flight intersected both a tropopause fold and

[†]HIAPER: High-performance Instrumented Airborne Platform for Environmental Research.

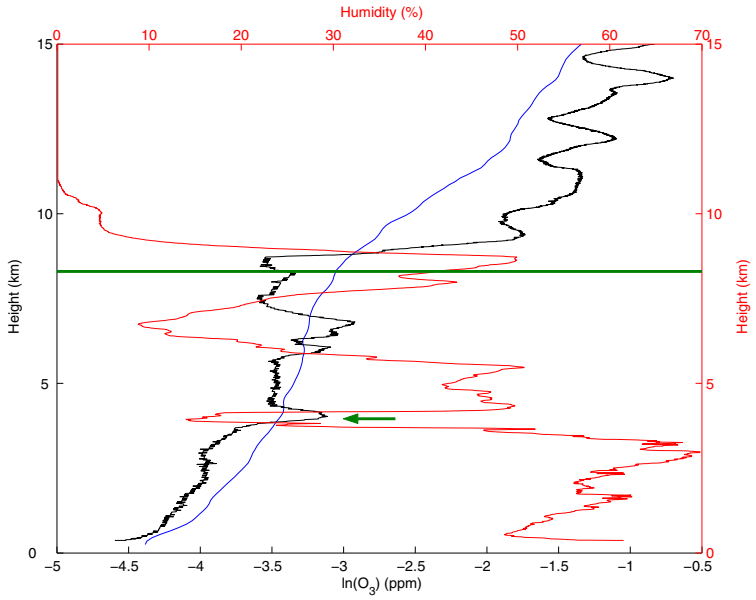

Figure 4.6: Ozonesonde profile from Lauder for 0842UT 27th Jan 2003, with the black line giving the ozone profile, the blue line the climatological ozone mean at Lauder for January and the red line the humidity profile. The thermal tropopause height for this flight was 8.3 km which is marked by the horizontal green line. A TPF peak is indicated by the green arrow.

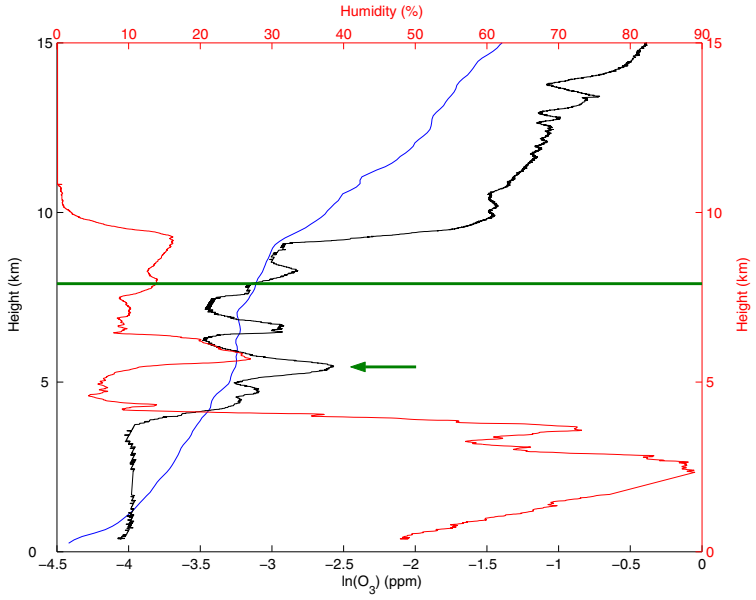

Figure 4.7: Ozonesonde profile from Lauder for 2004UT 20th Feb 2003, with the black line giving the ozone profile, the blue line the climatological ozone mean at Lauder for February and the red line the humidity profile. The thermal tropopause height for this flight was 7.9 km which is marked by the horizontal green line. A TPF peak is indicated by the green arrow.

the jet stream. Additionally the lower panel of Figure 4.8 shows a second flight where a region of unperturbed layers of stability were flown through. This second panel provides contrast for a non-TPF region. The TPF can be clearly seen in the top panel as an increase in the stability at lower altitudes, along with a separation in the thermal tropopause and the 2 PVU (dynamic tropopause) contour. There is also a relatively abrupt change in the thermal tropopause over the fold region. In comparison, the lower panel has no increase in stability around the tropopause region, with little variation in the thermal tropopause and the 2 PVU height.

Equivalent figures for the TPF events identified by the algorithm can be created using NNR, providing a confirmation of the algorithm. The NNR data available for use is of a lower vertical and horizontal resolution than the data used in *Pan et al.* [2007b] which will impact the magnitude of the TPFs identified.

This method has varying levels of success and is somewhat subjective in the analysis process. Two of the best examples are shown in Figure 4.9, which coincide with Figures 4.6 and 4.7. A clear variation in the stability at lower altitudes, along with variations in the thermal and dynamic tropopause (2 PVU) are seen for both cases. An increase in the stability similar to that observed in Figure 4.8a is observed in both panels, accompanied by a change in the thermal and dynamic tropopause heights. These variations are at approximately the correct longitude for Lauder. Of note is that Figure 4.9 is a longitude cross section, whereas Figure 4.8 is a latitude cross section. Figure 4.9 is a longitude cross section as the impact of the TPF through changes in the stability and tropopause height were not observed in the latitude cross section. As TPFs are three dimensional structures, they can be viewed as a cross section from various angles. For the examples in Figure 4.9, the variation in the tropopause height and stability was most clearly seen as a longitudinal cross section.

Most of the stability cross sections examined do not show such a clear relationship, with either smaller or no variations in the stability and tropopause heights observed. A number of days where no TPF was identified in the ozonesonde data were also examined and it was not possible to separate non TPF days from TPF days. Although the NNR data has a low vertical resolution, it is expected that large TPFs should produce a visible variation in the stability. However, this has not been observed. This may suggest either problems in the TPF identification algorithm or in the NNR data. It is likely that the inaccuracy is a result of the vertical and horizontal resolution of the NNR data being lower than that used for Figure 4.8.

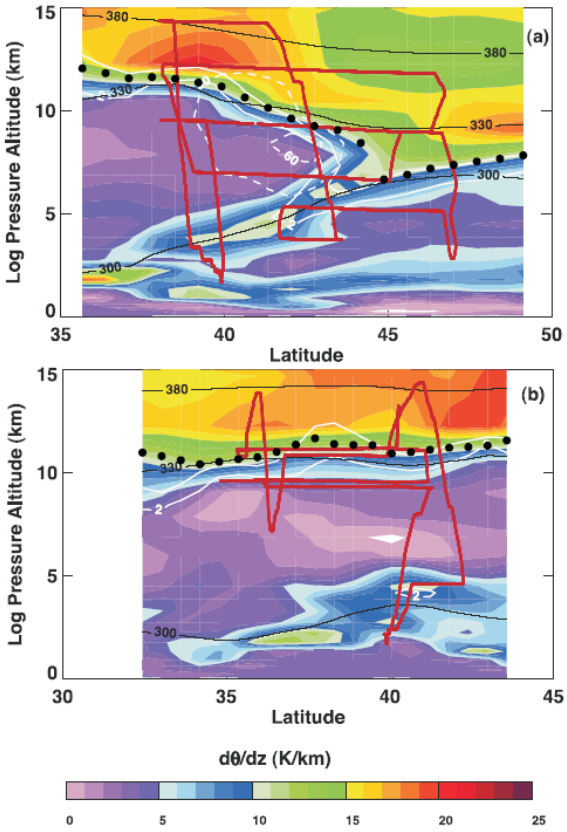

Figure 4.8: Cross sections for the flight paths (red solid lines) in *Pan et al.* [2007b], panel a is from 1st Dec 2005 and panel b is from 9 Dec 2005. Background colours show the static stability, potential vorticity (units of PVU) are the white contours, thermal tropopause are the black dots, with the flight tracks in dark red. Data is from NCEP (National Centers for Environmental Prediction) Global Forecast System (GFS) and NCEP Final Global Data Assimilation System (FNL) which has a $1° \times 1°$ spatial resolution. Figure from *Pan et al.* [2007b].

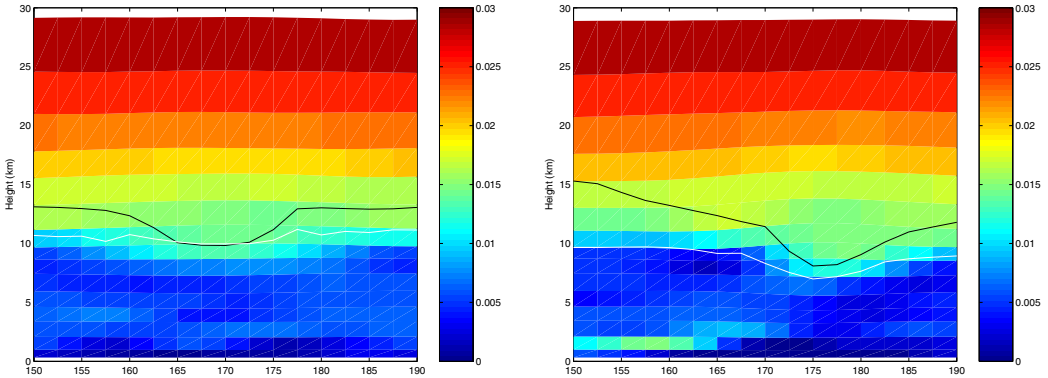

(a) 27th January 2003 (b) 20th February 2003

Figure 4.9: Stability of tropopause fold region from Lauder ozonesondes on a) 27th January 2003 as in Figure 4.6 and b) 20th February 2003 as in Figure 4.7. The x-axis shows the longitude for the cross section. Thermal tropopause is shown by the black line, dynamic tropopause (2 PVU) is shown by the white line. Colour scale shows stability $\frac{d\theta}{dz}$ in units of Km^{-1}.

4.3 Application of TPF Identification Algorithm

The previous section has demonstrated that the TPF identification algorithm is able to identify possible TPF events, however, these events cannot be confirmed through the use of stability from the NNR data. There are also a large number of adjustable parameters which have the potential to significantly change the TPF identification algorithm. The effect of adjustment to these parameters is investigated in Section 4.4.

This algorithm is now applied to the Lauder and Boulder ozonesondes, with the number of positively identified TPFs using the default parameter values given in Tables 4.2, 4.3, 4.4 and 4.5. These tables show the number of folds per season, along with the total number of ozonesondes released. It should be noted that the values in Table 4.5 are derived from a very small number of measurements.

As regions with large variations in tropopause heights are likely to be important for exchange, the variation in the tropopause heights from NNR at Boulder and Lauder as a function of time are shown in Figure 4.10. It should be noted that the ozonesondes and NNR have the same trend for tropopause height, although the ozonesonde tropopause heights are approximately 2 km lower with slightly more variation. This is likely a result of the low vertical resolution of the NNR data. The NNR tropopause heights are used here as there are too few ozonesondes at Boulder to produce statistically significant trends. The bimodal structure in the Boulder tropopause heights during the summer months is clearly observed. A similar but much weaker pattern is observed at Lauder.

The number of folds for Lauder is largest in the summer months, whereas for Boulder the largest number of TPFs is during the spring. Both of these seasons coincide with the period of the year when there is the largest variation in the tropopause height as shown in Figure 4.10. This is in agreement with TPFs being associated with the jet stream, resulting in large variations in the tropopause height and STE. Despite the smaller number of ozonesondes released at Boulder, the number of TPFs is about three times greater than at Lauder. This probably reflects the different nature of the tropopause structure and the influence of the jet stream at Boulder compared to Lauder. There may also be a strong maritime influence at Lauder which would not be observed at Boulder.

As TPFs are associated with downward transport, it is expected that there will be higher ozone values in the troposphere when there are larger numbers of TPFs.

Table 4.2: Ozonesondes recording a TPF event at Lauder from 1990 to 2007, using default condition values, without the application of condition 4. Final row gives the percentage of ozonesondes with positively identified TPFs.

	DJF	MAM	JJA	SON	
# TPF	42	28	10	25	105
# Ozonesondes	260	256	248	334	1098
	16.2%	10.9%	4.0%	7.5%	9.6%

Table 4.3: Ozonesondes recording a TPF event at Lauder from 1990 to 2007, using default condition values, with the application of condition 4. Final row gives the percentage of ozonesondes with positively identified TPFs.

	DJF	MAM	JJA	SON	
# TPF	15	8	2	5	30
# Ozonesondes	260	256	248	334	1098
	5.8%	3.1%	0.8%	1.5%	2.7%

Table 4.4: Ozonesondes recording a TPF event at Boulder from 2002 to 2006, using default condition values, without the application of condition 4. Final row gives the percentage of ozonesondes with positively identified TPFs.

	DJF	MAM	JJA	SON	
# TPF	2	9	6	5	22
# Ozonesondes	15	16	13	17	61
	13%	56%	46%	29%	36%

Table 4.5: Ozonesondes recording a TPF event at Boulder from 2002 to 2006, using default condition values, with the application of condition 4. Final row gives the percentage of ozonesondes with positively identified TPFs.

	DJF	MAM	JJA	SON	
# TPF	1	2	1	2	6
# Ozonesondes	15	16	13	17	61
	7%	13%	8%	12%	10%

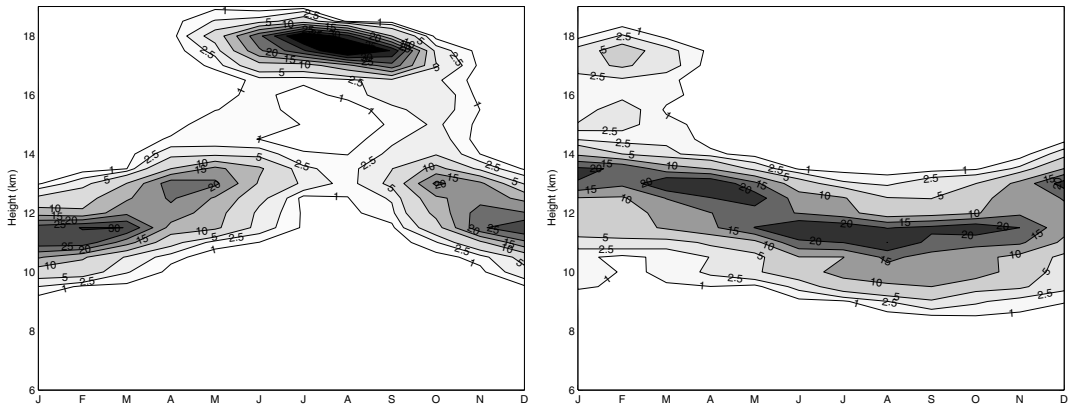

(a) Boulder (b) Lauder

Figure 4.10: Variation in tropopause height from NCEP/NCAR reanalyses, shown as a percentage of the total number of ozonesondes per month for a) Boulder and b) Lauder. Tropopause height is from 1990 to 2006 and is sorted into 500 m bins.

Figure 4.3 shows that there is some increase in ozone at lower altitudes during the spring/summer months. On a global scale, previous studies have shown a spring (and/or late summer) maximum in ozone. This enhancement is not as pronounced in the Southern Hemisphere as in the Northern Hemisphere [*Wang et al.*, 2006]. The maximum in TPFs in *Van Haver et al.* [1996] occurred during the spring, which is within the period of expected ozone enhancement. The maximum in TPFs from Boulder and Lauder is therefore in agreement with the increased ozone and other studies.

The application of condition 4 reduces the number of TPFs identified to less than a third at both locations. Of interest is that the application of condition 4 to the Lauder ozonesondes results in the final percentage of ozonesondes measuring folds being similar to the final results of *Van Haver et al.* [1996], which were between 2-4%. However, as the wind data is taken from lower resolution reanalyses data, there is an amount of uncertainty in the application of condition 4. Ideally higher resolution wind data or wind data from the ozonesondes would be used.

The application of a wind speed condition does not change the seasonal variation in the number of TPFs identified. The highest occurrence of TPFs remains during the spring for Boulder and the summer for Lauder. It also follows that this region still coincides with the period of maximum variation in the tropopause height. Of interest is that the three examples in Section 4.2 are all selected by condition 4. However, the algorithm may adequately identify TPFs based on the first three conditions, but this is difficult to confirm.

4.4 Sensitivity Testing

Of particular concern for this identification algorithm is the large number of parameters that can be varied, namely each of the numerical values for the conditions outlined in Section 4.1. Ideally these values should be robust, meaning that a significant change in the value, say 20% should have little impact on the final result. If the values are robust, then the number of TPFs identified and their seasonal distribution can be considered to be an accurate representation of the occurrence of TPFs in the atmosphere. However, if changing the values used in the algorithm produces a large difference in the number of TPFs identified, then it is difficult to determine which values enable the algorithm to correctly identify TPFs. Additionally, sensitivity to seasonal variations and the climatological mean may cause problems.

To test the sensitivity of the algorithm, the parameters given in Section 4.1 along with the vertical resolution are varied. To quantify the robustness, the number of positively identified TPFs are compared to the number identified using the default values using the following relationship:

$$\%\ change = \frac{\#TPF_{new} - \#TPF_{old}}{\#TPF_{old}} \times 100 \tag{4.2}$$

For example if 20 TPFs were identified using the default values and 16 with a variation to one of the parameters, then the resulting percentage change is -20%. Each parameter is varied individually, giving a total of seven adjustable parameters. The results of these comparisons are given in Table 4.6 for the Lauder ozonesondes only. As the Boulder ozonesondes are similar to the Lauder ozonesondes used after 1998, it is not necessary to repeat these calculations. In addition the small number of Boulder ozonesondes used for this study would be unsuitable for these statistical tests. The results are calculated both separately for the different types of ozonesondes mentioned previously (see Table 3.1), and as a whole. This was done to provide a check whether the initial resolution of the ozonesonde had an impact on the sensitivity. Note that condition 4 is not given in the table as the results in Section 4.3 are presented both with and without the application of condition 4.

Varying some of the conditions has very little impact on the number of TPFs identified. Conditions 1a and 1b have small impacts on the number of TPFs identified (approximately 14%). Small changes to Condition 2 and to the range of

Table 4.6: The percentage change in the number of TPFs identified at Lauder by the algorithm when variations are made to the parameters discussed in Section 4.1. The ozonesonde records into three groupings based on vertical resolution - low resolution from 1990-1998, high resolution from 1998-2007, then the whole data set. The default value for each parameter, along with the new value to test are listed in columns 2 and 3 respectively. Percentages are calculated using Equation 4.2.

	Default	Trial	1990-1998 (%)	1998-2007 (%)	1990-2007 (%)
Condition 1a	25%	30%	-6.8	-6.5	-6.7
		20%	+6.8	+2.2	+4.8
Condition 1b	30%	24%	+13.6	+6.5	+10.5
		36%	-13.6	0	-7.6
Condition 1c	80%	70%	-37.3	-28.3	-33.3
		90%	+28.8	+10.9	+21.0
Condition 2	25%	10%	-33.9	-30.4	-32.3
		20%	-5.1	-6.5	-5.7
		30%	+3.4	+6.5	+4.8
		40%	+15.3	+21.7	+18.0
Condition 3	±200 m	± 100 m	-37.3	-37.0	-37.1
		± 300 m	+33.9	+21.7	+28.6
		± 400 m	+57.6	+34.8	+47.6
Resolution	30 m	15 m	+108.5	+97.8	+103.8
		45 m	-27.1	-26.1	-26.7
R	150 m	50 m	-52.5	-54.3	-53.3
		100 m	-5.1	-6.5	-5.7
		200 m	+3.4	-4.3	0

the local mean (R) used at the beginning of Condition 1, also have a small impact on the number of TPFs identified (<10%). However, large variations to these values have a larger impact on the resultant number of TPFs (between 30-50%). *Van Haver et al.* [1996] also found that variations to Condition 2 had very little impact. All the other conditions change the number of TPFs identified by more than 20%, with one variation causing a difference of over 100%. In particular, changing the interpolated resolution has a large impact. This is interesting as the original resolution of the ozonesonde, indicated by the different year ranges examined, has little effect. However, it is expected that the vertical resolution will have a big effect as this changes the size of the layers sampled and hence the thickness of the TPFs sampled. Variations in the stability from condition 3 also has a large impact (20-60%) as this is also related to the thickness of the TPFs examined.

The large variations in the number of TPFs identified as the parameters are adjusted is very undesirable, since it indicates that the TPF identification algorithm is highly sensitive to the values used in the identification algorithm. Hence it is difficult to select a set of "correct" parameters to use for the identification algorithm. In order to confirm which set of parameters to use, an additional data set would be required to confirm the existence of TPFs in the ozonesonde records. The NNR data has been shown in Section 4.2 to be too inaccurate as a measure to confirm the existence of TPFs, this is likely a result of its low vertical resolution. A higher resolution data set may provide a better means for the confirmation of the parameters for the identification algorithm.

4.5 Limitations of TPF Algorithm

The TPF identification algorithm has some severe limitations and problems. The main limitation is that it is only useful for high resolution data sets, as the resolution limits the size of the folds that can be identified. This limits the procedure to ozonesondes which provide data sparse measurements in terms of global and temporal coverage. In addition, the location of the data measurement site has an impact on the number of folds identified, as is seen by the large differences between Lauder and Boulder. Therefore, the number of TPFs at any one location cannot be used to determine the impact of TPFs in a hemispheric or global sense.

The main concern with the identification algorithm is that a number of the parameters are not robust, meaning a small variation in the parameter can vastly change the number of TPFs identified. This shows that the identification algorithm is highly sensitive to the values used. This is a very undesirable result as it makes it difficult to conclude which parameters are correctly identifying TPFs without a priori knowledge or an additional data set. Comparison of the algorithm to a different data set (ie. NNR) to confirm the identification process has been inconclusive, with few TPFs being positively identified.

There is an additional limitation to using ozonesondes for TPF identification. It was stated earlier that this algorithm is particularly good at locating well developed folds which manifest in ozonesonde profiles as layers of stratospheric air within the troposphere. The sampling of these folds is highly dependent on the location of the ozonesonde cross section with respect to the TPF structure. An example of this is shown in Figure 4.11, with three different ozonesonde profiles indicated. Flight 1 would see a clear layer of stratospheric air within the troposphere and would be positively identified by the algorithm. Flights 2 and 3 are both sampling the same fold but at different locations. These ozonesondes do not see a layer of stratospheric air and would not have a positive TPF identification. These flights are sampling a well developed fold, however, as they are at the wrong location the fold will be undetected. This indicates a further fault in the use of ozonesondes for TPF identification, although how large an impact this has is unknown.

Due to these significant limitations, it is desirable to find another method to identify the occurrences of STE. An ideal method would be robust with regards to any input parameters and would not have any spatial sampling issues. One solution to this could be to use a global data set that is satellite based. while satellites still have spatial sampling issues, both vertical and horizontal, they have the potential to provide better spatial information for the identification of TPFs than ozonesondes. In the subsequent chapters, alternative methods for identifying TPFs and other types of mixing and transport are outlined, based on a satellite instrument.

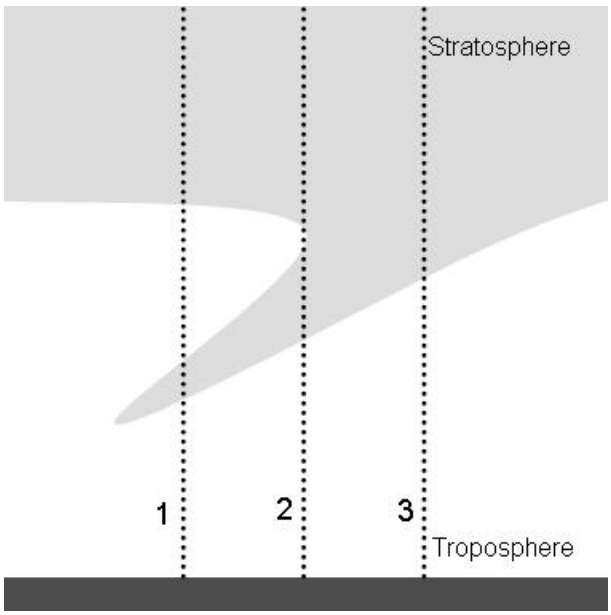

Figure 4.11: Three ozonesonde soundings of a tropopause fold. The light grey shading shows air with stratospheric characteristics, while the unshaded region shows air with tropospheric characteristics. The path of the ozonesondes are indicated by the dotted lines.

Chapter 5

Validation of AIRS v4 ozone profiles in the UTLS using ozonesondes from Lauder, NZ and Boulder, USA*

The upper troposphere/lower stratosphere (UTLS) is a region of key interest for understanding global change and chemistry climate coupling. Two-way exchange in the UTLS, known as stratosphere troposphere exchange (STE), is extremely important as water vapor and ozone have large gradients in this region. The exchange processes in this region are discussed in depth in Chapter 2. As water vapor and ozone are radiatively important trace gases, it is essential to have an understanding of the UTLS. Hence the need for ozone measurements is critical. This chapter compares AIRS version 4 (v4) ozone profiles against ozonesonde observations to assess the potential for this product to provide ozone concentration information in the UTLS region. While the ozone product's main purpose is to improve the quality and accuracy of the temperature product, and hence it is not a focus of the AIRS retrieval, the ozone product may be useful in its own right.

The aim of this chapter is to further assess the quality of the AIRS vertical ozone profiles and in particular to examine the potential use of these data for STE studies. The AIRS level 2 ozone product on 28 levels are compared to ozonesondes from Lauder, NZ (45.0°S, 169.7°E) and Boulder, USA (39.9°N, 105.3°W). Ozonesonde ozone measurements are considered to be very accurate as they are measured in-situ by chemical methods. The ozonesonde data and the AIRS data is discussed in more depth in Chapter 3. This comparison is an extension of

*This chapter is based on the publication Monahan, K. P., L. L. Pan, A. J. McDonald, G. E. Bodeker, J. Wei, S. E. George, C. D. Barnet, and E. Maddy, Validation of AIRS v4 ozone profiles in the UTLS using ozonesondes from Lauder, NZ and Boulder, USA, *Journal of Geophysical Research-Atmospheres*, 112, D17304, doi: 10.1029/2006JD008181, 2007. [*Monahan et al.*, 2007]

previous studies [*Bian et al.*, 2007; *Fetzer et al.*, 2005] and utilises two larger and better established data sets.

A recent study by *Bian et al.* [2007] has compared the AIRS ozone profiles with ozonesonde data from Beijing using a new type of ozonesonde called the Global Positioning System Ozone sensor (GPSO3). They found that AIRS ozone concentrations appear to be biased high by 20% in the middle troposphere, and biased low by about 20% near the stratospheric ozone peak. Their study also indicated that the agreement between 400-70 hPa, the UTLS region, is usually within 10%. They also show a consistent variability and positive correlation between the ozonesonde and AIRS in the UTLS region.

The ability to measure ozone variability has widespread application. For example, *Randel and Park* [2006] have used AIRS to show how transient convective events, associated with the Asian summer monsoon, lead to vertical transport of low ozone and high water vapor into the UTLS region. In *Pan et al.* [2007b], three-dimensional AIRS ozone fields were also effective in providing a large scale background for in situ measurements during a field campaign. High horizontal resolution AIRS ozone data helped map out the region of large ozone gradient and showed a high degree of correlation with the dynamic features of the UTLS region.

Fetzer et al. [2005] used ozonesondes at 6 locations to validate the AIRS ozone column and ozone profile. The comparison on AIRS pressure levels showed the stratosphere had about a -10% bias and the troposphere had a bias of between +20% and +70%. Details for this study regarding the number of ozonesondes and the comparison method used are limited. The AIRS total column value was within a few percent of the Total Ozone Mapping Spectrometer (TOMS) observations in their study; this is attributed to the positive and negative biases working to cancel one another.

Section 5.1 describes the AIRS retrieval method. A discussion of the comparison methods and related results are presented in Section 5.2. Section 5.3 describes sets of analyses which test a number of potential explanations for the observed biases between the instruments, including sampling biases and problems with the retrieval technique. Section 5.4 summarises the conclusions made.

Ozonesondes and AIRS have two distinct methods for measuring ozone, this results in different measurement ranges for each instrument. On a profile by profile basis, the measurement range also varies due to different factors, such as

clouds. The overlapping measurement region between AIRS and the ozonesondes always covers the UTLS, hence this region is the focus for this paper.

5.1 AIRS Retrieval

A detailed description of the AIRS retrieval method is presented in *Susskind et al.* [2003, 2006]. Briefly, the retrieval method can be separated into three stages:

1. cloud-clearing
2. regression retrieval
3. physical retrieval

The cloud-clearing stage is necessary as clouds have a significant effect on observed infrared radiances. Therefore, an accurate treatment of the effects of clouds on the observed AIRS radiances is critical to obtaining accurate soundings. The cloud clearing processing uses the multiple AIRS observations within the 3 by 3 array of AIRS spots in a single AMSU-A[†] footprint to determine information about the fractional cloud coverage and altitude associated with a number of cloud layers. This allows the radiance that would be observed under clear sky conditions to be obtained (see *Susskind et al.* [2003] for more detail). It should be noted that the reliance on cloud clearing results in a bias towards cloud free regions. If there is no cloud free region in the 3 by 3 array, then no AIRS profiles are retrieved. AIRS may therefore miss some tropopause folds and baroclinic regions with large amounts of cloud cover.

The methodology of the regularised regression retrieval (the second step) is described in *Goldberg et al.* [2003]. This process uses a predetermined relationship between AIRS radiances and atmospheric profiles, including temperature, water vapor and ozone, to produce a first estimate of the profiles. The relationship is a coefficient-matrix obtained using least squares regression and principle component analysis relating an ensemble of atmospheric profiles and the simulated AIRS radiances. The profile ensemble is created using three days of the European Centre for Medium Range Weather Forecasts (ECMWF) reanalyses (6th September 2002, 25th January 2003, and 8th June 2003) and is referred to as the training

[†]AMSU-A: Advanced Microwave Sounding Unit-A

data set. The profiles produced by the regression retrieval are then used in the AIRS physical retrieval (the final retrieval step) as the initial profile of iteration. The physical retrieval iterates to minimise the radiance differences between the forward model results and measurements, details are given in *Susskind et al.* [2003, 2006]. In principal, the training data set can be observationally data based, but a data set that meets the required needs of the training process, i.e., coverage that accommodates different observing geometry of the AIRS instrument, does not exist. One of the goals of this work is to show the potential issues related to using ECMWF profiles as a training data set in the regression retrieval. It was recognised during the pre-launch retrieval studies using simulated data, that biases in the training data set can affect the retrieval results, and the physical retrieval step should serve to minimise the biases [*Goldberg et al.*, 2003].

While AIRS makes measurements in 2378 spectral channels, considerably fewer channels are used in the AIRS physical retrieval. *Susskind et al.* [2006] indicates that 58 channels are used for the temperature profile retrieval, 49 channels for water vapour, and 26 channels for ozone. AIRS data are collected in granules with 1350 profiles per granule. Each granule represents 6 minutes worth of data. AIRS has a resolution of roughly 50km by 50km along the orbital track. Profiles within an AIRS granule are spatially separated on average by 0.15 degrees in latitude and 0.2 degrees in longitude. Hence the AIRS profiles are relatively dense spatially, particularly in comparison to many other data sets. Profiles are selected using the quality and pressure validity flags to ensure that only high quality ozone retrievals are used. In particular, only profiles where the quality flag was equal to zero (ie. Qual_O3=0), indicating the best quality are used. Any measurements at levels that have pressures greater than the valid bottom pressure (ie. Press_valid_bottom) are also removed from the analysis.

Further information about the retrieval method can be found in *Susskind et al.* [2006] and *Goldberg et al.* [2003]; the calibration of the AIRS infrared channels is available in *Pagano et al.* [2003]; instrument, data flow and processing in *Aumann et al.* [2003] and on the AIRS web site at http://www-airs.jpl.nasa.gov/Technology.

5.2 Comparison of Ozonesonde and AIRS data

All AIRS profiles to be compared with ozonesondes must be nearly coincident in both space and time to reduce the effect of variations in the ozone field. In this

study the following coincidence criteria are applied to select the AIRS profile. The nearest AIRS profile within an approximately 100 km radius of the ozonesonde launch site and the closest available in time are selected. The impact of time and spatial sampling is examined in Section 5.3.1.

The AIRS retrieval provides ozone concentrations on 28 pressure levels. With the exception of the uppermost level, the values reported at the bottom boundary are the mean value between layers [*Olsen et al.*, 2005]. To enable comparison, the high-resolution ozonesonde data are converted to layer averages on the AIRS grid. There are 6 levels that cover the UTLS region - 250, 200, 150, 100, 70 and 50 hPa.

The Lauder ozonesondes have a response time of about 20 seconds to changes in ozone, which corresponds to an overestimation of the altitude by about 150 m [*Brinksma et al.*, 2000]. A comparison study at Lauder by *Brinksma et al.* [2000] using ozonesondes, Differential Absorption Lidar (DIAL) and Stratospheric Aerosol and Gas Experiment II (SAGE II)measurements found that an offset of 125 m ($\pm$50 m) gave the best comparison. Due to the low vertical resolution of the AIRS data, the Lauder AIRS/ozonesonde comparisons were found to be relatively insensitive to any altitude adjustment. An equivalent correction factor for the Boulder ozonesondes is not available. Hence, as the correction factor had minimal effect and to maintain consistency with the Boulder ozonesondes, no altitude adjustment is applied to the ozonesonde data.

Ozone mixing-ratio relative difference profiles (d) are calculated using:

$$d_i = \frac{x_i - r_i}{r_i} \times 100 \tag{5.1}$$

where r is the reference profile (ozonesonde), x is the validation profile (AIRS in this case) and i is the vertical level. This creates a comparison profile for each AIRS/ozonesonde pair.

To provide an overview of the relative differences discussed later in this paper, the mean ozone mixing ratio profile and standard deviation of all of the ozonesonde and AIRS profiles used in the later comparisons are presented in Figure 5.1. The mean profiles of the measurements from AIRS and the ozonesondes are similar in shape and have similar standard deviations. However, a t-test shows the instrument sample-means to be statistically different on all vertical levels (above the 90% significance level). It should be noted that the Lauder tropospheric

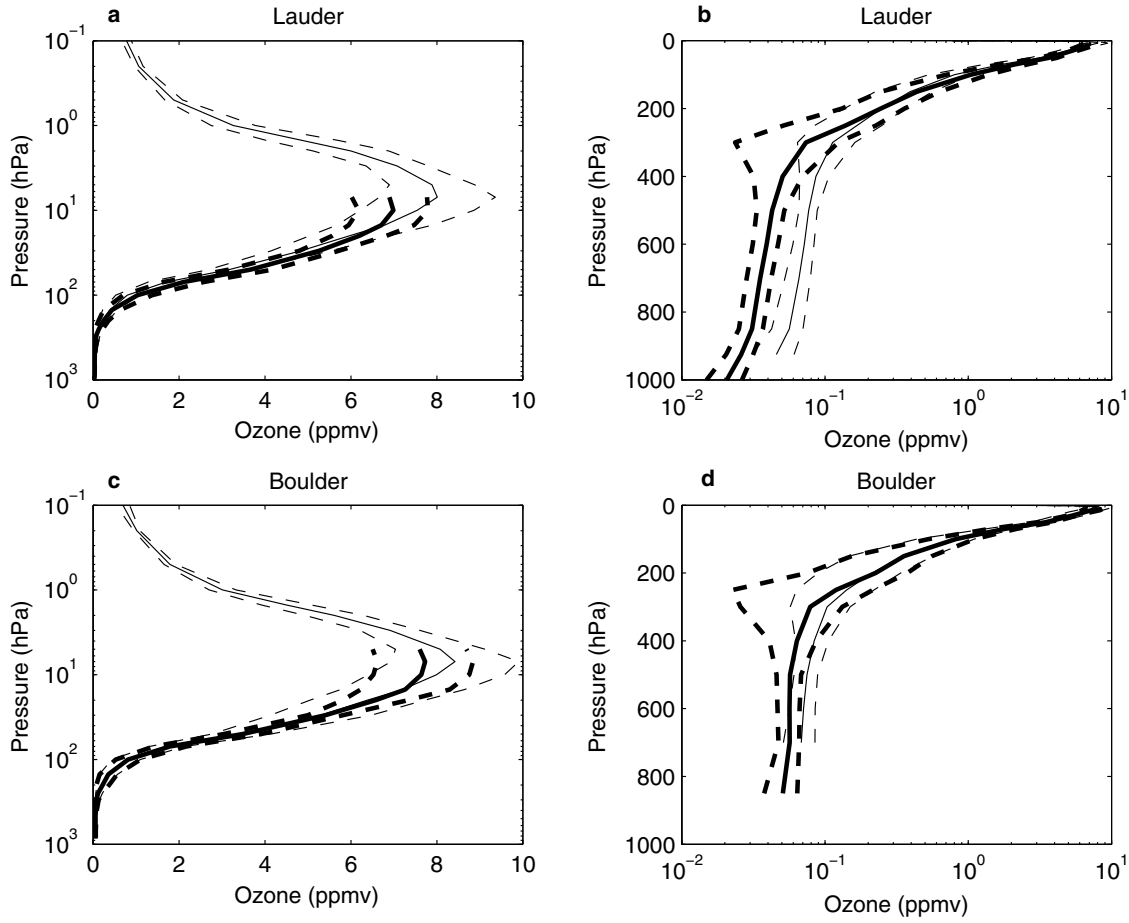

Figure 5.1: Mean ozone mixing ratio profiles observed at Lauder and Boulder. There are 189 Lauder profiles and 111 Boulder profiles for each instrument. Thick lines display the means defined by the ozonesonde profiles, thin lines show the mean profiles from AIRS. Dashed lines display one standard deviation either side of the mean. b) and d) repeat the data in a) and c), with a logarithmic ozone scale and linear pressure scale to emphasise tropospheric ozone.

values are smaller than the Boulder tropospheric values.

5.2.1 Direct Comparison

Comparison of the ozone values on the AIRS pressure levels is the simplest comparison possible. Figure 5.2 shows relative difference between AIRS and ozonesonde ozone mixing ratios (calculated with Equation 5.1) on each of the pressure levels that overlap between the instruments. The vertical solid lines give the median bias of AIRS measurements in relation to the ozonesonde measurements. A positive bias indicates that the ozone mixing ratio from AIRS is

higher than from the ozonesondes and a negative bias indicates the opposite. In comparison to Figure 5.1, it may be unexpected that the tropospheric bias should be so large. However, as the tropospheric ozone values are small, the relative differences are extremely sensitive to small changes in ozone, resulting in a large relative bias. Medians and interquartile ranges are used as they are less sensitive to the outliers and skewed distribution of the relative differences observed.

Boulder shows a positive median bias of ∼40% between ∼700-200 hPa and little bias of 0-5% between 100-30 hPa. This would indicate that for low to mid-stratospheric studies over Boulder, the AIRS data are unbiased. The Lauder comparison shows a large positive median bias of ∼80% between 700-250 hPa, and a smaller negative median bias of ∼0 to -20% between 100-30 hPa. The seasonal change in ozone, with regards to the relative difference, is smaller in the lower stratosphere than in the troposphere (figure not shown). Hence the interquartile range in Figure 5.2 is smaller at lower pressure levels (100-30 hPa) than at higher pressure levels (700-200 hPa).

Fetzer et al. [2005] show a similar range of biases in their comparison. *Bian et al.* [2007] indicate much smaller biases than this study. However, it should be noted that *Bian et al.* [2007] use a different type of ozonesonde which displays a 30% bias in the troposphere compared to the conventional ozonesondes used in this study. On adjusting for differences in location and ozonesonde instrumentation, the relative bias in AIRS data observed by *Bian et al.* [2007] are of comparable magnitude to those observed in the present study.

5.2.2 Comparison Relative to the Tropopause

While Section 5.2.1 provides some information on the vertical structure of the bias in the AIRS data, it does not account for variations in the UTLS region caused by changes in the tropopause height between profiles, for example, the natural temporal variation in the tropopause height due to the movement of synoptic weather systems. In order to compare only like types of air (e.g. stratospheric air with stratospheric air etc), profiles from the two instruments are aligned using a tropopause relative vertical coordinate system. This improves the stratospheric component of profile comparison and increases the accuracy of the comparison in the UTLS region. The adjustment with respect to the tropopause acts to remove the seasonal variations in the UTLS region that were present in the pressure level

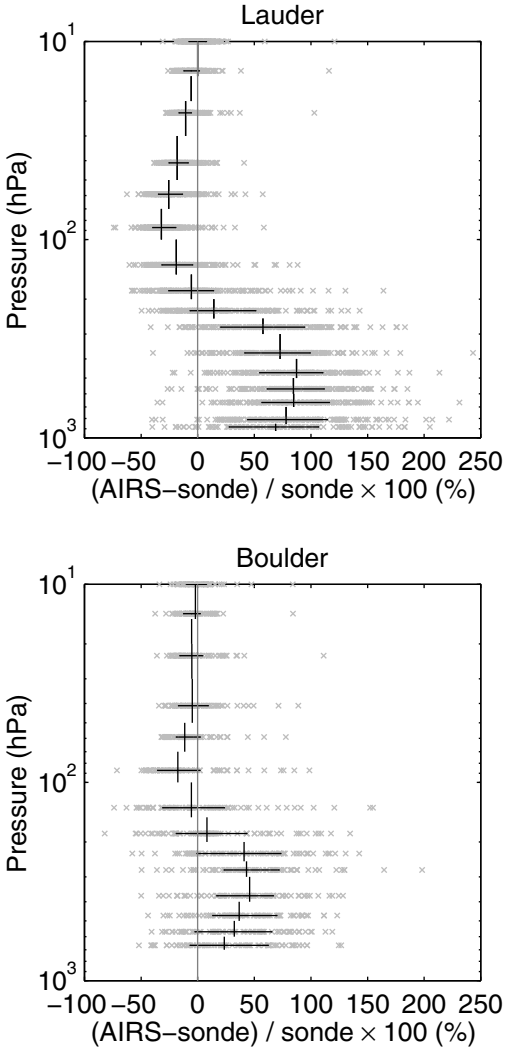

Figure 5.2: AIRS/ozonesonde comparison for closest profile averaged on AIRS pressure layers. Black vertical solid lines show the median value and the layer thickness. Horizontal bars display the interquartile range. Crosses show the individual data points and the grey vertical line highlights the zero bias.

comparison.

Individual tropopause heights are calculated for each temperature profile on geopotential heights from each instrument. To allow continuity between the tropopause calculations, the ozonesonde data are reduced to the same 28 levels as the AIRS data. Tropopause height is calculated at a subgrid scale [*Reichler et al.*, 2003] using the standard thermal definition of the tropopause [*World Meteorological Organization*, 1957]. The tropopause level is slightly different for each of the measurements of a AIRS/ozonesonde comparison pair. There are several possible factors that could cause the differences in the tropopause levels calculated, such as slightly different air masses being measured, or differences in the measurement techniques.

Each AIRS/ozonesonde profile pair can then be aligned based on the tropopause level. Any pair where the tropopauses from the two instruments are more than 3 km apart are discarded as either the air masses being sampled are considerably different, or there is large error in the tropopause heights due to the coarse vertical resolution of the AIRS data above 150 hPa. It should be noted that this only removes a small number of comparisons. The tropopause height is set to zero for each profile. This results in the zero point being at a slightly different position with respect to the 28 levels on each of the profiles. In order to easily calculate difference profiles between instruments, it is necessary to have the measurements on the same levels, as opposed to the multitude of levels that result from changing to tropopause relative height. To remove the necessity of interpolating, the ozonesonde profiles on the 28 levels are recalculated from the original high resolution ozonesonde data using the new tropopause relative levels from the corresponding AIRS profile. Relative difference profiles are then calculated using Equation 5.1. Figure 5.3 displays relative differences using tropopause adjusted heights along with the median and quartile ranges for 2.5 km layers.

This method for aligning tropopauses was selected as it produces the best alignment of the two instruments.[†] If the profiles are incorrectly aligned, for example AIRS stratospheric measurements are not matched with ozonesonde stratospheric measurements, then the resultant profile displays a positive spike below the 'common' tropopause level. This was confirmed through Monte Carlo simulations and is a result of the sharp gradients in the tropopause region. There is a slight signal from mismatched tropopauses located at the layer centered at tropopause-

[†]A possible alternative method would be to interpolate the ozonesonde data to the new 28 levels.

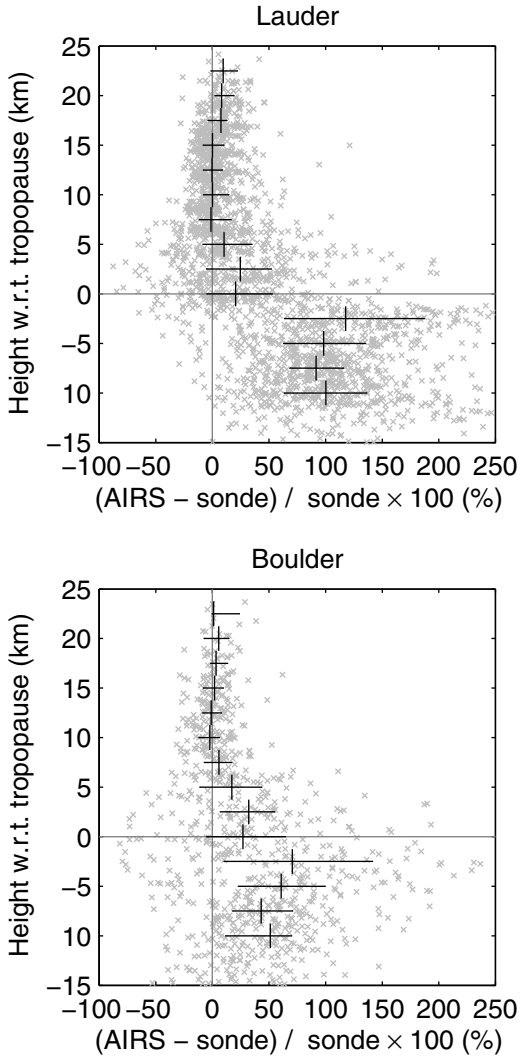

Figure 5.3: AIRS/ozonesonde relative difference comparison for Lauder and Boulder with the altitude adjusted to make the tropopause height the vertical zero baseline. Vertical solid lines show the median value of the differences and the layer thickness. Horizontal bars display the interquartile range. The dashed lines highlight the zero bias in the vertical and the tropopause level in the horizontal. Crosses indicate the individual relative differences. Note a few of the individual differences have been cut off by the horizontal scale selection.

2.5 km. This signal has the highest bias value and has a large interquartile range, indicating that there is a large amount of variation in the relative difference values in this region. This signal causes some reduction in the amount of correlation in this layer through the increase in the bias. However, it is of little consequence as the effect is small when compared to the expected value suggested from the tropopause layers lower in altitude.

A comparison of Figures 5.2 and 5.3 shows that the same general pattern is observed. However, the bias in the troposphere has become slightly larger, and the bias in the lower stratosphere has become smaller and at some levels becomes positive. Lauder has a median bias of +90 to +120% in the troposphere and 0 to +25% in the stratosphere. Boulder has a median bias of +45 to +70% in the troposphere and 0 to +30% in the stratosphere.

The larger bias at the Southern Hemisphere site in comparison to the Northern Hemisphere site shown in Figures 5.2 and 5.3 would indicate that there is a factor that is location or hemisphere dependant. A hemispheric instrument bias due to a satellite-specific error is highly unlikely. The quartile range is similar for both locations, this suggests that while the bias is different at the two locations, the variation of the ozone values is similar and displays seasonal patterns. This would indicate that the measurements at each location are consistent apart from the bias.

The correlation between the ozone measurements from AIRS and the ozonesondes is shown in Figure 5.4 using scatter plots on three relative altitude layers. The correlation coefficients are shown for the three layers used in Figure 5.4. Over the range of tropopause relative altitudes from tropopause-10 km to tropopause+20 km, the correlation coefficients range from 0.5 to 0.85. The region of maximum correlation is the layer between the tropopause and 10 km above the tropopause, with decreasing values either side of this layer. Hence the results are clearly correlated but they do not lie on the one-to-one line. The shapes of the profiles from the different instruments will be similar but the numerical values will be different. This was shown earlier with regards to Figure 5.1. This implies that while AIRS does not measure the absolute value correctly, it does accurately represent changes in ozone. This is a significant result as it indicates that the AIRS ozone measurements can be used for studies where the variability of the ozone is important rather than the absolute value.

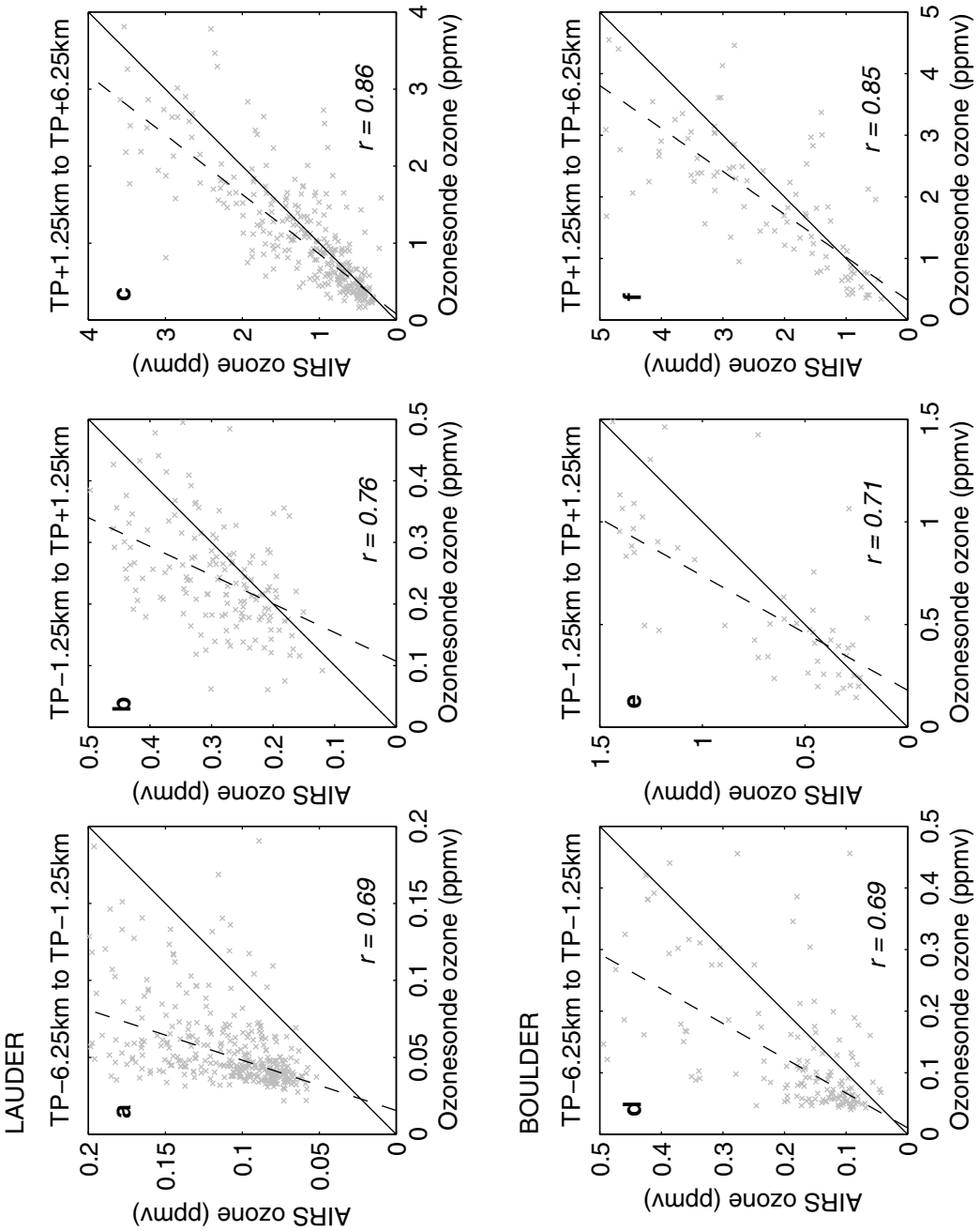

Figure 5.4: Scatter plots showing the relationship between AIRS ozone and ozonesonde ozone at different tropopause(TP) relative altitude layers. The one-to-one line is shown as the solid line, best fit is the dashed line. Correlation coefficients (r) are given for each layer.

5.3 Bias Analysis

Figures 5.2 and 5.3 show both locations have some bias in the ozone values, with a larger bias at Lauder. The observations also suggest the biases observed are generally larger in the lower troposphere than in the stratosphere, and that the biases are smallest in the UTLS. The two most likely reasons for the patterns observed are either sampling differences at the two sites which are discussed in Section 5.3.1; or biases introduced by the retrieval which could come from any of the three steps detailed in Section 5.1. The possible bias from the cloud clearing step is discussed in Section 5.3.2 and from the regression and physical retrieval steps in Section 5.3.3.

5.3.1 Time and Space Sampling

Multiple AIRS profiles are often within 100 km of the ozonesonde launch site allowing a measure of the geographical variation in the AIRS measurements. The original AIRS profile selected for comparison using the coincidence criteria outlined in Section 5.2, is used as the base profile. All other profiles within 100 km of the launch site are then compared to the base profile using the following formula:

$$base/other\ comparison = \frac{base - other}{\frac{1}{2}(base + other)} \times 100 \tag{5.2}$$

Hence, for each of the original base profiles there are a number of base/other comparison profiles. The mean of all the comparison profiles is zero as the variations in the profiles have a similar magnitude in either direction. The standard deviation of the base/other comparisons gives the best measure of the variation between profiles. The standard deviation is calculated twice, with any extreme outliers (more than three standard deviations) removed from the data set after the first calculation. This ensures a more accurate standard deviation rather than one affected by extreme outliers. As the standard deviation shows very little altitudinal dependence, the mean of the standard deviation gives a measure of the bias that could potentially be explained by geographical variations. For Lauder this value is 6.4 % and for Boulder is 9.7 %.

As indicated previously, the Aqua satellites orbit provides a roughly twice daily global coverage. From this it follows that no ozonesonde launch should be further

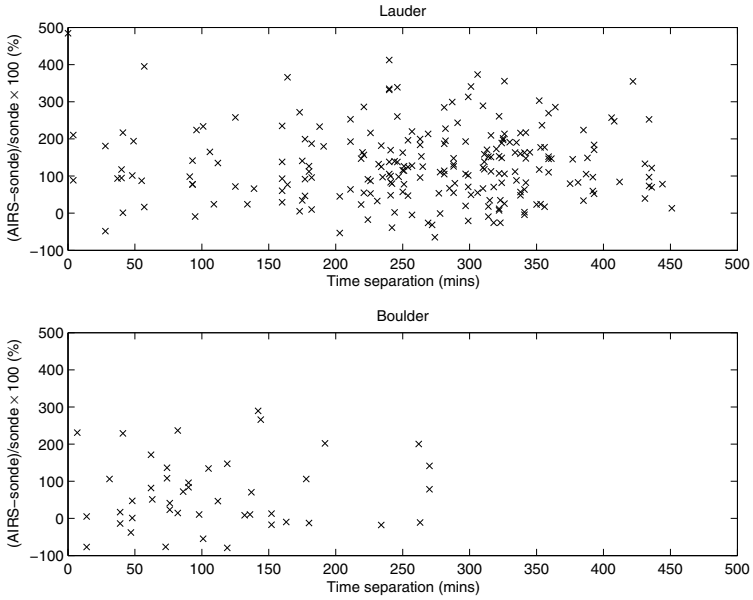

Figure 5.5: Relative difference derived using Equation 5.1 and time separation for AIRS and ozonesonde measurements for a relative altitude layer of tropopause-3.75 km to tropopause-1.25 km

than 6 hours from an AIRS measurement, however, as a result of the orbital pattern, this is not always true. The Lauder AIRS and ozonesonde profiles are separated by a mean of 4.4 hours with a standard deviation of 1.7 hours. In comparison, Boulder has a mean of 1.9 hours with a standard deviation of 1.2 hours. The relative difference, calculated using Equation 5.1, is compared on relative altitude layers to the time separation between the AIRS overpass and ozonesonde launch. An example of the relationship between the time separation and relative difference is shown in Figure 5.5 for the relative altitude layer from 3.75 km below the tropopause to 1.25 km below the tropopause (tropopause−3.75 km to tropopause−1.25 km). The equivalent figure for each layer displays a similar relationship between time separation and relative difference. A larger time separation should produce larger relative differences as the air mass being sampled by the two instruments is likely to have varied by a larger amount. However, for the time separations used in this study, there is no noticeable change in the relative difference in any relative altitude layer.

5.3.2 Cloud Clearing

As previously indicated, the cloud clearing stage of the retrieval takes the observed radiances and adjusts them to provide estimates of the radiances if no clouds were

in the field of view. A useful way to examine whether this stage of the retrieval scheme explains the form of the bias is to examine the relationship between the differences observed as a function of cloud fraction [*Susskind et al.*, 2006]. If the bias is dependent on the cloud fraction, then it would imply that the bias is related to this step. However, comparison on several altitude levels both in the troposphere and the stratosphere shows no relation between the cloud fraction and the bias. From this we can conclude that the bias is not likely to be a result of the cloud clearing stage in the retrieval.

5.3.3 Examination of the Regression Retrieval

The physical retrieval is the third step of the retrieval process and creates the final profile product. To understand how much the physical retrieval contributes to the final profile product in version 4, we have examined a number of cases and performed some basic statistical analyses. Figure 5.6 gives an example using a single profile retrieval. The case selected is for a Lauder ozonesonde, launched at 20UT, 24 March 2005. The AIRS retrieval process for this case is shown by three profiles: a reference profile, a first estimation profile associated with the regression retrieval and the final retrieval profile. The reference profile is the mean state of the ECMWF based training data set. The first estimation is produced by the regression step and further used as the first guess for the physical retrieval. It is readily apparent in the figure that the initial reference state has a very different shape from the true profile in the upper troposphere. The regression retrieval produced a profile shape that is similar to the true profile. The physical retrieval in this case added little information. The final retrieval is therefore almost identical to the regression result in this case.

To find out how representative this case is, we completed a statistical analyses, the results of which are presented in Figure 5.7. The statistics are produced from 11623 profiles, retrieved from AIRS global measurements on 30 January 2005 including both ascending and descending orbits but spatially sub-sampled in 3×3 degree latitude and longitude intervals. This figure shows the amount of change produced in each step of the retrieval, starting from a reference profile, for this particular profile ensemble. Figure 5.7a shows how the regression retrieval modifies the mean state significantly, especially in the UTLS region. This is a result of the ozone values in this region having a large gradient and large variability due to the tropopause. The size of the "error bar" in this case shows the percent variation in the shape of the profiles. The percentage of modification

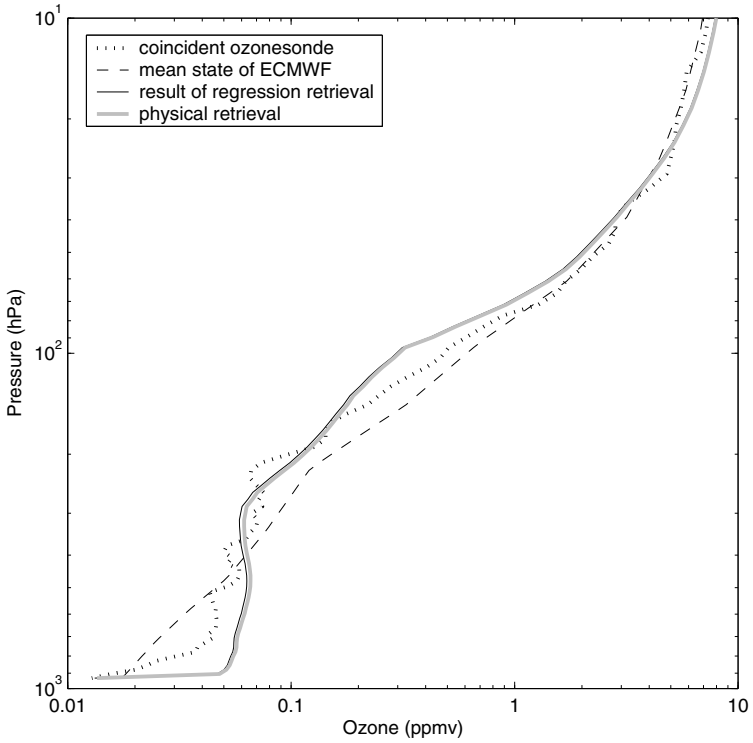

Figure 5.6: An example of AIRS ozone profile retrieval. The "true" ozone profile (dotted curve) is represented by the ozonesonde measurement, launched from Lauder at 20 UT, 24 March 2005. The AIRS retrieval for this case is shown by 3 profiles: the mean state of the ECMWF training data (dashed curve), result of the regression retrieval (solid black curve), and the result of the physical retrieval (thick solid grey curve).

from the physical retrieval is smaller, roughly 10% or less (see Figure 5.7b). However, it shows the vertical distribution of ozone measurement information used in the physical retrieval. The additional information appears to have two layers, one peaks near 50 hPa (LS), the other near 400 hPa (UT). The physical retrieval appears to contribute more in the LS than in the UT. The amount of extra information diminishes toward the surface.

This indicates that the source of the bias results from stages prior to the physical retrieval, as the physical retrieval has very little impact on the final profile. The physical retrieval has been unable to adjust the profile away from the regression step of the retrieval. It should be noted that the result of the regression retrieval has the correct shape when compared to the ozonesonde profile.

The regression step is based on ECMWF data which are known to have biases [*Dethof and Holm*, 2004; *Morcrette*, 2003], therefore the source of the bias may be related to this step. The comparisons shown in Section 5.2 show a much larger bias at the Lauder site than at the Boulder site. If the ECMWF reanalyses data used to create the regression retrieval profile differs significantly from the local ozonesonde climatology, it may lead to consistent inaccuracies in the AIRS retrieval. This bias is also likely to be location dependant. To examine how representative the ECMWF reanalysis training days are for the situation at Lauder and Boulder, comparisons of the data sets are shown in Figure 5.8. This figure shows a climatology of the Lauder and Boulder ozonesondes compared with the three training days from the ECMWF reanalyses as discussed in Section 5.1. The ECMWF ozone has a positive bias at pressures between ∼100 to 800 hPa and a smaller negative bias above 100 hPa. This shows that the ECMWF reanalysis is not a perfect representation of the conditions at Lauder or Boulder, particularly at low altitudes. Figure 5.8 also displays the mean relative difference profiles from the data in Figure 5.2 for comparison purposes. The comparisons of the ozonesondes to ECMWF and to AIRS are extremely similar. This indicates that the AIRS data are highly dependent on the ECMWF training data as might be expected from the data displayed in Figures 5.6 and 5.7.

As the AIRS data has been seen to be strongly affected by the ECMWF training set, the distribution of ECMWF values could provide further insight into the retrieved AIRS values. The ECMWF data were converted from pressure levels to altitude, the tropopause calculated using the thermal definition, then the altitudes were adjusted to be tropopause relative as used earlier in the study. The probability distribution of the ozone mixing ratio for three different layers is shown

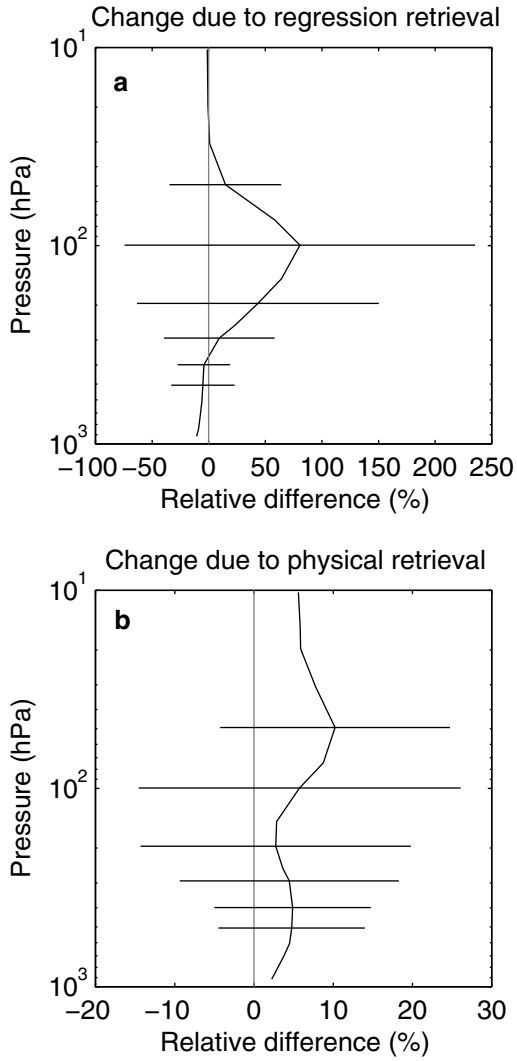

Figure 5.7: An ensemble estimation of retrieval information from the regression and the physical retrieval. a) shows the mean and standard deviation, represented by solid curve and error bars, respectively, of the relative change (in percent) of the climatology of the training data set and the ozone profile produced by regression. b) shows the mean and standard deviation of the relative change between the ozone profile produced by the regression and the ozone profile produced by the physical retrieval step. The error bars mark the pressure levels of AIRS ozone profile standard product in the UTLS region. Note the different horizontal scales in Figures a and b.

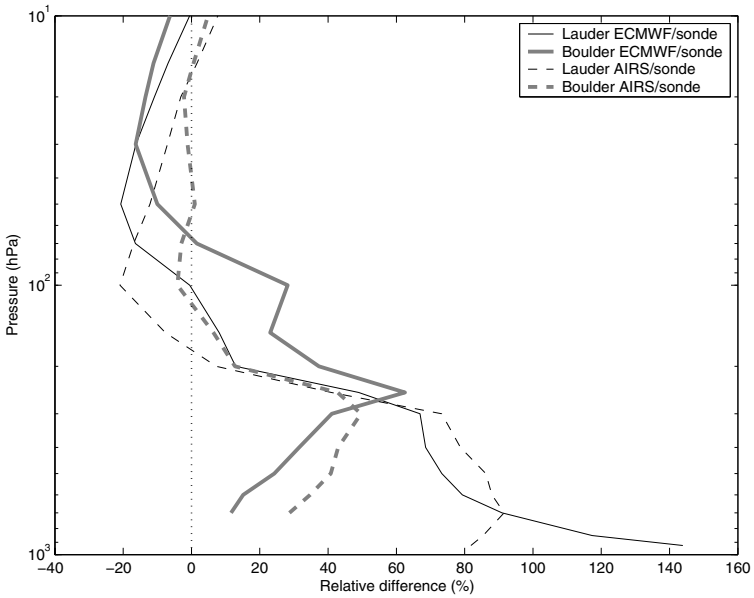

Figure 5.8: Dashed lines are AIRS/ozonesonde mean relative differences for Lauder (thin) and Boulder (thick). Solid lines are the differences between the mean of the ECMWF climatology and the mean of the ozonesonde climatology for Lauder (thin) and Boulder (thick). The dotted line gives the zero percent level.

in Figure 5.9. Each panel shows the probability distribution of ozone mixing ratio values for Lauder, Boulder and the ECMWF training days. A higher value for the occurrence frequency (vertical axis) indicates the corresponding mixing ratio is more likely to occur than a lower occurrence frequency. It can be seen that the distribution patterns of ozone mixing ratio varies between the Lauder and Boulder climatologies and the ECMWF training days. The probability distribution of the ozone mixing ratio for Boulder is more similar to the ECMWF climatology, which indicates that the ECMWF data are a better match for Boulder than for Lauder. In the tropospheric layer (tropopause−6.25 km to tropopause−1.25 km) the occurrence frequencies are quite different, with the ozonesondes having a lower ozone mixing ratio than the ECMWF reanalyses. In particular, the Lauder distribution is significantly different from the ECMWF distribution in the troposphere. The comparison of the occurrence frequencies is similar in the tropopause region (tropopause−1.25 km to tropopause+1.25 km). The overlap between the distributions with increasing altitude seems to explain the increasing correlation between the AIRS and ozonesonde data set. An additional contribution to the higher bias at Lauder could be the fact that the ozone in the UT is generally much lower compared to Boulder. The maximum occurrence is ∼0.04 ppmv, as shown in Figure 5.9. It is possible that this value is below the detection limit of the

AIRS instrument, currently estimated to be 0.06-0.08 ppmv. Results presented in this study should lead to a better characterisation of the AIRS ozone detection limit and other measurement sensitivity issues.

Figure 5.8 shows that the bias between the AIRS and ozonesonde data is similar to that between the ozonesondes and ECMWF. Hence the AIRS data are strongly affected by the ECMWF data. Figure 5.9 more closely pinpoints that the bias is a result of the distribution of the ozonesondes being significantly different from the ECMWF climatology. These results along with Figures 5.6 and 5.7 indicate that in the operational retrieval, the biases created in the regression step are not effectively corrected for in the physical retrieval. Since only 26 channels (out of 2378) are used in the operational retrieval for ozone profiles, this could be due to the lack of spectral information in the upper troposphere region in the physical retrieval or that the physical retrieval is over constrained.

Previous comparison studies of the ECMWF ozone product (both the forecast and the ERA-40 models) and ozonesonde data display an overestimation of ozone in the lower troposphere [*Dethof and Holm*, 2004; *Morcrette*, 2003]. This problem is smaller during the summer months and at low and middle latitudes. During the winter, the comparison is worse as multiple ozone peaks and reduced ozone levels cause the model to severely overestimate and mislocate ozone. These seasonal variations may explain the seasonal variation in the bias of AIRS/ozonesonde (not shown), where the summer shows a smaller tropospheric bias and the winter has a larger bias.

5.4 Conclusion

Comparison of the AIRS v4 vertical ozone profiles in the UTLS with ozonesonde observations at Lauder and Boulder has shown the accuracy and sources of error in the data set. Two methods of comparison between AIRS and ozonesondes are displayed. Comparison on pressure levels show that Lauder has a median bias of 80% at low altitudes (∼700-200 hPa) and of 0 to -20% at high altitudes (∼100-30 hPa). Boulder has a median bias of 40% at low altitudes (∼700-200 hPa) and of 0 to 5% at high altitudes (∼100-30 hPa), as shown in Figure 5.2. By using a tropopause relative vertical coordinate, the effects of variations in the tropopause level are removed which allows conclusions to be drawn based on the troposphere and stratosphere. The tropospheric measurements have a large bias,

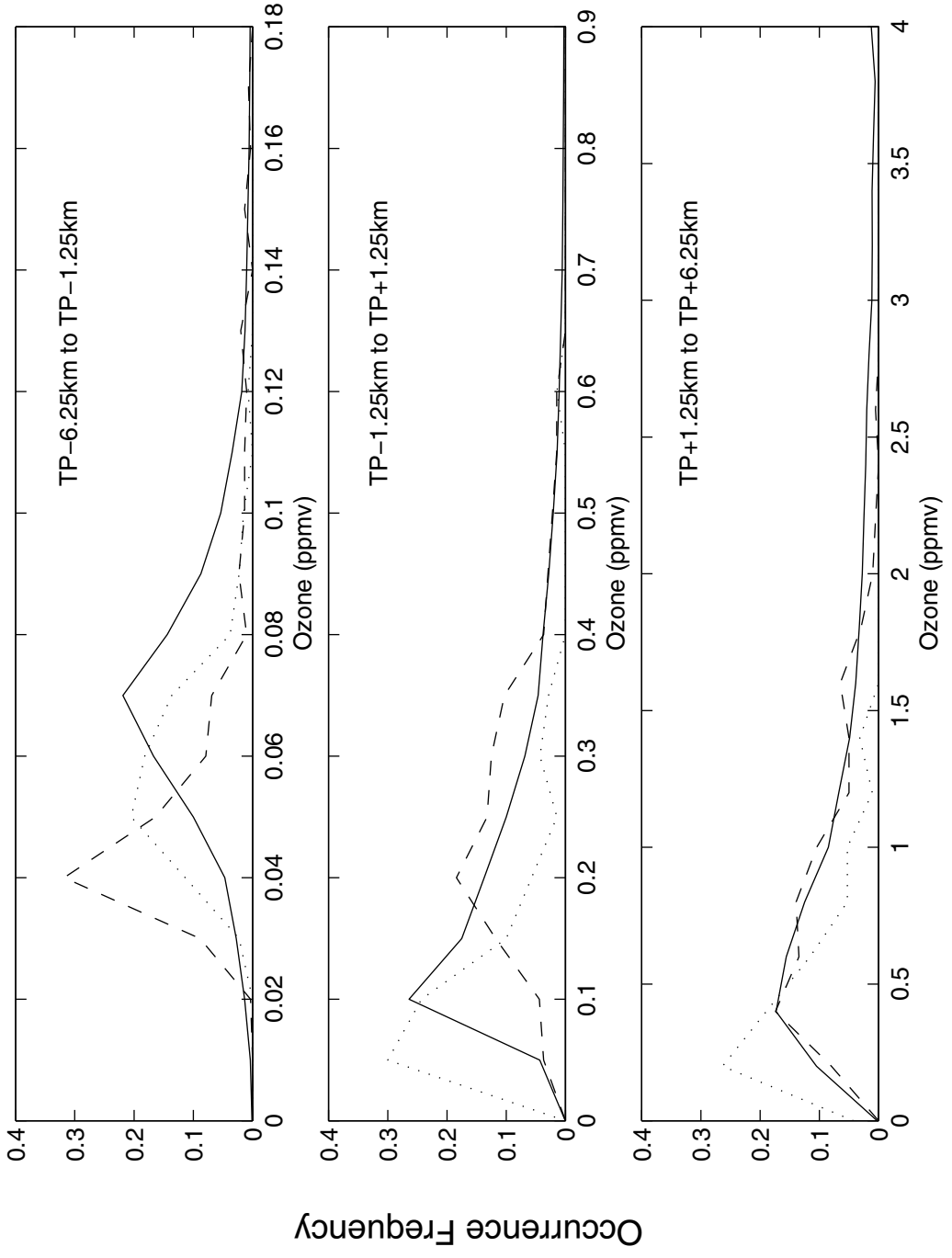

Figure 5.9: Probability distribution of climatology for ozone mixing ratio for Lauder (dashed), Boulder (dotted) and the ECMWF reanalyses training days (solid) on relative altitude layers.

with a median of +90 to +120% for Lauder and +45 to +70% for Boulder. The stratospheric measurements have a smaller bias, with a median of 0 to +25% at Lauder, and 0 to +35% for Boulder, as shown in Figure 5.3.

The observations from the Southern Hemisphere site (Lauder) display a much larger troposphere/UTLS bias than those from the Northern Hemisphere site (Boulder). The source of the bias and the cause of this difference were investigated. Uncertainties associated with geophysical variation were found to be 6.4% for Lauder and 9.7% for Boulder. This would only account for small scale variation. The difference in time separation between the instruments is also shown to have a negligible effect. Analysis shows that the bias is likely to be the result of deficiencies in the regression stage of the retrieval scheme. This is exemplified by the difference between the ECMWF training days probability distribution and the ozonesonde probability distribution almost matching the bias in the AIRS/ozonesonde comparison (see Figure 5.8 and 5.9). The physical retrieval adheres very closely to the result from the regression retrieval in the upper troposphere (see Figure 5.7b) and adds little information to the final result.

While significant biases exist in the AIRS ozone data, it has been shown to correctly measure changes in ozone. This was demonstrated by the high positive correlation between the AIRS and ozonesonde ozone (see Figure 5.4). This indicates that the data are useful for studies where the variability is important rather than the absolute value of ozone. This is a positive outcome in view of the current ozone profile being a by-product of the temperature and the channel selection has been optimised for total ozone. An improved retrieval algorithm and channel selection to optimise the ozone profile in the UTLS region will enhance the value of this data set in research applications and is in development for version 5.[‡]

Candidate's contribution to this work

The majority of the analysis for the publication upon which this chapter is based, was carried out by the candidate. Figure 5.6 was provided by J. Wei and Figure 5.7 was provided by L. L. Pan. The Monte Carlo simulations detailed in Section

[‡]Version 5 data was released on 26 July 2007, with the back processing completed on 31 August 2007 (http://disc.gsfc.nasa.gov/news). The changes from version 4 to version 5 are outlined in *Olsen et al.* [2007]. Specifically the number of channels in the ozone retrieval has been increased from 26 to 41. The training data set is also no longer based on ECMWF, instead using TOMS (Total Ozone Mapping Spectrometer) and SBUV (Solar Backscatter Ultra Violet) data.

5.2.2 were provided by S. E. George. Discussions on the interpretation of the results were held with the majority of the co-authors.

Chapter 6

Entropy - Definition and Calculation

A tracer is a chemical or property present in a parcel of air that allows the movement of the air to be tracked. When two tracers are examined with respect to one another, this is known as tracer space. Tracer space was briefly explained in Section 2.1.5. When the relationship between tracers with different atmospheric properties is analysed, this can allow for a greater understanding in atmospheric processes. When using tracers for atmospheric studies, we generally require the tracer to have a long chemical lifetime compared to the timescale of the dynamics being studied. This allows the dynamics to be displayed in tracer space, rather than chemical reactions.

Tracer space can be used for a number of different types of studies. One possible use is as a means for quantifying polar ozone loss [*Proffitt et al.*, 1990; *Tilmes et al.*, 2006], where the decrease in ozone during the spring can be clearly observed. Of particular interest to this thesis is the use of tracer space to study transport and mixing processes. Mixing processes change the shape of the tracer relationship in tracer space and allow the mixing process to be examined (For example *Fischer et al.* [2000]; *Pan et al.* [2006]; *Patmore and Toumi* [2006]; *Waugh et al.* [1997]).

In an unmixed state an 'L' shape is observed between the stratosphere and the troposphere in tracer space for tracers representative of these regions, as shown by the solid lines in Figure 2.3b. Deviations from the 'L' shape indicate mixing has occurred shown by the dotted lines. Mixing will occur along the mixing lines that can be drawn between the tropospheric and stratospheric branches. Figure 6.1 shows four different mixed states; point A and B identify unmixed air; point C shows a fully mixed airmass with equal contributions from the stratosphere and troposphere; point D is a partially mixed airmass [*Patmore*, 2006]. The partially mixed nature of points along the mixing lines was confirmed by *Pan et al.* [2006] using model studies. Regular mixing of two air masses will create a stable tracer

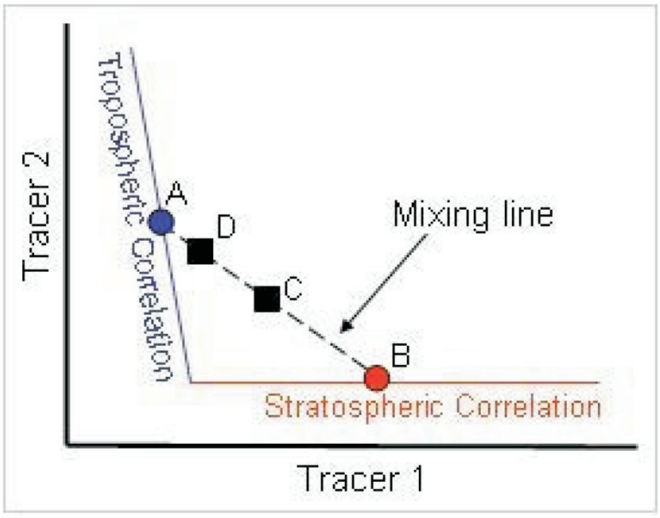

Figure 6.1: Effect of mixing in tracer space of a tropospheric and stratospheric tracer. Air is mixed from point A to point B via the mixing line indicated. Point C and D are partially mixed air parcels. Figure from *Patmore* [2006].

space, that is, one that does not vary with time. Any anomalous mixing will create deviations from the stable state [*Plumb et al.*, 2000].

The slope of the mixing lines is highly dependant on the initial air masses and the time elapsed since the mixing event [*Hoor et al.*, 2002]. Hence the slopes are expected to vary on a seasonal basis if there is seasonal variation in the tracers or if there are changes in the transport mechanisms [*Pan et al.*, 2007a]. Straight mixing lines are suggestive of single mixing events, whereas multiple mixing events, and hence multiple mixing lines, will produce curved relationships in tracer space as shown in Figure 6.2. This figure shows the cumulative effect of individual mixing lines. *Hoor et al.* [2002] showed that curvature in the mixing lines can also be a result of photochemical effects along with dynamic effects. If mixing lines maintain the same shape and compactness over a period of time, this indicates frequent mixing processes rather than isolated and localised events.

There are a number of studies that have used different chemicals in tracer space as a method of studying mixing, the most common being aircraft measurements with ozone-carbon monoxide used as the variables to form the tracer space [*Cooper et al.*, 2005; *Fischer et al.*, 2000; *Hoor et al.*, 2002; *Pan et al.*, 2004, 2006, 2007a; *Zahn and Brenninkmeijer*, 2003]. Using ozone-water in tracer space is also common, either from aircraft [*Pan et al.*, 2007a], AIRS [*Pan et al.*, 2007b] or HALOE (Halogen Occultation Experiment) [*Patmore and Toumi*, 2006]. Other studies

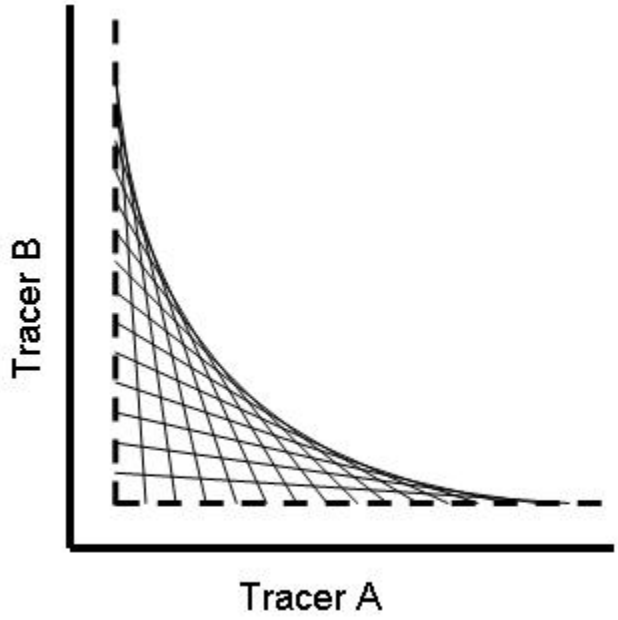

Figure 6.2: Mixing lines can have a cumulative effect resulting in a curved relationship in tracer space. The dashed lines show the stratospheric and tropospheric branches. The solid lines show the possible mixing lines. The overall shape of the tracer relationship is the curved edge resulting from the effects of all the mixing lines. The spacing of the mixing lines is arbitrary, with more lines spaced closer together giving a smoother curve and vice versa.

using HALOE have used hydrogen fluoride-methane and ozone-carbon monoxide [*Luo et al.*, 1995].

When ozone and water vapour are utilised as tracers, a transition layer around the tropopause region is observed. This is a layer of air that displays both tropospheric and stratospheric characteristics. The composition of this transition layer is not constant as it is dependent on mixing processes that can vary the amount of ozone or water vapour in this layer. These mixing processes can be defined by mixing lines. The location along the mixing line in tracer space can describe the strength of the mixing processes and its location in tracer space can potentially describe the process. Photochemistry may also potentially impact the location of the mixing line as some tracers can be created or destroyed through reactions involving UV light. This changes the concentrations of the tracers, thereby changing the signature of the tracer and making the concentration not just dependent on the amount of time since mixing occurred [*Cooper et al.*, 2002;

Hoor et al., 2002, 2004; *Monks*, 2000].

Ideally we want tracers that have strong gradients across the tropopause and with chemical lifetimes longer than the transport time scale, such as ozone and carbon monoxide. Water vapour is not a perfect tracer as under some conditions, namely very low temperatures, it is not conserved. However, it does have strong cross tropopause gradients and is sufficiently conserved for most studies [*Pan et al.*, 2007b]. The tracer space studies in Chapters 6 to 8 use ozone and water as these were the most readily available measurements for the instruments used. Water can be considered to be conserved in this study, as the tropics are not utilised in this study and the high latitude water measurements do not reach the coldest regions of the atmosphere.

As a means to quantitatively measure the mixing in tracer space, several parameters are proposed. The first of these is entropy, developed by *Patmore and Toumi* [2006], which examines the distribution of air within tracer space. Entropy is traditionally used as a measure of disorder in a system. The application of this parameter to atmospheric data allows air that is more mixed to have a higher weighting and hence more entropy. The other parameter to quantitatively describe mixing in tracer space is the value of ozone and water vapour concentrations at the boundaries of the transition layer. This parameter is dealt with in Chapter 7.

The application of entropy to AIRS and ozonesonde/hygrometers is covered in this Chapter. Section 6.1 contains descriptions of standard entropy theory and the application to atmospheric data. The parameters required for the entropy calculation are then detailed in Section 6.2, with quality control discussed in Section 6.4.

6.1 Entropy Theory and Calculation

Entropy is a measure of disorder of a system and is traditionally a concept associated with thermodynamics [*Chang*, 1998; *Halliday et al.*, 2005]. For this thesis, the use of entropy focuses on its application to atmospheric mixing between the stratosphere and the troposphere. This application of entropy to atmospheric mixing has its origins in traditional entropy theory.

Generally entropy is calculated using the following equation:

$$S = k_B \ln \Omega \tag{6.1}$$

where k_B is the Boltzmann constant, and Ω can be described in various ways. *Price* [1998] describes Ω as the number of ways of arranging the molecules of a system, with a larger number of arrangements leading to a larger entropy value. Along similar lines, *Ott and Boerio-Goates* [2000] defines Ω as the thermodynamic probability which "is equal to the number of arrangements or microstates that a molecule can be in for a particular macrostate". Macrostates with high probability have a large number of microstates and large disorder, hence large entropy. This is shown in *Maczek* [1998] as

$$\Omega = \frac{N!}{n_0! n_1! n_2! n_3! \ldots} \tag{6.2}$$

where N is the total number of particles in a system, and n_i is the number in each state. A detailed development of this statistical entropy definition is given in *Maczek* [1998].

This theory was then applied to the atmosphere by *Patmore and Toumi* [2006], where the calculation method developed is a weighted sum based on the number of data points in different regions of tracer space using a tropospheric and stratospheric tracer. Entropy provides a way of studying the amount of mixing in a system or pair of profiles (ie. ozone and water vapour mixing ratios). Air parcels that have deviated furthest from the unmixed states are assigned the highest mixing value, whereas air parcels that are in the unmixed states (tropospheric or stratospheric) are assigned a mixing value of zero.

In our context, tracer space must be separated into tropospheric, stratospheric and mixed/transition regions. Then the entropy is applied to the transition region, which is subsequently divided up into smaller sections to allow the application of different weightings. The transition region is initially defined by fitting tropospheric and stratospheric branches to the tracer space data. The transition region is then partitioned into 5 mixing states, from m=0 to 4. The selection of these mixing states is discussed in Section 6.3.4 and is based on the angular distribution of the data points within tracer space. The tropospheric and stratospheric branches along with the mixing state regions are shown in Figure 6.3. The tropospheric and stratospheric branches are marked by the dashed lines and select air that is entirely tropospheric or stratospheric. The selection of these

Table 6.1: The approximate percentage of tropospheric and stratospheric air for the different mixing states, m.

m	% tropospheric	% stratospheric
0	100	0
1	75	25
2	50	50
3	25	75
4	0	100

branches is described in detail in Section 6.3.2. This figure also contains a number of other parameters that will be described in following sections. Each mixing state represents a different approximate ratio of tropospheric to stratospheric air, this is summarised in Table 6.1. Of note is that the tropospheric and stratospheric branches are assigned mixing state values of m=0 and m=4.

The calculation for entropy is as follows:

$$\frac{S}{k_B} = \sum_{m=0}^{4} \ln \Omega_m \tag{6.3}$$

where s is the entropy, k_B is the Boltzmann constant. The state number, m, for 5 regions in tracer space ranges from 0 to 4. Ω_m is given by:

$$\Omega_m = \frac{N_m!}{(0.25mN_m)!((1-0.25m)N_m)!} \tag{6.4}$$

A comparison of Equation 6.4 and 6.2 shows a clear relationship between the traditional entropy theory and the application to an atmospheric mixing situation.

Prior to taking factorials, each value must be rounded. N_m is the number of points in any given m state as a fraction of the total number of points given by:

$$N_m = \frac{number\ in\ state}{total\ number} \times scaling\ factor \tag{6.5}$$

The scaling factor enables factorials to be used and is discussed in more depth with regards to the application on AIRS and ozonesonde/hygrometer data in Section 6.3.5.

To account for the number of mixing states, Equation 6.4 has the appropriate

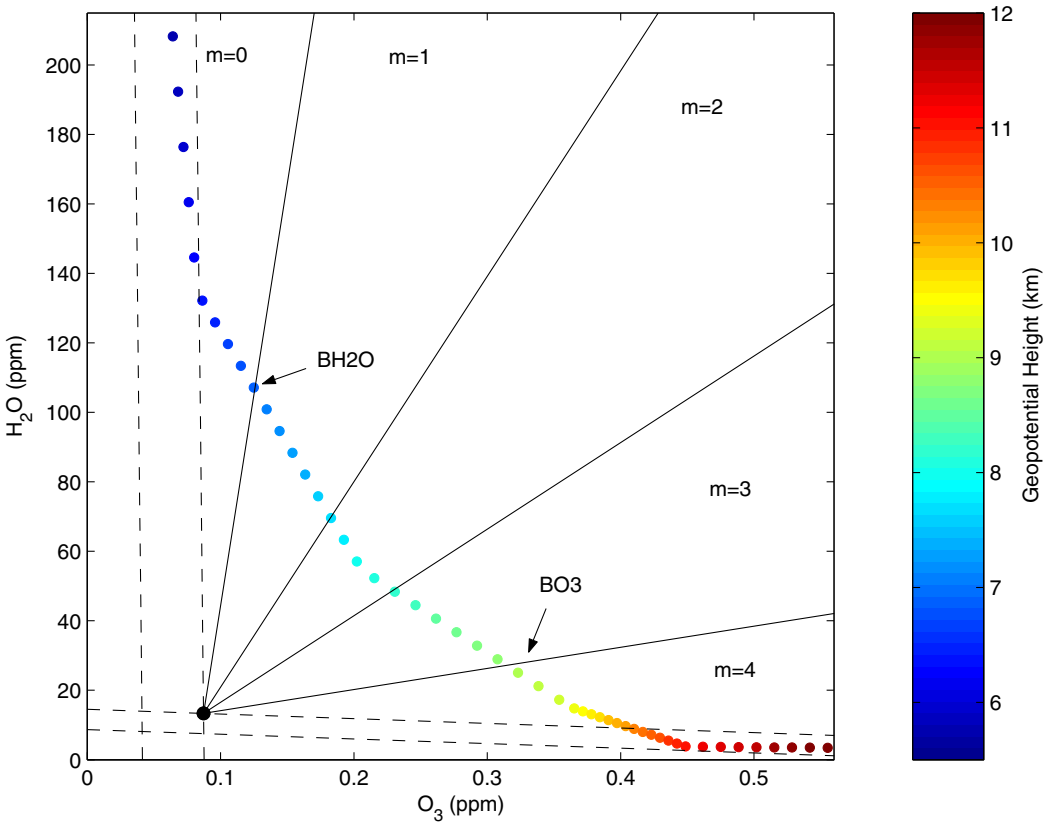

Figure 6.3: Division of tracer space for entropy calculation. The data points are the interpolated ozone and water vapour mixing ratios with the colour scale indicating the geopotential height. Solid lines show the angular division of tracer space, with the mixing states identified by the m values. m=0, 4 are the unmixed states (tropospheric and stratospheric, respectively) and m=1, 2, 3 are the mixed states. The approximate percentage of mixing is shown in Table 6.1. Dashed lines indicate the linear fit limits ($\bar{x}\pm 2\sigma$) used for the selection of the tropospheric and stratospheric branches. The black dot shows the transformed origin. The ozone and water vapour values at the boundary of the mixing layer are marked by BO3 and BH2O, respectively. The difference in height between BO3 and BH2O gives the thickness of the transition region. Note there is data outside the selected x and y range. The data that is not shown in this figure is still used for the branch fitting calculations. Data displayed is from a single AIRS profile.

scalar values (ie. 0.25), for this number of regions. This results in states m=0 and m=4 with $\ln \Omega$=0, hence the values in the tropospheric and stratospheric branch have no effect on the final entropy. The highest weighting is given to state m=2, as this is the region of evenly mixed air. It is possible that the number of regions could be increased and Equation 6.4 adjusted accordingly. This would give a greater sensitivity to the location of data points within tracer space, namely highly mixed points would be given a higher weighting and less mixed points given a lower weighting. By increasing the number of regions the weighting differences between the regions becomes more extreme which creates a highly discrete range of entropy values. While this is an option, five regions is sufficient to give a range of entropy values to separate mixing processes. Through the use of scaling factors and factorials, entropy still displays a discrete nature.

The higher the entropy, the more mixed the region. The process outlined above has been designed to allow the comparison of entropy regardless of location or time of measurement. In this way we have a quantitative measure to examine the mixing in a set of profiles.

The application of this method and further discussion as to the selection of the various parameters, such as the branch fitting, is detailed in Section 6.3. The accumulation of each step to tracer space is shown in Figure 6.3, with the division of data points in tracer space indicated by the branches (dashed lines) and angular regions (solid lines). This figure also shows how data points vary with height.

Some evidence for entropy being a valid measure of mixing in tracer space is shown in Appendix C. Through the use of synthetic profiles it is shown that variations in the distributions of ozone and water vapour in the transition region create different signatures in tracer space. The application of a mixing scheme shows that larger strengths of mixing, or mixing over a larger depth, increase the entropy value. These are desirable properties for a parameter to measure how mixed the transition region is.

6.2 Additional Parameters from Tracer Space

There are two additional parameters that are utilised in the following chapters that are based on tracer space. The first of these parameters is the thickness of the transition layer. Tracer space used for entropy calculations shows a number of discrete points displaying the ozone and water vapour mixing ratio profiles with

respect to one another. Each of these points therefore is representative of a layer of air and hence has an associated geopotential height. This is indicated in Figure 6.3 by the colour scale showing the height of each data point. The thickness of the transition region can therefore be determined by taking the difference between the heights of the points at the edges of the transition layer. The edges of the transition layer are defined as the boundary between the m=0 and m=1 mixing states, and the boundary between the m=3 and m=4 mixing state.

There is a limiting factor involved with the thickness value. If the transition layer has a thickness of less than the vertical resolution of the data set, the transition layer can no longer be detected. As the data sets are interpolated for calculating entropy, an artificial resolution has been introduced. This is important to remember when interpreting results related to height. The use of thickness is mainly important as a quality control factor, as discussed in Section 6.4.

The second additional parameter utilises the ozone and water vapour values at the edges of the transition region as a means for further defining the mixing lines displayed in tracer space. It has previously been shown that entropy describes the distribution of air within the regions in the transition regions. A problem arises with entropy as it is possible to have different tracer spaces, displaying different mixing processes, yet having the same distribution within the angular divisions in tracer space. This is demonstrated in Figure 6.4, where two different profiles are displayed. Each profile has the same number of points in each of the angular divisions. However, the profile marked with diamonds has a larger deviation from the tracer space origin which is indicative of a different mixing line and potentially a very different mixing process. Despite the different mixing lines, each of these profiles has the same entropy due to the distribution of points. It is therefore potentially desirable to have additional parameters to describe tracer space since entropy does not describe all the information associated with the mixing line.

These additional parameters are shown in Figure 6.3 indicated by BO3 and BH2O, where these are the ozone and water vapour mixing ratios at the edges of the transition layer. These parameters are discussed in depth in Chapter 7. The development and use of entropy, BO3 and BH2O will be shown in subsequent chapters. Together these measures are able to provide more information about the system than if entropy was used as a single measure.

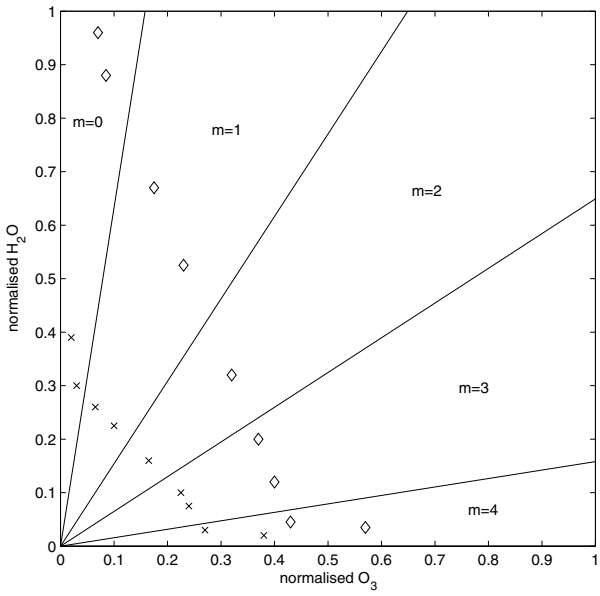

Figure 6.4: Two synthetic profiles with the same entropy yet with different arrangements in tracer space.

6.3 Application of Entropy and Tracer Space to AIRS and Ozonesonde/Hygrometer Data

The entropy calculation method is dependant on a number parameters that effect the resultant entropy value, for example the scaling factor and the angle of the different states. This section discusses the selection of the appropriate parameters for the entropy calculation on the AIRS and ozonesonde/hygrometer data. The parameters are selected to emphasise the transition region.

Note that while the parameters can cause variations in the absolute entropy values, entropy is a relative measure describing how mixed a set of ozone and water vapour profiles are. The selection of some of these parameters has an element of arbitrary selection involved, however, they are based on the information from the AIRS and ozonesonde/hygrometer data sets.

The key requirement for these parameters are that they are robust to variations in the value selected. Variations to the values selected should have only a small impact on the resultant entropies. This is in stark contrast to the tropopause fold identification algorithm in Chapter 4, where small variations in some of the algorithm parameters changed the outcome significantly.

6.3.1 Input Data

For accurate values of entropy that correctly identify the mixing in tracer space, it is required that the input data has a sufficient number of points that are not biased with respect to their location within tracer space. This is a key issue when determining how to input data into the entropy calculation. As entropy is a statistical method, it is vital that their be a sufficient number of points within tracer space. Too few points results in entropy values of little meaning as there will not be enough data to accurately describe tracer space.

Patmore and Toumi [2006] developed an entropy calculation method using HALOE[†] data, which is a solar occultation instrument on the UARS.[‡] The measurements from this instrument are sparse, both spatially and temporally. To obtain enough data points within tracer space, measurements were grouped together by season for grid boxes of 5° latitude by 20° longitude. This reduces the resolution of the data further and restricts the ability to draw any conclusions with regards to intraseasonal or interannual variability. However, it does produce enough data points to allow the calculation of entropy for further study. AIRS has a significantly better spatial and temporal resolution that HALOE and it would be advantageous to retain some of this resolution.

An alternative method to increase the number of data points is to interpolate the ozone and water vapour data with respect to height to artificially increase the vertical resolution of the AIRS data. This method results in a sufficient number of data points within tracer space to allow the calculation of entropy from a single profile while retaining its spatial and temporal resolution.

These two methods of increasing the number of points in tracer space are compared in Figure 6.5. The entropy values for vertical interpolation on the AIRS ozone and water vapour data is shown in the left panel, with the entropy for the grouping together of multiple profiles shown in the right panel. For the multiple profile method, nine profiles in a $3° \times 3°$ grid square from the AIRS L3 data are used to calculate a single entropy value. While the main features are the same between the two methods, the spatial resolution is reduced for the multiple profile method. In addition the use of this method on a global scale has some spatial sampling issues as a $3° \times 3°$ grid has a different area at different locations on the globe. This was not an issue in *Patmore and Toumi* [2006] as their study only

[†]HALOE - HALogen Occultation Experiment
[‡]UARS - Upper Satellite Research Satellite

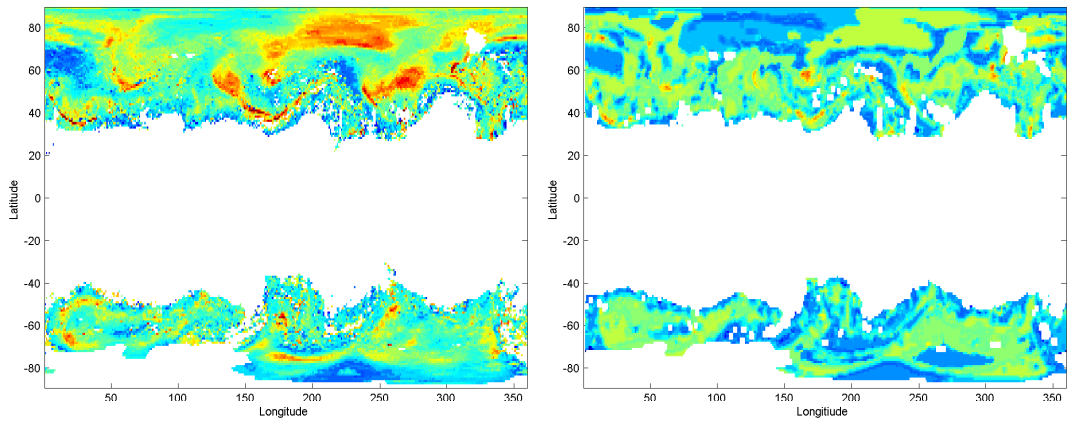

(a) (b)

Figure 6.5: Comparison of two different entropy calculation methods, a) interpolation and b) multiple profiles, for the same day. The colour scale is the same for each panel and shows the entropy value.

focused on the extratropics. It should be noted that the multiple profile method is unsuitable for use on the ozonesonde/hygrometer data as it would likely result in all the records at each location creating a single value. The vertical resolution available from the ozonesonde/hygrometers should allow the interpolation method with fewer difficulties than AIRS.

The vertical resolution of the AIRS data and its distribution within tracer space is also a key factor as to the data input method. Biasing within tracer space can result if the input tracer data (ie. ozone and water vapour) have a low vertical resolution with respect to some altitude measure, such as pressure or geopotential height. This could cause clumping of the data points within tracer space, where some regions in tracer space have a higher probability of occurrence due to instrument sampling issues. This is particularly problematic if the altitude measure is unevenly spaced vertically. This results in the measurements in the transition region being dependant on their location with respect to the instrument's sampling heights. This is highly undesirable as the distribution in tracer space should only describe the mixing processes involved. If the heights were evenly spaced vertically, this would produce sufficient sampling of tracer space. Geopotential height is a useful vertical measure to use as it increases evenly with altitude.

As previously mentioned in Section 3.4, the AIRS ozone and water vapour are provided as layer quantities with the value reported at the bottom of the layer

[*Olsen et al.*, 2005]. The layer limits are listed in Appendix B.1. It was shown in Figure 3.4 that the layers are of different thicknesses, therefore the measurement given for any layer does not represent the same depth of the atmosphere as a different layer. This will cause the tracer space sampling and hence the entropy value to be highly biased. The grouping of multiple profiles together will not change the vertical sampling of the heights, hence this input method would not be sufficient. However, vertical interpolation provides a partial solution to this problem. The sampling of tracer space does not seem to have caused a problem for *Patmore and Toumi* [2006] as their tracer space looks to be evenly sampled.

6.3.1.1 Effect of the original data resolution

A key question for the entropy calculation method is how the vertical, horizontal and temporal resolution of the input data affects the value of the entropy calculated. This may have a considerable impact on whether this methodology is transferable to different instruments. It is beyond the scope of this work to investigate how the horizontal and temporal resolutions will affect the entropy value. Likewise, the impact these factors will have on the application to different data sets is also beyond the scope of this work. The effect of the vertical resolution is covered in this section through the application of layer means to the ozonesonde/hygrometer data set. This will allow a comparison of the entropy differences between a high vertical resolution data set, such as the ozonesonde/-hygrometers, and a lower vertical resolution data set, such as AIRS.

As has been stated previously, AIRS views the atmosphere as a profile of layer averages. In addition, AIRS also has a measurement bias, as has been shown in Chapters 5 and 3. By applying layer averaging to the ozonesonde/hygrometer data, this will change the vertical resolution of the data. By applying the measurement bias, this will provide some indication as to how differences between instruments can affect the resultant value.

The ozonesonde/hygromether data is taken as the true state of the atmosphere due to the high vertical resolution of this data set. The AIRS layer averages are applied to the ozonesonde/hygrometer data, with the entropy calculation applied to the data both in its original form and as layer averages. An example of the layer averaging compared to the original data for the ozone measurements from an ozonesonde/hygrometer is shown in Figure 6.6. Note that the layer averages are displayed both at the bottom of the layer (solid black line) and at the central point

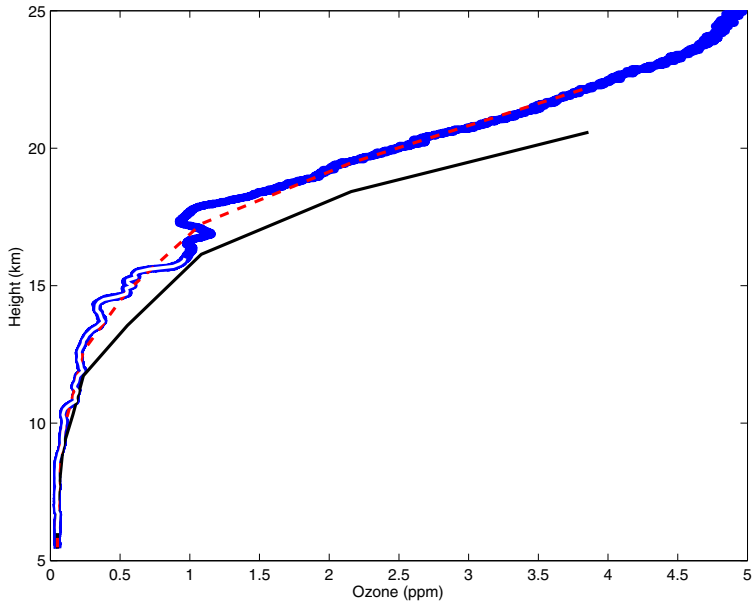

Figure 6.6: Ozone mixing ratio profile from a Lauder ozonesonde/hygrometer on 11th Nov 2004. The thick solid blue line is the ozonesonde data at the original resolution. The red dashed line is the ozonesonde data at AIRS resolution with the mean value for the layer reported at the centre of the layer. The solid black line is the ozonesonde data at AIRS resolution with the mean value of the layer reported at the lower limit of the layer. The thick white line is the ozonesonde data interpolated to 100 m layers from 6 to 16 km.

of the layer (dashed red line). The value at the bottom of the layer indicates how the AIRS layers are related to the real profile, whereas the values at the center points show that the layer profile is representative of the original profile, that is it captures its general tendency. For the entropy calculation the layer means are reported at the lower limit of the layer as for the AIRS data.

By interpolating based on layer means rather than the original ozonesonde/-hygrometer data, the shape of the profile in tracer space is altered. An example of how tracer space is affected by the resolution is shown in Figure 6.7. Note that this is the same ozonesonde/hygrometer as in Figure 6.6. The data in Figure 6.7 are either interpolated from the original ozonesonde/hygrometer data, or from the layer mean. Hence, the difference can be observed between the interpolation increasing the resolution, as from the layer means, or decreasing the resolution as from the original data. Both sets of data follow the same general trend for the mixing lines in tracer space, although the interpolation from the original data has points which are more clumped in tracer space. This is the result of the smaller scale variations in the mixing ratios. The interpolation from the original data

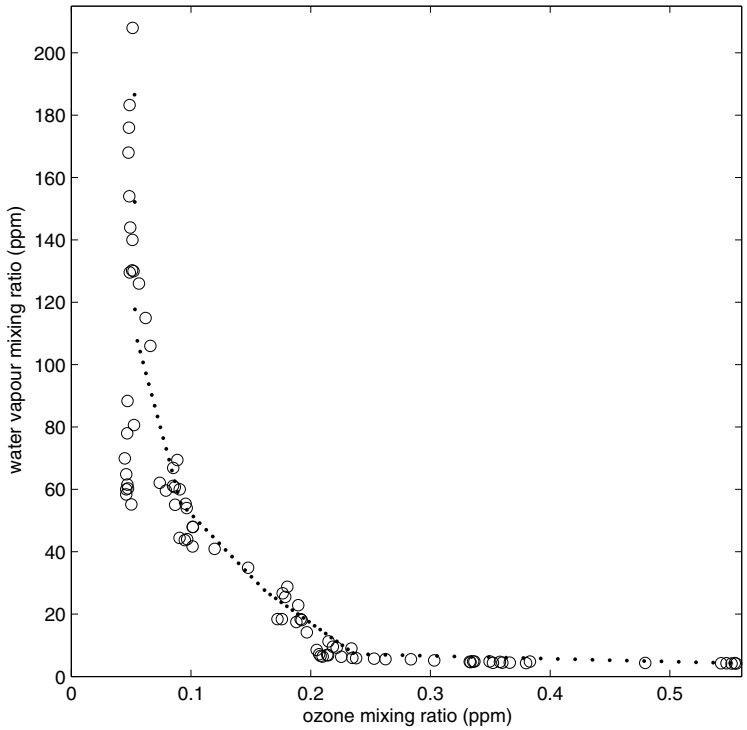

Figure 6.7: Tracer space for the Lauder ozonesonde/hygrometer from 11th Nov 2004, demonstrating the effect of the resolution on the interpolation. The ◯ shows the ozonesonde/hygrometer resolution data interpolated to 100 m layers from 6 km to 16 km, with the · showing the AIRS resolution ozonesonde/hygrometer data interpolated to 100 m layers from 6 km to 16 km.

(white line in Figure 6.6), has a greater variation in the ozone mixing ratio than the interpolation from the AIRS resolution data (black line in Figure 6.6).

Entropy is calculated from the original and the layer averages of the ozonesonde/-hygrometer data. The comparison of the resultant entropy values is shown in Figure 6.8. The two methods are positively correlated with a significant correlation coefficient of 0.579. Slightly more than half of the ozonesonde/hygrometers have higher entropy values after they are interpolated from layer means rather than the original resolution data. In general the entropy values are approximately the same. This suggests that while the vertical resolution of the data is different, the overall impact on the resultant entropy is small. This has further significance when examining the validity of the interpolation of the data as part of the calculation. There appears to be little impact based from reducing the resolution of the data as long as the layer data still captures the general trend of the data.

In Chapter 5 the AIRS ozone measurement bias is shown, and in Section 3.4 the

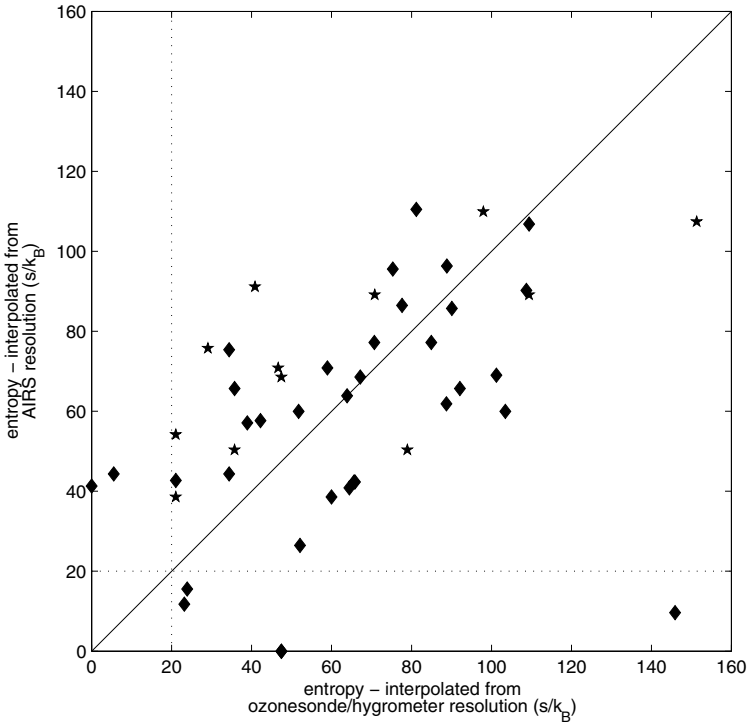

Figure 6.8: Comparison of entropy from ozonesonde/hygrometers based on whether the interpolation is from the original resolution or on layer means. The ★ shows the Lauder ozonesonde/hygrometers, and the ♦ shows the Boulder ozonesonde/-hygrometers. The relationship has a correlation coefficient of 0.579, with P$\approx 10^{-4}$ therefore the correlation is significant. The line of best fit for the relationship has a slope of 0.431, y-intercept of 40.50 and a standard deviation of 18.6. Note that the data has been filtered prior to the correlation calculation as described in Section 6.4.

AIRS water vapour measurement bias is outlined. As these measurement biases affect the way that AIRS observes the atmosphere, it is useful to examine how these biases effect the resultant entropy. The biases from Figure 5.2 for ozone, and from *Fetzer et al.* [2005] for water vapour are applied to the ozonesonde/-hygrometers at Lauder and Boulder. The biases are given as the mean value for the AIRS layer, therefore the biases are interpolated to give an even variation to the bias at different pressures.

After the application of the biases, the entropy is calculated with a comparison to the unbiased AIRS averaged data shown in Figure 6.9. The branch limits for the data upon which the AIRS bias has been applied are those used for AIRS (see Section 6.3.2) rather than for the ozonesonde/hygrometers. These limits are more appropriate for the biased data as the ozonesonde/hygrometer limits are too low and produce mainly null entropy values. There is a high positive correlation between these entropy values, with a correlation coefficient of 0.783. The entropy values without the bias tend to be slightly higher than those with the bias. In general this shows that the AIRS measurement bias has a small impact on the resultant entropy as it is the ability to measure the variability of the data rather than absolute values as was shown in Figure 5.4 and the surrounding discussion. Therefore, the entropy values are not adversely affected by the bias, and the bias requires no correction or consideration in the analysis of the entropy results.

As AIRS views the atmosphere as layers with a measurement bias on both the ozone and the water vapour, both these measurement characteristics will affect the resultant entropy simultaneously. Figure 6.10 shows the comparison of the original entropy values from the ozonesonde/hygrometers with the entropy values after layer means and the AIRS measurement bias have been applied. The measurements are positively correlated with a correlation coefficient of 0.573. Neither method consistently produces higher entropy than the other. This shows that while the measurement characteristics of AIRS affects the resultant entropy value, the overall trend of the data is the same as if the measurements were from a higher vertical resolution instrument without bias.

These comparisons have shown that the original resolution of the data, along with how the instrument views the atmosphere, has minimal impact on the resultant values. Using the interpolation method for calculation allows the spatial and temporal resolution of the AIRS data to be retained. This method also allows entropy to be calculated using the ozonesonde/hygrometer data.

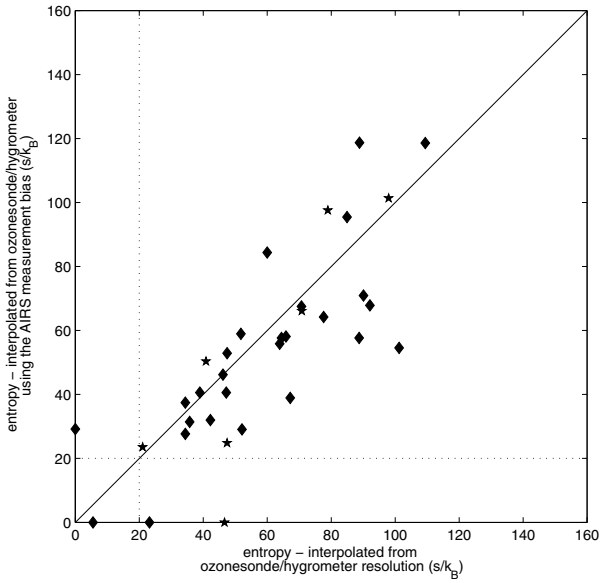

Figure 6.9: Comparison of entropy from ozonesonde/hygrometers using data that has had the AIRS measurement biased applied and non-biased data. The ★ shows the Lauder ozonesonde/hygrometers and the ♦ those from Boulder. The relationship has a correlation coefficient of 0.783, with P$\approx 10^{-7}$ therefore the correlation is significant. The line of best fit has a slope of 0.891, y-intercept of 2.26 and a standard deviation of 17.3. Note that the data has been filtered prior to the correlation calculation as described in Section 6.4.

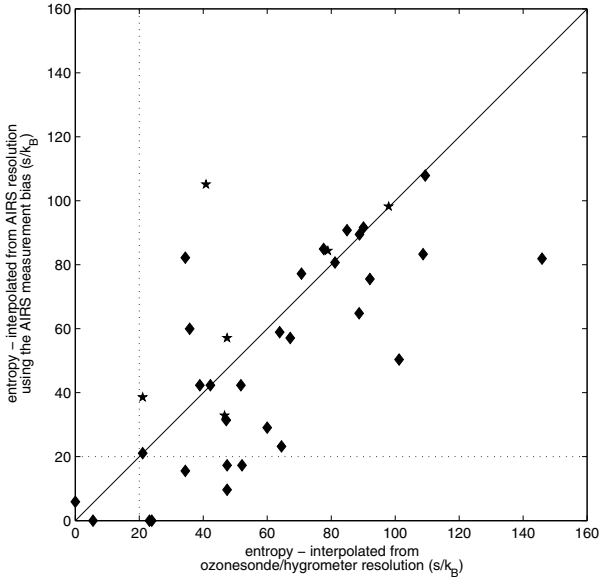

Figure 6.10: Comparison of entropy from ozonesonde/hygrometers using the original data versus the application of the AIRS layers and measurement bias. The ★ shows the Lauder ozonesonde/hygrometers and the ♦ those from Boulder. The relationship has a correlation coefficient of 0.573, with P$\approx 10^{-3}$ therefore the correlation is significant. The line of best fit has a slope of 0.497, y-intercept of 30.7 and a standard deviation of 22.2. Note that the data has been filtered prior to the correlation calculation as described in Section 6.4.

Upper and lower limits are selected for the interpolation heights. These limits are selected to cover the transition region and the region where the majority of the AIRS and ozonesonde measurements have been made. This also creates a standardised number of data points in the analysis region. The limits are different for the two instruments, with AIRS from 3-13.5 km and the ozonesonde/-hygrometers from 6-16 km. This range must cover the transition region, otherwise the range has little impact.

A vertical resolution for the interpolation is required for the data. As the N_m value in Equation 6.5 is a ratio, changing the vertical resolution also changes the number of data points, thereby leaving the fraction unchanged. Hence, the vertical resolution of the interpolation is relatively unimportant. Variations in the step size between 10-400 m has little impact on the resultant entropy, with a correlation coefficient of greater than 0.95 measured for a number of different vertical resolutions. The vertical resolution for the AIRS interpolation is 130 m, and for the ozonesonde/hygrometers is 100 m.

6.3.2 Tropospheric and Stratospheric Branches

In order to focus on the transition region, it is necessary to remove the data points from tracer space that are clearly tropospheric or stratospheric. These points are assigned mixing states of m=0 or m=4 and hence have no effect on the resultant entropy value. These data points are referred to as belonging to the tropospheric or stratospheric branches.

There are three different steps used for assigning data points to the tropospheric and stratospheric branches. The first step uses a fixed value to select all values below a certain ozone or water vapour mixing ratio. These values are then used to fit a polynomial with uncertainties to this data giving the branches indicated by the dashed lines in Figure 6.3. The second step assigns data points to the branches as a result of dividing the transition region into segments. The final addition to the branches is a result of the normalisation procedure. The first of these steps are dealt with in this section, with the remaining two in Sections 6.3.4 and 6.3.3, respectively.

Several steps for the tropospheric and stratospheric branch selection are required to ensure that all data points that represent unmixed air are selected. A key part of this is that fixed limits do not take into account smaller scale variations that may be present in individual profiles. This also means that the values selected

Table 6.2: Branch limits for AIRS and Ozonesondes.

	Ozone (ppm)	Water Vapour (ppm)
Ozonesonde	0.075	7
AIRS	0.09	10

for the initial branch limits are not critical as there are other definitions of the tropospheric and stratospheric regions of tracer space utilised.

Different branch limits are required for AIRS and the ozonesonde/hygrometers. The branch limits are mainly based on the distribution of the ozone and water vapour mixing ratios. The exception is the AIRS water vapour branch limit which is restricted by the instrument limit of 10ppm discussed in *Gettelman et al.* [2004]. The mixing ratio distributions upon which the other three branch limits are based is shown in Figures 6.11 and 6.12. Enough data needs to be selected to allow the polynomial fit to produce a useful result. The branch limit should also occur after the peak of the occurrence frequency. While the branch limits are based on the distributions shown in Figures 6.11 and 6.12, there is also a degree of adjustment to achieve the best results. This is not an ideal methodology, however it will be shown later in this section that the limits have a degree of robustness.

The AIRS limit is selected closer to the peak, with the ozonesonde/hygrometers slightly further from the peaks. It is desirable to pick the branch limit slightly higher than the peak value in Figure 6.11, as this allows the majority of the ozonesonde/hygrometer data records to produce valid entropy values. Lower limits result in a number of the records producing invalid entropy values. It should be noted that the higher branch limit is still within the peak region. The final branch limits for the ozonesonde/hygrometers are 0.075 ppm for ozone, and 7 ppm for water vapour. For AIRS, the final branch limits are 0.09 ppm for ozone and 10 ppm for water vapour. These values are given in Table 6.2, with the branch limits indicated in tracer space in Figure 6.13.

The data points selected by the branch limits are used for a linear fit. This also produces a measure of uncertainty around the fit. The uncertainty or range of the fit is marked by the dashed lines in Figure 6.3, where these lines indicate the mean plus or minus two standard deviations. All data points within these lines are assigned an m=0 or m=4 value as appropriate. In addition, any data points

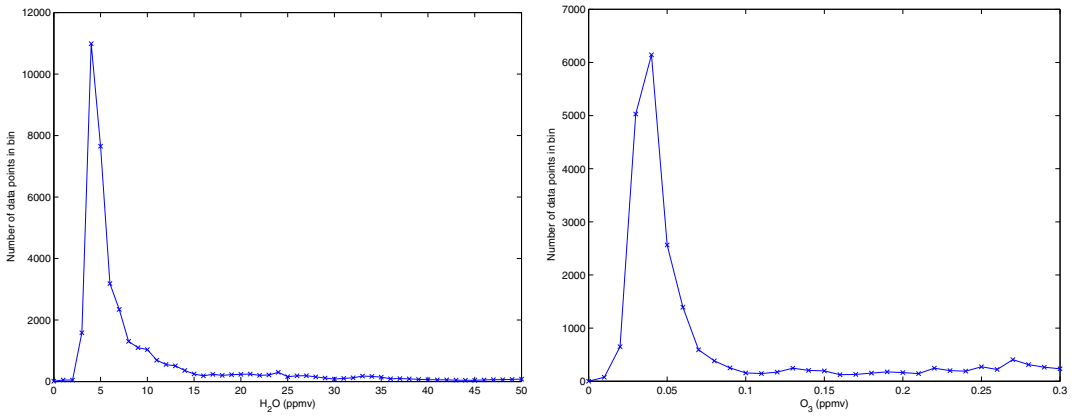

(a) Water Vapour (b) Ozone

Figure 6.11: Distribution of ozonesonde/hygrometer ozone and water vapour data points for branch limit selection.

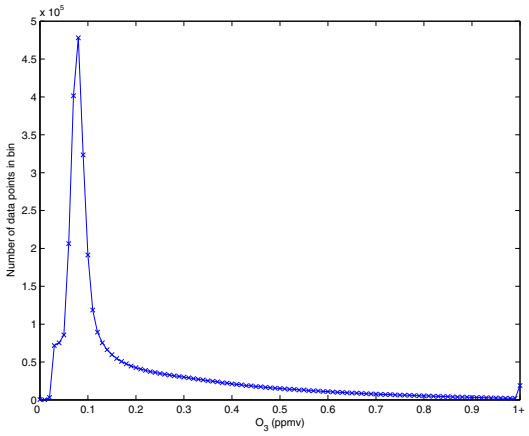

Figure 6.12: Number of data points in bins of width 0.01ppmv, with values marked at bin centre for a single day of AIRS ozone data.

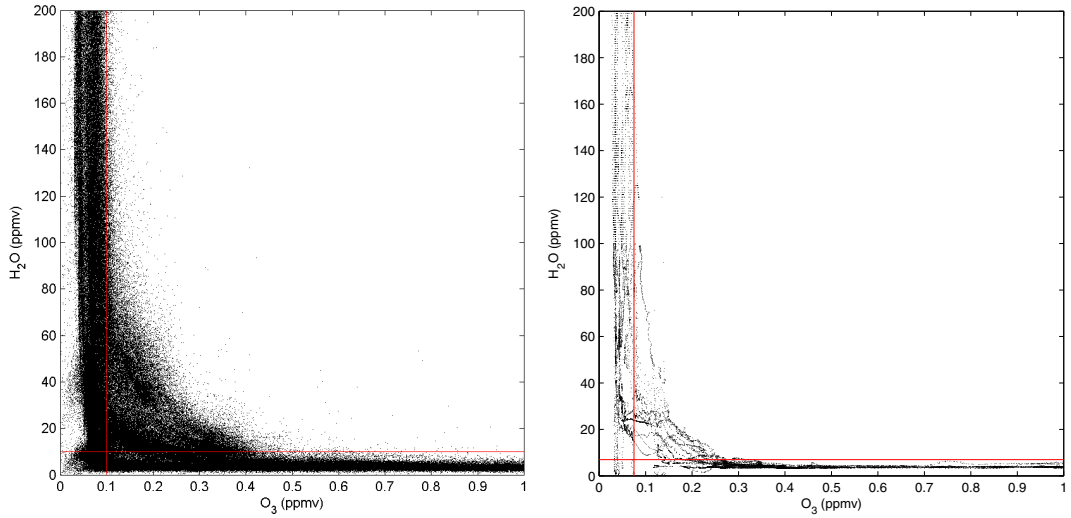

(a) A day of global AIRS data (b) 11 Ozonesonde/hygrometer flights

Figure 6.13: Tracer space using ozone and water vapour mixing ratios for AIRS and ozonesonde/hygrometers. The tropospheric and stratospheric branch limits are marked by solid red lines to show their position in relation to data from instruments. Note that there is data outside the displayed axes limits.

below the mean plus two standard deviation polynomial fit lines are assigned to the branches. These data points have small ozone or water vapour values and hence have little or no impact to the resulting entropy value.

It is desirable that the branch limit values be robust, where varying the branch limits by a small amount has a small impact on the final entropy values calculated. Variation of the branch limits is only applied to the AIRS data as there is an insufficient amount of ozonesonde/hygrometer data to produce statistically significant results. The variation in the branch limits and their associated correlations are presented in Figure 6.14. If the AIRS ozone branch limit is varied between 0.08 to 0.14 ppm, the entropy values have a greater than 0.84 correlation. For the AIRS water vapour branch limits, the correlation is greater than 0.95 for variations between 8 to 15 ppm for the assigned branch limit. It is not logical to reduce the trial range to smaller values as this would result in none of the branch being sampled. Alternatively, increasing the trial range would result in the entire transition region being selected by the branch limit. As the entropy values do not vary by a large amount when the branch limits are varied, this shows that this parameter is robust.

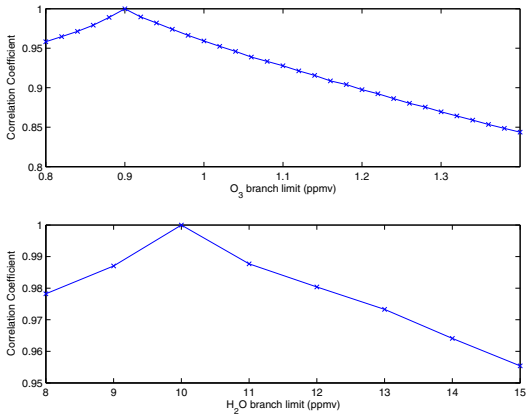

Figure 6.14: Correlation coefficients for varying the AIRS ozone (top panel) and water vapour (lower panel) branch limits.

6.3.3 Setting the Transition Region Window

As entropy is based on the location of data within tracer space, it is important to have an appropriately scaled transition region window to enable the entropy calculations to work correctly. This also allows the calculation to focus on the region of interest in the atmosphere. The transition window must encompass the majority of locations that data points are located in within tracer space. As parts of the entropy calculation require the angular division of tracer space (see Section 6.3.4), it is useful to have the x and y axes of similar scales to allow trigonometric functions to be utilised for angle calculation. For example, the angle of a data point in tracer space can be calculated as follows:

$$\theta_{mixed\ point} = \tan^{-1}\left(\frac{H_2O\ mixing\ ratio}{O_3\ mixing\ ratio}\right) \tag{6.6}$$

For this calculation to be able to be carried out, the ozone and water vapour mixing ratios must be well scaled with respected to one another. The easiest way to achieve this is to normalise the mixing ratios. As entropy is a relative measure, rescaling the mixing ratios will not change the resultant entropy values. A transition window is selected and then scaled to have values between 0 and 1. Additionally, this removes excess data points which are outside the transition region.

The transition region window for the normalisation limits is selected using the statistical distribution of the maximum ozone or water vapour mixing ratio within

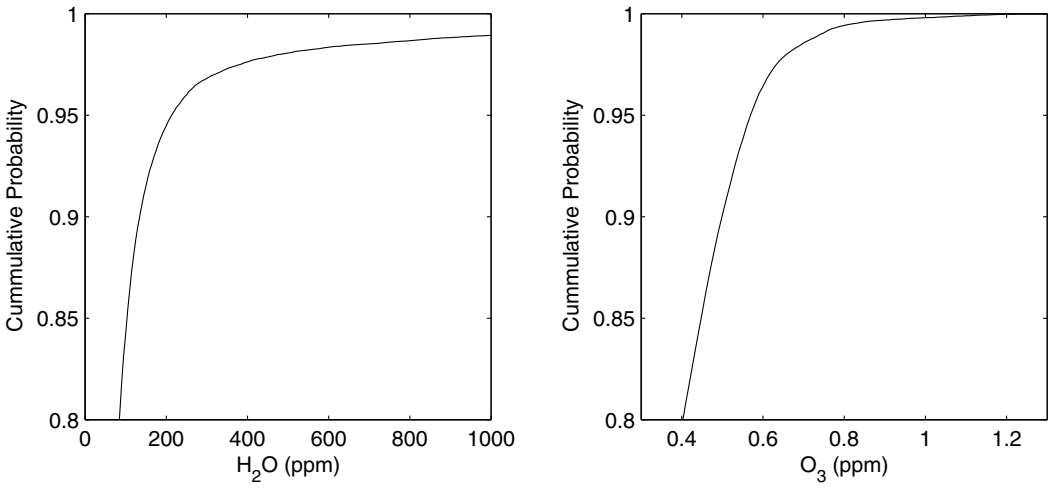

Figure 6.15: The fraction of the maximum mixing region values below a given mixing ratio for AIRS.

the transition layer region.† Note that this is carried out after the tropospheric and stratospheric branches are removed using the method outlined in Section 6.3.2. The cumulative probability for each mixing ratio value in the transition region for AIRS ozone and water vapour is shown in Figure 6.15. Over 95% of the ozone values are below 0.56 ppm, and the water vapour values below 215 ppm. These values are selected for the normalisation limits as the majority of data in tracer space is within these values, resulting in a useful transition region window.

Alternatively, the transition region window could be set using the maximum ozone and water vapour values within the mixing region. These points are called BO3 and BH2O and are discussed in Chapter 7. This has a minimal impact on the resultant entropy values, with a correlation of approximately 0.92 between the two different methods for setting the transition region window. As there is little difference between the methods, the first method discussed in this section is used for the entropy calculation.

Varying the normalisation values by 20%, that is from 0.45 to 0.67 ppm for ozone, and 172 to 258 ppm for water vapour, has little effect on the resultant entropy values. The correlation coefficient between entropies calculated using different values is greater than 0.98 for all variations, showing that the selection of the window does not rely on a critical value.

†These values are different from the transition boundary values, BO3 and BH2O. The transition boundary ozone and water vapour values are taken after the angular division of tracer space, rather than before as with these values.

The data outside the window selected by the normalisation limits is assigned to the tropospheric or stratospheric branches as is appropriate. The values outside the window are nearly always close to the axes therefore they have little or no impact on the entropy value.

6.3.4 Angular Division of Tracer Space

The entropy calculation method requires the division of tracer space up into different regions, or mixing states (denoted by m). This allows each region to be assigned a different weighting, where large weightings are indicative of larger amounts of mixing. This use of mixing states allows the mixing line to be described. The different regions assigned are shown in Figure 6.3, where the data points are assigned the m value from the relevant region for use in Equation 6.4. It has been stated in Section 6.1 that the choice of five mixing states gives an appropriate range of entropy values without giving an extreme range of entropy values, for example, zero to two hundred rather than zero to two million. In addition the choice of the angles for the mixing states would ideally emphasise the central region and remove any perturbations from the tropospheric and stratospheric branches. As branch selection has already been applied (see Section 6.3.2), this has removed the majority of stratospheric and tropospheric data, therefore only small angles are required to define the m=0 and m=4 mixing states.

Prior to dividing tracer space into angular divisions, it is necessary to define an origin for the angular divisions. This origin is indicated by the black dot in Figure 6.3, and we chose the intersection of the polynomial fits from the tropospheric and stratospheric branches as this point. If the angular divisions were made from the (0,0) origin, the angular division would not be representative of the same region due to variations in the tropospheric and stratospheric branches. By using a new origin, the angular division is focussed on the transition region.

The angles used for the division of the mixed region are somewhat arbitrary. A small angular amount is assigned to the stratospheric and tropospheric states, with the remaining angular amount assigned to the remaining three states. These angular values could be varied to give different emphasis to different regions of tracer space. The angular divisions used for this study are as follows:

m=0 $\theta \leq 9°$ plus tropospheric branch

m=1 $9° < \theta \leq 33°$

m=2 $33° < \theta \leq 57°$

m=3 $57° < \theta \leq 81°$

m=4 $81° > \theta$ plus stratospheric branch

Several alternative angular arrangements are given in Table 6.3, along with the correlation coefficients for the arrangement outlined above (also row one of the table). In general there is a high correlation between all the listed arrangements despite their differences in the angular divisions. Of note is that some of these variations are significantly different, with some having very small edge sectors, or larger central regions, or having all regions of equal size, yet the change in the resultant entropy is very small. This shows that the method is robust to variations in the sectors selected, which is a highly desirable quality. The arrangement chosen has small edge sectors and evenly distributed sectors in the mixing region, which highlights differences in the mixing region.

Table 6.3: Correlation coefficients, r, for varying the angles of the entropy bins. Angle given in the table is the angular width of each mixing state.

angle (°)					r
m=0	m=1	m=2	m=3	m=4	
9	24	24	24	9	*1*
18	18	18	18	18	*0.973*
0	30	30	30	0	*0.913*
3	28	28	28	3	*0.966*
5	20	40	20	5	*0.980*

6.3.5 Scaling Factor

To enable the use of factorials in Equation 6.4, is is necessary to have a scaling factor as was shown in Equation 6.5. This scaling factor ensures the number of points in a given state is a whole number of sufficient magnitude for a factorial to be determined. The entropy has discrete levels due to the use of factorials, shown in Figure 6.16. If the scaling factor is too small, there is a very small range of entropy values. Alternatively if the scaling factor is too large, the entropy values have a large range but have large gaps between the entropy levels. This is an

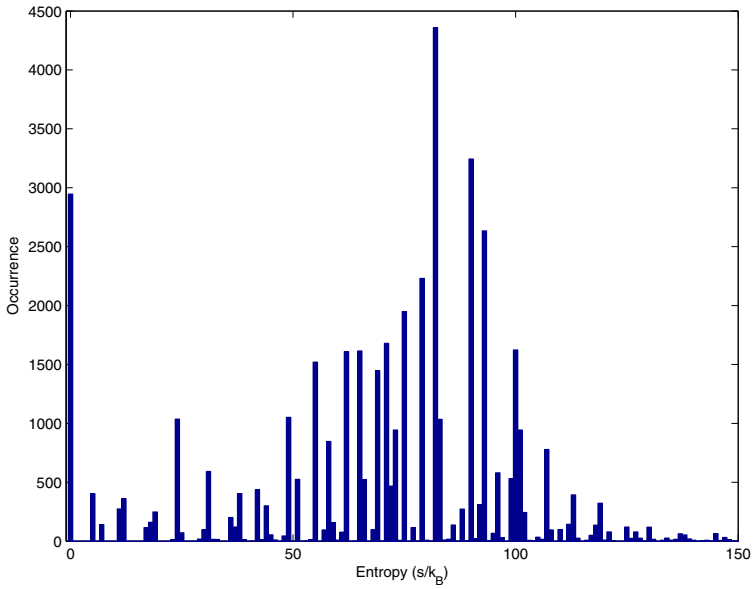

Figure 6.16: The entropy calculation results in discrete entropy values. Data is from AIRS for the 23 February 2004.

undesirable result as it makes entropy difficult to work with. Hence a balance needs to be found where the scaling factor is large enough to give a good range of values with small gaps between the discrete entropy levels.

For AIRS and the ozonesonde/hygrometers, the scaling factor used is 1000. This gives a good balance between providing a good range and a low amount of discrete levels. The exact number is relatively unimportant as the relationship between entropy values calculated with different scaling has a strong positive correlation. For example a scaling factor of 500, a 50% decrease, has a correlation of 98% when compared to a scaling factor of 1000. It should be reiterated at this point that the absolute value of entropy is not important, rather the relative value of the entropy in relation to other entropy values calculated using the same method and instrument is the key requirement for the measure.

6.3.6 Restrictions on Entropy Calculation

There are some restrictions on where entropy can be calculated from the AIRS data. For the calculation, there must be tracer information in both the tropospheric and stratospheric branch. This is a key issue in the tropics where the ozone profile changes at a slower rate than at higher latitudes. As there is a limitation in the pressure at which water vapour can be retrieved, there is often

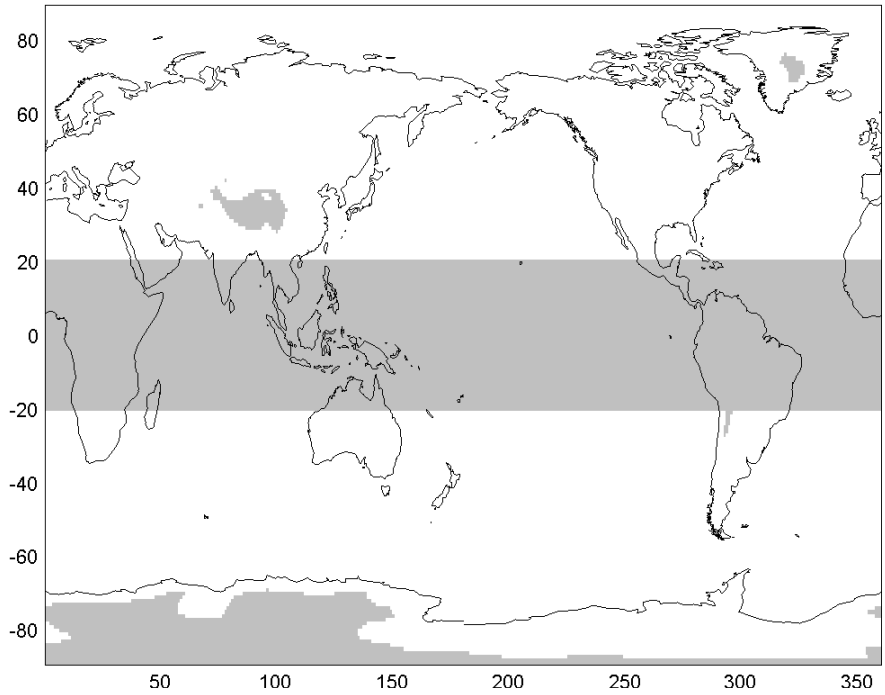

Figure 6.17: Regions where entropy cannot be calculated are shaded gray. Using the AIRS data from 2003 to 2005.

insufficient data to calculate the entropy in this region. Hence the tropics ($\pm 20^\circ$) are removed from the analysis. Additionally there are regions where the AIRS retrieval does not retrieve profiles due to the high altitude of the Earth's surface, such as the Andes and the Plateau of Tibet, or if there are ice sheets such as in parts of Greenland and Antarctica. The regions where entropy can never be calculated are shown in Figure 6.17. In addition to these regions, on a daily basis there are gaps in the satellite coverage.

The inability to calculate entropy either due to unsuitable AIRS measurements, incorrect retrieval or data gaps reduces the amount of data considerably. In any given year, there are approximately 23.7 million possible locations for entropy to be calculated assuming perfect global coverage on a $1^\circ \times 1^\circ$ grid. In 2003, valid entropy values were only calculated for 64.41% of these points. The equatorial region accounts for 22.22% of the missing data, and the remaining 13.37% from bad retrievals or gaps in the orbital path.

The calculation restrictions on the ozonesonde/hygrometer data are not significant due to the differences in measurement method (ie. single location rather than global), and the limited number of measurements.

6.4 Quality Control

It is useful to have an understanding of the uncertainties in the entropy calculation along with an understanding of any problems in the calculation. The quality control procedures utilised are based on both the ozonesonde/hygrometer and the AIRS data.

As a quality control measure, the relationship between entropy and the thickness of the transition region is examined. In general, entropy and the thickness of the transition region have a linear relationship as shown in Figure 6.18. This comparison includes not only the linear relationship of a single instrument, but also demonstrates that the relationship is the same across instruments. It should be noted that the normalisation limits and scale factor values are the same across instruments, but not the vertical resolution or branch limits. This further confirms that the vertical resolution of the input data is unimportant. While only a single day of AIRS data is shown, it is indicative of any day.

The outliers for AIRS and ozonesonde/hygrometers can be defined as those data points where

$$thickness > 20 \times entropy \tag{6.7}$$

as this approximates a line at the edge of the main correlation. For the data shown in Figure 6.18, there are 218 AIRS outliers (0.5%), 1 from Lauder and 8 from Boulder. The outliers could indicate exchange events or errors in the entropy and thickness calculations.

An examination of tracer space shows that the outliers in the Lauder and Boulder data are a result of errors in the location of the transition region. The minimum height for the mixing layer is clearly outside of the transition region in tracer space. It can be assumed from this examination that all outliers are a result of errors in the identification of the transition region.

This is further confirmed by adjusting the angles of the entropy bins. The number of outliers can be decreased by enlarging the angles of the entropy bins for states m=0 and m=4, as this decreases the error in the identification of the transition region. For example, if the angles are changed from (9, 24, 24, 24, 9) as in Section 6.3.4, to (18,18,18,18,18) for the AIRS data on 1 January 2003, the number of outliers decreases from 218 to 124 points. This is a percentage change of total valid points of about 0.25%. The removal of the outliers, using either set of angles, makes little difference to the overall entropy pattern. As the decrease in outliers is

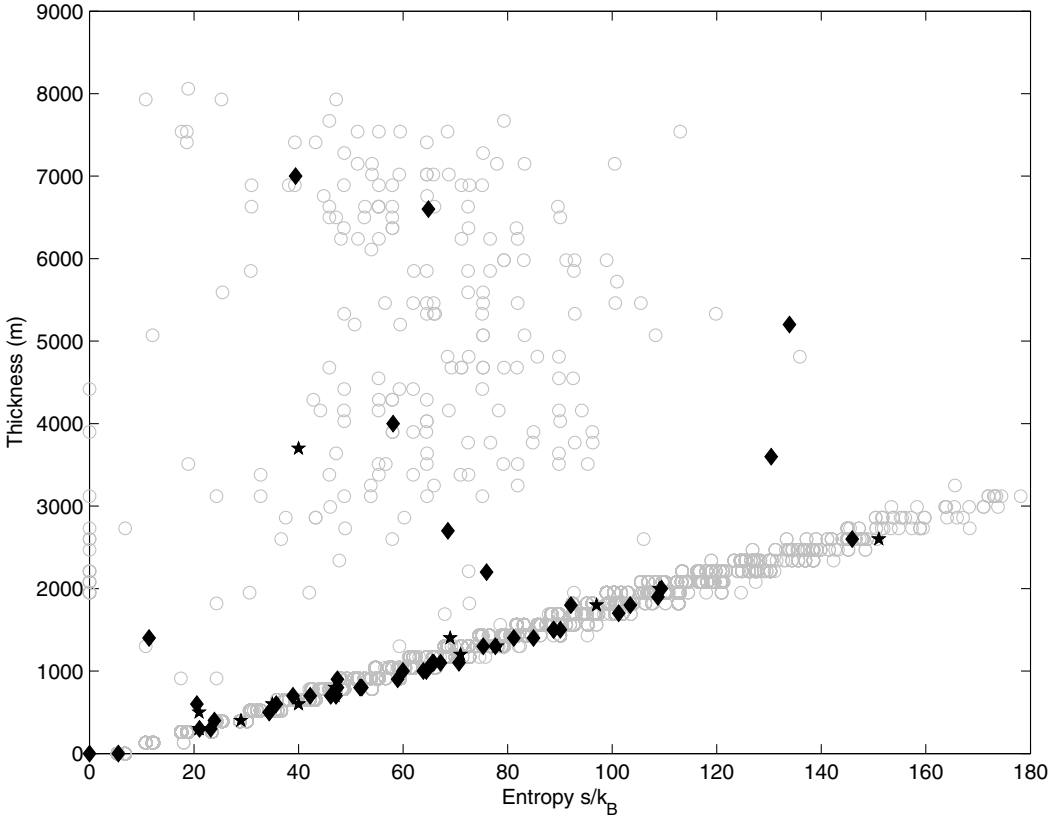

Figure 6.18: Relationship of entropy and thickness from different instruments. ◯ single day of global AIRS data (44622 points), ♦ Boulder ozonesonde/hygrometer (45 points), ★ Lauder ozonesonde/hygrometer (15 points).

small, the original angular divisions are retained for the reasons discussed earlier in Section 6.3.4.

For quality control of the entropy data, it is essential that we have an understanding of the uncertainty on the entropy values. This measure of uncertainty is required to show the range of accuracy of entropy and to assist with interpretation. A simple method for achieving this is to add noise to ozone and water vapour mixing ratio profiles and recalculate the entropy value. Noise is added a number of times to the same original profile to allow a statistical measure of the uncertainty in the entropy values.

For each ozone and water vapour profile pair, the original or unperturbed profile is calculated, giving e_0. Noise is then added to the profile pair and the entropy is recalculated. The noise is calculated as follows

$$Noise_i = NP \times R \times x_i \tag{6.8}$$

where NP is the noise percentage, x is the ozone or water vapour value at altitude i. R is a normally distributed random number with $\bar{x}_R = 0$ and $\sigma_R = \frac{1}{3}$, resulting in a distribution where Rϵ[-1 1]. The addition of noise to the ozone and water vapour profiles is carried out 1000 times to allow a range of statistics which represents the effects of noise on the entropy values. The statistic of the most use is the standard deviation of these values, e_σ, which shows us how much the entropy values are affected by noise.

Various levels of noise are added to a range of AIRS entropy values at different locations and different times of the year. The standard deviation of entropy is found to reach a steady value for higher entropy values or as the noise level is increased. Larger noise levels give greater standard deviations. This is demonstrated in Figure 6.19, where 3 different entropy values from different locations have different levels of noise added and the standard deviation of the subsequent entropy values (e_σ) is shown.

On a global scale, the global mean e_σ reaches a maximum value of approximately $18\,\frac{s}{k_B}$ at 99% noise. A noise level of 99% would be a worse case scenario and would only result from very poor quality data. It has been previously shown in Chapter 5 that in the UTLS region the AIRS data is generally of good quality, hence it is expected to have a much lower noise level than this.

This indicates that the uncertainty on the entropy calculations has a standard

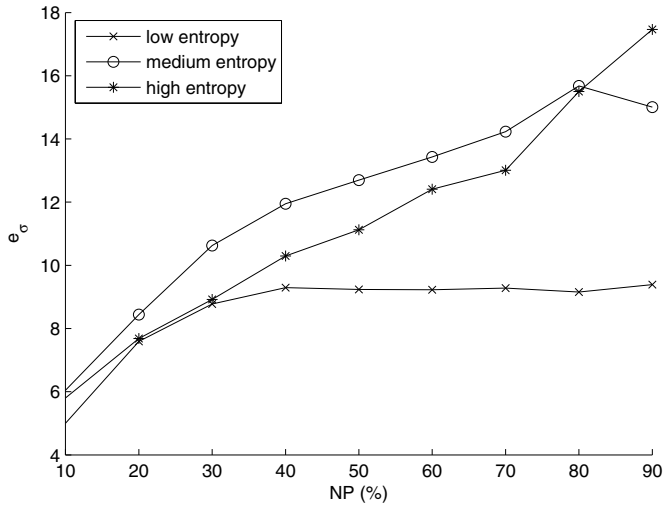

Figure 6.19: Variation of standard deviation of the entropy value for the addition of noise. The noise parameter, NP, is varied from 10 to 90%. The low entropy value is 17.60 $\frac{s}{k_B}$ at 7.5°E 36.5°S. The medium entropy value is 55.31 $\frac{s}{k_B}$ at 49.5°E 45.5°S. The high entropy value is is 100.59 $\frac{s}{k_B}$ at 82.5°E 56.5°N.

deviation of less than 18 $\frac{s}{k_B}$, possibly considerably less than this value. It is also indicated that smaller entropy values will be more affected by noise than larger values. Using an extremely conservative threshold, entropy values less than 20 $\frac{s}{k_B}$ are removed from the data. From Figure 6.20, this removes approximately 9% of the valid entropy values. These values are likely to not be statistically significant from zero based on the likely uncertainty range, and will be highly affected by noise.

It must be noted that while the relationship shown in Figure 6.18 is extremely useful in finding outliers and errors in the selection of the transition region, the relationship between entropy and thickness may be artificial. As the vertical distribution of the data is standardised as part of the entropy calculation, this may create an artificial relationship between entropy and thickness due to the definition of entropy.

6.5 Conclusion

Entropy is a relative measure of mixing calculated using the distribution of the ozone and water vapour in tracer space. Different regions in tracer space represent different amounts of mixing and are hence assigned different weightings in the

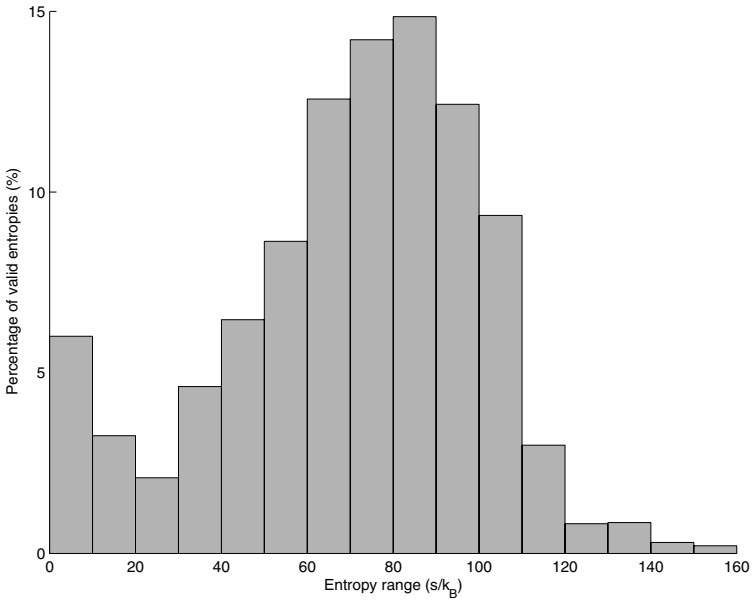

Figure 6.20: Percentage of entropies in a given entropy range for 2003. Percentage is calculated from the total number of valid entropies calculated.

resultant entropy value. There are a number of parameters required for the calculation in order to correctly select the transition window and divide up tracer space. These parameters have been shown to be robust, as variations in the values used do not considerably change the entropy value.

Two quality control conditions were developed to produce a measure of the uncertainty in the entropy calculation. Entropy values of less that 20 are removed as they cannot be considered significantly different from zero. Where the thickness is greater than 20 times the entropy value, values are removed as being erroneous calculations. This 'Entropy Filtering Criteria' is applied to all AIRS derived values for the remainder of this work, including but not limited to entropy. The application of this criteria to the ozonesonde/hygrometers reduces the number of records at Lauder from 15 to 14 and Boulder from 45 to 36.

A further tracer space parameter is developed in Chapter 7 to be used in conjunction with entropy to more fully describe mixing and transport processes. These measures are applied to the AIRS and ozonesonde/hygrometer data in Chapter 8.

6.6 Interpretation of Entropy

The concern has been raised as to what entropy physically represents. Does entropy have a direct relationship to any of the terms in the governing equations. This section will include a cursory discussion of this, as to answer these concerns in-depth is beyond the scope of this work.

There are multiple mechanisms of mixing which can redistribute chemical species throughout the atmosphere. If the mixing occurs in a region where the troposphere and stratosphere signatures can become mixed, then changes will occur in the tracer space as a result of mixing. These changes may be reflected in the entropy value. However, as there are a limited number of arrangements of points within tracer space, there is a limit number of entropy values. From this it can also be determined that there are multiple mixing mechanisms which can produce the same distribution in tracer space, and hence the same entropy.

Entropy represents the probability distribution function in tracer space, but lacks any further information as to how the distribution occurred. Therefore, there is no distinction in the entropy values based on whether the mixing occurred via horizontal or vertical mechanisms, or a combination of the two. Entropy also contains no time information as to when the mixing event, or events, occurred that produced the observed distribution in tracer space. The entropy calculation can only describe how the chemical species are distributed with respect to one another at a given time. While entropy can be calculated from a data set for a period of time, as air parcels are not stationary, it cannot easily be determined what has occurred in terms of mixing for a given air parcel.

Through comparing entropy to other measures of mixing, it may be possible to assign mixing mechanisms to entropy values. However, as entropy is dependent on how the tracers overlap in the mixing region, there are other factors which are important. For example, water vapour in the tropics and at the poles has a different vertical distribution. Hence, the same mixing mechanism occurring in the tropics and the poles will create a different distributions in tracer space. Therefore, it can be concluded that the same mixing mechanism in two different locations will not necessarily produce the same entropy or distribution in tracer space. Likewise the reverse is also true, similar entropy values and tracer space distributions in two different locations or two different times, may not have had the same mixing mechanism.

Entropy has some relationship to the governing equations through the diffusivity terms. However, this is not a direct relationship. While entropy and diffusivity are similar concepts, the entropy values cannot be used in these equations. Entropy is mainly a qualitative measure, rather than a quantitative. Although entropy is described in terms of numerical values, they only have meaning in relation to other values of entropy, that is, they are not definitive values.

Entropy cannot easily be related to any particular physical term. While entropy can qualitatively describe mixing, it lacks any information as to the mixing process or when mixing occurred.

Chapter 7

Ozone and Water Vapour at the Transition Region Boundaries - BO3 & BH2O

As previously indicated in Section 2.1.5 and at the beginning of Chapter 6, tracer space displays the relationship between two different tracers. For the study of mixing between the troposphere and the stratosphere, a tracer from each region is utilised. Ozone is used as a stratospheric tracer, and water vapour is used as a tropospheric tracer. The relationship between these two tracers can be used to describe mixing and transport in the transition layer between the troposphere and the stratosphere.

Entropy was described in Chapter 6 as a measure of mixing within tracer space. Different regions within tracer space represent different amounts of mixing, hence the distribution of data points can be used to assign a total mixing value, or entropy to a given tracer space or mixing line. However, entropy fails to describe all aspects of a mixing line because it is possible to have identical entropy values describing very different arrangements in tracer space (see Figure 6.4). Hence a second measure is proposed to provide a more comprehensive description of tracer space.

A measure is proposed using the ozone and water vapour mixing ratios at the edge of the transition region, defined as BO3 and BH2O, respectively. Using the tracer space divisions as detailed in Section 6.3.4, the transition layer boundary values of ozone and water vapour are defined as locations where the mixing profile intercepts the upper boundary of the m=1 state (BH2O), and the lower edge of the m=3 state (BO3), as shown in Figure 6.3.

The location of BO3 and BH2O with respect to altitude are shown in Figure

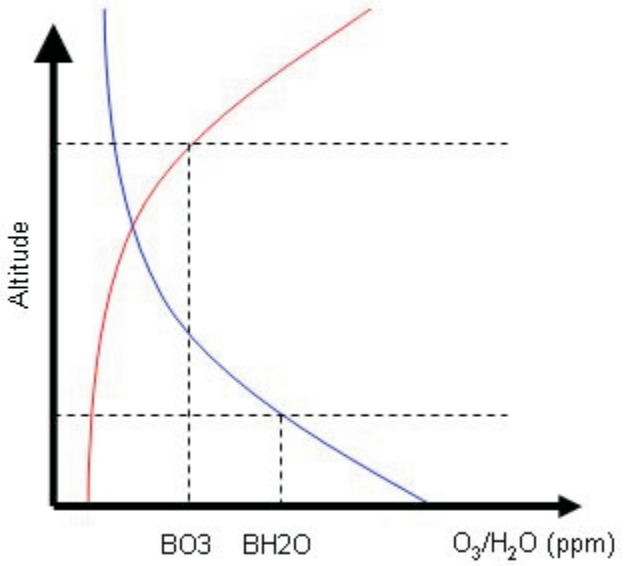

Figure 7.1: Profile view of ozone (red) and water vapour (blue). The values of ozone and water vapour at the boundaries of the transition layer (marked by the horizontal dashed lines) are indicated by the BO3 and BH2O, respectively.

7.1. The ozone and water vapour profiles shown give an indication of the large scale structure of these chemicals in the transition region. The horizontal dashed lines indicate the edges of the transition layer. It follows that as the gradient of the ozone and water vapour mixing ratios varies, the BO3 and BH2O values will vary. Examples of how the transition region and tracer space vary as the vertical relationship between two tracers changes are shown in Appendix C (Figures C.2 to C.6). The overlap between the tracer profiles, in this case ozone and water vapour, is crucial to the resulting mixing line and the derived metrics of entropy, BO3 and BH2O values derived from the mixing line.

The relationship between entropy, BO3 and BH2O is shown in Figure 7.2. As might be expected, there is a positive relationship between entropy, BO3 and BH2O. Higher BO3 and BH2O values tend to correspond to a larger number of data points within the transition region, resulting in larger entropy values. However, the relationship is not compact, with a range of BO3 and BH2O values resulting in the same entropy value. This initially confirms that the entropy, BO3 and BH2O values are different but complimentary measures for application on

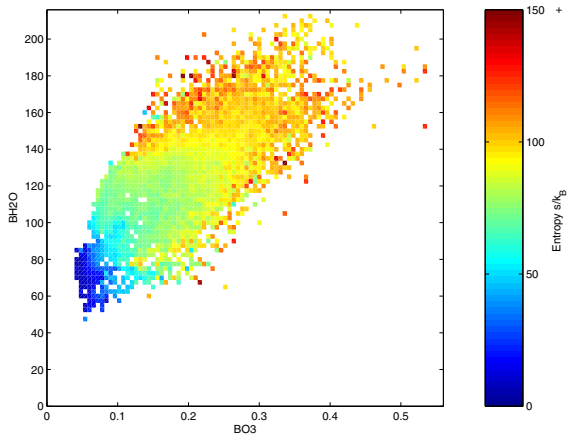

Figure 7.2: Relationship between entropy, BO3 and BH2O. Mean entropy value is the colouring with bins based on the BO3 and BH2O values. Data is from AIRS for 23 February 2003. The standard deviation for each grid box is on average about 10.

tracer space.

It is proposed that entropy, BO3 and BH2O can be used to determine mixing and transport processes. Entropy describes the mixing of the profile based on the distribution of data within tracer space. As BO3 and BH2O are closely related to the form of the mixing lines, they potentially describe the mixing or transport process. This idea is tested in the remainder of the thesis. Previous studies, such as *Hoor et al.* [2002]; *Pan et al.* [2004]; *Patmore and Toumi* [2006] have used the end point of the mixing line as part of understanding the mixing process but these points have not been used as a measure in themselves. The use of entropy, BO3 and BH2O will be shown to provide a more complete description of tracer space and the associated mixing and transport processes.

This chapter compares BO3 and BH2O to a number of parameters that confirm the validity of this measure and also compares these to some alternative measures that have been used in other studies. The BH2O value is compared in Section 7.1 to the water vapour at the tropopause as described in *Hoinka* [1999]. This ensures that the BH2O is a valid measure and that it follows the results previously observed. *Patmore and Toumi* [2006] used a second measure to describe tracer space called the mean mixing depth. This measure in association with the tropopause height allowed the determination of mixing processes associated with tracer space. A comparison between BO3, BH2O and mean mixing depth is presented in Section 7.2. The final part of this chapter, Section 7.3, covers the

selection of threshold boundaries. Application of thresholds to BO3 and BH2O provides a possible method for separating different mixing processes within tracer space.

A discussion of the features in BO3 and BH2O at both seasonal and daily time scales, is included in Chapter 8, along with the application of this measure to transport and mixing studies.

7.1 Water Vapour at the Tropopause

The water vapour mixing ratio given by BH2O is located at the lower boundary of the transition region. A comparison to an alternative measure is useful to ensure that BH2O is a sensible metric of water vapour mixing ratios in the transition region. *Hoinka* [1999] provides the water vapour mixing ratio at the tropopause for comparison purposes.

The water vapour at the tropopause for DJF and JJA is shown in Figure 7.3 from *Hoinka* [1999]. This data is from the ECMWF ERA-15 reanalysis which spans from 1979 to 1993, with a spatial resolution of $1.125° \times 1.125°$. The tropopause is defined differently at different latitudes due to the dynamic tropopause definition being undefined at the equator (see Section 2.1.3). At latitudes greater than 36° the dynamic tropopause definition using the 3.5 PVU surface is utilised. At latitudes less than 19° the thermal tropopause is used. At the latitudes between, a weighted average of the two is used. Of particular note is that the tropopause is drier at the equator, along with the summer pole being wetter than the winter pole. This follows the same pattern as ozone, where the ozone mixing ratio at the tropopause is lower in the tropics than at mid and high latitudes [*Wang et al.*, 2006].

For comparison to the water vapour at the tropopause, the seasonal means are shown for BH2O in Figure 7.4, and entropy in Figure 7.5. There is a qualitative positive correlation between these figures and Figure 7.3. However, the water vapour mixing ratio at the bottom of the transition region, BH2O, is significantly higher than at the tropopause. This is as expected at BH2O is likely to be lower in altitude and hence should have a larger mixing ratio. There will also be differences resulting from the different data sources (ie. reanalysis data vs. AIRS data).

For DJF, the high regions in mean BH2O (Figure 7.3a) match well to the water

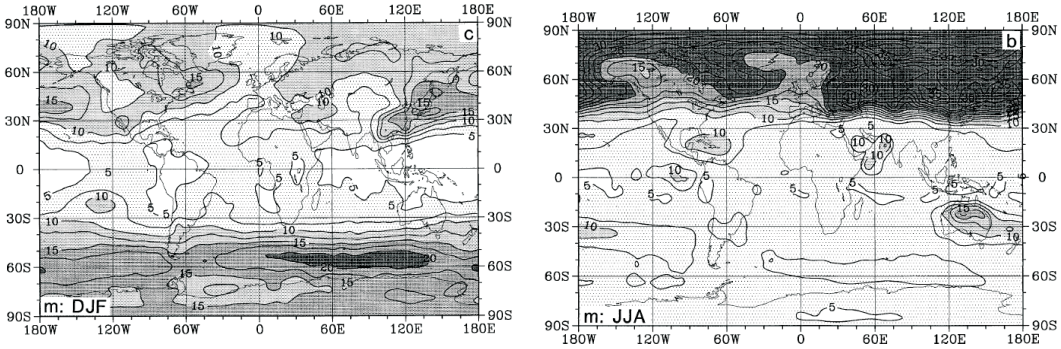

(a) December to February (b) June to August

Figure 7.3: Global mean water vapour mixing ratio in ppm at the tropopause from ECMWF ERA-15 from 1979-1993. The pale shading is for mixing ratios >5 ppm, medium light shading >10 ppm, medium dark shading >15 ppm and dark shading >20 ppm. Figure from *Hoinka* [1999].

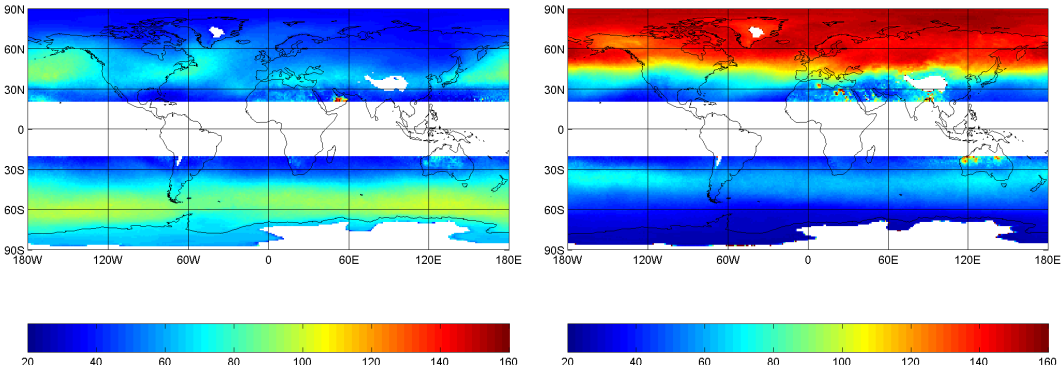

(a) December to February (b) June to August

Figure 7.4: Mean BH2O from 2003 to 2005. Units are ppm.

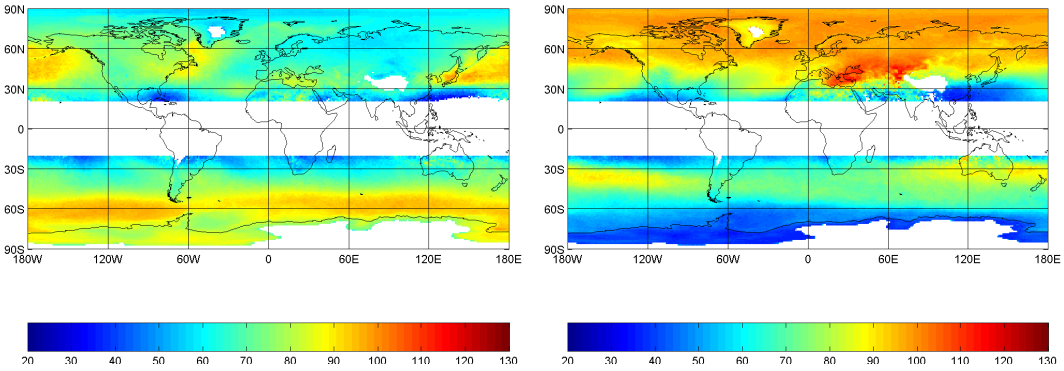

(a) December to February (b) June to August

Figure 7.5: Mean entropy from 2003 to 2005. Units are $\frac{s}{k_B}$.

vapour at the tropopause (Figure 7.4a). Particularly the high regions off the east coast of Asia, the east coast of North America, the band to the south of the Indian Ocean, and a small patch that is approximately to the north of Africa. For JJA, the main similarity between BH2O (Figure 7.3b) and the water vapour at the tropopause (Figure 7.4b) is the high mixing ratio values in the Northern Hemisphere, and the lower values in the Southern Hemisphere. Of particular note in Figure 7.4b are the lower values on the west coast of North America heading up into Alaska. The other lower patch in the mixing ratio at the tropopause that is approximately in the Greenland area does not see a decrease in BH2O. Overall the agreement is good.

The corresponding mean entropy maps have similar relationship to BH2O and the mixing ratio at the tropopause. The high BH2O regions mentioned previously tend to also correspond to regions with high entropy values, or lower entropy values in the case of the Alaskan region in JJA.

This comparison confirms that BH2O is a sensible measure as it produces similar results to other data sets. It is also shown that entropy is related to BH2O and the water vapour mixing ratio at the tropopause. While this comparison does not tell us about transport processes, it does confirm that there are regions where the water vapour values are larger at higher altitudes and that this is seen across data sets.

7.2 Comparison of Mean Mixing Depth to BO3 and BH2O

Patmore and Toumi [2006] use two additional measures in conjunction with entropy in an attempt to describe mixing processes. The key measure they use is called Mean Mixing Depth (MMD). However, relate entropy, mixing processes and MMD it is necessary to have an accurate tropopause height as a third measure. While MMD can be calculated using the AIRS data, the tropopause heights from AIRS have a large uncertainty due to the limited number of altitude levels. While this was not a significant issue for the AIRS ozone validation, its effects were still observed (see Section 5.2.2). The inaccuracies in the AIRS tropopause are also observed as unphysical results in Section 8.1.2. If an accurate tropopause height is required, the AIRS data is unsuitable and therefore BO3 and BH2O are proposed as an alternative to MMD and perhaps a simpler measure. BO3 and BH2O can be considered more intuitive with respect to mixing processes due to their direct

relationship to the mixing lines. A comparison between MMD, BO3 and BH2O for both AIRS and the ozonesonde/hygrometers is presented in this section to relate between these measures.

Mean mixing depth is utilised by *Patmore and Toumi* [2006] as an alternative measure of the thickness of the mixed region. They believe this measure is more accurate than thickness as it relies on the total distribution in tracer space rather than individual observations. This measure is calculated by dividing tracer space into regions defined by diagonal lines with a vertical spacing of H_2O 0.5 ppmv and a horizontal spacing of O_3 13 ppbv as shown in the left panel of Figure 7.6. The diagonal lines for calculating MMD are the grey lines running from the upper left of tracer space to the lower right. Each region has a weighting of 0.038 ppmv (H_2O)/ppbv (O_3).[‡] The distribution of the data points within tracer space is assigned a mixing depth weighting. The mean of the weightings for tracer space gives the mean mixing depth. This is demonstrated in the right panel of Figure 7.6. A large mean mixing depth should reflect mixing over a greater vertical depth as there is a larger deviation from the unmixed state in tracer space. From HALOE data, *Patmore and Toumi* [2006] find that regions with the transition layer centered above the tropopause have a lower mean mixing depth, indicating that mixing is on a smaller scale. This is in agreement with the reasoning that a transition layer mainly above the tropopause is more influenced by stable stratospheric air, hence we expect less vertical mixing.

For use on the AIRS and the ozonesonde/hygrometer data, the vertical (water vapour mixing ratio) and horizontal (ozone mixing ratio) spacings were found by taking the region of tracer space defined by the normalisation limits from Section 6.3.3, and dividing the x and y axes into 10 equal regions, as per *Patmore and Toumi* [2006]. This results in a vertical spacing for H_2O of 21.5 ppmv and a horizontal spacing for O_3 of 56 ppbv. Each region therefore has a weighting of 0.38 ppmv (H_2O)/ppbv (O_3).[§] The division of tracer space into regions is shown in Figure 7.7 with the region weighting (RW) indicated by the colour scale. The mean mixing depth is given by:

$$\text{MMD} = \frac{\sum_{i=1}^{n}(RW_i \times 0.38)}{n} \tag{7.1}$$

[‡] As a result of the following calculation $0.5 \div 13 = 0.038$. Note that these are the values used by *Patmore and Toumi* [2006] for data from the Halogen Occultation Experiment(HALOE) and are therefore instrument dependent.

[§] As a result of the following calculation $21.5 \div 56 = 0.38$.

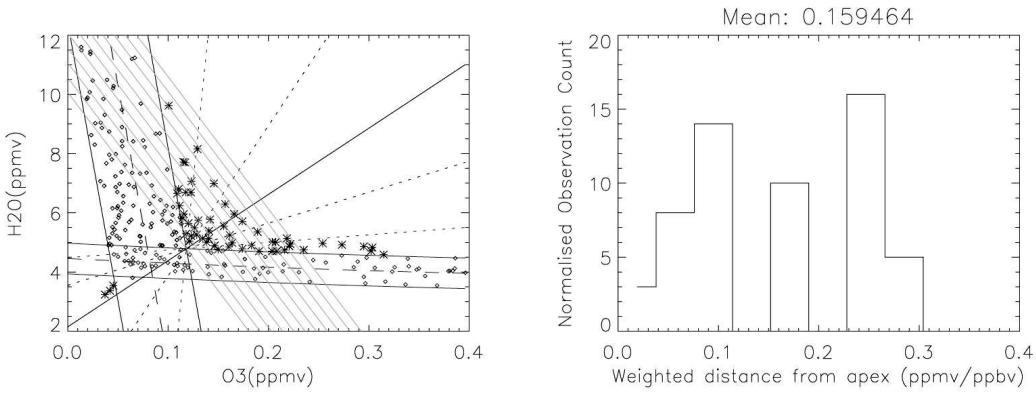

Figure 7.6: An illustration of how the tracer mean mixing depth is calculated: (left) an example tracer correlation showing the depth scaling lines (grey lines running from upper left to lower right); (right) a histogram showing the normalised count of observations within the scaling intervals. Each scaling interval corresponds to 0.038 ppmv (H_2O)/ppbv (O_3); giving a mean mixing depth of 0.15 ppmv/ppbv. Figure and caption from *Patmore* [2006].

where n is the number of points in the transition region. Rather than multiplying the RW values by 0.38 to give the MMD, it is possible to work with the RW without the multiplying factor. This is equivalent to just dealing with the mean RW value, giving larger numbers which are easier to work with. Hence the mean RW will be referred to as MMD when discussing this measure applied to the data from AIRS and the ozonesonde/hygrometers.

The mean mixing depth measure is calculated from ozonesonde/hygrometer data from Lauder and Boulder, and compared with BO3 and BH2O values shown in Figure 7.8. A near linear relationship is observed with more scatter in BH2O than in BO3. This is likely a result of the BH2O values being more evenly distributed across a range of mixing ratios, compared to BO3 which has a narrower range of mixing ratios. It is interesting that the relationship between the two factors is similar between the different locations, indicating that at least for these locations, there is no geographic dependance. The clear relationship between MMD, BO3 and BH2O suggests that these are similar measures.

The application of MMD to the AIRS data is more complicated due to the larger number of data points (compared to the ozonesonde/hygrometer records). A single day comparison between MMD, entropy, BO3 and BH2O is shown in Figure 7.9, where clear correlations in features can be observed between the 4 fields, for example, to the south of Australia. As with the ozonesonde/hygrometer comparison, the BO3 and MMD fields correlate more closely. AIRS MMD are

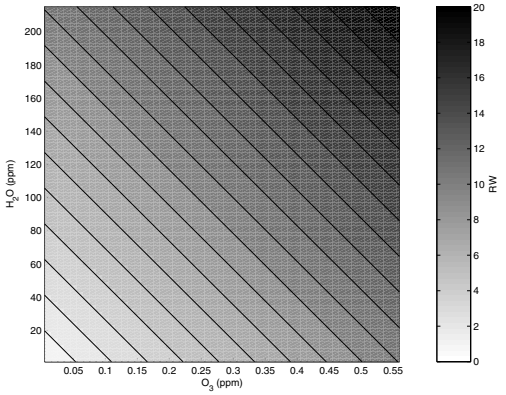

Figure 7.7: Division of tracer space into regions for calculating mean mixing depth. Colour scale shows the region weightings (RW) used in Equation 7.1.

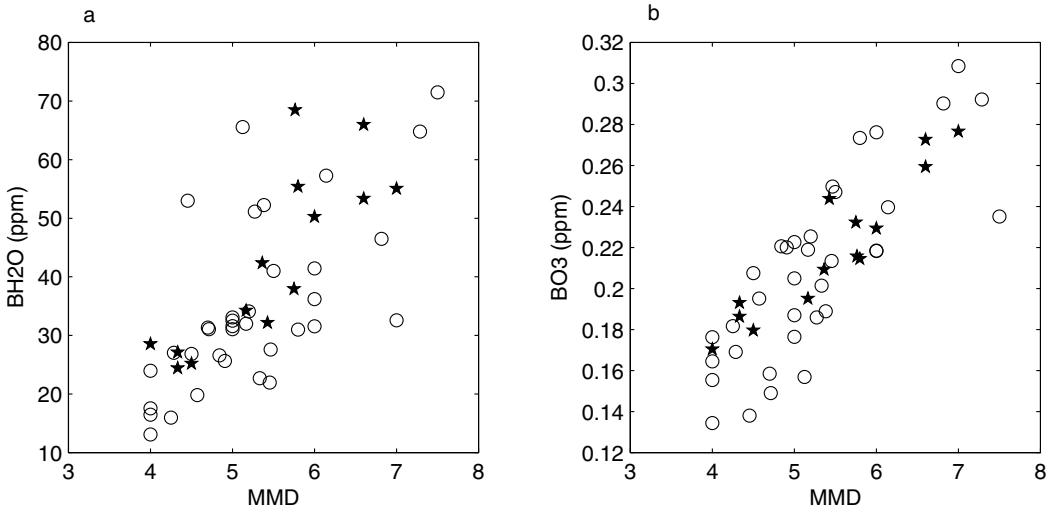

Figure 7.8: Comparison of mean mixing depth (MMD) to a) BH2O and b) BO3, for the Boulder ozonesonde/hygrometers (marked by ◯) and the Lauder ozonesonde/-hygrometers (marked by ★).

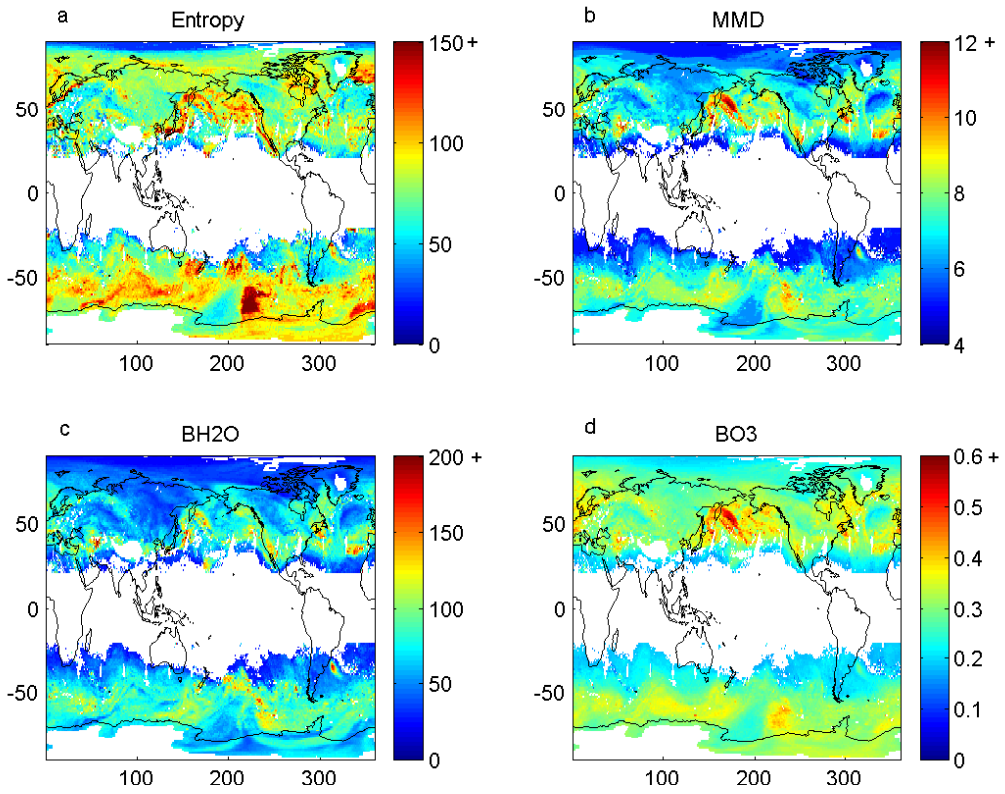

Figure 7.9: Mixing fields for 23rd Feb 2004; a) Entropy in units of $\frac{S}{k_B}$; b) mean mixing depth (MMD) in units of weighting factor; c) Water vapour as the edge of the transition layer (BH2O) in units of ppm; d) Ozone at the edge of the transition layer (BO3) in units of ppm; Note that the colour scale have been adjusted to provide the best contrast for the data. As a result some data points are oversaturated.

compared to AIRS BO3 and BH2O in Figure 7.10. The relationship of each parameter to MMD is approximately linear. This further reinforces that MMD, BO3 and BH2O are equivalent measures, however, there will be some variations in their results. Of note is that the slopes of the BO3 and BH2O relationships to MMD are similar for the ozonesonde/hygrometers in Figure 7.8 and AIRS in Figure 7.10. AIRS demonstrates a larger range of MMD values which is mostly likely a result of having more input profiles than the ozonesondes.

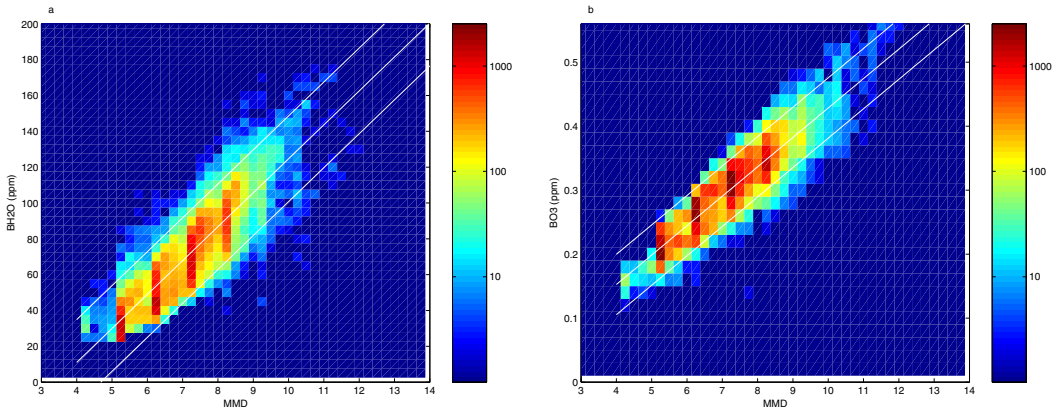

Figure 7.10: Relationship between a) MMD and BH2O, b) MMD and BO3 for AIRS on the 23 Feb 2004. The colour scale shows the number of points in each bin and is logarithmic. The white lines show a linear fit with 2 standard deviation limits.

7.3 Gradient Categories for BO3 and BH2O

The BO3 and BH2O values describe the edges of the transition region and cover a continuous range of mixing ratio values. It would be useful to apply some thresholds to separate the BO3 and BH2O values into categories which could potentially allow exchange processes to be separated and studied individually.

BO3 and BH2O can be thought of as identifying the entry and exit points of the transition region as discussed at the beginning of this Chapter and shown in Figures 7.1 and 6.3. If the values of BH2O and BO3 are divided into three regions - high, medium and low, then mixing lines could be described as shown in Figure 7.11. The labelling on the mixing lines describes the end points in relation to the regions, with three regions for each of BO3 and BH2O. The region where the mixing lines have their end points describes the gradient of the mixing process, as shown in Figure 7.12. The distance from the horizontal dashed line indicates the difference in the ozone or water vapour value between the entrance and exit point of the transition layer, for example

$$\Delta H_2O = H_2O(\text{upper edge of transition layer}) - H_2O(\text{lower edge of transition layer})$$

This shows that an exchange between high (H) BH2O and high (H) BO3 parcels is representative of a large change in mixing ratios, whereas between low (L) BH2O and low (L) BO3 parcels is a smaller change. Note that a large displacement

within tracer space, resulting in high mixing ratios, does not necessarily coincide with large vertical displacement with in the atmosphere. It is possible to have air parcels with vastly different compositions in close proximately to each other, thereby resulting in large displacement within tracer space.

Categories based on BO3 and BH2O are called gradient categories, referring to the slope of the mixing lines that would result if the BO3 and BH2O values were used. The selection of three regions for BO3 and BH2O results in nine gradient categories. The gradient categories for BH2O and BO3 are indicated by a two letter code, with the BH2O limit range listed first, followed by the BO3 threshold. For example, MH indicates that the medium limits on the BH2O and the high limits on the BO3. The nine gradient categories and their relationship to the regions used to separate BO3 and BH2O is shown in Table 7.1. The BO3 and BH2O regions are defined by the following limits:

L $< \bar{x}$

M $\geq \bar{x}$ and $< \bar{x} + \sigma$

H $\geq \bar{x} + \sigma$

where $\bar{x}$ is mean of the region limits of BO3 or BH2O and σ is the standard deviation for the associated region. There are a number of different approaches through which the mean and standard deviation for the region limits of BO3 and BH2O could be based, whether they should be on a daily, monthly or seasonal time scale, and whether they should encompass the whole globe, hemispheres, latitude bands or some other spatial division. The region limits need to have sufficient robustness to handle seasonal variation while not being overly sensitive as it is desirable that the categories select the same types of events and mechanisms.

The limits are chosen to group the majority of the low values together and to provide greater sensitivity to the higher values. The higher gradient categories are expected to be associated with stronger mixing, therefore the associated exchange may have a greater importance. Note that the division of these categories can be selected to focus the study on a different scaled events. For this study, it was decided to group the smaller gradient tracer spaces together, and focus on the larger gradient processes.

Firstly it is necessary to have an understanding of the seasonal and latitudinal patterns of BO3 and BH2O to identify how best to define the spatial and temporal

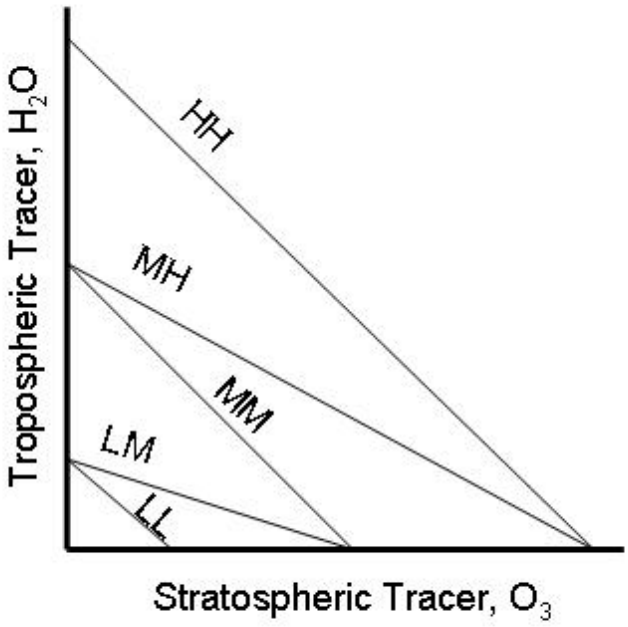

Figure 7.11: Mixing lines with respect to different BO3 and BH2O values. The labelling represents the region where the mixing lines end points reside. The first letter indicates the BH2O region, and the second letter indicates the BO3 region. There are three regions for each of BO3 and BH2O, these are low (L), medium (M) and high (H).

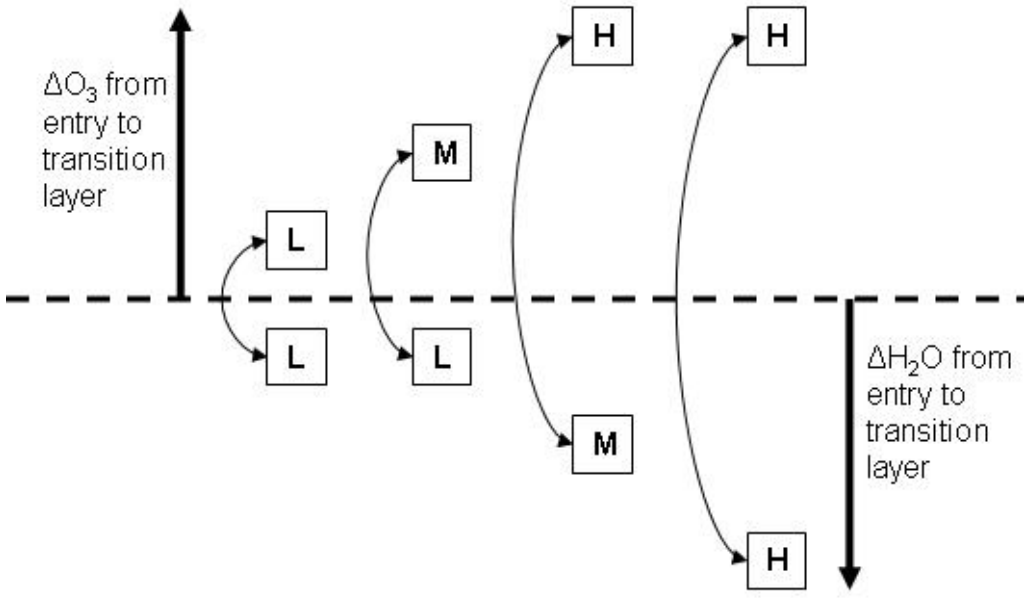

Figure 7.12: Schematic of the exchange process with respect to change in mixing ratio within the ozone or water vapour profile and relationship to the transition layer.

Table 7.1: Naming convention for the gradient categories based on the region limits used to separate BO3 and BH2O is detailed in the table. Naming of gradient categories has the BH2O limit listed first, followed by the BO3 limit.

		BO3		
		L	M	H
BH2O	L	LL	LM	LH
	M	ML	MM	MH
	H	HL	HM	HH

averages. Figure 7.13 shows the distribution of BO3 and BH2O values for each hemisphere as a progression through the year. The seasonal pattern repeats in each hemisphere with more variation in the summer months. The Northern Hemisphere also experiences more variation in BO3 and BH2O values. The truncation at lower values of BO3 and BH2O observed in Figure 7.13 is likely to be a result of the entropy filtering procedure (see Section 6.5).

The large variation in BO3 and BH2O values during the summer months is a result of different distributions for different latitudes, as shown in Figure 7.14 for the Northern Hemisphere. These distributions seem to be grouped into two distinct schemes (ie. subtropical vs. high latitude) for BO3 and BH2O.[‡] However, the mean value for the equivalent distributions for 10° latitude bands by month, as shown in Figure 7.15, do not display a well defined boundary in the values with latitude. Hemispheric seasonal patterns are similar (although out of phase which is expected), along with higher values progressing from lower to high latitudes. The BO3 and BH2O patterns are similar, indicating a correlation between ozone and water vapour values.

While latitude bands are a good tool for examining patterns, it is also important to consider the location dependance of BO3 and BH2O values. Region limits based on latitude bands are likely to be overly sensitive to variations and will result in different types of events being selected at different latitudes which is undesirable. It is clear from Figures 7.13 and 7.15 that global region limits would be inappropriate as the hemispheres have very different ranges in BO3 and BH2O values. A yearly value would also be inappropriate as there is a large seasonal variation in both hemispheres. Hence the most appropriate method for selecting the region limits is hemispheric based and would ideally be calculated on a daily

[‡]The distributions in Figure 7.14 are approximately gaussian using the Kolmogorov test, however, they do not fulfill the conditions required to apply a t-test to investigate the similarities of the distributions. [*Barlow*, 1989]

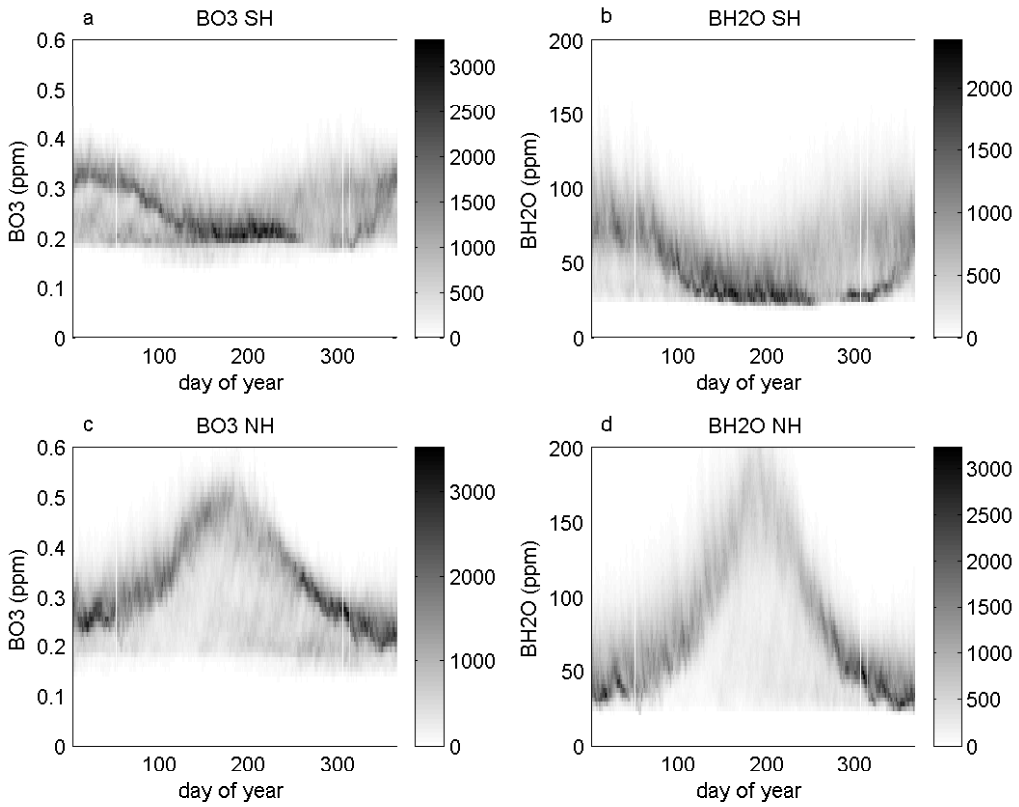

Figure 7.13: a) shows the distribution of the BO3 values for the Southern Hemisphere for 2004. b) shows the distribution of BH2O values for the Southern Hemisphere for 2004. c) and d) show the same parameters for the Northern Hemisphere for 2004. The shading in each panel gives number of values in bin for that day. The truncation at lower mixing ratios is a result of filtering the data based on the criteria in Section 6.4

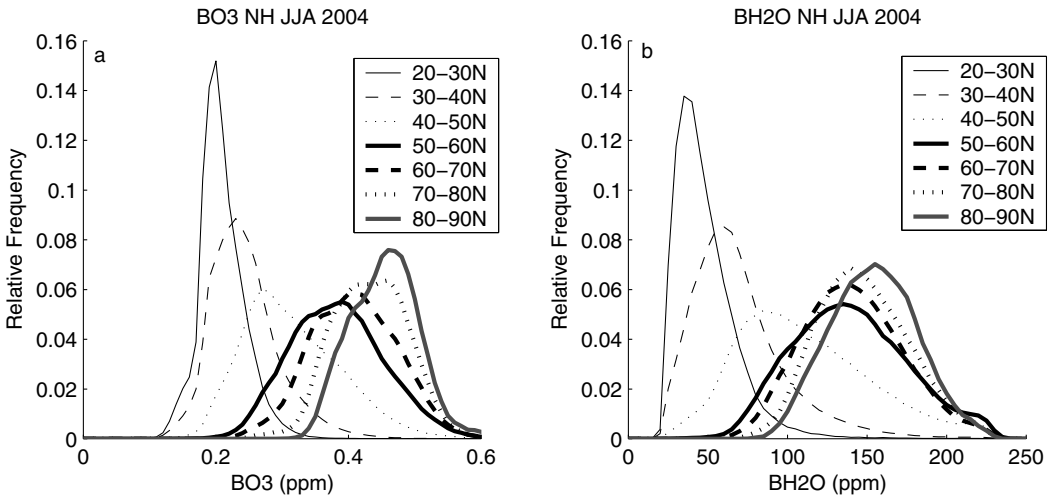

Figure 7.14: Panel a shows the distribution of BO3 for the Northern Hemisphere for July 2004 to August 2004 in 10° latitude bands. Panel b shows the distribution of BH2O for the Northern Hemisphere for July 2004 to August 2004 in 10° latitude bands. Vertical scale for both panels is relative frequency.

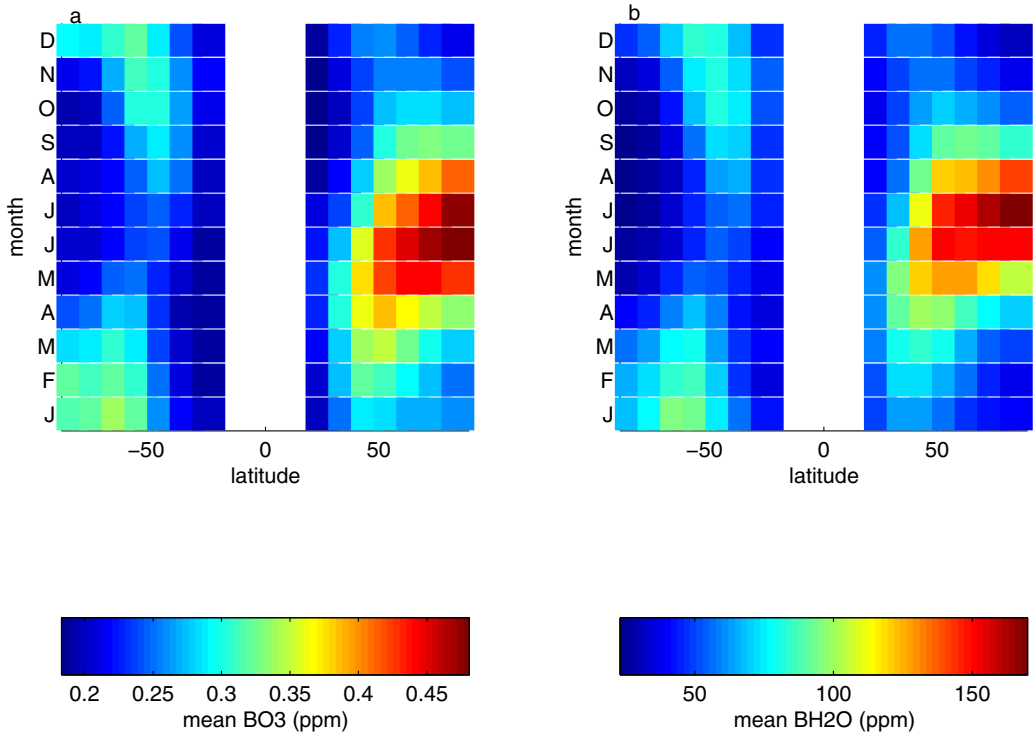

Figure 7.15: 2004 monthly mean and standard deviation for BO3 and BH2O for 10° latitude bands. Colour scale has units of ppm.

Table 7.2: Parameters for Equation 7.2.

			A	B	C	D	Z
NH	BO3	$\bar{x}$	-0.064	0.030	0.010	-0.006	0.30
		$\bar{x}$+1s	-0.090	0.036	0.017	-0.003	0.371
	BH2O	$\bar{x}$	-38.7	3.9	8.9	1.6	79.1
		$\bar{x}$+1s	-51.2	6.4	13.7	4.9	107.7
SH	BO3	$\bar{x}$	0.033	-0.004	-0.002	0.007	0.257
		$\bar{x}$+1s	0.044	-0.009	-0.007	0.009	0.308
	BH2O	$\bar{x}$	16.0	-0.5	-1.4	4.1	59.4
		$\bar{x}$+1s	20.4	-5.5	-2.8	4.9	83.1

time scale which will allow for seasonal variations. A daily scale is chosen as it removes the possibility of having piecewise discontinuities.

To produce the region limits, the monthly averages and standard deviations for each month from 2003 to 2005 of BO3 and BH2O over each hemisphere were calculated. To this data, a four term Fourier fit was applied as follows:

$$\text{region limit} = A\cos\frac{2\pi\text{doy}}{365} + B\sin\frac{2\pi\text{doy}}{365} + C\cos\frac{4\pi\text{doy}}{365} + D\sin\frac{4\pi\text{doy}}{365} + Z \quad (7.2)$$

where doy is the day of the year, and the fourier coefficients are A, B, C, D and Z. A four term fourier fit was chosen because it gives sufficient periodic variation for the data without being too sensitive to yearly fluctuations. The resultant parameters are given in Table 7.2, with region limits shown in Figure 7.16. This creates threshold limits which can be easily calculated (ie. without complex look up tables) and which are sensitive to seasonal changes without any discontinuities.

7.4 Conclusion

The ozone and water vapour mixing ratios at the boundaries of the transition layer (BO3 and BH2O) have been developed as a second measure to describe tracer space. The aim of this measure is for it to be used in conjunction with entropy to potentially describe mixing and transport processes (see Chapter 8).

BO3 and BH2O have been compared with the mean mixing depth from *Patmore and Toumi* [2006] and the water vapour at the tropopause from *Hoinka* [1999]. BO3 and BH2O were found to be similar measures.

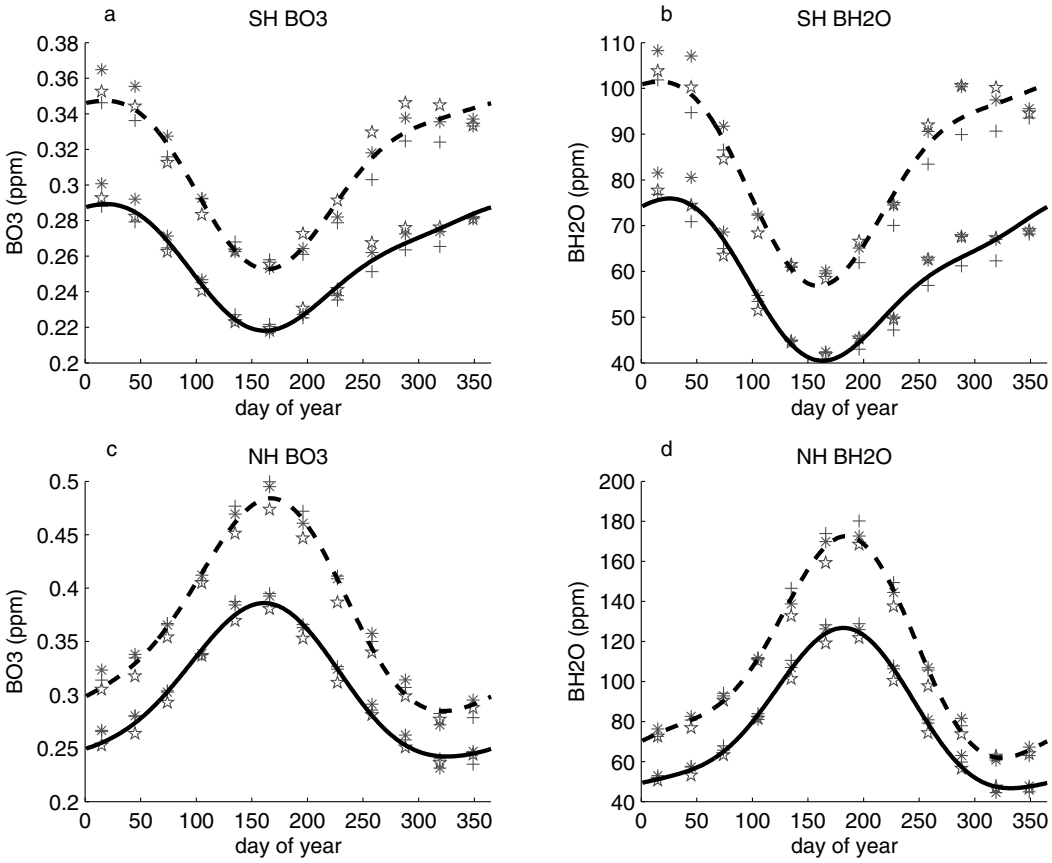

Figure 7.16: Variations in BO3 and BH2O values. The individual monthly values are marked by asterisk-2003, plus-2004, star-2005 data. The solid line is a 4 term fourier fit (see Equation 7.2) for $\bar{x}$, dashed line is Fourier 2 fit for $\bar{x} + 1s$. Note the different vertical scales on each of the subfigures.

BO3 and BH2O essentially describe the entry and exit points of the transition layer and can be thought of as the ends of the mixing lines. By applying regions to the BO3 and BH2O values, nine gradient categories can be created. These categories have the potential to separate out mixing and transport processes. For example when used in conjunction with entropy, an HH gradient category with high entropy could indicate exchange over a large vertical distance, whereas an LL gradient category with high entropy could indicate exchange over a small vertical distance.

Chapter 8

Application of Entropy, BO3 and BH2O

The previous chapters have described the entropy, BO3 and BH2O metrics which can be utilised to describe mixing and transport in tracer space. It is proposed that entropy describes the quantity of mixing in a given tracer space, whereas BO3 and BH2O describe the gradient or depth of the mixing. Furthermore, BO3 and BH2O can be divided up into gradient categories to group together tracer space regions with similar properties. In this chapter the gradient categories are shown to potentially highlight different mixing processes.

Section 8.1 shows entropy, BO3 and BH2O to be useful measures through daily scale variations and presents an aircraft comparison case study to show the ability of these measures to identify specific mixing events. Section 8.2 shows on a seasonal and yearly scales, that these measures are able to show the vertical extent (depth) and amount of mixing. Section 8.4 shows that different gradient categories have geographical preference for occurrence and are likely to be related to different mixing processes and transport directions.

8.1 Daily Scale Variations in Entropy, BO3 and BH2O

Daily measurements made by the AIRS (Atmospheric Remote Sounder) instrument allow entropy, BO3 and BH2O to be calculated on a daily time scale. A single day of BO3, BH2O and entropy on a global scale is shown in Figure 8.1. Of particular interest is that Figures 8.1a-c show small scale structures with filamentary and wave-like structures. These spatially coherent structures suggest that entropy, BO3 and BH2O relate to real geophysical structures, as opposed to the values being random over the globe.

As was shown previously in Figure 7.2, entropy, BO3 and BH2O are closely

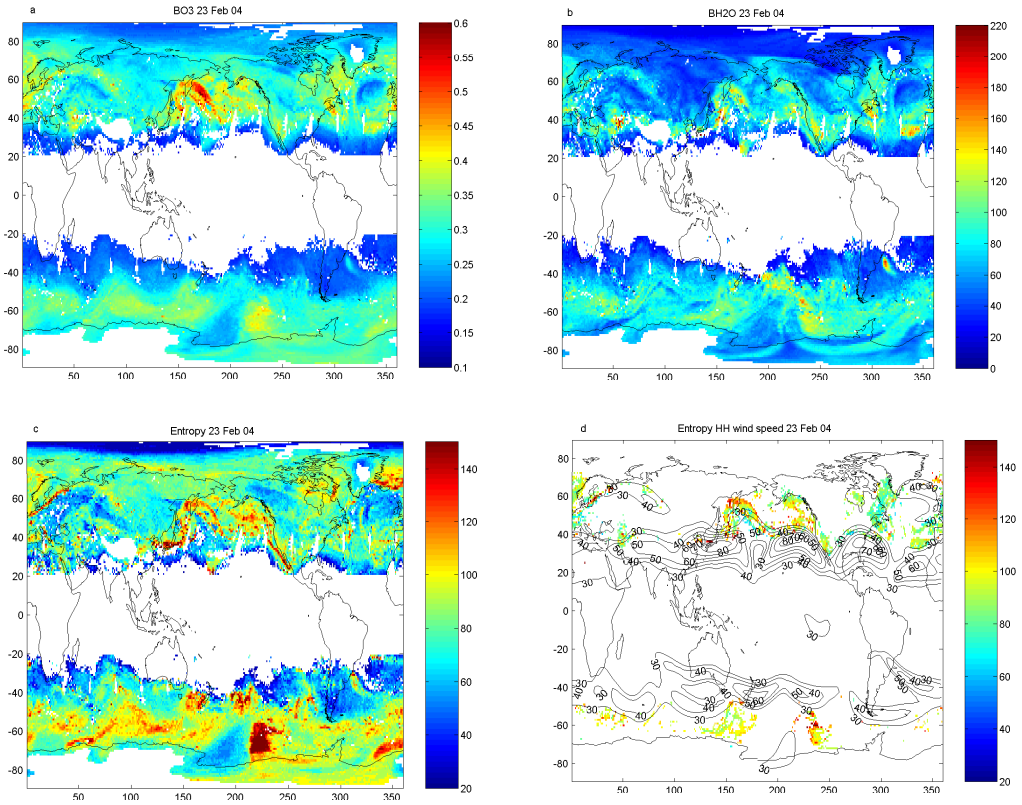

Figure 8.1: Daily fields from AIRS for 23 February 2004. a) BO3 in units of ppm. b) BH2O in units of ppm. c) Entropy in units of s/k$_B$. d) Entropy for the HH gradient category with the wind speed shown by the contours. Units for entropy are s/k$_B$ and the units for uv-wind are ms^{-1}.

related due to their relationship within tracer space. Hence it follows that high BO3 and BH2O values are generally accompanied by high entropy values. This is observed in Figures 8.1a-c, where the high regions in the three panels tend to be collocated. For example, in the South Pacific, centered approximately a latitude of 60°S and longitude of 230°, there is a region of high BO3, high BH2O and high entropy. However, if only one of BO3 or BH2O is large, then the entropy value does not necessarily have to be as large, as is observed over Russia. It also follows that low values in both BO3 and BH2O will relate to regions of low entropy, as is seen in the South West Pacific, centered at approximately at a latitude of 70°S and a longitude of 180°. There are also regions where neither BO3 or BH2O is particularly high, however there are high entropy values, as is observed over the Southern Indian Ocean. This shows that, while these measures are related, it is not a direct relationship and the different measures do provide extra information. As previously indicated, BO3 and BH2O describe the gradient of the mixing line, while entropy describes the amount of mixing.

The variation in entropy over the globe for a six day period is shown in Figure 8.2, along with the horizontal wind speed (jet stream) . Regions of entropy of similar values in the same region, that is coherent structures, move eastwards over the period shown and tend to follow the location of the jet stream and interact with the surroundings. An example of this is the low entropy region on the 23rd that is located in the South West Pacific at approximately a latitude of 70°S and a longitude of 180°. Over the six days, the low region becomes gradually diluted or mixed into the surrounding regions as it moves eastwards. By the 28th this low entropy region has lost most of its definition. Also of note in this sequence is that the data gap regions vary from day to day, along with the constant data gap regions as discussed in Section 6.3.6.

A single day of entropy data and its associated HH gradient category are shown in Figure 8.1d. This highlights the impact of separating the entropy values based on the gradient categories and their relationship to the jet stream. Jet streams provide regions for mixing due to the large variation in the tropopause height in those regions [*Hoinka*, 1999]. This is displayed in Figure 8.3 where the jet stream produces a rapid change in tropopause height and a tropopause fold region on the poleward side. In this region we expect higher entropy values as the air is being dragged downwards into the troposphere. The relationship between the jet stream location and entropy is discussed in more detail in Sections 8.1.1 and 8.4 along with Figure 8.14.

The application of the HH gradient category selects regions where the deviation of the mixing line from the origin is greatest (see Figures 7.11 and 7.12). The majority of the regions selected by the HH gradient category in Figure 8.1d are associated with high entropy values, however, there are a number of high entropy regions in 8.1c that are not selected by this category.

If this process is applied to several days worth of continuous data, as shown in Figure 8.4, it is possible to examine whether features in the HH gradient category are stationary with respect to the surface or the jet stream, and whether they have long term trackable or temporary features. In general these features tend to stay "attached" to a specific region of the jet stream. If the jet stream position moves then the region of entropy moves in the corresponding direction. An example of this is the region in the South Pacific to the west of South America that is centered at a latitude of 60°S and a longitude of 240° on the 23rd. Over the six days shown, this feature moves eastwards. In contrast, the region of entropy off the east coast of Asia which is basically stationary as the jet stream remains in

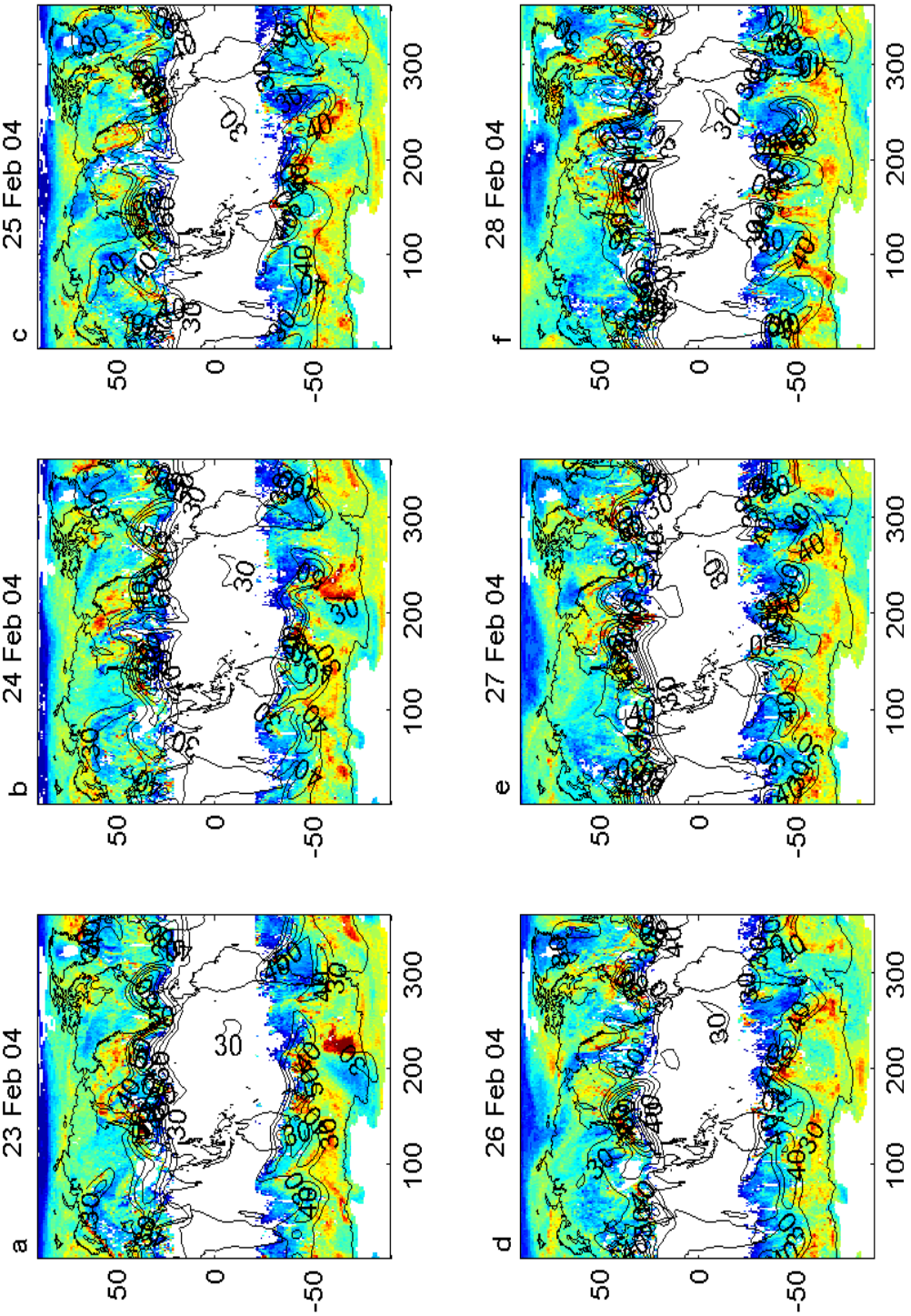

Figure 8.2: Entropy for 23-28 February 2004. Colour scale shows the entropy values with a range of 20 to 150. Contours show the jet stream (uv-winds) on the 200 hPa pressure level from NNR in units of ms^{-1}.

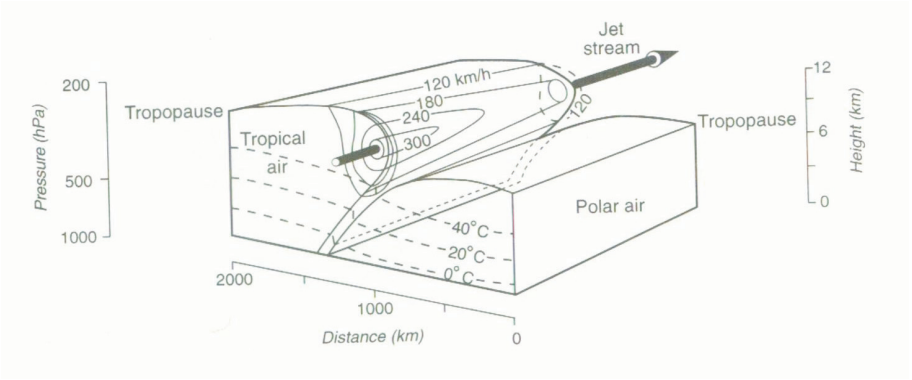

Figure 8.3: Active cold front, showing the wind speed (solid contours) and temperature (dashed contours) structure. Temperatures shown are negative. A wind speed of 120 kmh^{-1} is approximately equivalent to 33 ms^{-1} Figure from *Sturman and Tapper* [1996].

this region. This examination suggests that the HH gradient category is closely related to the location of the jet stream and STE processes related to this feature. This hypothesis is tested in a more statistical manner later in Section 8.4.

8.1.1 Case Study: Tropopause Fold and Cutoff Low

To be able to determine whether the entropy measure and the BO3, BH2O gradient categories previously described in Chapters 6 and 7 are effective measures of stratosphere troposphere exchange (STE), data sets are required which have well-defined analyses of STE and coincide with the AIRS observation period. *Pan et al.* [2007b] provides aircraft measurements where there are clearly identified STE events during the AIRS observation period. By comparing the interpretations and data from *Pan et al.* [2007b] with entropy, BO3 and BH2O, the effect of these measures can be examined in the identification and interpretation of STE events.

Pan et al. [2007b] discusses the analysis of two High-performance Instrumented Airborne platform for Environmental Research (HIAPER) flights showing contrasting conditions for STE. Flight 1 (1 December 2005) intersects a tropopause fold as indicated by Figure 8.5 showing the intersection of the jet stream. In comparison flight 5 (9 December 2005), shown in Figure 8.6, intersects a relatively flat region in terms of the wind and PV structure (see Section 2.1.3 for a description of PV). Of note in Figure 8.6 is the cutoff low just off the west coast of North America. Altitude-latitude cross sections of the thermal stability for

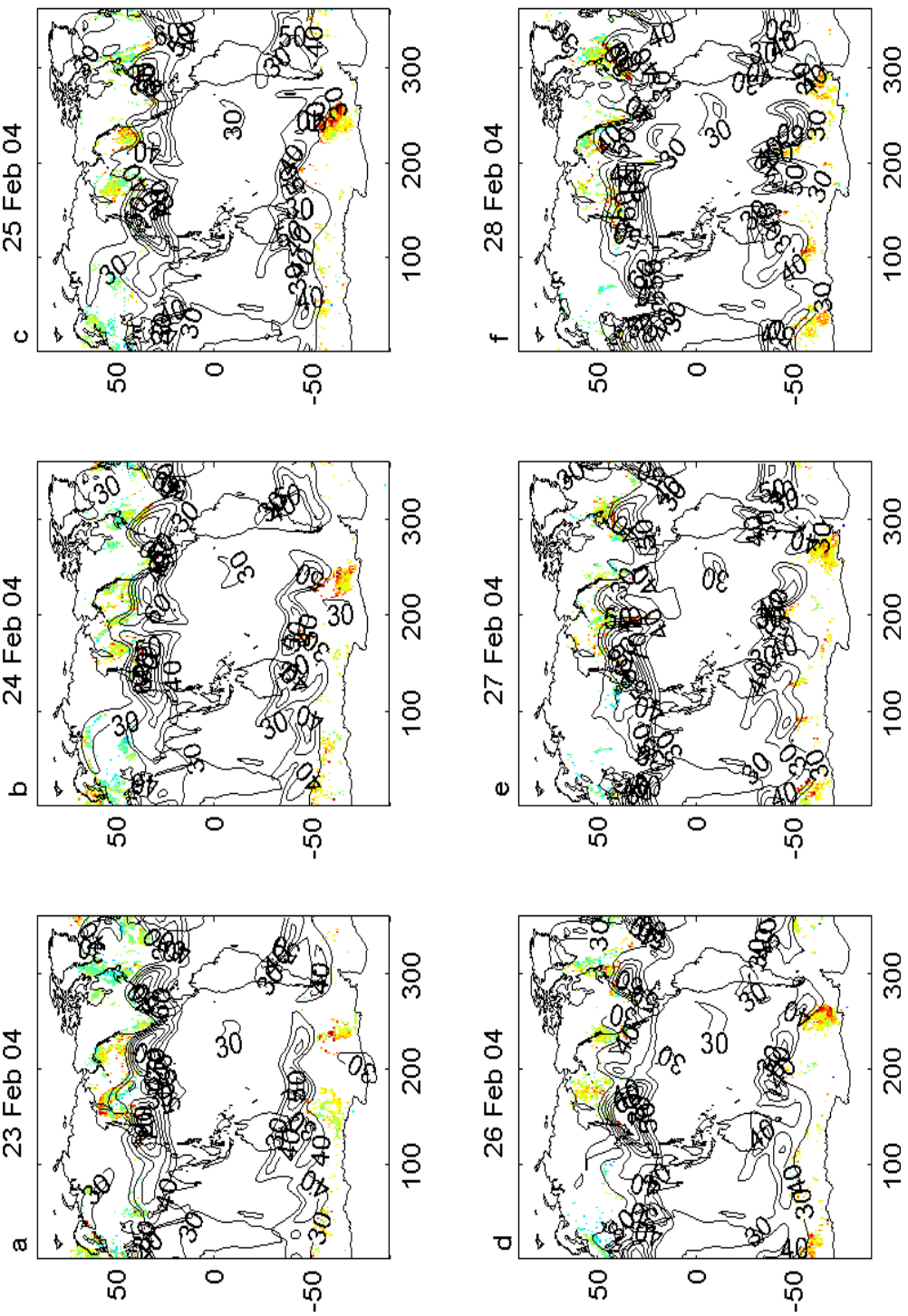

Figure 8.4: Entropy for the HH gradient category from 23-28 February 2004. Colour scale shows the entropy values with a range of 20 to 150. Contours show the jet stream (uv-winds) on the 200 hPa pressure level from NNR in units of ms^{-1}.

both these flights are shown in Figure 8.7, with dynamic and thermal tropopause heights also indicated.†

These flights and the STE events observed are examined using the AIRS entropy values for the same days. Figure 8.8a shows the entropy for flight 1, which intersects a tropopause fold. Examinations show a clear variation in the entropy values from high to low/medium values (ie. a gradient in the entropy values), along the flight path (red line) through the tropopause fold. The region of highest entropy values coincides with the lower tropopause values as shown in Figure 8.7a between latitudes of 42-49°. This is more clearly shown in Figure 8.9a, which displays the entropy-latitude cross section for the flight path. The region of increased entropy clearly matches the region of increased stability in Figure 8.7a. The descent of stratospheric air changes the stability and isentropic structure, and hence results in a region with stratospheric and tropospheric properties. This also corresponds to the region of high potential vorticity to the north of the jet stream in Figure 8.5, where high potential vorticity indicates high thermal stability.

The application of the BO3 and BH2O gradient categories potentially allows the separation of different types of transport out of the key features in the entropy field as shown 8.8b-j. Examination suggests that the high entropy region of interest associated with the tropopause fold is selected mainly by the HH category. The regions of high PV to the north of the jet stream in Figure 8.5 are mainly associated with the MM/MH/HM/HH gradient categories. These categories are indicative of larger gradients in tracer space and are in the region where we expect mixing as a result of the jet stream which is confirmed by the high entropy values. Table 8.1 shows that these categories have a high mean entropy value, particularly in comparison with the mean entropy from the LL gradient category.

The entropy for flight 5, shown in Figure 8.10 shows little variation over the flight path. Figure 8.7b also suggests little likelihood of vertical movement as the $\frac{d\theta}{dz}$ levels are relatively flat around the tropopause region. This is further confirmed in Figure 8.9b, where the entropy cross section shows some variation but does not reach high entropy values, indicating that the air is relatively unmixed. Of interest in Figure 8.10a is a region of high entropy off the west coast of North America, which coincides with the cutoff low identified in Figure 8.6. The increase

†Data for analysis of the flights is from NCEP (National Centers for Environmental Prediction) GFS (Global Forecast System) and NCEP FNL (Final Global Data Assimilation System), which are on $1° \times 1°$ global grid with 26 pressure levels from 1000 to 10 hPa. More information about these data sets can be found in *Pan et al.* [2007b] and online at http://wwwt.emc.ncep.noaa.gov/gmb/para/parabout.html

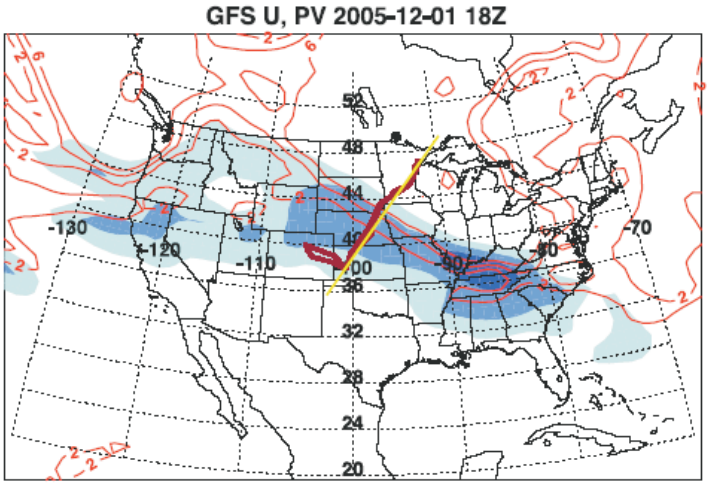

Figure 8.5: U winds (30, 40, 50 ms^{-1}, blue shadings) and the PV field (2, 4, 6 PVU, orange contours) at 300 hPa from NCEP GFS analyses, coinciding with the START flight 1 (1 Dec 2005), indicated by the flight path shown as the red line, with the yellow line the flight cross section for analyses. Figure from *Pan et al.* [2007b].

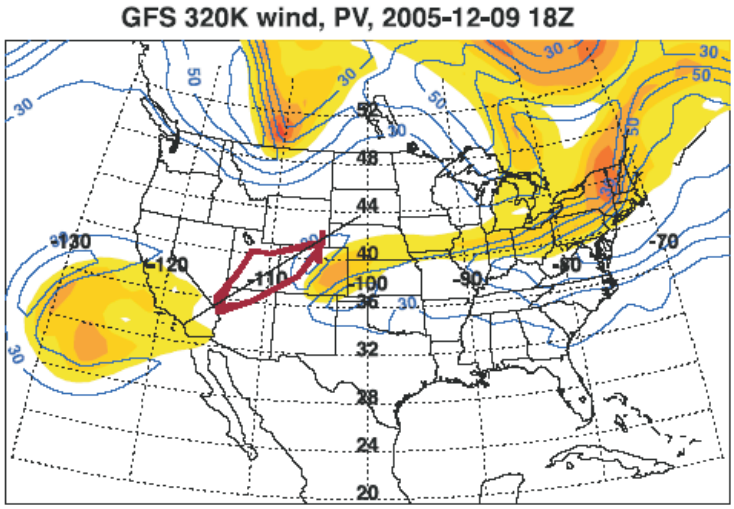

Figure 8.6: U winds (30, 40, 50 ms^{-1}, blue contours) and the PV field (2, 4, 6 PVU, orange shadings) at 320 K isentropic surface from NCEP GFS analyses, coinciding with the START flight 5 (9 Dec 2005), indicated by the flight path shown as the red line, with the black line the flight cross section for analyses. Figure from *Pan et al.* [2007b].

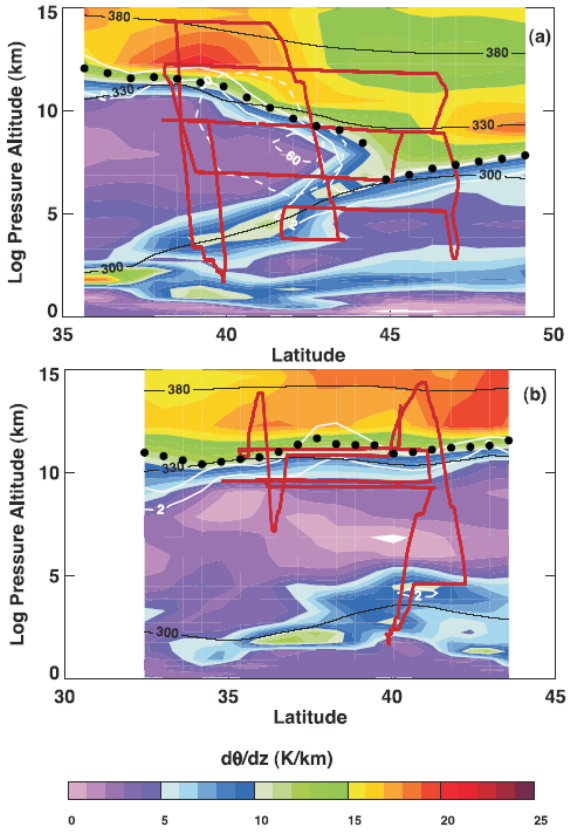

Figure 8.7: Cross sections for the flight paths shown in Figures 8.5 and 8.6, a) is flight 1 (1 Dec 2005) and b) is flight 5 (9 Dec 2005). Background colours show the thermal stability, potential vorticity (PV) is shown by the white contours, tropopause height with the black dots, isentropes are the black lines with the flight tracks shown in dark red. Figure from *Pan et al.* [2007b].

in entropy at approximately 33°N in Figure 8.9b is a result of the entropy-latitude cross section intersecting the edge of the cutoff low. The application of the gradient categories presented in Figures 8.10b-j shows that the cutoff low is selected by the HM category (panel i). An additional region of high entropy at approximately 40°N 80°W is split between HM (panel i) and HH (panel j). The regions of high entropy are associated with the regions of high PV in Figure 8.6, along with a location close to the jet stream. This is consistent with the results from flight 1. The mean entropy values for the MM/MH/HM/HH categories shown in Table 8.1 are larger than for the LL category as expected. As the region has less vertical disturbance in vertical stability for flight 5 than for flight 1, it also follows that the mean entropy values are lower for flight 5.

The application of the gradient categories to the entropy data has allowed the selection of regions of transport previously identified by *Pan et al.* [2007b]. This

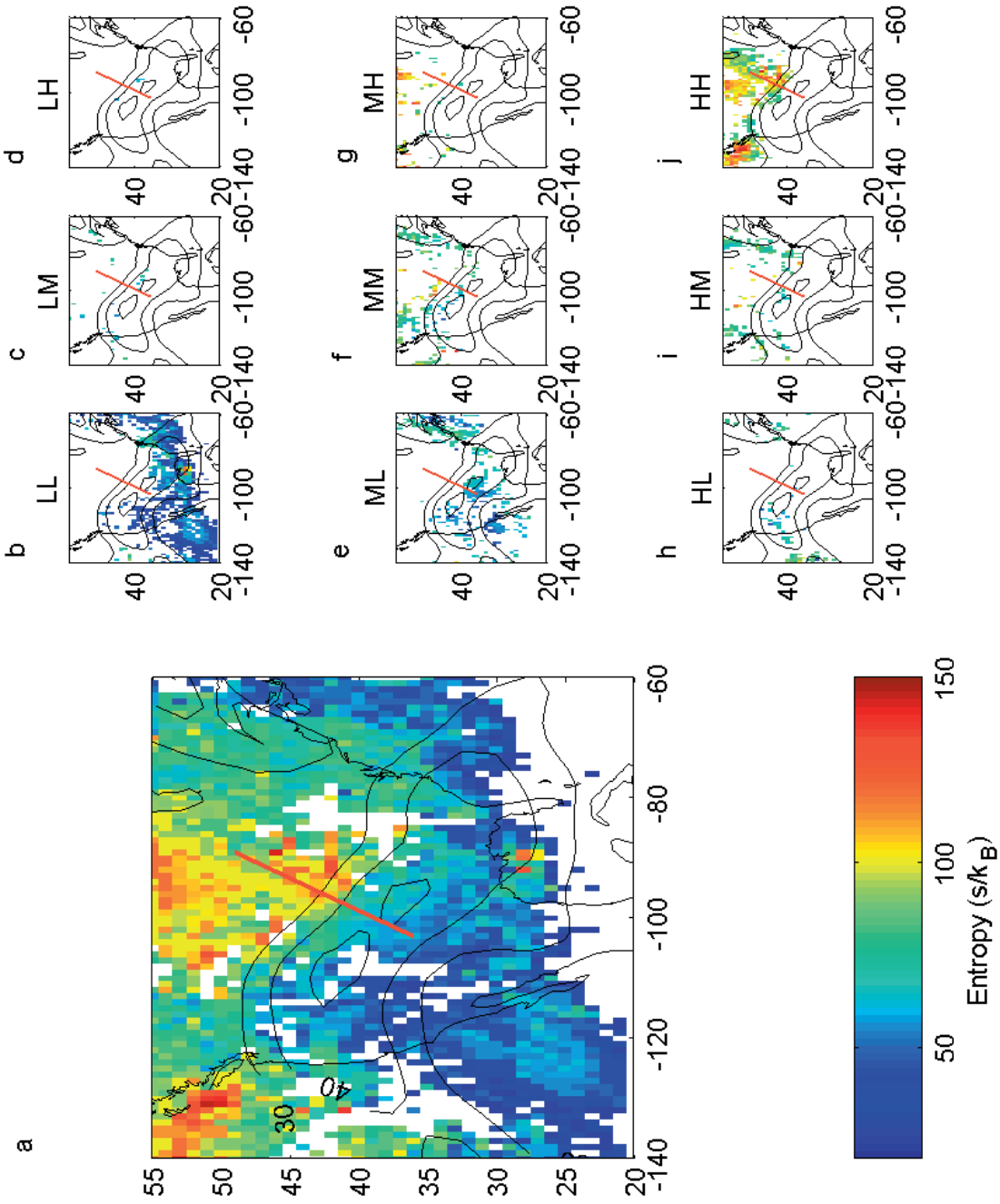

Figure 8.8: North American region (20°N-55°N 140°W-60°W) for 1 December 2005 showing entropy before (panel a) and after (panels b-j) the application of the gradient categories. Contours give the 24hr NCEP/NCAR reanalysis $\sqrt{u^2 + v^2}$ winds at 200 hPa in units of ms^{-1}. The flight path from Figure 8.5 is marked by the red line in each panel. Colour scale has units of entropy with a range of 20 to 150.

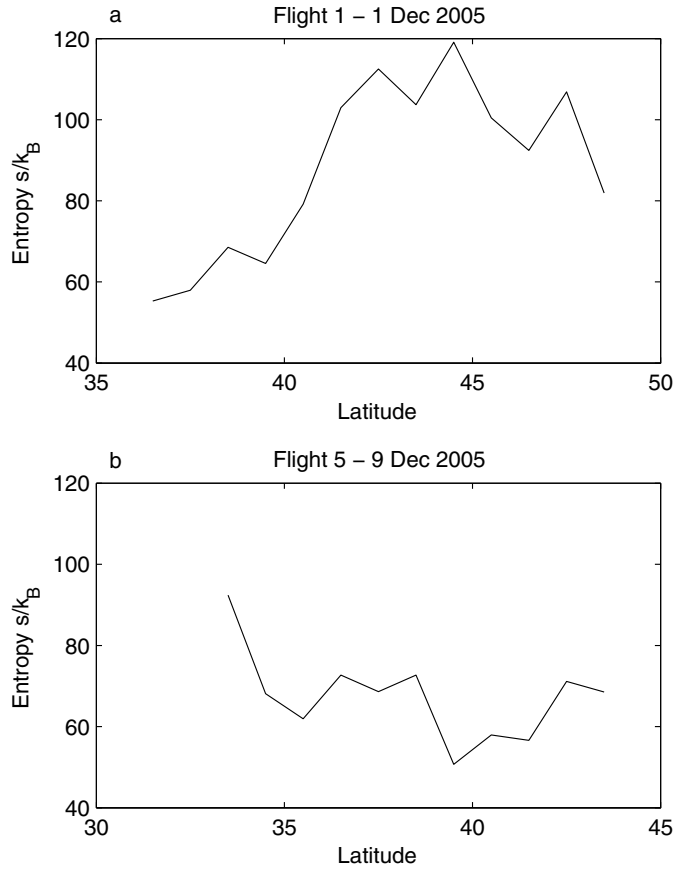

Figure 8.9: Entropy along the flight path cross sections shown in Figure 8.7. a) is for flight 1 intersecting a tropopause fold. b) is for flight 5 which covers a flat region in terms of potential vorticity and winds. Note that the scales are the same in each panel.

Table 8.1: Mean and standard deviation of entropy within the North American region, latitude 20°N-55°N, longitude 140°W-60°W, for each gradient category. Shown in Figures 8.8 and 8.10. Note that not all categories are shown.

Category	1 Dec 05		9 Dec 05	
	$\bar{x}$	σ	$\bar{x}$	σ
LL	47.089	14.800	43.764	13.608
MM	79.740	13.953	70.150	15.122
MH	97.888	14.806	76.045	16.536
HM	79.961	10.807	84.004	19.006
HH	96.990	13.919	85.518	14.679

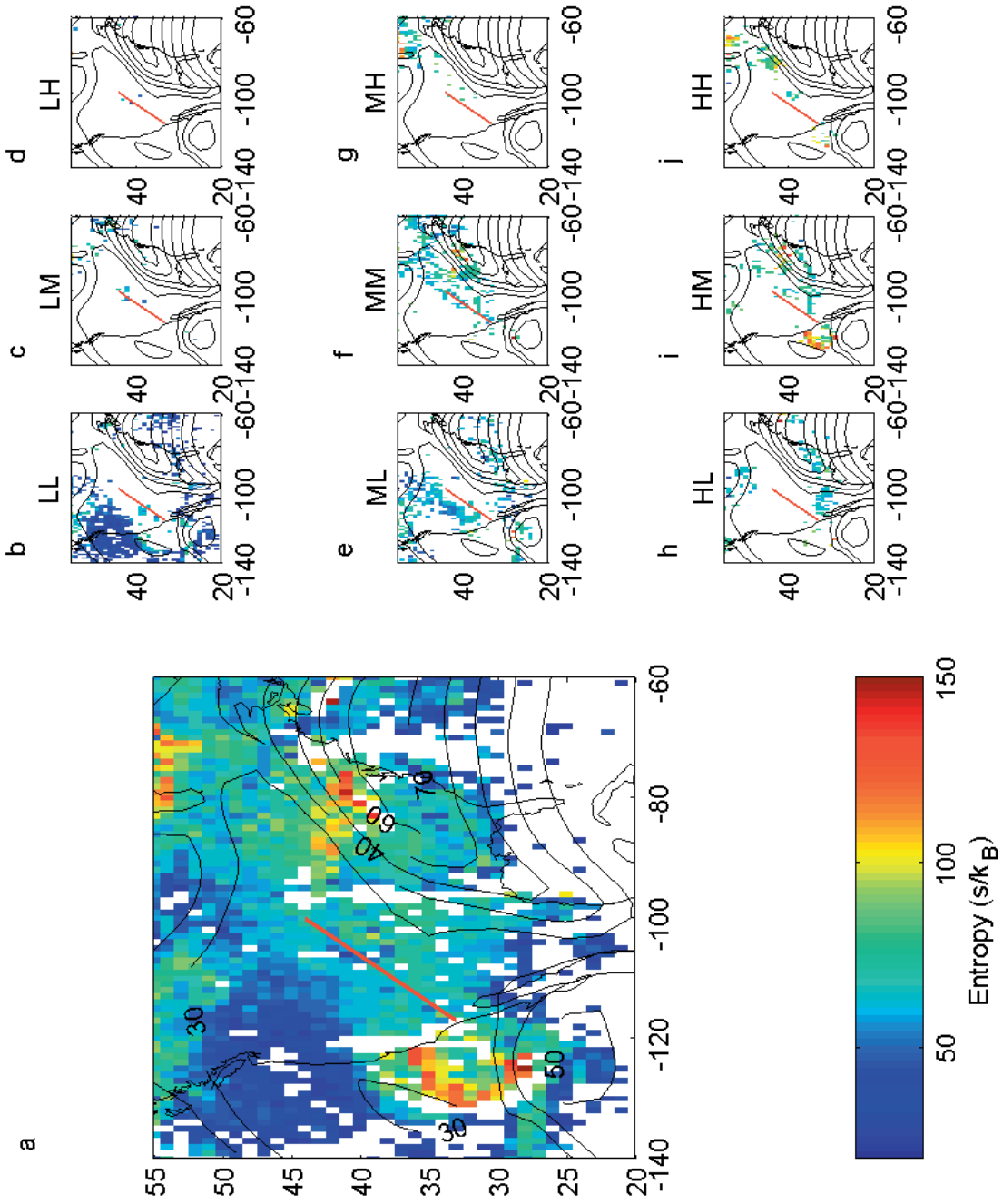

Figure 8.10: North American region (20°N-55°N 140°W-60°W) for 9 December 2005 showing entropy before (panel a) and after (panels b-j) the application of the gradient categories. Contours give the 24hr NCEP/NCAR reanalysis $\sqrt{u^2 + v^2}$ winds at 200 hPa in units of ms^{-1}. The flight path from Figure 8.6 is marked by the red line in each panel. Colour scale has units of entropy with a range of 20 to 150.

suggests that individual, well-defined STE events can be observed in the entropy field and that some details of these fields can be enhanced by using the BO3 and BH2O gradient categories.

8.1.2 Location of the Transition Layer with respect to the Tropopause

There are a number of different ways of defining the troposphere and the stratosphere. This was discussed in Section 2.1 with regards to the tropopause. The various tropopause definitions describe different properties of the troposphere and stratosphere and do not necessarily correspond to the same altitude. As a result, the relationship of the different tropopause definitions can describe different features of a profile.

The transition region, as used in the entropy calculation, defines the region where the stratospheric ozone and tropospheric water vapour properties overlap and potentially can describe mixing. Additionally, information about the thermal properties of the troposphere and stratosphere is also available for the ozonesonde/hygrometer profiles. By examining the relationship between the thermal stability, through the thermal tropopause location, and the transition layer, we can potentially gain some insight into the relationship of vertical mixing and thermal stability.

The configuration of the transition layer with respect to the thermal tropopause is examined to examine the relationship between entropy values and the tropopause height. Previous studies have used similar comparisons as a means of identifying active mixing and the signature of old mixing [*Bithell et al.*, 2000; *Hoor et al.*, 2002; *Pan et al.*, 2007b]. There are three possible configurations of the thermal tropopause and transition layer: the transition layer entirely within the troposphere; the transition layer entirely within the stratosphere; or the tropopause within the transition layer. The final configuration can be broken down into two subconfigurations, based on whether a larger proportion of the transition layer is above (stratosphere¿troposphere) or below (troposphere¿stratosphere) the tropopause. Only two of these configurations have been observed previously in literature. *Hoor et al.* [2002, 2004] and *Fischer et al.* [2000] observe the transition layer in the stratosphere. *Pan et al.* [2004, 2007b]; *Patmore and Toumi* [2006] and *Shepherd* [2007] observe the tropopause within the transition layer. There are no previous studies which have observed the transition layer in multiple configurations between different profiles for the same instrument.

The location of the transition layer with respect to the thermal tropopause is examined at Lauder and Boulder from the ozonesonde/hygrometers. The number of records in each of the configurations is recorded. When the thermal tropopause is within the transition layer, the number of results in the two subconfigurations is recorded. The mean tropopause height (and standard deviation) for each configuration is also calculated. The results of this comparison are shown in Table 8.2. In addition, the corresponding entropy values for each of the records is used to calculate the mean and standard deviation of entropy for each of the configurations. Note that a similar procedure cannot be carried out on the AIRS data as a comparison of this nature requires high vertical resolution data to reduce the uncertainties associated with height.

At both Lauder and Boulder, it is common for the transition region to be entirely within the stratosphere. Mixing signals are expected to last longer in the stratosphere due to its relatively stable nature [*Hoor et al.*, 2002]. Therefore, it is expected that this would be the most common configuration. This configuration is associated with low tropopause heights and with low entropy values. This suggests that when the transition layer is entirely within the stratosphere, we are observing the signature of old mixing. This is indicated by low entropy and the transition layer being located within a region of low vertical mixing caused by thermal stability.

At Boulder, we observe the transition layer being located entirely within the troposphere. This is not observed at Lauder, nor in any previous studies. When this occurs, there are typically high tropopause values. This may be a result of the jet stream being poleward of Boulder, which would cause higher tropopause values. As Boulder has a lower latitude than Lauder, the jet stream is more likely to be poleward of Boulder, hence accounting for the difference between the locations. Alternatively, the difference and occurrence of the high tropopause heights at Boulder and not a Lauder could be a result of another effect. For example, the altitude of Boulder and its location near the Rocky Mountains could have an effect.

When the tropopause is located within the transition layer, high entropy values are observed at both Lauder and Boulder. Signals within the troposphere are expected to mix in quickly due to the unstable of the troposphere. In comparison, signals in the stratosphere are expected to have longer lifetimes due to the stable nature of the stratosphere. As the transition layer is overlapping both the troposphere and the stratosphere, this may indicate active mixing. The

Table 8.2: Configuration of the transition layer and the thermal tropopause height for Lauder and Boulder ozonesondes/hygrometers. Mean and standard deviation for Entropy and the thermal tropopause height are also included. Note that 'Trop>Strat' means a larger proportion of the transition layer is below the tropopause (ie. in the troposphere), whereas 'Strat>Trop' means a larger proportion of the transition layer is above the tropopause (ie. in the stratosphere).

	Position of transition layer	% in category	Tropopause height (km) mean	std dev	Entropy ($\frac{s}{k_B}$) mean	std dev
Lauder	Trop	0	-	-	-	-
	Strat	64	9.7	1.5	36.9	15.6
	Trop>Strat	14	11.8	1.0	100.8	28.7
	Strat>Trop	22				
Boulder	Trop	25	14.0	1.9	56.0	28.2
	Strat	42	10.2	0.6	51.9	17.3
	Trop>Strat	14	11.3	0.7	90.0	22.6
	Strat>Trop	19				

transition region is asymmetric around the tropopause and can have more of the region either in the troposphere or in the stratosphere. The asymmetric properties of the configuration may reflect the speed or development of the mixing, depending on whether there is more of the transition layer in the troposphere or the stratosphere.

There appears to be a relationship between the configuration of the transition layer and the thermal tropopause with entropy and the tropopause heights. It is suggested that the configuration may help to define whether mixing is active or old. When entropy is low, we tend to observe the transition layer in the stratosphere, where mixing is slow. In comparison, when entropy is high we observe the transition layer in both the troposphere an the stratosphere, which may be active mixing.

8.2 Seasonal Variations in Entropy, BO3 and BH2O

Daily analysis of entropy, BO3 and BH2O can allow individual events to be studied. This has been shown in the previous section where the small scale structures can be observed. Comparison of entropy, BO3 and BH2O to high resolution data from an aircraft also showed the potential of these measures in identifying mixing

associated with STE processes. By examining the climatological scale, using either monthly or seasonal means, we can identify where exchange processes are prevalent, along with seasonal and hemispheric differences.

Representative monthly means for Entropy, BO3 and BH2O for January and July 2004 are shown in Figures 8.11, 8.12 and 8.13.[††] In general, the relationships between the mean entropy, BO3 and BH2O are similar to those discussed in Section 8.1, with regards to high values of BO3 and BH2O and how they relate to the resultant entropy value. There are clear seasonal and hemispheric patterns visible in these figures. The summer hemisphere has higher mean entropy, BO3 and BH2O than the winter hemisphere. The Northern Hemisphere values are larger than the Southern Hemisphere values for the equivalent season.

The region of high mean entropy over the summer pole creates a wash out effect for the majority of the hemisphere, with small scale features becoming part of the background level. In comparison, the mean entropy over the winter pole allows other features to stand out, such as the region of high entropy over the North Pacific in Figure 8.11a. This suggests that the use of mean entropy in some areas, or at some times of the year, may not be the most useful measure. In these cases, it may be more useful to look at the entropy anomaly, which is the difference between the mean entropy and the entropy at a particular location. This will allow smaller features to be observable above the hemispheric background level.

These regions of high and low values of BO3 and BH2O are in agreement with previous studies. As was discussed in Section 7.1 from *Hoinka* [1999], the water vapour in the Southern Hemisphere is generally lower than the Northern Hemisphere, and the summer is moister than the winter. This is a result of dehydration occurring as part of the ozone hole forming process, thereby resulting in less water vapour during the winter. As the ozone hole is stronger in the Southern Hemisphere, this also accounts for the hemispheric differences [*Birner et al.*, 2002]. There is also more moisture in the Northern Hemisphere as the core of ascending tropical air is more northward when the tropical temperatures are the warmest. Similar results are observed for ozone in *Wang et al.* [1998]. Ozone depletion accounts for the seasonal variation. The hemispheric differences in ozone can be account for by the poleward and downward transport of ozone from the tropics is

[††]The mean entropy, BO3 and BH2O for each month in 2004 is shown in Figures D.2, D.3 and D.4 These figures are not discussed explicitly in the text but allow the reader to view the yearly progression rather than just a subset. In addition the mean monthly entropy for 2003 is also shown in Figure D.1. This is provided as proof that 2004 is a representative year as there is little difference in the monthly means between the two years.

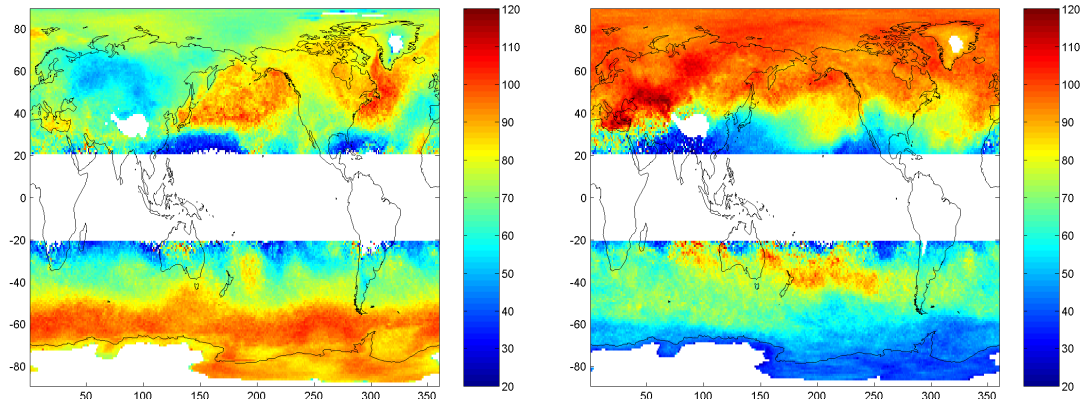

(a) (b)

Figure 8.11: Mean entropy values from AIRS for a) January 2004 and b) July 2004. Colour scale shows entropy values with units of $\frac{s}{k_B}$.

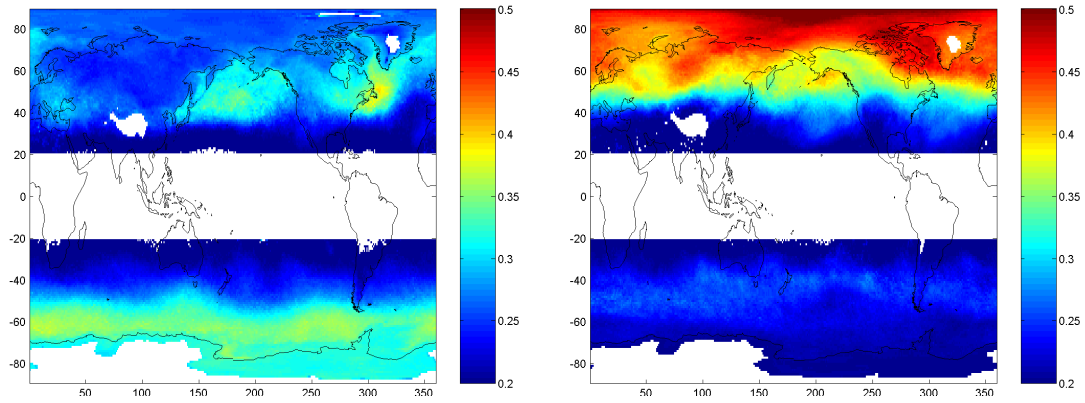

(a) (b)

Figure 8.12: Mean BO3 values from AIRS for a) January 2004 and b) July 2004. Colour scale shows BO3 values with units of ppm.

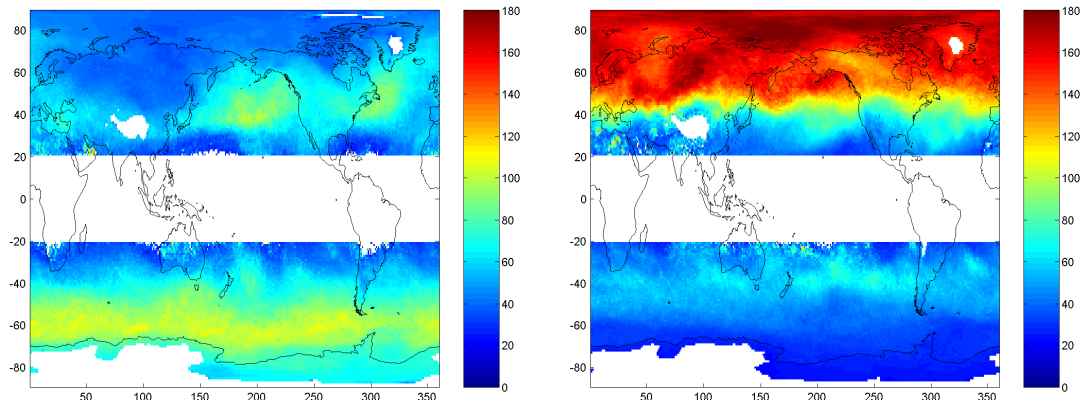

(a) (b)

Figure 8.13: Mean BH2O values from AIRS for a) January 2004 and b) July 2004. Colour scale shows BH2O values with units of ppm.

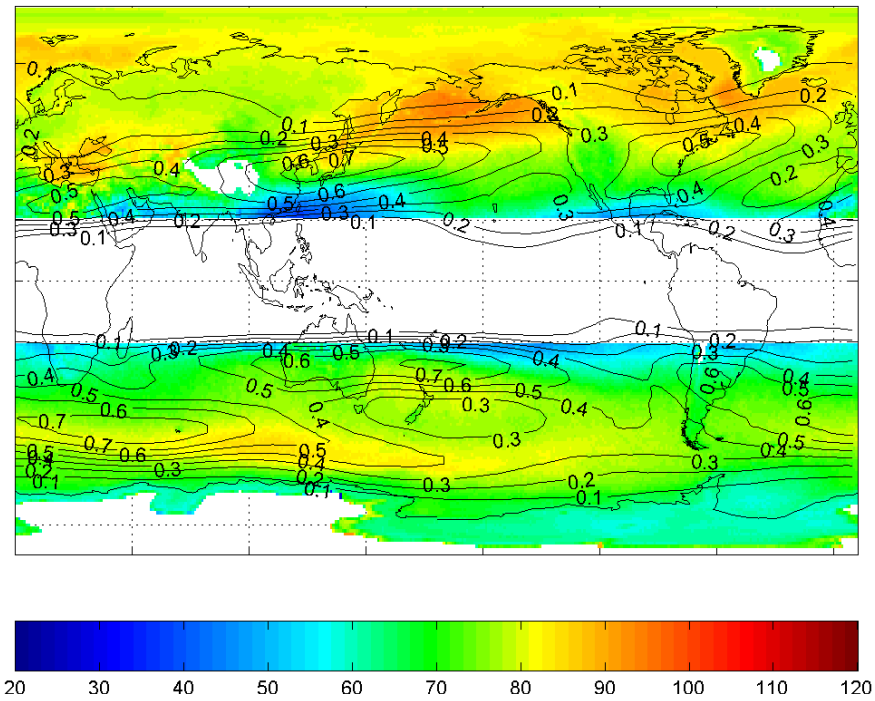

Figure 8.14: Mean AIRS entropy from 2003 to 2005. Colour bar has units of $\frac{s}{k_B}$. Contours show the occurrence fraction of wind speed $\sqrt{u^2+v^2}$ greater than 30ms^{-1} at 200 hPa in units of ms^{-1} as shown in Figure 3.3.

stronger in the Northern Hemisphere [*World Meteorological Organization*, 2003], thereby transporting more ozone to the Northern Hemisphere.

Some features of note in Figure 8.11 are that the summer hemisphere tends to have less small scale structure, displaying hemispheric wide increases in entropy. In comparison the winter hemisphere has smaller scale structure which is clearly defined. An example of this is the regions of high entropy in Figure 8.11a in the North Pacific ocean off the east coast of Asia, and the second high region off the east coast of North America, just south of Greenland. The Southern Hemisphere during the winter (Figure 8.11b) also has a more zonal structure than the Northern Hemisphere.

As a way to identify the mechanisms behind the increase in entropy, particularly the smaller scale structures which are clearly visible during the winter, the yearly mean entropy is presented in Figure 8.14. In conjunction with the mean entropy, the occurrence of horizontal wind speeds greater than 30 ms^{-1} on the 200 hPa surface from NNR are displayed (see Section 3.3), as these can be used to represent

the position of the jet stream. The majority of regions of high entropy are located slightly poleward and eastward of the greatest occurrence of the jet streams. This suggests that the location of the jet stream will be important for mixing based on our interpretation of large entropy values. This linkage between the jet stream and high entropy has been shown previously in Figure 8.3, where on the poleward side of the jet stream, air is moved downwards thereby creating a region of vertical mixing.

One of the most significant relationships between increased entropy and jet stream position is found off the east coast of Asia, associated with the East Asian Jet Stream (EAJS). This jet steam has been shown to be closely associated with cyclogenesis, frontogenesis, monsoon blocking and storm tracking, along with having a significant impact on surface temperature and rainfall in both Asia and North America, along with the strength of convection [*Yang et al.*, 2002]. It has also been shown that there is an ozone enhancement and potential vorticity increase associated with the poleward side of the EAJS from tropopause folds and cutoff lows [*Tsutsumi et al.*, 1998]. It follows that the other jet stream regions may have a similar effect on the surrounding region and hence result in higher entropy values. This possibility is investigated in Section 8.4.

8.2.1 Climatological Case Studies

As a means to confirm that entropy, BO3 and BH2O are able to highlight mixing and transport, they are compared to three climatological case studies. These studies allow a qualitative comparison by which the entropy, BO3 and BH2O can be interpreted.

8.2.1.1 Case Study: Cross-tropopause Mass Flux Distributions

Sprenger et al. [2003] created a global tropopause fold frequency climatology for March 2000 to February 2001 using ECMWF data (60 levels, $1^\circ \times 1^\circ$). The tropopause folds are defined as vertical soundings where there are multiple crossings of the 2PV surface (dynamic tropopause), which identifies purely geometric folds, unlike a number of other studies which use more complex methods (eg. *Van Haver et al.* [1996]). Shallow folds have a depth of between 50 hPa and 200 hPa; Medium folds have a depth of between 200 hPa and 350 hPa; Deep folds have a depth of greater than 350 hPa. The results from December to February

(DJF) and June to August (JJA) are shown in Figure 8.15. Tropopause folds are preferentially observed in the subtropics and are shallow. Deep folds occur less often and mainly occur in the winter and at midlatitudes.

Sprenger et al. [2003] also calculate the cross-tropopause mass flux using a Lagrangian transport model. An exchange event is considered valid or significant if it crosses over the dynamic tropopause and remains in its new sphere for at least 24 hours. The mass flux is shown in Figure 8.16 for the same period as the tropopause fold frequencies. Their study also looks at the probability that exchange occurs in the region of a tropopause fold. There is a high probability that exchange occurs near a shallow fold between latitudes of about 20°-40°/50°, with the probability dropping as latitude or depth of fold is increased. Midlatitude folds are associated with larger mass fluxes than subtropical folds for both troposphere to stratosphere transport (TST) and stratosphere to troposphere transport (STT). A number of locations where tropopause fold occurrence and large mass flux are observed simultaneously are indicated by the letters in Figure 8.16, and will be discussed in the following paragraphs. Of note is that not all regions of high tropopause fold occurrence correspond to regions of high mass flux and vice versa. These discrepancies are likely to be a result of the mass flux accounting for a number of STE mechanisms rather than specifically tropopause folds.

The corresponding AIRS mean entropy fields are shown in Figures 8.17a and 8.18a for DJF and JJA, respectively. Note that the figures from *Sprenger et al.* [2003] are from 2000/2001 whereas Figures 8.17 and 8.18 are from 2004 as the AIRS observation period does not cover the 2000/2001 period. The entropy fields are representative of the mean values of any year. This comparison treats the Sprenger figures as a one year climatology therefore there are some differences expected due to the different time periods.

As the mass flux from *Sprenger et al.* [2003] is a measure of the movement across the tropopause, it is expected that there will be some relationship between the entropy value and the mass flux. A larger mass flux indicates more movement and is likely to be observed as a larger signature of mixing. Likewise, as mass flux is measured in both directions, whether the flux is in one direction or two should also have an impact on the resultant entropy. The tropopause fold depth might be expected to be related to the gradient categories as both are a measure of the gradient of mixing. Thus, regions associated with deep tropopause folds are expected to be related to regions in the higher gradient categories, such as HH and MH.

For DJF the main features are indicated by points L and M in Figures 8.16(a and c) and Figure 8.17. Points L and M correspond to a maximum in the deep folds and maximum in STT. In Figure 8.17a, points L and M correspond to regions of high mean entropy. When the BO3 and BH2O gradient categories are applied, as shown in Figure 8.17b, there is a clear match between the HH category and the regions of high entropy indicated by points L and M. This correspondence can be interpreted as a region where deep folds are occurring, with large amounts of downward flux (STT) that correspond to a region of high mixing (indicated by the high entropy) across a large vertical depth (indicated by the HH category). The other gradient categories are not shown. The band of high flux across the Southern Hemisphere corresponds roughly to high values in the HH and MH gradient categories. The other letters on Figures 8.16a and 8.16c when compared to Figure 8.17 either correspond to blank patches in the entropy (point H) as discussed in Section 6.3.6, or have no features in the entropy (points I, J and K). These regions with no features in the entropy correspond to regions of weak mass flux in Figures 8.16a and 8.16c, and are therefore likely to have a smaller impact on the mixing and hence lower entropy.

For JJA there are a number of features that match between Figures 8.16(b and d) and 8.18, labelled A through to G. In general there is good matching between these figures with the exception of points D and G. Point D is on the edge of the entropy calculation region, therefore the entropy is not always calculated in this region. This may account for the lack of any entropy feature at this location. Point G is in a blank region due to reasons discussed in Section 6.3.6. The mean entropy for JJA shows generally high entropy throughout the Northern Hemisphere and low entropy in the Southern Hemisphere. Most of the high flux regions in Figure 8.16(b and d) in the Southern Hemisphere are associated with Antarctica where there is no entropy data.

Point A in Figure 8.16b is a associated with downwards mass flux (STT) and is associated with shallow tropopause folds. This point corresponds to a region of higher entropy in Figure 8.18a. This region of high entropy is not associated with a single gradient category, and is hence visible in several - HH, HM and MM (not shown). Point B is observed in the entropy, as well as the high entropy region on the east coast of Australia, both of which correspond to STT mass flux and a region of shallow and medium folds. This signal is also not observed in any one gradient category, with elements in ML, MM, HM and HH (not shown). Point F is associated with deep tropopause folds and high flux and is accompanied by a

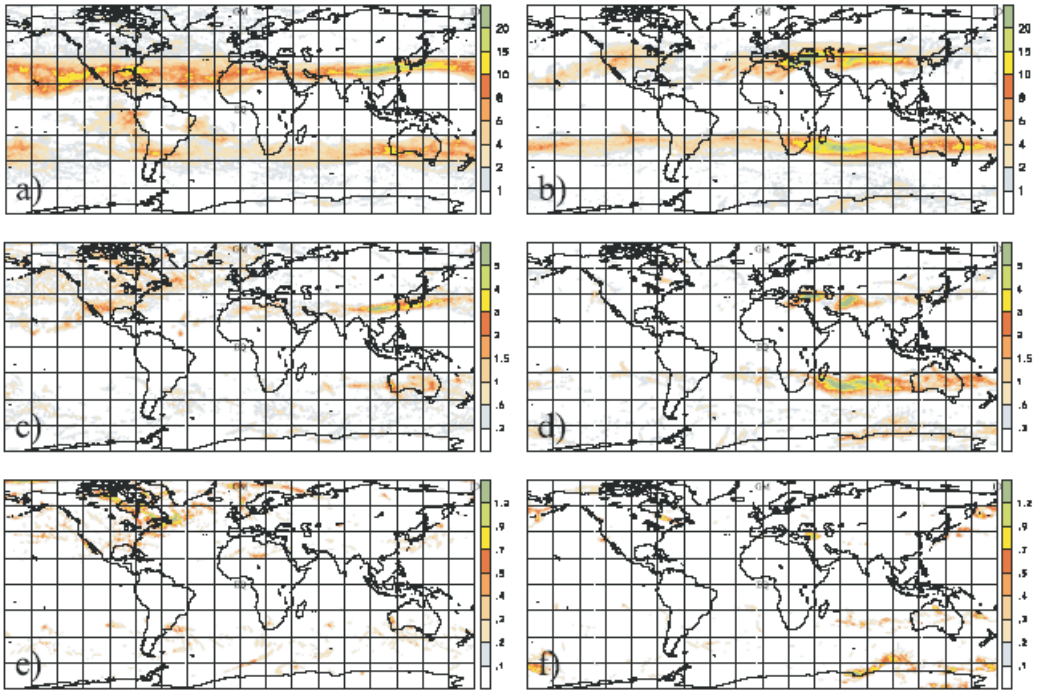

Figure 8.15: Tropopause fold frequency (in %) using the dynamic tropopause definition from the ECMWF data from March 2000 to February 2001. Left panels are for DJF and right panels for JJA. Panels a and b are for shallow folds, c and d for medium folds, e and f for deep folds. Figure from *Sprenger et al.* [2003].

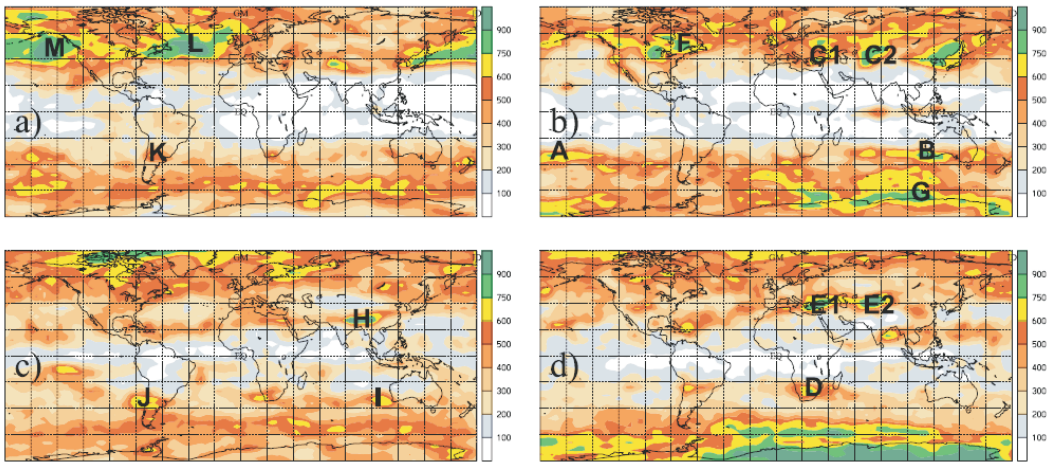

Figure 8.16: Geographical cross-tropopause mass flux distributions (in kg km^{-2} s^{-1}) for DJF (left panels) and JJA (right panels) for (a and b) STT and (c and d) TST. Figure from *Sprenger et al.* [2003].

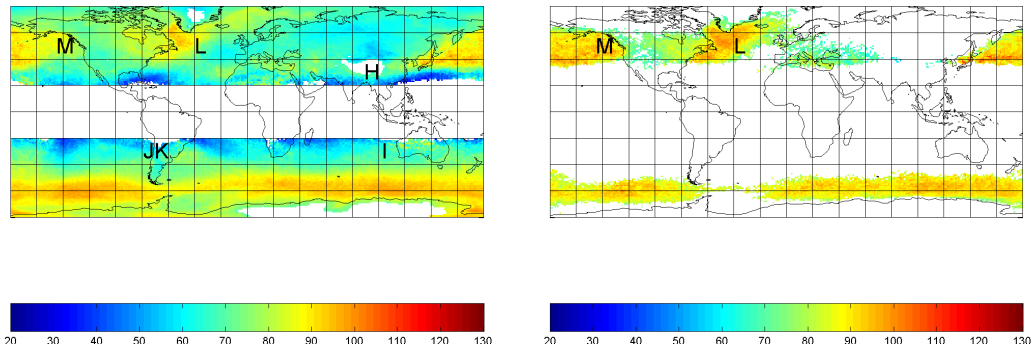

(a) (b)

Figure 8.17: Mean entropy for DJF 2004 in units of $\frac{s}{k_B}$. a) shows the mean entropy for the globe and b) showing the mean entropy for points in the HH gradient category only.

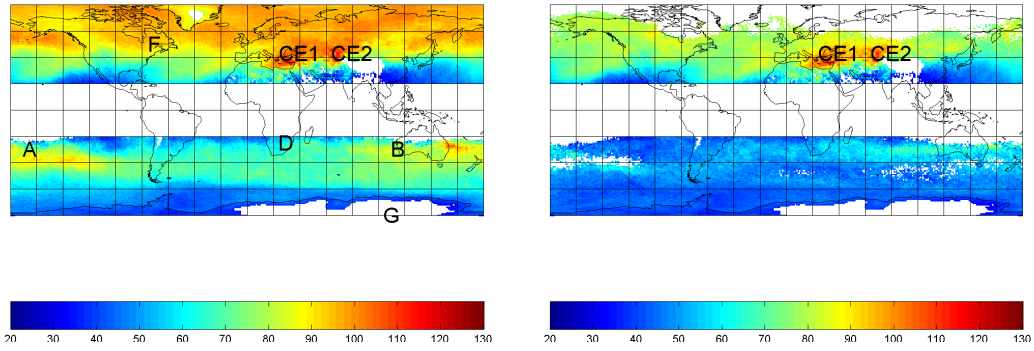

(a) (b)

Figure 8.18: Mean entropy for JJA 2004 in units of $\frac{s}{k_B}$. a) shows the mean entropy for the globe and b) showing the mean entropy for points in the LL gradient category only.

high entropy value. However, this high entropy region is not an isolated region of high entropy and is part of the nearly hemisphere wide increase in entropy that is present in the Northern Hemisphere summer.

Of particular interest are the regions marked by E1, E2, C1 and C2. In the mean entropy shown in Figure 8.18a, these regions are indistinct and meld with the background. Under the application of the gradient categories, these regions become clearly associated with the LL category as shown in Figure 8.18b. From Figures 8.15b and 8.16(panels b and d) we can see that these regions are associated with shallow folds and strong mass flux for both STT and TST. This corresponds clearly to high entropy values, which indicate that there is vertical movement causing the region to be well mixed. The selection of the area in the LL category indicates that the mixing is shallow (see Figure 7.12), which clearly relates to having a high occurrence of shallow folds.

It should be noted that there is an unusual region of TST flux over the South Pole during the winter months, shown in Figure 8.16d. Upwards vertical motion is not expected over the winter pole, as the winter polar region is dominated by downwards descent. This creates some concern for the accuracy of the cross tropopause mass flux discussed in this paper, as this is clearly an undesirable feature of the model. However, as a number of the other features in Figure 8.16 are in agreement with known features, a comparison is valid in regions away from the South Pole.

This comparison has allowed a number of locations of entropy, BO3 and BH2O values to be matched with a particular mechanism and depth of vertical mixing from tropopause folds. Those regions of most interest are those off the east coast of Asia which are associated with deep tropopause folds mainly in the downwards direction, along with the shallow bidirectional mixing in eastern Europe/west Asia.

In general, the comparisons between entropy and the results of *Sprenger et al.* [2003] show excellent correspondence. This is particularly notable given the methodologies are very different.

8.2.1.2 Case Study: Climatology of COLs in Southern Hemisphere

A climatology of cutoff lows (COLs, previously discussed in Section 2.2.2) in the Southern Hemisphere derived from NNR data is discussed in *Fuenzalida et al.*

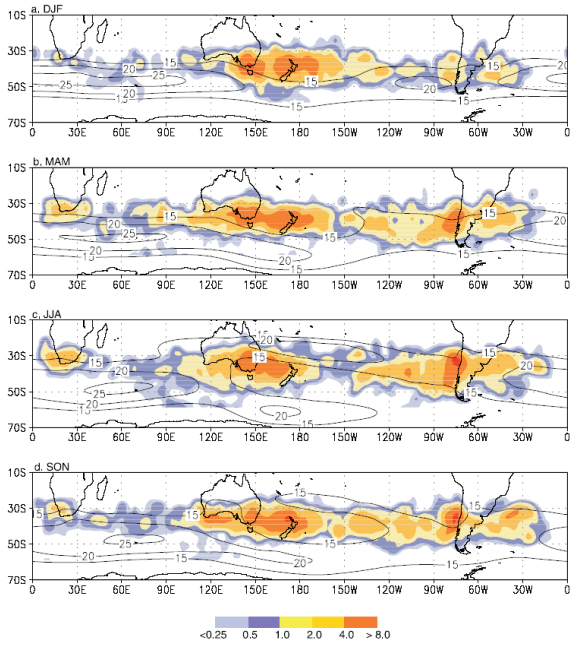

Figure 8.19: Seasonal average of the number of COLs in a 2.5° × 2.5° box normalised by area. Contours show the climatological mean at 500 hPa for zonal wind in ms^{-1}. Figure from *Fuenzalida et al.* [2005].

[2005] and is shown in Figure 8.19. For a COL to be counted in their study, it had to be strong, closed and last for at least 36 hours. The climatology is based on 31 years worth of data. COLs are relatively rare events, with approximately 40 occurring in the Southern Hemisphere per year. Comparing the occurrence of COLs to the jet stream frequencies shown in Figure 3.3 shows that the maximum COL frequency is observed between the jet streams in the Australia/New Zealand region and northward of the jet stream below Africa and in the jet stream break on the west coast of South America.

A comparison of Figure 8.19 with Figure 8.15(all panels) from *Sprenger et al.* [2003], shows that the regions of high COLs correspond to tropopause fold regions for DJF and JJA. However, these are not regions of high flux shown in Figure 8.16(all panels) from *Sprenger et al.* [2003]. The exception is the high number of COLs over South Africa in JJA, which corresponds to a region of high flux.

The formation of COLs is closely related to the location of the jet stream. Figure 8.14 showed that regions of high entropy are related to the jet stream, therefore it is possible that there may be a similar relationship for COLs. A comparison of the COL frequency with the gradient categories (not shown) does not show a clear relationship between the categories and the COLs. As entropy and COLs

are both related to the jet stream there is a broad agreement between them, however, there is no agreement in the small scale structure. The regions of high COL frequency over South America and South Africa do not correspond to the gradient categories or increased entropy values. In Figure 8.10, a single identified COL was thresholded into the HM category. However, an examination of this category by season with relation to COL frequency shows no clear relation.

The lack of relationship between the COL frequency and entropy gradient categories is likely a result of the limited number of COLs identified over the study period of *Fuenzalida et al.* [2005]. Approximately 40 COL events per year over the whole Southern Hemisphere are identified, making them relatively rare events. This is further demonstrated in Figure 8.19 where the darkest shading refers to less than eight events in a three month period. Compared to the gradient category occurrence, this small number of events is lost in the number of entropy values in each gradient category. This suggests that while we can see an increase in entropy for a single COL event as was observed in Figures 8.9 and 8.10, the longer term averaging may remove or smear out the signal. Therefore, COLs do have an impact on STE, but their signal is not observable in entropy in the same manner as other mechanisms such as those linked to the EAJS.

8.2.1.3 Case study: Mean Diabatic Flux of Mass

Olsen et al. [2004] calculate the mean diabatic flux across the 380 K surface using the NASA Goddard chemistry and transport model (CTM) and general circulation model (GCM) for 5 years of data from 1979 to 1983. The mean diabatic mass flux across the 380K surface is shown in Figure 8.20. They also calculate the adiabatic and net tropopause flux, however, there is no spatial information on these values. The extratropics are the focus of their study, hence the tropics are not shown in Figure 8.20. Note that the 380 K surface is a very high level in altitude at middle latitudes (see Figure 2.5) and is likely to be above the transition region. Hence, this surface is related exchange occurring over a large vertical range and will thereby is likely to be related to high BO3 and BH2O gradient categories.

The regions of high flux across the 380 K surface in the Northern Hemisphere match approximately to regions of high mean entropy in Figure 8.14. In particular it matches reasonably with the areas marked L and M in Figures 8.16a and 8.17, which are regions of large vertical depth exchange associated with deep

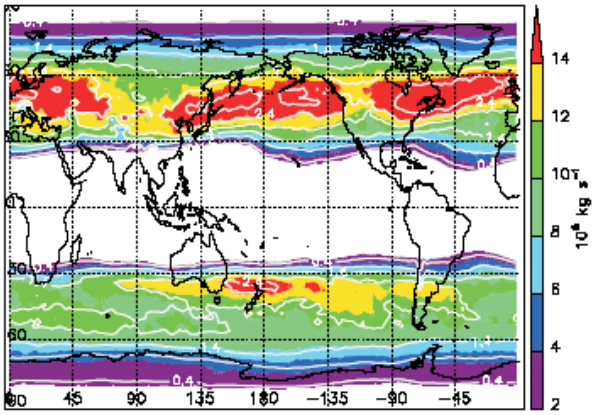
14
12
10
8
6
4
2
10^{-4} kg s
60
0.4
0.4
0.4

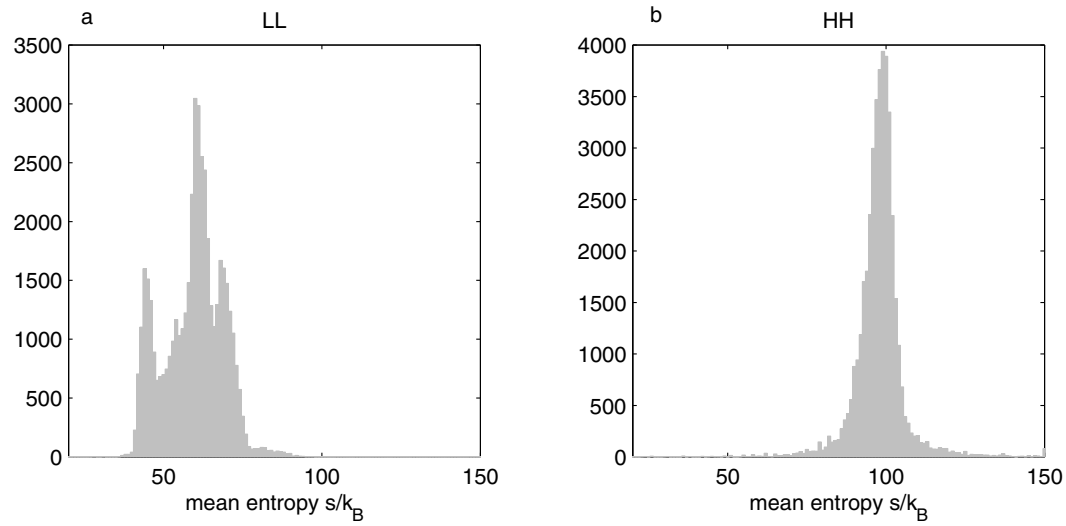

Figure 8.21: Mean entropy over the whole globe for 2003 to 2005, separated by gradient category. a) shows the distribution for the LL gradient category. b) showing the distribution for the HH gradient category.

8.3 Variation in mean entropy for LL and HH gradient categories

The case studies in Sections 8.1.1 and 8.2.1.1 have shown a qualitative relationship between the gradient categories and entropy values associated with different STE processes. For example, it was shown in Section 8.1.1 that tropopause folds can be observed clearly in the HH category (Figure 8.8j). Case study comparisons have also shown that the gradient categories are likely to related to the depth of the vertical mixing by tropopause folds and transport.

Furthermore, Figure 8.21 shows that the mean entropy distribution for the LL and HH gradient categories are significantly different. As entropy, BO3 and BH2O are closely related, the means of the distributions of the LL and HH gradient categories are expected to be different. However, it is somewhat unexpected that the forms of the distributions in Figure 8.21 would be so different. The HH category distribution in Figure 8.21b has a single mode, whereas the LL category in Figure 8.21a of the same figure has a multi-modal structure. A single mode is suggestive of a single process being selected by the HH gradient category. Whereas the multiple modes observed in Figure 8.21a are suggestive of multiple processes being selected by the LL gradient category.

Rather than solely examining the mean entropy for the categories, it is useful

to examine the anomalies from the mean. This can show if there are periods of the year where the anomalies are larger, and if the seasonal patterns for the categories are the same.

The anomalies (e′) from the mean entropy ($\overline{e}$) for the LL and HH categories are calculated from 2003 to 2004 using:

$$e' = e - \overline{e} \tag{8.1}$$

The mean entropy value for 2003-2005 from AIRS for the LL gradient category is $59.45\frac{s}{k_B}$, and for the HH gradient category is $97.88\frac{s}{k_B}$. Note that the entropy mean is a yearly global value, which will allow the anomalies to be compared for differences across hemispheres and seasons. The relative variations for the mean of the anomalies by season is shown in Figure 8.22. The seasonal anomalies indicate whether the entropy is higher or lower than the mean and hence whether mixing is stronger or weaker than the average amount of mixing for that gradient category.

It should be noted that a seasonal mean for calculating the anomalies is not used, as we are interested in the seasonal variations in the anomalies. It may be a concern that, due to the seasonal gradient category limits in Section 7.3, this would bias the anomalies. If there was a bias, we would probably expect that the form of Figures 8.22 and 7.16 would be similar and also that the bias would be similar in LL and HH. As Figure 8.22 is not in phase with the gradient category limits in 7.16 it is unlikely that we have a bias and the majority of what is observed is a real signal.

The seasonal variations in the anomalies show a clear seasonal variation with a hemispheric offset. The maximum entropy anomaly values occur during the spring-summer for the LL category and during the summer-autumn for the HH category. Transport across the tropopause is inhibited during the winter months [*Dethof et al.*, 2000], therefore it follows that the lowest anomalies should occur during the winter, as is observed in Figure 8.22. Large horizontal trace gas gradients, such as at the polar frontal region, could also result in HH correlations.

The LL gradient category is expected to represent small scale mixing or mixing in regions without large gradients in tracer properties. This was observed in the case study in Section 8.2.1.1, where the LL category was shown to represent shallow vertical mixing. It is likely that one of the processes for the LL cate-

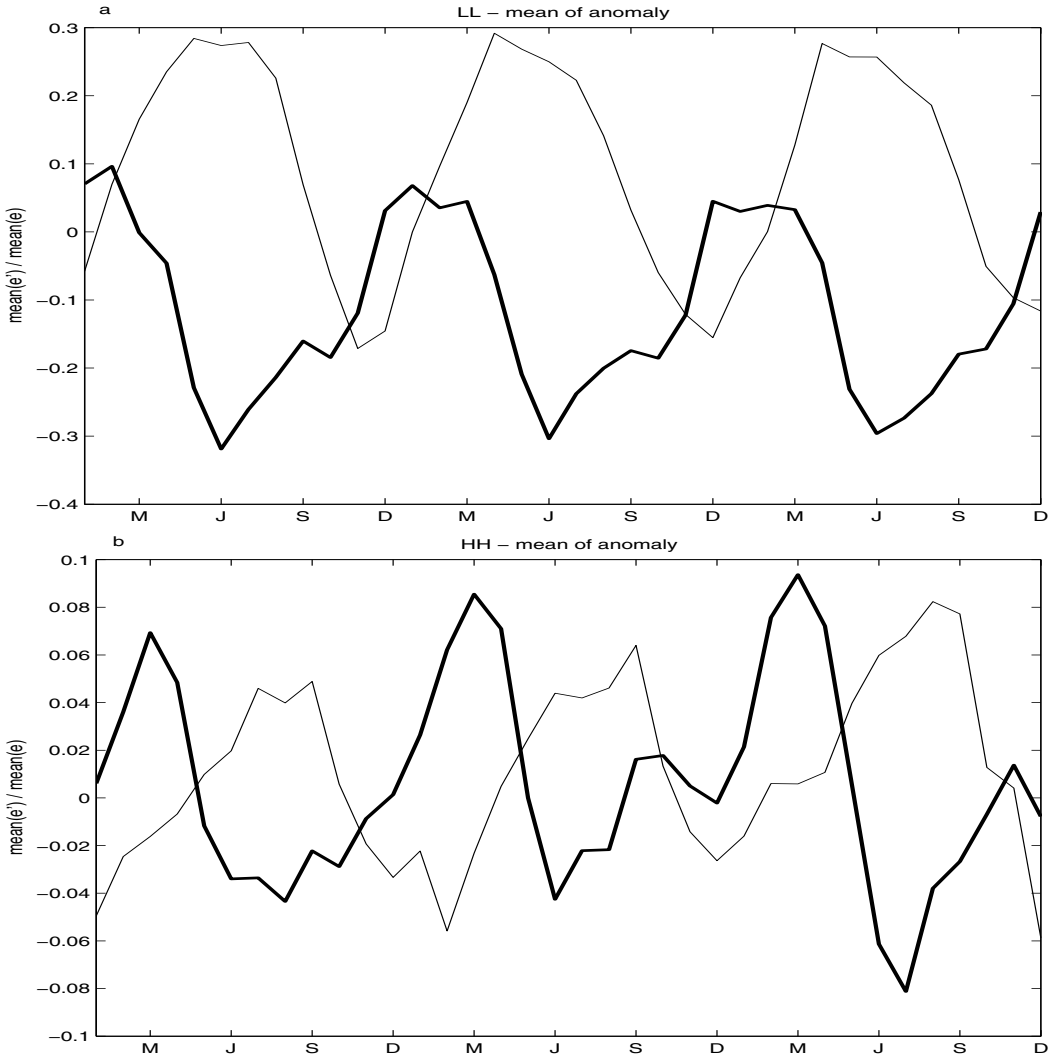

Figure 8.22: Monthly anomaly statistics for AIRS. The LL gradient category is shown in panel a and the HH gradient category in panel b. The thin lines show the Northern Hemisphere values and the thick lines show the Southern Hemisphere values. The vertical axis gives the mean of the entropy anomaly ($\overline{e'}$), with the final value divided by the mean entropy value ($\overline{e}$) for the gradient category. Time series is from January 2003 to December 2005.

gory shown in Figure 8.21b is isentropic transport, as this is a shallow process. *Dethof et al.* [2000] show that global isentropic transport is a two way process with a net direction of stratosphere to troposphere transport (STT). On the 360 K isentropic surface, isentropic transport is largest in the summer and in the Northern Hemisphere. This transport may contribute to the hemispheric increase in entropy that is observed during the summer months. *Ovarlez et al.* [1999] suggest that the summer increase in background water vapour is a result of isentropic transport. This would account for the increase in ozone and water vapour during the summer months and hence the larger entropy. The range in the LL category entropy anomaly for the Northern Hemisphere is larger than in the Southern, this would follow from the results of *Dethof et al.* [2000] where isentropic transport is indicated to be weaker in the Southern Hemisphere.

8.4 Occurrence of Gradient Categories and Relationship to the Jet Stream

Different transport and mixing processes are likely to have a geographic preference depending on how the transport mechanisms relate to other atmospheric and geographic processes, such as jet streams, storm tracks, convection and mountain ranges. The number of times an entropy value occurs in each gradient category is indicated as a yearly average in Figure 8.23. These occurrence diagrams can be used to identify hot spots for each category. It is clearly evident in this figure that different categories have different geographic preferences. The Southern Hemisphere occurrence patterns tend to have a zonal structure, whereas the structure in the Northern Hemisphere is more influenced by orography. This suggests that some types of mixing are highly dependant on the underlying terrain.

Several of the categories, namely MH, HM and HH, coincide with regions of higher mean entropy and the jet stream location as is shown in Figure 3.3. These three categories represent strong mixing occurring over a large vertical range or large gradients of mixing and are likely to be associated with tropopause folds (see Figure 8.8j) and other strong mixing processes. These three categories have a single mode for the distribution of entropy (see Figure 8.21b for HH, the other two are not shown), which indicates that the number of processes is small if not singular (perhaps just strong deep tropopause folds). In particular the Northern Hemisphere high occurrence regions in the HH category coincide with the regions of high flux in Figures 8.16a and 8.20. The band of high entropy in the Southern

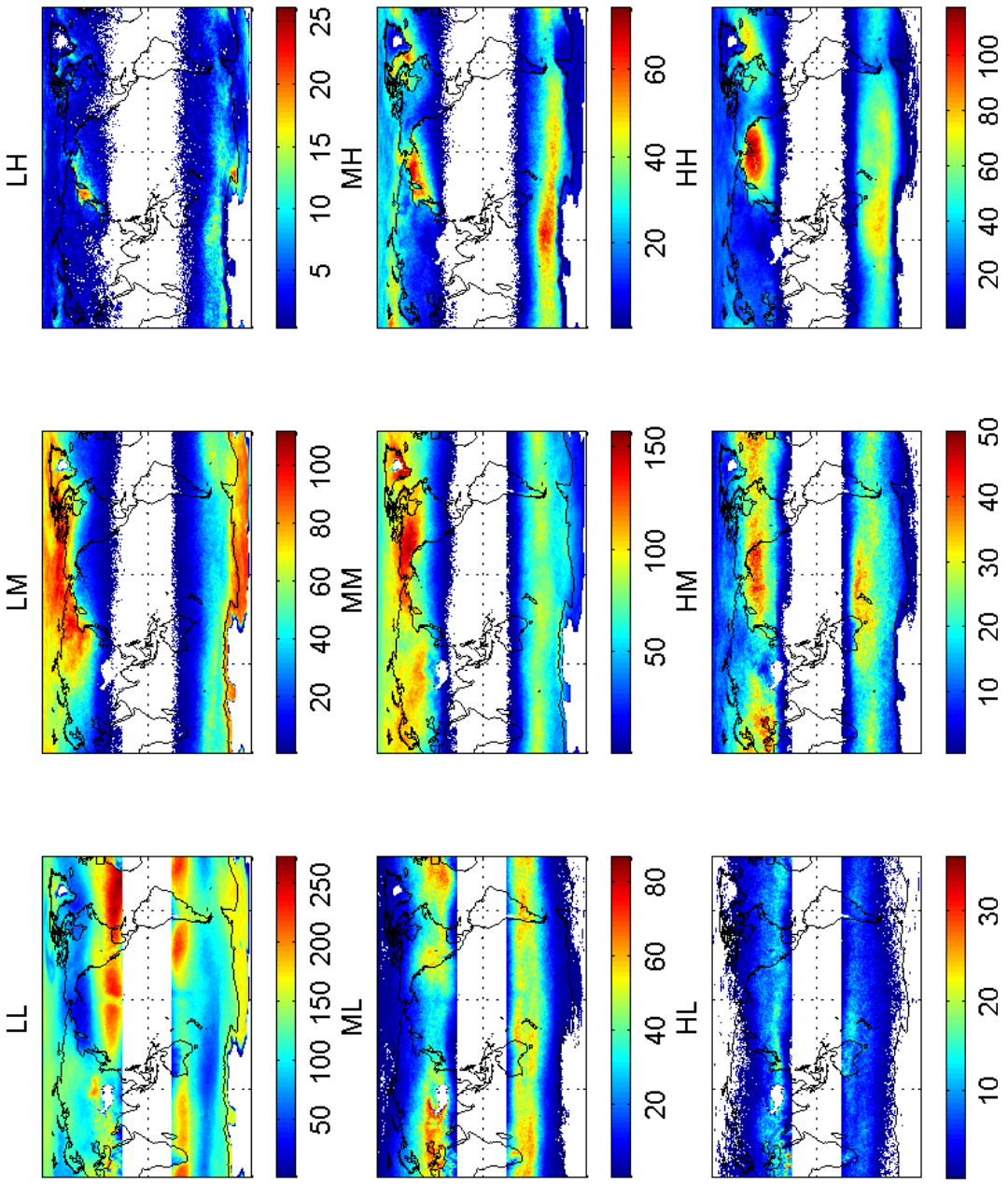

Figure 8.23: Mean number of days for a given global grid point to be in each of the nine gradient categories for AIRS from 2003 to 2005. Colour scale gives the number of days. Note that the colour scales are different for each subplot.

Hemisphere between about 40-60° is evident in several categories and is likely to be related to the jet stream at approximately the same latitude range.

Some of the occurrence patterns also display reversed patterns, with the clearest of these being between the ML and LM category. These categories have the opposite gradient in tracer space to one another and have very different distributions in tracer space. ML tends to be closer to the equator, whereas LM is along the equator, this signifies that these categories probably represent different transport processes.

The jet stream region in the midlatitudes looks to be associated with a number of the occurrence patterns, with some categories more strongly linked. The jet stream region can be viewed as also creating a barrier between the different category types. This leads to the question of whether some gradient categories are more strongly related to the jet stream location than others. By finding the distance and direction of the entropy values in each category with respect to the jet stream, we should be able to examine the relationship between the gradient categories and the jet stream. Variations in the distance between categories provides some evidence that different STE processes may be highlighted in different categories. It may also be different aspects of the same process.

The distances in kilometers, between the entropy values in each gradient category and the nearest jet stream are calculated using the winds from NNR. In the case that an entropy value is located between two jet streams, the distance and direction to the closest jet stream is calculated. The jet stream is defined as a region where the horizontal wind speed is greater than $30\,\mathrm{ms}^{-1}$ on the 200 hPa surface (see Section 3.3, *Ding* [2006]; *Yang et al.* [2002] and Californian Regional Weather server[‡]).

An overall distribution of the distances from the jet stream for 2004 is shown in Figure 8.24, which will be referred to as the total distribution, where 2004 is a representative year. Application of the BO3 and BH2O gradient categories to the entropy values divides the data into nine categories, with a percentage of the total data in each category. The percentage in each gradient category for 2004 by hemisphere is shown in Tables 8.3 and 8.4. It should be noted that the Northern Hemisphere has a larger percentage of the valid points in the higher gradient categories than the Southern Hemisphere. This is expected, based on our interpretation as previous figures (eg. *Olsen et al.* [2004]) have shown that

[‡]http://squall.sfsu.edu/crws/jetstream.html

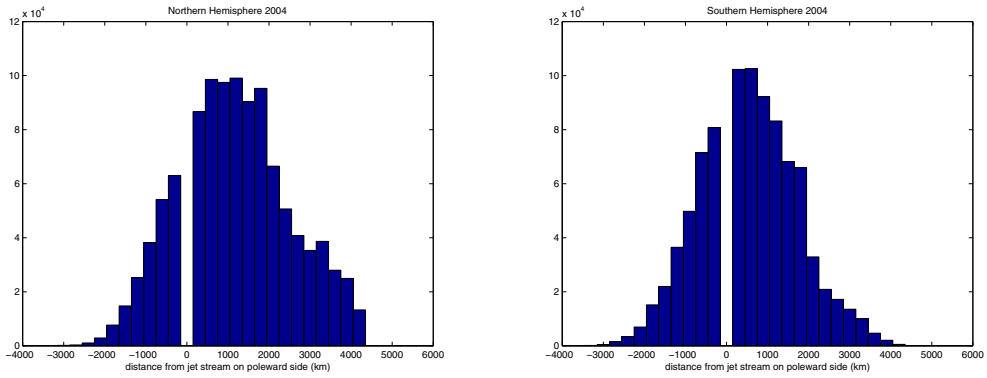

Figure 8.24: The distribution of distances from the jet stream for 2004. Northern Hemisphere is shown on the left, and the Southern Hemisphere on the right. Positive values are on the poleward side of the jet and negative values are on the equatorward side of the jet.

the mixing occurs over a larger vertical range and is stronger in the Northern Hemisphere.

If there is no relationship between the distance from the jet stream and the gradient category then we would expect the distributions to be the same in all categories. This expected distribution, as a percentage of the total distribution in each category, is given by:

$$\text{expected distribution} = \%\text{ of data in category} \times \text{total distribution} \tag{8.2}$$

We can then compare the actual distance distributions to the expected distribution for each category.

The distributions for the Northern Hemisphere are shown in Figure 8.25 and the Southern Hemisphere in Figure 8.26. The distributions are in 300 km bins, with the white central region a result of the binning method. Similar structures are observed between hemispheres and across different years. The red shading in Figures 8.25 and 8.26 shows where occurrences of a distance are higher than predicted, assuming evenly distributed data in each category. Likewise the blue shading shows where the occurrences of a distance is observed less than predicted. The categories associated with higher BO3 and BH2O values, namely MM, MH, HM and HH, show higher occurrences than expected near the jet stream and on the poleward side of the jet stream. This could mean that these categories are associated with tropopause folds in the region of the jet stream which will be preferentially observed in that region as discussed previously in Section 8.1.1,

Table 8.3: Percentage of valid entropy points in each gradient category for the Northern Hemisphere for 2004 from AIRS.

Gradient category	Number of points	Percentage (%)
LL	369259	34.4
LM	137340	12.8
LH	7314	0.7
ML	78889	7.4
MM	240265	22.4
MH	67346	6.3
HL	10783	1.0
HM	65363	6.1
HH	96343	9.0
Total	1072902	

Table 8.4: Percentage of valid entropy points in each gradient category for the Southern Hemisphere for 2004 from AIRS.

Gradient category	Number of points	Percentage (%)	Difference from NH (%)
LL	364419	40.3	5.9
LM	125872	13.9	1.1
LH	9876	1.1	0.4
ML	73126	8.1	0.7
MM	161881	17.9	-4.5
MH	50895	5.6	-0.7
HL	6560	0.7	-0.3
HM	40173	4.4	-1.7
HH	71319	7.9	-1.1
Total	904121		

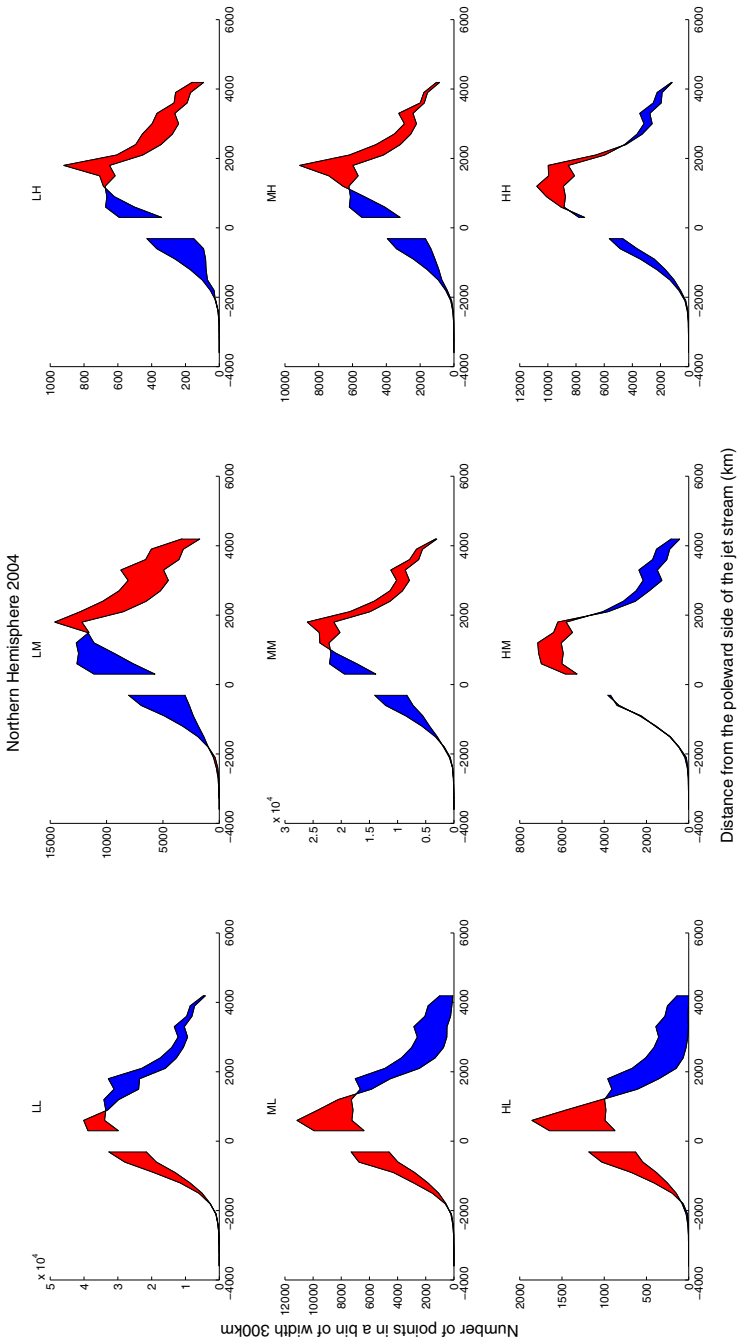

Figure 8.25: Distance of entropy values from the jet stream in each gradient category, with positive values towards the pole and negative values towards the equator. The red shading indicates where there are more values than expected, and the blue shading for less values than expected. For the Northern Hemisphere for 2004.

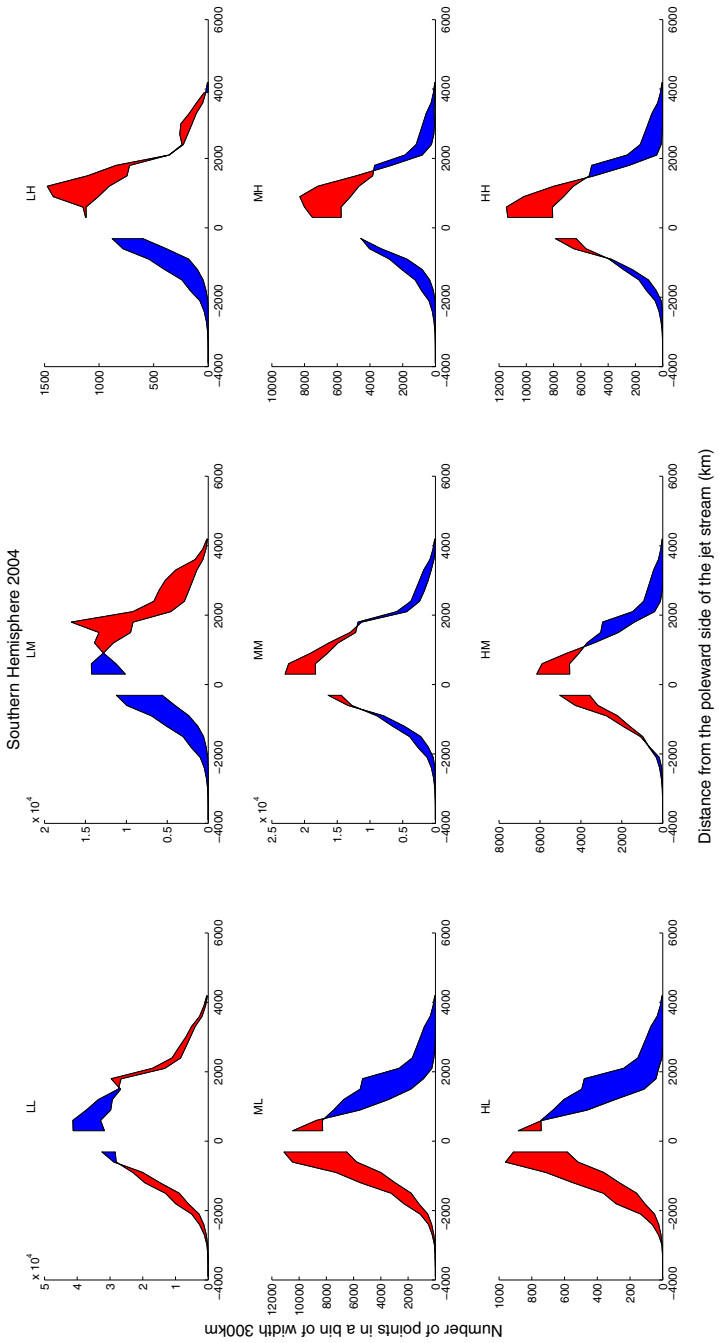

Figure 8.26: Distance of entropy values from the jet stream in each gradient category, with positive values towards the pole and negative values towards the equator. The red shading indicates where there are more values than expected, and the blue shading for less values than expected. For the Southern Hemisphere for 2004.

Figure 8.3 and *Pan et al.* [2007b]. In comparison, the LL category tends to have lower than expected occurrences near the jet stream; this is particulary clear in the Southern Hemisphere.

Olsen et al. [2004] show that at midlatitudes the net transport is STT, and in the tropics the net transport is TST, with the changeover region occurring roughly at the subtropical jet. This suggests that the location either poleward or equatorward of the jet stream may help describe the direction of vertical movement. *Holton et al.* [1995] state that mixing processes involving more stratospheric air are likely to be drier. Therefore, based on these two studies, we expect that STT processes will be drier and TST process will be more moist.

It is also suggested by *Dessler et al.* [1995] that the path by which air is transported across the tropopause can have an impact on the water content of the air, primarily as a result of the tropospheric temperature differences between the tropics and midlatitudes. Air parcels which have encountered the colder temperatures of the tropical tropopause will have a lower water vapour content. In comparison, those air parcels which have been transported via the warmer midlatitude tropopause have higher water vapour contents.

It has been discussed previously and highlighted in Figures 7.11 and 7.12 that the gradient categories provide some information on the origin of the air being mixed. Following from the previous paragraph, this would suggest that gradient categories with BH2O less than BO3 could be associated with STT, as they are mixing processes with lower water vapour levels. Likewise, where the BH2O is greater than BO3 may be associated with TST as they have higher water vapour levels.

Also worthy of note is the mirroring between the results of ML/HL and LM/LH, where the red and blue shadings are reversed. As the categories move downwards in Figures 8.25 and 8.26 in the vertical direction, this indicates the air is more moist at the transition boundary, or larger BH2O values (ie. HL has a larger BH2O value than ML). This mirroring is also observed in Figure 8.23.

Linking this information together with Figures 8.25 and 8.26 can lead to some conclusions with regards to the gradient categories and the direction of transport. The ML and HL categories have more values than expected on the equatorward side of the jet stream as indicated by the red shading. These gradient categories correspond to more tropospheric air (high BH2O) and less stratospheric air (low BO3). The combination of these factors suggests that the ML and HL categories

Table 8.5: Summary of the relationship between the gradient category and the direction of transport.

Gradient category	BH2O	BO3	Direction of transport	Distribution of data points (Fig 8.25 & 8.26)
LM	L	M	STT	poleward
LH	L	H	STT	poleward
ML	M	L	TST	equatorward
HL	H	L	TST	equatorward

correspond to TST. Likewise, the LM and LH categories have more values than expected on the poleward side of the jet stream, with more stratospheric air and less tropospheric air. This suggests that the LM and LH categories correspond to STT. A summary of these gradient categories and their potential relationship to transport are presented in Table 8.5.

8.5 Conclusion

Entropy, BO3 and BH2O have been shown to vary on a daily scale with some of the features moving from west to east over the course of several days. A case study using the aircraft data from *Pan et al.* [2007b] has shown that entropy increases in regions associated with tropopause folds and cutoff lows. The application of gradient categories also allows these regions to be highlighted, suggesting that the gradient categories may be related to different transport/mixing processes.

The location of the transition layer with respect to the tropopause was shown to provide information as to whether mixing was active or old. This was carried out using the Lauder and Boulder ozonesonde/hygrometers. When the tropopause is within the transition region, the entropy values are high, indicating active mixing. When the transition region is within the stratosphere, entropy values are low, indicating the signature of aged mixing.

The seasonal variations in entropy, BO3 and BH2O allow the long term patterns and regions of the most influence to be identified. The regions of high entropy tend to be associated with the regions of highest occurrence of the jet stream. Climatological case studies have shown that the gradient categories are likely to be representative of the vertical depth of mixing or the deviation from the origin in tracer space, while the entropy value representative of the strength of mixing.

The occurrence of gradient categories show a clear geographic locational preference. The gradient categories have been shown to be related to the direction of transport, whether stratosphere to troposphere or vice versa. This is shown through the relationship of the different categories to the jet stream. The locational preferences for the different gradient categories are potentially indicative of regions which have different transport direction preferences.

Chapter 9

Conclusion

As the occurrence of Stratosphere Troposphere exchange (STE) has been found to be fairly frequent [*James et al.*, 2003a,b; *Wernli and Bourqui*, 2002], it is therefore important to study STE as it has the potential to have a large impact on the atmosphere. It has been recognised that STE can effect the chemical balance of the atmosphere and it's effect on radiative forcing [*Levy et al.*, 1980]. STE can also have a large impact on the ozone depletion cycle, namely by transporting ozone destroying chemicals into and out of the stratosphere [*World Meteorological Organization*, 2003, 2007; *Butchart and Scaife*, 2001].

The aim of this study is to produce measures that can identify STE on a global scale with high spatial and temporal resolution. A number of previous studies have achieved this using model data, such as *Sprenger et al.* [2003] with ECMWF data and a Lagrangian trajectory model. Alternatively, there are studies which lack the spatial or temporal resolution, such as *Patmore and Toumi* [2006] or *Seo and Bowman* [2002], where the original resolution of the data has been reduced to provide sufficient information for the calculation method. Other studies may provide excellent spatial and temporal resolution but lack coverage, such as the aircraft studies by *Pan et al.* [2007b]. It is of particular interest to determine whether an observational data set can be used to study STE on a global scale while maintaining high spatial and temporal resolution. It is also of considerable interest to determine whether the results of this work are comparable to those obtained from model studies, or from very high resolution but low coverage studies, such as those obtained by aircraft. This will help to show that the methodology is valid.

In this thesis, two different methods are tested for the identification of STE. The first of these uses ozonesondes to identify tropopause folds. A tropopause identification algorithm based on *Van Haver et al.* [1996] was applied to Lauder

and Boulder ozonesonde data, in Chapter 4, to examine the utility of this algorithm. The algorithm examines the properties of layers in the ozonesonde profiles, looking for the signature of stratospheric air in the troposphere. The properties examined are ozone, humidity, stability and the relationship of the profile to the NCEP/NCAR reanalysis (NNR) winds. For a positive identification, there must be a layer of ozone rich, humidity poor air which is thermally stable within the troposphere. As the majority of the ozonesondes do not measure wind speed, an optional property related to the winds from NNR is also included. However, the final results are given both with and without this final property. In total there are nine properties or parameters that can be varied in the algorithm.

Using a series of default parameters for each of the properties required for a tropopause fold, the algorithm is applied to the ozonesonde records. Of the 61 ozonesonde records from Boulder, 36% have a tropopause fold without the wind condition, and 10% with the wind condition. Maximum occurrence was observed in spring. For Lauder, there are 1098 ozonesonde records, with 9.6% having a tropopause fold without the wind condition and 2.7% with the wind condition. The maximum occurrence for Lauder was during summer. The time of the maximum occurrence of tropopause folds for both locations coincides with the period of the year when there is the largest variation in tropopause height in the climatologies. These periods for maximum tropopause fold occurrence are also in agreement with the literature (eg. *Van Haver et al.* [1996] and *Wang et al.* [2006]).

However, sensitivity testing of the parameter values used in the algorithm shows that the values of some parameters have a large effect on the number of tropopause folds identified, while others have only a small effect. For the algorithm to be most useful, there needs to be a set of parameters that are "correct". This requires a comparison of the tropopause folds to some additional data set to confirm the existence of a fold.

Using NNR temperature data, cross sections of the stability and tropopause structure for the surrounding regions of positively identified tropopause folds are investigated. While some of these cross sections show a clear enhancement in stability along with changes in the dynamic and thermal tropopause height, there are also an equal number of cases where no difference was observed. Furthermore it is not possible to separate non-tropopause fold days from those with a positive identification.

In general, this method of tropopause fold identification using ozonesondes seems to have too many variable parameters to be certain of the results and it is difficult to decide/confirm which parameters are correct. Additionally, ozonesonde data is spatially and temporally sparse. Ideally, we want a method that is robust to parameter selection and has a greater spatial and temporal coverage.

The second method and the focus of this study utilises the idea of a transition layer between the troposphere and stratosphere. The troposphere and stratosphere have different physical and chemical properties, by which exchange between the two layers can be traced. The transition layer has characteristics of both layers, and the form of these changes in composition could potentially be used to develop measures to determine the amount and type of mixing between the regions. In this study, water vapour is used as a tropospheric tracer and ozone as a stratospheric tracer. The relationship between these two tracers in tracer space is used to develop measures of STE.

This methodology is applied to data from the Atmospheric Infrared Sounder (AIRS) instrument on NASA's EOS Aqua which is a potentially excellent data set for the study of stratosphere troposphere exchange. This data set has twice daily global coverage and a high spatial resolution. Through a retrieval process, the infrared measurements from the instrument are processed into a number of products, including ozone and water vapour profiles.

To be able to use this data set it is necessary to confirm that the ozone data from AIRS is sufficiently accurate in the upper troposphere/lower stratosphere (UTLS) region for use in STE studies. The water vapour product has been previously validated by *Gettelman et al.* [2004] and *Hagan et al.* [2004]. In Chapter 5, the ozonesonde observations from Lauder and Boulder are used to examine the quality of the AIRS v4 vertical ozone profile product in the UTLS. At lower altitudes ($\sim$700-200 hPa pressure range), AIRS ozone mixing ratios are larger than those from ozonesonde measurements, and at higher altitudes ($\sim$100-30 hPa pressure range), AIRS ozone mixing ratios are smaller. Compared to the ozonesondes, AIRS retrieval results at Lauder have a median bias of 80% in the region 700-200 hPa, and 0 to -20% in the region 100-30 hPa. For Boulder these values are 40% and 0 to 5%, respectively. Using a tropopause adjusted vertical coordinate system, Lauder has median biases of +90 to +120% in the troposphere and 0 to +25% in the stratosphere whereas Boulder shows median biases of +45 to +70% in the troposphere and 0 to +35% in the stratosphere.

Despite the bias, AIRS retrieval in the UTLS region shows a statistically significant positive correlation with the ozonesonde data, indicating that although the absolute values have a large uncertainty, the retrieval captures the variability of ozone in the UTLS region. Hence AIRS ozone is suitable for studies where relative abundance of ozone is important rather than the absolute ozone mixing ratio. Examinations of the training data set used in the AIRS retrieval show that the retrieval biases are likely influenced by the deficiency of the training data to represent the true ozone distribution during the regression step of the retrieval. Furthermore the physical retrieval adds little additional information to the final result.

Following the confirmation of the validity of the AIRS data to at least first order; a data driven method for identifying mixing is developed based on the entropy methodology detailed in *Patmore and Toumi* [2006]. Chapter 6 describes the development of the entropy calculation to the AIRS and ozonesonde/hygrometer data sets. The entropy measure is based on the distribution of the data points in tracer space, with different regions in tracer space having different weightings corresponding to different mixing amounts. Entropy is a measure of the strength of mixing. An unmixed tracer space would have an entropy of zero. As mixing increases, the profile deviates from the zero state.

There are a number of parameters to be selected for the entropy calculation. The transition window must be focused on the regions of interest, that is the transition layer, and the region must be well scaled. This involves removing any data points that represent purely tropospheric or stratospheric air. This is achieved by the selection of branches, where a linear fit is applied to all data points with mixing ratios less than a fixed limit. This limit is adjusted depending on the chemical and the measurement instrument. The transition window is focused and well scaled by removing any data points outside of the range of interest, where only ozone mixing ratios of less than 0.56 ppm, and water vapour mixing ratios of less than 215 ppm, are retained. These values are determined from statistical analysis. The selection of the angles in the transition region for the application of the weightings is also important. These angles must be carefully considered as we wish to highlight differences in the mixed region. This is obtained by setting small edge sectors and larger, evenly spaced sectors in the mixed region.

The parameters used in the entropy algorithm are varied to test how they effect the resultant entropy value. All of the parameters are found to be robust, that is, variations in the values selected are found to have only a small impact on the

resultant entropy. This is a highly desirable quality as the exact value used in the calculation is unimportant, as long as the value used is appropriate.

The nature of the input data must also be taken into consideration. The entropy calculation is a statistical method and therefore it is essential that there is sufficient data available. This can be achieved in two different ways, either several profiles in the same region can be gathered together, or a single profile can be interpolated. *Patmore and Toumi* [2006] gather multiple profiles together for their entropy values, however, this results in entropy values with low spatial resolution and with information about the time of measurement removed. The alternative interpolation produces entropy values that retain their spatial resolution and temporal information. The application of these two different methods to AIRS data produced similar entropy patterns. Therefore, the vertical interpolation method is chosen in order to retain resolution.

To ensure that the entropy values utilised are sensible, a set of tests were performed to identify quality control techniques. Through the application of noise both to a mean profile and to a day of AIRS data, uncertainties on the entropy data were obtained. Any entropy values less than $20\,\frac{s}{k_B}$ were determined not to be significantly different from zero. Hence these values were removed from the analysis. In addition, it was found that any values where the thickness of the transition layer was more than 20 times greater than the entropy value, were a result of computational and selection errors in the entropy calculation. These values are also removed from the data set.

The ozone and water vapour mixing ratios at the edges of the transition layer are identified by BO3 and BH2O respectively, as described in Chapter 7. These values provide a metric of the gradient of mixing. BO3 and BH2O can be divided into gradient categories based on the mean and standard deviation of BO3 and BH2O, separated by hemisphere and as a function of the time of year. These gradient categories allow the entropy fields to be separated into nine categories which are shown to be useful in separating mixing processes.

The combined use of entropy, BO3 and BH2O provides more information about tracer space than a single measure can provide. These measures allow the mixing line to be described along with the distribution within tracer space. The application of these measures to the data sets is detailed in Chapter 8, with the key findings outlined in the following paragraphs.

There is a strong positive relationship between high entropy, high BO3 and high

BH2O. This is expected, due to the nature of the entropy calculation. However, the relationship is not perfectly linear and there is some spread of values which means that the multiple measures provide more information of the form of the curve in tracer space than the entropy measure alone.

Regions of entropy of similar values, forming coherent structures, are shown in Section 8.1 to vary on a daily scale. Some of the high entropy structures can be observed to move eastwards, in the direction of synoptic systems, over several days. Others are observed to be stationary. For example, for entropy values in the HH gradient category, the structures seem to follow the jet stream structure, whether moving or stationary.

To examine the ability of the measures to identify STE, we compared the results with previous high resolution studies. *Pan et al.* [2007b] studied STE over North America using aircraft mounted instruments. These flights identified a tropopause fold region, a cutoff low (COL) and a region of low mixing. A comparison between this study and the entropy and gradient categories derived from AIRS observations for the same period is given in Section 8.1.1. For the tropopause fold region and the COL, the entropy values were found to be high, with the application of the gradient categories clearly highlighting these features. In comparison, the region of low mixing was found to have low entropy values. The ability of this method using AIRS data to select out equivalent features to a high resolution aircraft study is very significant. It shows the potential capability of this method to study STE on a global scale, with equivalent results to a more detailed study.

Sprenger et al. [2003] studied the mass flux across the tropopause and the occurrence of tropopause folds using ECMWF data and a Lagrangian model. In Section 8.2.1.1, a comparison between this study and climatological entropy fields has shown several strong relationships. There is a linkage between high entropy, the HH gradient category, deep tropopause folds and large stratosphere to troposphere transport (STT) mass fluxes, off the east coast of Asia and the north east coast of North America during DJF. This indicates and confirms that deep tropopause folds can cause strong vertical mixing which seems to be observable by the entropy methodology. In comparison, over west Asia and the Middle East during JJA, a region of high entropy in the LL category corresponds to shallow tropopause folds and a large mass flux in both STT and troposphere to stratosphere transport (TST). This is a region of strong shallow mixing. This comparison confirms that entropy and the gradient categories may be related to the vertical depth and mass flux of mixing.

Analysis of the climatological mean entropy from AIRS, shows a strong positive relationship between high entropy values and regions of high occurrence of the jet stream. The high entropy values tend to be located poleward and slightly west of the high occurrence positions of the jet stream. On examination, the different gradient categories are found to have different geographic preferences relative to the jet stream.

Furthering this investigation, in Section 8.4 the distance and direction of entropy values from the jet stream were divided up into the gradient categories to allow a comparison between the jet stream location and gradient of mixing. The key results from this comparison are shown in Figures 8.25 and 8.26. The MM, MH, HM and HH gradient categories are found to have more values close to and poleward of the jet stream than the expected distribution predicts. This is suggestive that these categories are likely to be strongly related to STE processes associated with the jet stream [*Tsutsumi et al.*, 1998]. This suggests that these categories are probably associated with tropopause folds. In comparison, the LL gradient category tended to be further from the jet. This category is likely to be associated with multiple small scale processes due to multiple peaks in the mean entropy shown in Figure 8.21. The seasonal cycle in entropy anomalies for the LL gradient category coincides with those for isentropic transport in *Dethof et al.* [2000].

The ML/HL and LM/LH categories have reversed patterns in regards to their occurrence with relation to the jet. The ML and HL categories tend to occur equatorward of the jet stream. *Olsen et al.* [2004] showed that the jet stream region tended to be the changeover point for net transport from TST in the tropics to STT at midlatitudes. It has also been detailed by *Holton et al.* [1995], that processes involving more stratospheric air, such as with STT, will be drier. From this it follows that gradient categories with higher BH2O values (eg. ML and HL) located on the equatorward side of the jet stream are likely to be associated with TST. In comparison, those with lower BH2O values (eg. LM and LH) located on the poleward side of the jet stream are likely to be associated with STT.

We conclude that the gradient categories have different locational preferences for occurrence and are likely to be associated with different directions and types of mixing. The occurrence of the different categories gives an indication of which processes and transport types occur in different locations on the globe. Initial analysis thus suggests that entropy and the use of gradient categories is useful for studying STE on a global scale. The key comparison is with the results of

Pan et al. [2007b], where high entropy has been shown to coincide with regions of increased vertical mixing. Ideally, further studies of this nature need to be carried out to further confirm this relationship. However, suitable data sets of this nature are currently unavailable.

This thesis has developed several measures based on low vertical resolution satellite data to describe mixing and transport in the transition region between the troposphere and stratosphere. Entropy describes the strength of the mixing whereas the gradient categories, from BO3 and BH2O, describe the deviation from the origin in tracer space and the direction of the transport. It is of considerable interest that these results have been obtained from a data set of this nature with regards to it's resolution and spatial coverage.

9.1 Further Work

There are a number of further investigations that can be carried out using the entropy and gradient category measures developed in this thesis. These involve the confirmation of the mechanisms associated with the gradient categories. Note that some of the categories have been tentatively assigned to processes, mainly those with a link to the location of the jet stream. More work would be possible with improved high resolution study inter-comparisons. However, the lack of observations within the AIRS observational period and the scope of this work means that this investigation is outside the possibilities of the current study.

The persistence of entropy patterns in the different gradient categories should be examined to show how mixing and deviation of the mixing line in tracer space from the origin, vary with time. This would show whether some patterns persist in some categories and whether features can be tracked between categories. This would also provide an analysis of whether STE processes are strengthening or weakening.

The AIRS data set used in this study is version 4. During the course of this thesis an updated version of the AIRS data has been released. *Divakarla et al.* [2008] have compared the version 4 and 5 ozone data with ozonesondes and have found that the version 5 algorithm improves the retrieval in the lower troposphere and the tropics. Note that this is mainly outside of our region of study. The application of this methodology to the AIRS version 5 data is not expected to result in a large difference in the outcome of the entropy studies as the AIRS data

is sufficiently accurate in the UTLS region, along with having a correct tendency, which is important for the method used for calculating entropy [*Monahan et al.*, 2007].

More case study work is required to confirm the type and direction of transport associated with the different gradient categories. This may require examination of aircraft data or other high resolution data sets.

Entropy, BO3 and BH2O methods could be applied to other data sets, preferably with higher vertical resolution while still having similar (or better) horizontal and temporal resolution to that of AIRS.

Currently the jet stream location is based on a single pressure level with a threshold value applied. There may be less scatter or variation in the values if a three dimensional approach to locating the jet stream was applied. One possible method is detailed in *Archer and Caldeira* [2008] where, using the NNR data, the jet stream is located using the mass weighted average between 400 and 100 hPa.

Appendix A

Abbreviations

AIRS Atmospheric Remote Sounder

AMSU-A Advanced Microwave Sounding Unit-A

BH2O Water vapour mixing ratio at the lower boundary of the transition layer

BO3 Ozone mixing ratio at the upper boundary of the transition layer

CHF Cryogenic Frostpoint Hygrometer

cm^{-1} per centimeter

CMDL Climate Monitoring and Diagnostics Laboratory

COL Cut off low

CTM Chemistry and Transport Model

DJF December January February

EAJS East Asian Jet Stream

ECC Electrochemical concentration cell

ECMWF European Centre for Medium-Range Weather Forecasts

EN-SCI Environmental Science Corporation

EOS Earth Observing System

ERA-15 ECMWF 15 year reanalysis

ERA-40 ECMWF 40 year reanalysis

FNL Final Global data Assimilation System

GCM General Circulation Model

GFS Global Forecast System

GPSO3 Global Positioning System Ozone Sensor

H_2O Water

HALOE Halogen Occultation Experiment

HIAPER High performance Instrumental Airborne Platform for Environmental Research

HH High BH2O, High BO3 gradient category

HL High BH2O, Low BO3 gradient category

HM High BH2O, Medium BO3 gradient category

hPa hectopascal

JJA June July August

K Kelvin

KI Potassium Iodide

km kilometer

L2 level 2

L3 level 3

lat latitude

LED Light Emitting Diode

LH Low BH2O, High BO3 gradient category

LL Low BH2O, Low BO3 gradient category

LM Low BH2O, Medium BO3 gradient category

lon longitude

LS Lower Stratosphere

m mixing state

MAM March April May

MH Medium BH2O, High BO3 gradient category

ML Medium BH2O, Low BO3 gradient category

MLS Microwave Limb Sounder

MM Medium BH2O, Medium BO3 gradient category

MMD Mean Mixing Depth

ms^{-1} metres per second

NASA National Aeronautics and Space Administration

NCAR National Center for Atmospheric Research

NCEP National Center for Environmental Prediction

NH Northern Hemisphere

NNR NCEP NCAR reanalysis

NOAA National Oceanic and Atmospheric Administration

NZ New Zealand

O$_3$ Ozone

OHP Observatorie de Haute Provence

ppb parts per billion. Equivalent to ppbv

ppbv parts per billion by volume. Equivalent to ppb

ppm parts per million. Equivalent to ppmv

ppmv parts per million by volume. Equivalent to ppm

PV Potential Vorticity

PVU Potential Vorticity Unit

r correlation coefficient

R range local maxima

RW Region Weighting

SBUV Solar Backscatter Ultraviolet

SH Southern Hemisphere

SON September October November

START Stratosphere Troposphere Analysis of Regional Transport

STE Stratosphere Troposphere Exchange

STT Stratosphere to Troposphere Transport

TOMS Total Ozone Mapping Spectrometer

TP Tropopause

TPF Tropopause Fold

TST Troposphere to Stratosphere Transport

UARS Upper Atmosphere Research Satellite

UKMO United Kingdom Meteorological Office

USA United States of America

UT Universal Time

UT Upper Troposphere

UTLS Upper Troposphere Lower Stratosphere

u-wind zonal wind

v4 version 4

v-wind meridional wind

WMO World Meteorological Organization

w.r.t. with respect to

Appendix B

AIRS and NNR Data Levels

B.1 AIRS Pressure Levels

L2 Data

28 Pressure Levels
1100 hPa, 1000 hPa, 925 hPa, 850 hPa, 700 hPa, 600 hPa, 500 hPa, 400 hPa, 300 hPa,
250 hPa, 200 hPa, 150 hPa, 100 hPa, 70 hPa, 50 hPa, 30 hPa, 20 hPa, 15 hPa,
10 hPa, 7 hPa, 5 hPa, 3 hPa, 2 hPa, 1.5 hPa, 1 hPa, .5 hPa, .200000003 hPa, .100000001 hPa

L3 Data

The level 3 files were created by A. Gettelman
1000 hPa, 925 hPa, 850 hPa, 700 hPa, 600 hPa, 500 hPa, 400 hPa, 300 hPa, 250 hPa,
200 hPa, 150 hPa, 100 hPa, 70 hPa, 50 hPa
Some files have additional data at 30 hPa, 20 hPa, 15 hPa, 10 hPa, 7 hPa, 5 hPa

B.2 NCEP/NCAR Reanalysis (NNR) Pressure and Potential Temperature Levels

17 Pressure Levels
1000 hPa, 925 hPa, 850 hPa, 700 hPa, 600 hPa, 500 hPa, 400 hPa, 300 hPa, 250 hPa,
200 hPa, 150 hPa, 100 hPa, 70 hPa, 50 hPa, 30 hPa, 20 hPa, 10 hPa.

11 Potential Temperature/Theta/Isentropic Levels
270 K, 280 K, 290 K, 300 K, 315 K, 330 K, 350 K, 400 K, 450 K, 550 K, 650 K.

Appendix C

Synthetic Mixing

Tracer space shows the relationship between two tracers. In this thesis, ozone is used as the stratospheric tracer and water vapour as the tropospheric tracer. These tracers have an overlapping region, where both tracers are present and varying at different rates.

The aim of this chapter is to show that entropy and tracer space are useful for identifying mixing between tracers. This chapter investigates how different vertical relationships between two tracers effects the resulting tracer space. A mixing scheme is then applied to the tracers to show how the mixing strength and mixing depth effect the resultant entropy values.

C.1 Synthetic Profiles

Profiles and the resultant tracer space are created using a tropospheric tracer, x, and a stratospheric tracer, y. Each of these tracers can have different background levels and can vary at different rates as the atmosphere changes from the troposphere to the stratosphere. The overlapping regions between the tracers can create a transition region, where there is some of each tracer present, rather than just one or the other. The different types of transition regions are indicated in Figure C.1. An abrupt transition from the troposphere to the stratosphere causes a zero order discontinuity and as a result has no transition region. As the overlapping region increases, the transition region also increases.

Several examples of different x and y tracer profiles and the resulting tracer space are shown in Figures C.2 through C.6. Each of these synthetic profiles demonstrates how different tracer profiles create different distributions in tracer space.

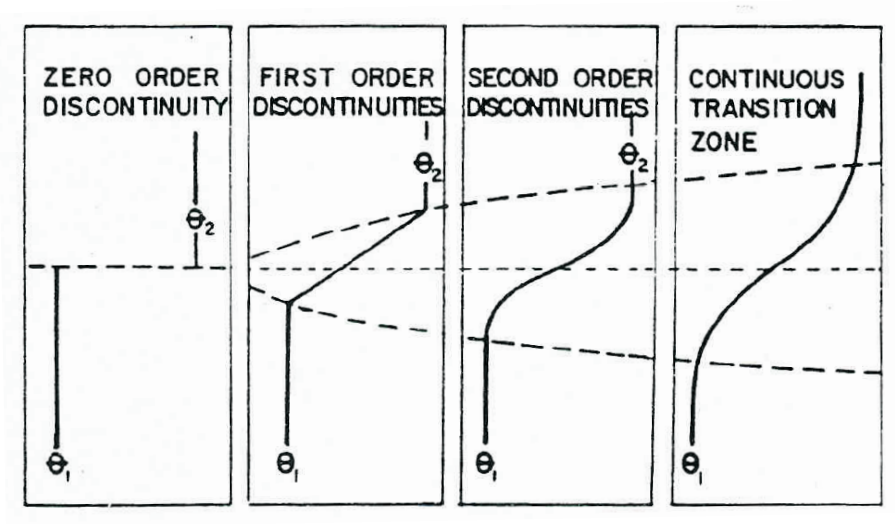

Figure C.1: Different forms of transition that are possible between the troposphere and stratosphere. Figure from *Hoinka* [1997].

Atmosphere 1 is displayed in Figure C.2. This profile displays an abrupt change in the tracers at 10 km, where the x tracer changes from 100 to 4, and the y tracer changes from 4 to 20. This abrupt change is a zero order discontinuity. Tracer space is represented by two points due to the nature of the profiles. As there is no transition region and the change between values is abrupt, there are no other data points visible in tracer space.

Atmosphere 2 is displayed in Figure C.3. This profile displays an abrupt change in the tracers at 10 km, however, rather than a change between two values, the profile begins to gradually change. This produces a profile that is a combination of the zero and first order discontinuities in Figure C.1. The tracers do vary gradually, however, there is no transition layer as they do not overlap. This is represented in tracer space as an 'L' shape. The 'L' shape is representative of there being no mixing between the two tracers. This profile will therefore have an entropy value of zero.

Atmospheres 3a and 3b in Figures C.4 and C.5 are similar to Atmosphere 2 except they have been shifted to create a transition region. Tracer x has been moved upwards 500 m and tracer y has been moved downwards by 500 m. This creates a transition layer that is 1 km thick. The transition region is a first order discontinuity from Figure C.1. Tracer space shows a clear transition region where the tracers gradually change with respect to one another, thereby creating a mixing line at an angle to the axes. The rate of the variation of each of the

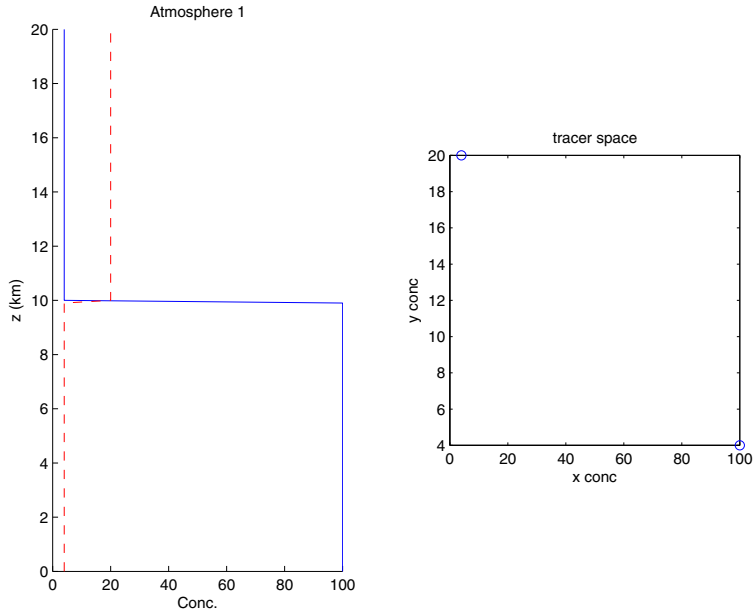

Figure C.2: Atmosphere 1. Tropospheric (blue solid line) and stratospheric (red dashed line) tracers have an abrupt discontinuity at 10 km with no transition region.

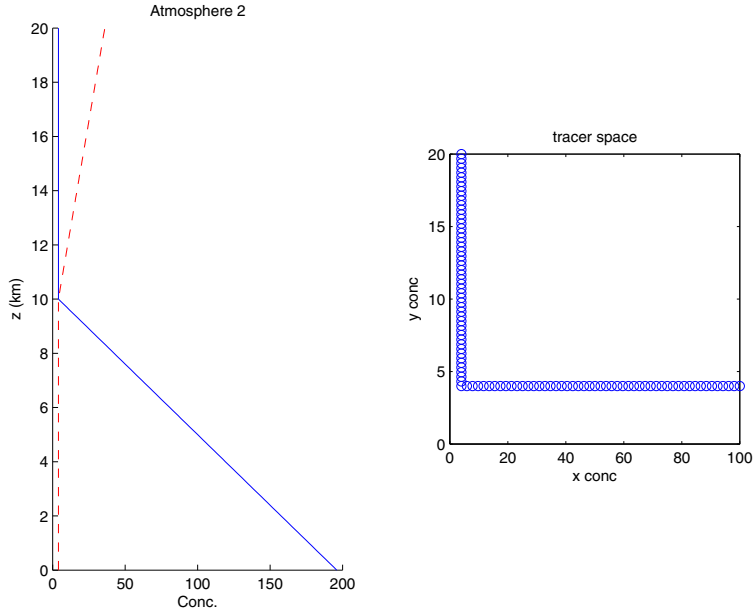

Figure C.3: Atmosphere 2. Tropospheric (blue solid line) and stratospheric (red dashed line) tracers vary gradually with height, with an abrupt change at 10 km.

tracers effects the slope of the transition region in tracer space. The mixing line for Atmosphere 3a is shallower than for 3b.

Atmosphere 4 is shown in Figure C.6 and is the yearly mean of the AIRS profiles from Lauder, defined by the region 44-46°S, 168-170°E. This gives a realistic sample profile and the relationship between the x and y tracers. The x and y tracers have a gradual variation and an overlap region. The transition region is best described as a continuous transition zone. The tracer space shows a transition region and a curved mixed region. Note that the profiles have been interpolated onto a number of fixed altitude levels as the original AIRS data is on only a few pressure levels.

C.2 Synthetic Mixing

A mixing scheme is developed to show the effect of mixing on tracer space and the resultant entropy values. The basic principle behind the mixing scheme is to utilise a number of layers within a set region centered on the tropopause and to exchange a percentage of the air between each layer. The initial transition region may be smaller in depth than the region over which the mixing scheme is applied.

There are six parameters in the mixing scheme. The region over which the mixing scheme is defined as z_T and is divided up into smaller layers of thickness L. z_T and L are both marked on Figure C.7. The thickness of the layers determines the scale of the mixing, where small layers represent small scale mixing and large layers represent large scale mixing.

The strength of the mixing is determined by s, which is the percentage of mixing per step. The final value of the mixing is a normal distribution about the tropopause, with the maximum strength at the tropopause and no mixing at the edges of the transition layer. The normal distribution is defined as P_u and P_d, for the upwards and downwards mixing, respectively. Two parameters for the strength of the mixing in different directions allows the mixing strength to be stronger in one direction than the other. An example of the scaling effect of P_u and P_d is given in Figure C.7. To adjust the strength of the different directions, the distributions can be adjusted with respect to one another. For example by reducing the peak of the distribution to 0.5 for P_d, while maintaining the distribution peak for P_u at 1, the strength of the downwards mixing is half that of the upwards mixing. The final parameter in the mixing scheme is the

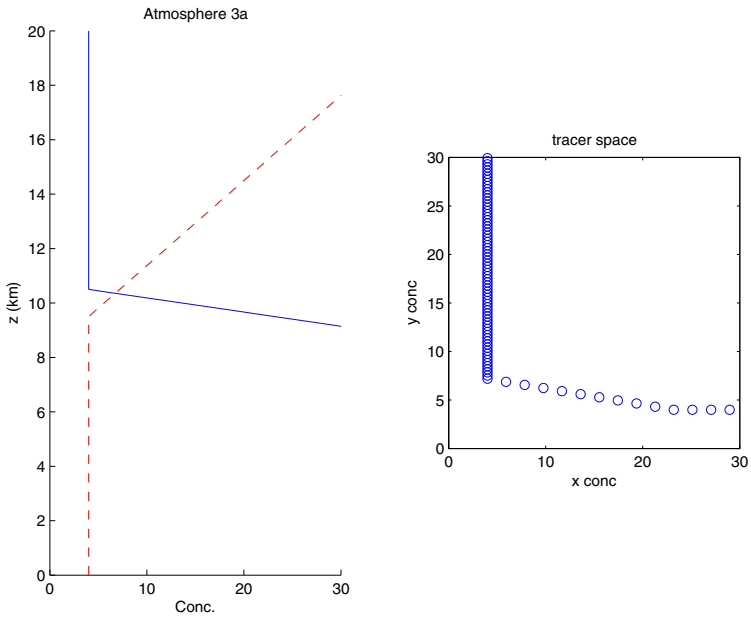

Figure C.4: Atmosphere 3a. Tropospheric (blue solid line) and stratospheric (red dashed line) tracers vary gradually with height. A transition layer of 1 km is present.

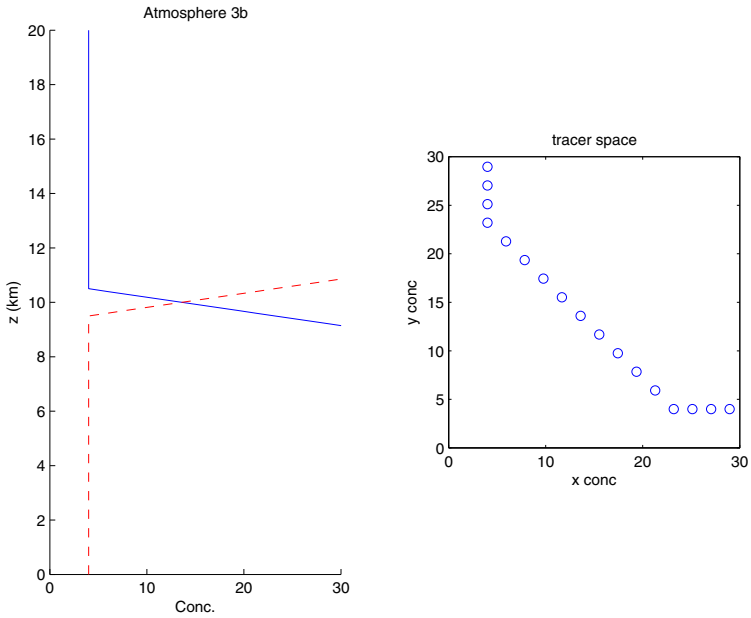

Figure C.5: Atmosphere 3b. Tropospheric (blue solid line) and stratospheric (red dashed line) tracers vary gradually with height. A transition layer of 1 km is present.

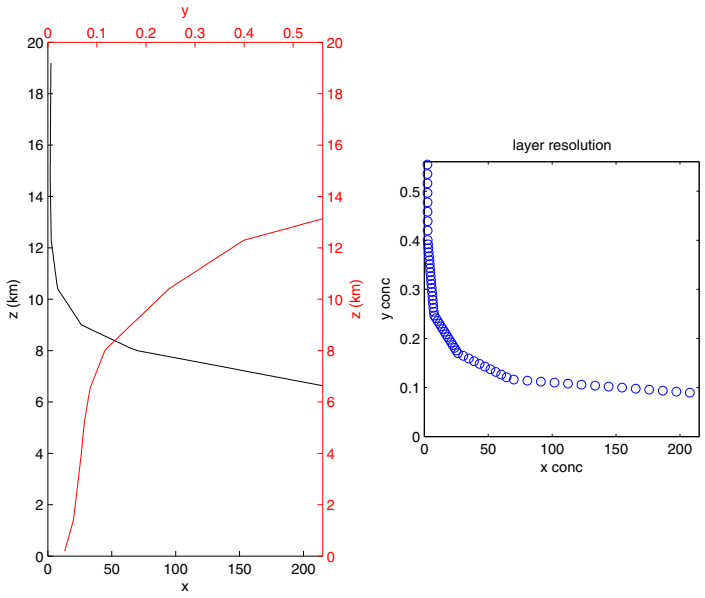

Figure C.6: Atmosphere 4. Tropospheric (black line) and stratospheric (red line) tracers are the yearly mean at Lauder of the AIRS water vapour and ozone, respectively.

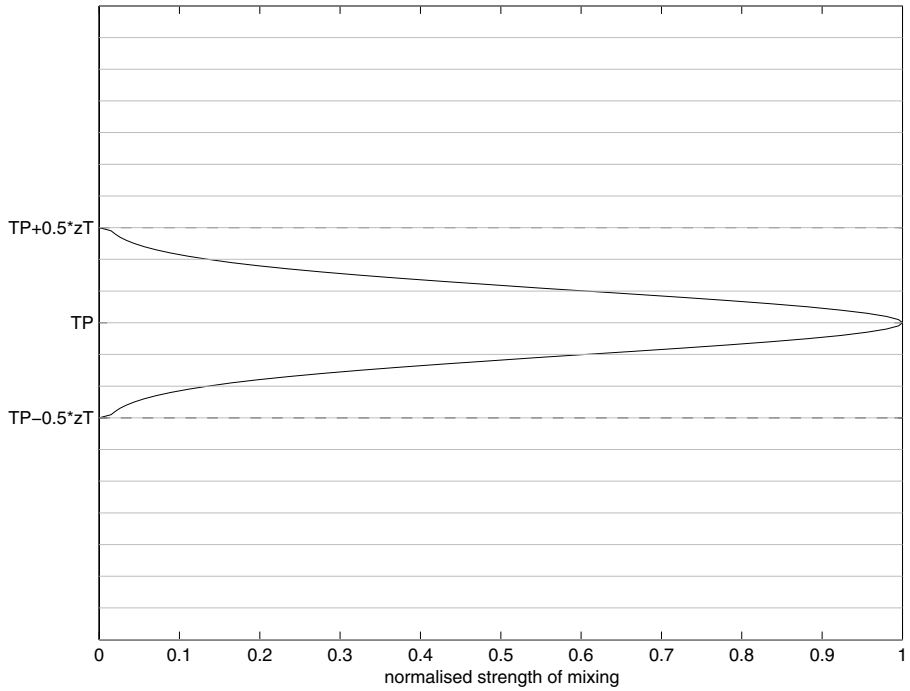

Figure C.7: The mixing region, z_T, is shown in relation to the tropopause (TP), and is indicated by the dashed horizontal lines. The layer thickness, L, is the spacing between the grey solid horizontal lines. The scaling factor for the strength of mixing is given by the distribution and can be assigned to P_u or P_d.

time step.

The mixing scheme equations are time and altitude dependant and are as follows:

$$x_{i,t} = \left(\frac{[(1 - s_i P_d)x_{i,t-1} + s_i P_d x_{i+1,t-1}] + [(1 - s_i P_u)x_{i,t-1} + s_i P_u x_{i-1,t-1}]}{2} \right) \tag{C.1}$$

$$y_{i,t} = \left(\frac{[(1 - s_i P_d)y_{i,t-1} + s_i P_d y_{i+1,t-1}] + [(1 - s_i P_u)y_{i,t-1} + s_i P_u y_{i-1,t-1}]}{2} \right) \tag{C.2}$$

where i is the altitude index, x is the tropospheric tracer and y is the stratospheric tracer for each time step t.

These mixing equations can then be applied to a set of initial profiles, such as Atmospheres 1 through 4 as described in the previous section. As the mixing scheme is applied to both the tropospheric and stratospheric tracer, the entropy value can be calculated as per Chapter 6, and should vary as the mixing scheme is applied.

C.3 Variation of Mixing Parameters

In general the use of different initial conditions only changes the amount of time the system takes to reach steady state. Theoretically applying a mixing scheme to an atmosphere for an infinitely long time should result in a perfectly mixed layer. This would produce an atmosphere structure that consisted of three layers; 100% tropospheric; 50% tropospheric 50% stratospheric; and 100% stratospheric. In tracer space this would be represented by all points in the layer converging to a single point. Over a finite period of time, mixing schemes tend to converge relatively quickly to a semi-steady state. Any large differences to entropy occur quickly, then entropy increases by only small amounts, hence a semi-steady state.

If the tracers do not have any overlap there are a few different results for applying mixing. If there is no overlap and the mixing occurs on a scale smaller than the gap between the profiles, then no increase in entropy is measured. If the mixing scale is larger than the gap between the tracers, then an increase in entropy eventual complete mixing will occur, but on a longer time scale.

Atmospheres 1 and 2 have the greatest potential for increasing their entropy with mixing as their initial entropy values are zero. This shows how entropy changes for a completely unmixed atmosphere. The converging to a single mixed

value in tracer space is dependent on the tracer concentrations at the edge of the mixing region and the amount of a tracer in the mixed region. Hence the distributions at infinite time will look different for Atmosphere 1 and Atmosphere 2. Atmospheres 3a and 3b will have a slower increase in entropy due to the initial state being partially mixed.

For the mixing scheme on Atmosphere 4, each parameter is varied while the others are held constant, the results are as follows. Increasing the strength of mixing increases the rate at which entropy increases. As the mixing region, Z_T, approaches the layer thickness, L, the time for the entropy to reach steady state (ie. As time increases the entropy value stays constant) decreases. Smaller layers result in a smaller rate of increase in entropy. Larger layers reach steady state more quickly. Uneven mixing, ie $P_u \neq P_d$ results in entropy decreasing with time. Uneven mixing causes tracers to be pushed in a single direction. These results would also hold true for application to Atmospheres 1, 2 and 3.

Figure C.8 shows the variation of entropy if both the mixing strength, s, and the mixing layer thickness, z_T, at several different time segments. As time increases, the entropy increases fastest for high mixing strengths and large mixing layer thickness. Of note is the speckled appearance of the entropy values which is likely a result of the discrete nature of entropy owing to the mixed region boundaries. Near the left and lower boundaries, some saturation of entropy has occurred, where the entropy has reached the limiting factor imposed by the mixing layer thickness. In relation to real world mixing, this indicates that large entropy values can be obtained by several different methods, either strong mixing and/or a large mixing region and/or mixing over a long period of time.

C.4 Conclusion

Different profiles of two tracers produce different resulting tracer spaces. The region of overlap between the profiles and the rate and which the profiles change are key to defining the distribution of points within tracer space.

The application of a mixing scheme to the tracers causes an increase in entropy due to mixing. Entropy can be seen to increase as a result of several different factors, such as the strength of the mixing, the depth over which mixing is applied and the time over which the mixing occurs.

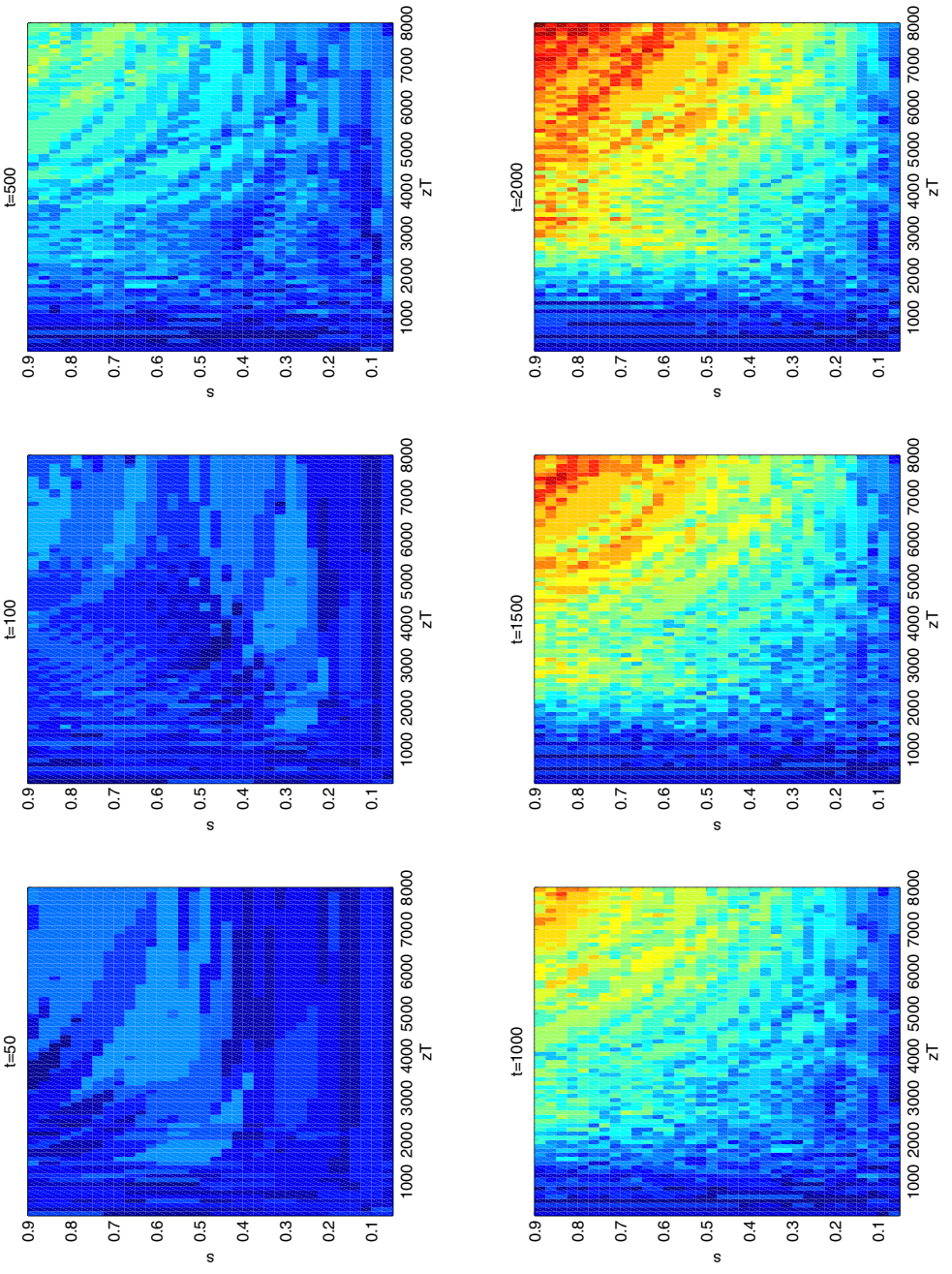

Figure C.8: Entropy values for Atmosphere 4 as time progresses for different values of the parameters for mixing depth, zT, and mixing strength, s. Redder values indicate a higher entropy value, exact numerical values are unimportant. The colour scale is the same for all subfigures. Mixing is even in both directions.

Appendix D

Entropy, BO3 and BH2O Fields

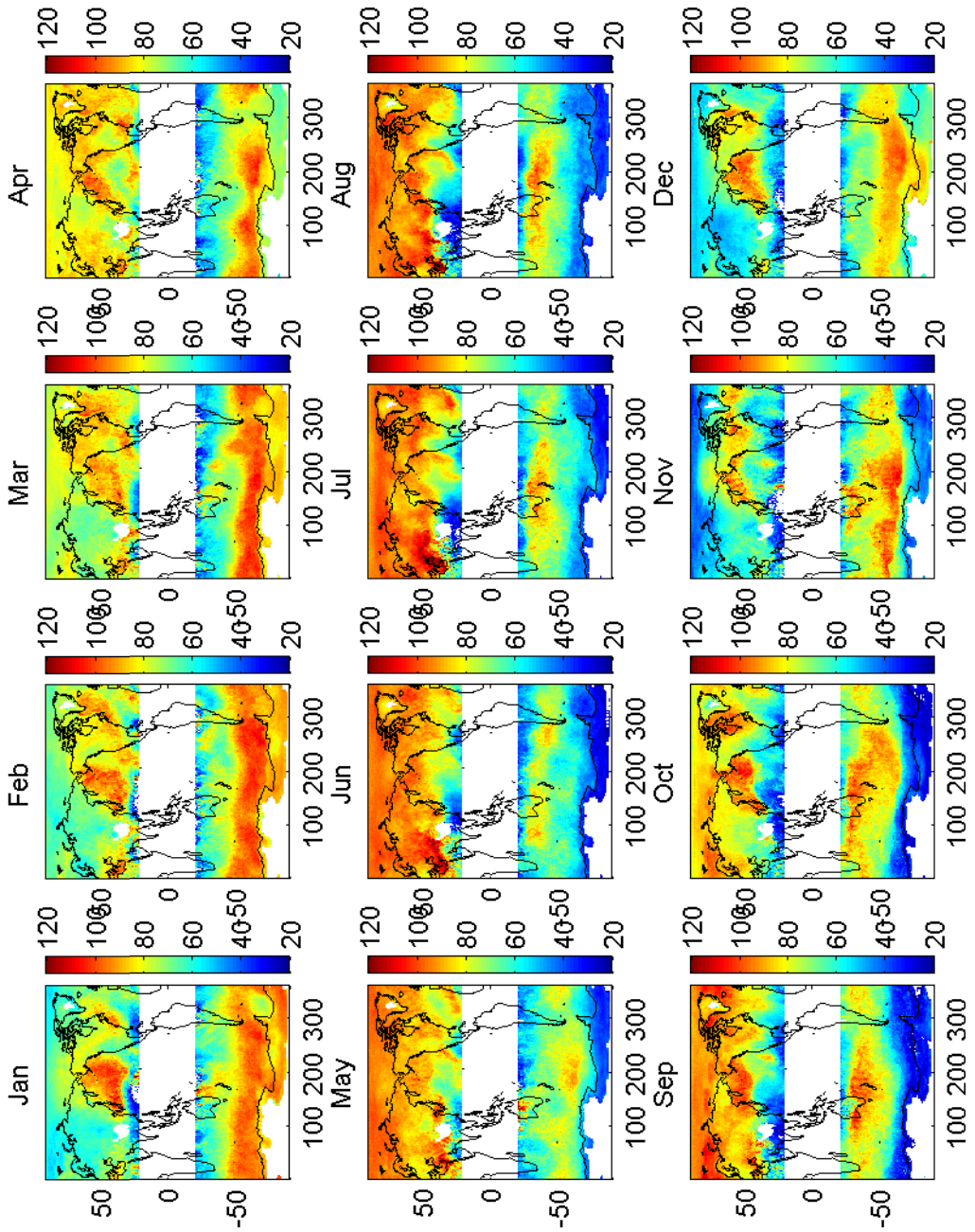

Figure D.1: AIRS mean monthly entropy for 2003. Colour scale is entropy $\frac{S}{k_B}$. Also have a 2004 version of this figure

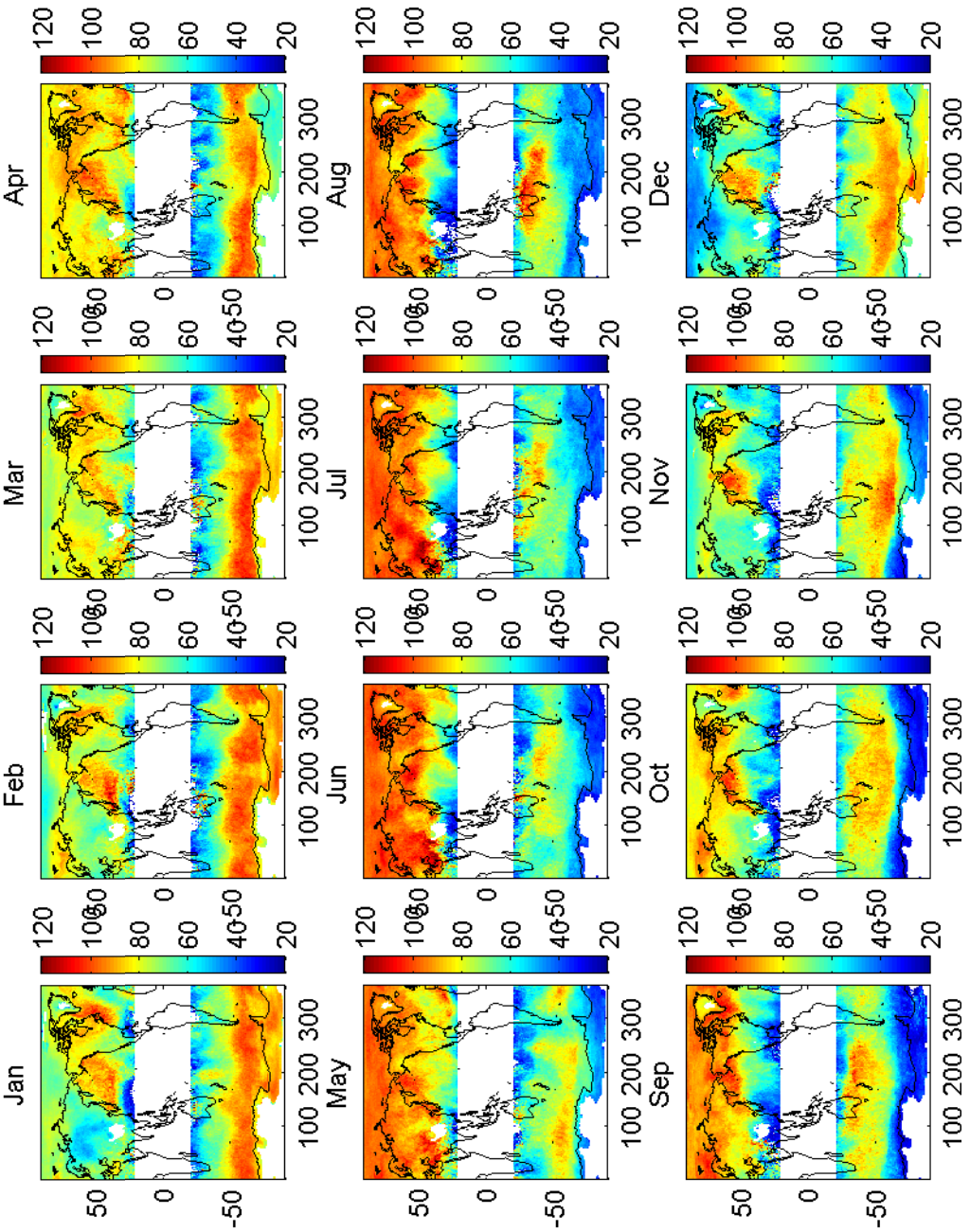

Figure D.2: AIRS mean monthly entropy for 2004. Colour scale is entropy $\frac{S}{k_B}$.

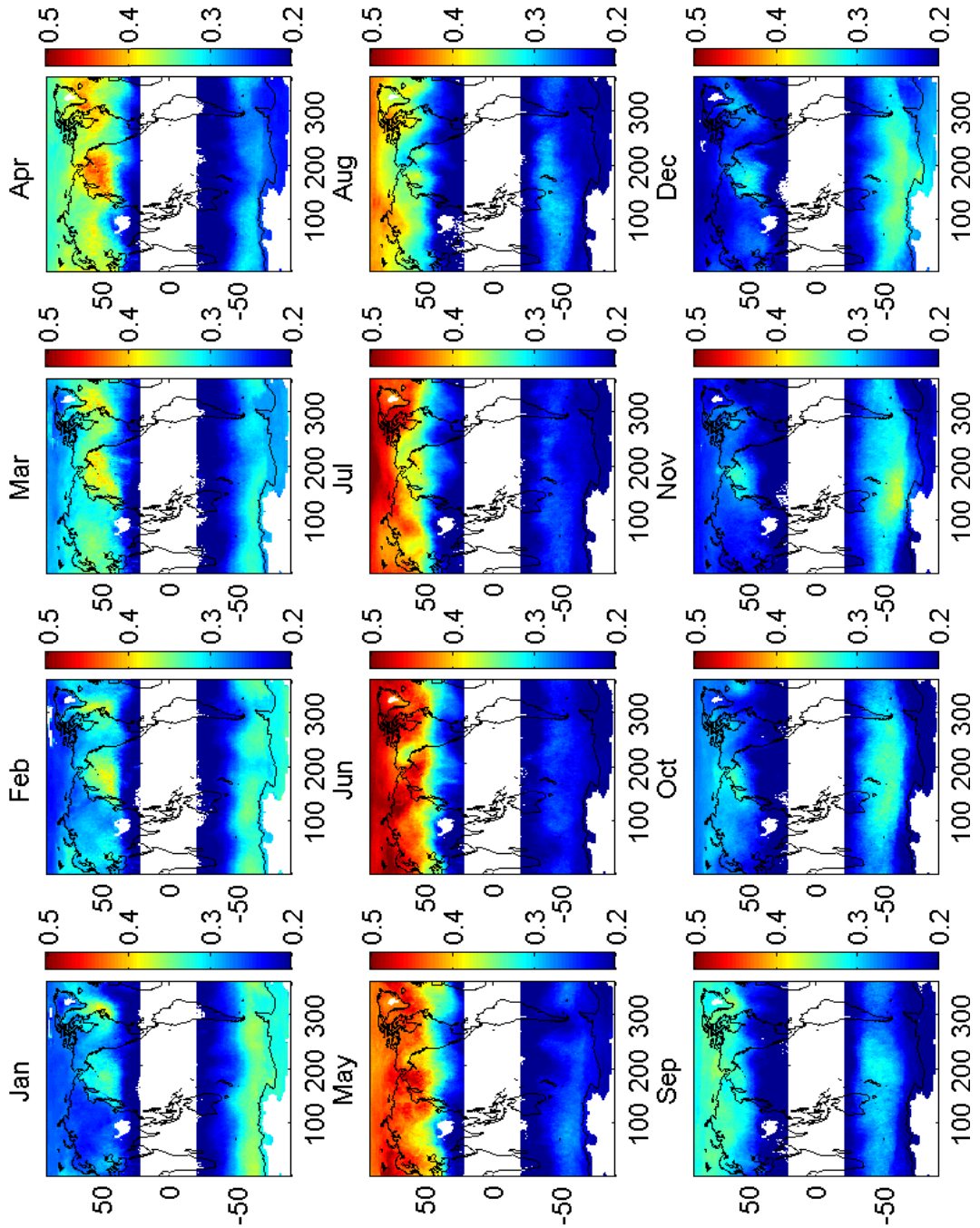

Figure D.3: Mean monthly BO3 values for 2004. Color scale gives the mean BO3 value in units of ppm.

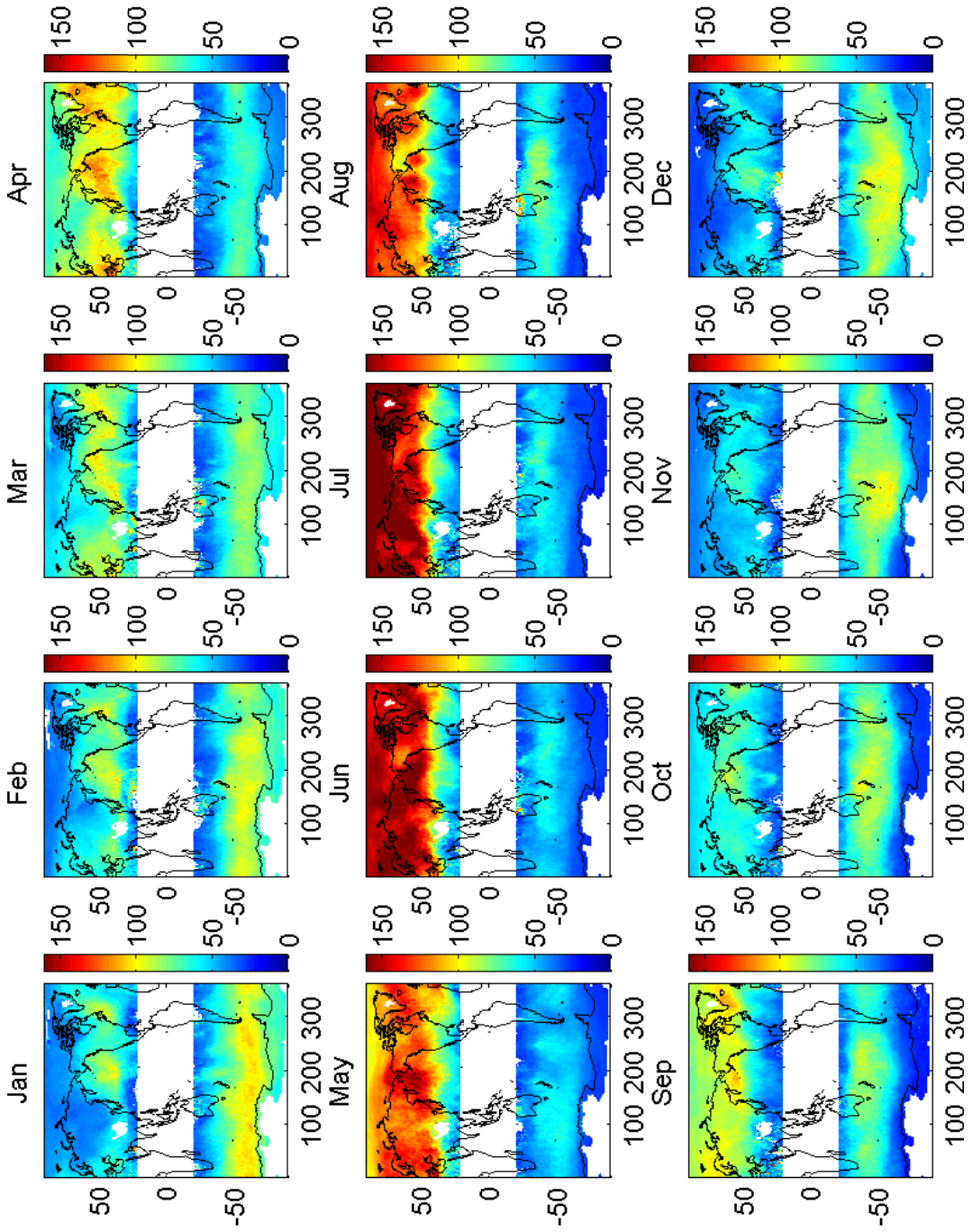

Figure D.4: Mean monthly BH2O values for 2004. Colour scale gives the mean BH2O value in units of ppm.

Bibliography

Ancellet, G., M. Beekmann, and A. Papayannis, Impact of a cutoff low development on downward transport of ozone in the troposphere, *Journal of Geophysical Research-Atmospheres*, *99*(D2), 3451–3468, 1994.

Archer, C. L., and K. Caldeira, Historical trends in the jet streams, *Geophysical Research Letters*, *35*, L08,803, doi:10.1029/2008GL033614, 2008.

Aumann, H. H., et al., AIRS/AMSU/HSB on the Aqua mission: Design, science objectives, data products, and processing systems, *IEEE Transactions on Geoscience and Remote Sensing*, *41*(2), 253–264, 2003.

Baray, J. L., G. Ancellet, T. Randriambelo, and S. Baldy, Tropical cyclone Marlene and stratosphere-troposphere exchange, *Journal of Geophysical Research-Atmospheres*, *104*(D11), 13,953–13,970, 1999.

Barlow, R. J., *Statistics:A guide to the use of statistical methods in the physical sciences.*, The Manchester physics series, John Wiley and Sons Ltd., 1989.

Bennetts, D. A., J. R. Grant, and E. McCallum, An introductory review of fronts. part i: Therory and observations, *The Meteorological Magazine*, *117*(1397), 357–370, 1988.

Bian, J., A. Gettelman, H. Chen, and L. L. Pan, Validation of satellite ozone profile retrievals using Beijing ozonesonde data, *Journal of Geophysical Research-Atmospheres*, *112*, D06,305, doi:10.1029/2006JD007502, 2007.

Birner, T., A. Dornbrack, and U. Schumann, How sharp is the tropopause at midlatitudes?, *Geophysical Research Letters*, *29*(14), doi:10.1029/2002GL015142, 2002.

Bischoff, S. A., P. O. Canziani, and A. E. Yuchechen, The tropopause at southern extratropical latitudes: Argentine operational rawinsonde climatology, *International Journal of Climatology*, *27*, 189–209, doi:10.1002/joc.1385, 2007.

Bithell, M., G. Vaughan, and L. J. Gray, Persistence of stratospheric ozone layers in the troposphere, *Atmospheric Environment*, *34*(16), 2563–2570, 2000.

Blonsky, S., and P. Speth, An algorithm to detect tropopause folds from ozone soundings, *Meteorologische Zeitschrift*, *7*(4), 153–162, 1998.

Bodeker, G. E., I. S. Boyd, and W. A. Matthews, Trends and variability in vertical ozone and temperature profiles measured by ozonesondes at Lauder, New Zealand: 1986-1996, *Journal of Geophysical Research-Atmospheres*, *103*(D22), 28,661–28,681, 1998.

Boyd, I. S., G. E. Bodeker, B. J. Connor, D. P. J. Swart, and E. J. Brinksma, An assessment of ECC ozonesondes operated using 1% and 0.5% KI cathode solutions at Lauder, New Zealand, *Geophysical Research Letters*, *25*(13), 2409–2412, 1998.

Brinksma, E. J., et al., Validation of 3 years of ozone measurements over network for the detection of stratospheric change station Lauder, New Zealand, *Journal of Geophysical Research-Atmospheres*, *105*(D13), 17,291–17,306, 2000.

Bromwich, D. H., and R. L. Fogt, Strong trends in the skill of the ERA-40 and NCEP-NCAR reanalyses in the high and midlatitudes of the Southern Hemisphere, *Journal of Climate*, *17*(23), 4603–4619, 2004.

Bromwich, D. H., and S. H. Wang, Evaluation of the NCEP-NCAR and ECMWF 15- and 40-yr reanalyses using rawinsonde data from two independent Arctic field experiments, *Monthly Weather Review*, *133*(12), 3562–3578, 2005.

Butchart, N., and A. A. Scaife, Removal of chlorofluorocarbons by increased mass exchange between the stratosphere and troposphere in a changing climate, *Nature*, *410*(6830), 799–802, 2001.

Chang, R., *Chemistry*, 6th ed., McGraw-Hill, 1998.

Collins, W. J., R. G. Derwent, B. Garnier, C. E. Johnson, M. G. Sanderson, and D. S. Stevenson, Effect of stratosphere-troposphere exchange on the future tropospheric ozone trend, *Journal of Geophysical Research-Atmospheres*, *108*(D12), doi:10.1029/2002JD002617, 2003.

Cooper, O., et al., Direct transport of midlatitude stratospheric ozone into the lower troposphere and marinae boundary layer of the tropical Pacific Ocean., *Journal of Geophysical Research-Atmospheres*, *110*, D23,310, doi:10.1029/2005JD005783, 2005.

Cooper, O. R., J. L. Moody, D. D. Parrish, M. Trainer, J. S. Holloway, G. Hubler, F. C. Fehsenfeld, and A. Stohl, Trace gas composition of mid-latitude cyclones over the western North Atlantic Ocean: A seasonal comparison of O_3 and CO, *Journal of Geophysical Research-Atmospheres*, *107*(D7-8), doi:10.1029/001JD000902, 2002.

Cristofanelli, P., et al., Stratosphere-to-troposphere transport: A model and method evaluation, *Journal of Geophysical Research-Atmospheres*, *108*(D12), doi:10.1029/2002JD002600, 2003.

Danielsen, E. F., R. S. Hipskind, S. E. Gaines, G. W. Sachse, G. L. Gregory, and G. F. Hill, Three-dimensional analysis of potential vorticity associated with tropopause folds and observed variations of ozone and carbon monoxide, *Journal of Geophysical Research-Atmospheres*, *92*(D2), 2103–2111, 1987.

Dessler, A. E., E. J. Hintsa, E. M. Weinstock, J. G. Anderson, and K. R. Chan, Mechanisms controlling water-vapor in the lower stratosphere - a tale of 2 stratospheres, *Journal of Geophysical Research-Atmospheres*, *100*(D11), 23,167–23,172, 1995.

Dethof, A., and E. V. Holm, Ozone assimilation in the ERA-40 reanalysis project, *Quarterly Journal of the Royal Meteorological Society*, *130*(603), 2851–2872, 2004.

Dethof, A., A. O'Neill, and J. Slingo, Quantification of the isentropic mass transport across the dynamical tropopause, *Journal of Geophysical Research-Atmospheres*, *105*(D10), 12,279–12,293, 2000.

Ding, T., A; Wang, Influence of stratosphere-to-troposphere exchange on the seasonal cycle of surface ozone at Mount Waliguan in western China, *Geophysical Research Letters*, *33*, doi:10.1029/2005GL024760, 2006.

Divakarla, M., et al., Evaluation of Atmospheric Infrared Sounder ozone profiles and total ozone retrievals with matched ozonesonde measurements, ECMWF ozone data and Ozone Monitoring Instrument retrievals, *Journal of Geophysical Research*, *113*, D15,308, doi:10.1029/2007JD009317, 2008.

Divakarla, M. G., C. D. Barnet, M. D. Goldberg, L. M. McMillin, E. Maddy, W. Wolf, L. Zhou, and X. Liu, Validation of Atmospheric Infrared Sounder temperature and water vapor retrievals with matched radiosonde measurements

and forcasts, *Journal of Geophysical Research-Atmospheres*, *111*, D09S15, doi:10.1029/2005JD006116, 2006.

Eisele, H., H. E. Scheel, R. Sladkovic, and T. Trickl, High-resolution lidar measurements of stratosphere-troposphere exchange, *Journal of the Atmospheric Sciences*, *56*(2), 319–330, 1999.

Elbern, H., J. Hendricks, and A. Ebel, A climatology of tropopause folds by global analyses, *Theoretical and Applied Climatology*, *59*(3-4), 181–200, 1998.

Esler, J. G., D. G. H. Tan, P. H. Haynes, M. J. Evans, K. S. Law, P. H. Plantevin, and J. A. Pyle, Stratosphere-troposphere exchange: Chemical sensitivity to mixing, *Journal of Geophysical Research-Atmospheres*, *106*(D5), 4717–4731, 2001.

Fetzer, E., A. Eldering, E. Fishbein, T. Hearty, W. Irion, and B. Kahn, Validation of AIRS/AMSU/HSB for data release version 4.0, http://disc.gsfc.nasa.gov/AIRS/documentation.shtml, 2005.

Fetzer, E., et al., AIRS/AMSU/HSB validation, *IEEE Transactions on Geoscience and Remote Sensing*, *41*(2), 418–431, 2003.

Fetzer, E. J., B. H. Lambrigsten, A. Eldering, H. H. Aumann, and M. T. Chahine, Biases in total precipitable water vapor climatologies from Atmospheric Infrared Sounder and Advanced Microwave Scanning Radiometer, *Journal of Geophysical Research-Atmospheres*, *111*, doi:10.1029/2005JD006598, 2006.

Fischer, H., F. G. Wienhold, P. Hoor, O. Bujok, C. Schiller, P. Siegmund, M. Ambaum, H. A. Scheeren, and J. Lelieveld, Tracer correlations in the northern high latitude lowermost stratosphere: Influence of cross-tropopause mass exchange, *Geophysical Research Letters*, *27*(1), 97–100, 2000.

Fuenzalida, H. A., R. Sanchez, and R. D. Garreaud, A climatology of cutoff lows in the Southern Hemisphere, *Journal of Geophysical Research-Atmospheres*, *110*(D18), doi:10.1029/2005JD005934, 2005.

Gettelman, A., and P. M. D. Forster, A climatology of the tropical tropopause layer, *Journal of the Meteorological Society of Japan*, *80*(4B), 911–924, 2002.

Gettelman, A., et al., Validation of Aqua satellite data in the upper troposphere and lower stratosphere with in situ aircraft instruments, *Geophysical Research Letters*, *31*(22), doi:10.1029/2004GL020730, 2004.

Goering, M. A., W. A. Gallus, M. A. Olsen, and J. L. Stanford, Role of stratospheric air in a severe weather event: Analysis of potential vorticity and total ozone, *Journal of Geophysical Research-Atmospheres*, *106*(D11), 11,813–11,823, 2001.

Goldberg, M. D., Y. N. Qu, L. M. McMillin, W. Wolf, L. H. Zhou, and M. Divakarla, AIRS near-real-time products and algorithms in support of operational numerical weather prediction, *IEEE Transactions on Geoscience and Remote Sensing*, *41*(2), 379–389, 2003.

Gouget, H., Case study of a tropopause fold and of subsequent mixing in the subtropics of the Southern Hemisphere, *Atmospheric Environment*, *34*(16), 2653–2658, 2000.

Hagan, D. E., C. R. Webster, C. B. Farmer, R. D. May, R. L. Herman, E. M. Weinstock, L. E. Christensen, L. R. Lait, and P. A. Newman, Validating AIRS upper atmosphere water vapor retrievals using aircraft and balloon in situ measurements, *Geophysical Research Letters*, *31*(21), 2004.

Halliday, D., R. Resnick, and J. Walker, *Fundamentals of physics*, 7th ed., John Wiley and Sons Inc., 2005.

Hegglin, M. I., et al., Tracing troposphere-to-stratosphere transport above a mid-latitude convective system, *Atmospheric Chemistry and Physics*, *4*, 741–756, 2004.

Hoerling, M. P., T. K. Schaack, and A. J. Lenzen, Global objective tropopause analysis, *Monthly Weather Review*, *119*(8), 1816–1831, 1991.

Hoinka, K. P., The tropopause: Discovery, definition and demarcation, *Meteorologische Zeitschrift*, *6*(6), 281–303, 1997.

Hoinka, K. P., Temperature, humidity, and wind at the global tropopause, *Monthly Weather Review*, *127*(10), 2248–2265, 1999.

Hoinka, K. P., M. E. Reinhardt, and W. Metz, North-Atlantic air-traffic within the lower stratosphere - Cruising times and corresponding emissions, *Journal of Geophysical Research-Atmospheres*, *98*(D12), 23,113–23,131, 1993.

Holton, J. R., P. H. Haynes, M. E. McIntyre, A. R. Douglass, R. B. Rood, and L. Pfister, Stratosphere-troposphere exchange, *Reviews of Geophysics*, *33*(4), 403–439, 1995.

Hoor, P., H. Fischer, L. Lange, J. Lelieveld, and D. Brunner, Seasonal variations of a mixing layer in the lowermost stratosphere as identified by the CO - O3 correlation from in situ measurements, *Journal of Geophysical Research-Atmospheres*, *107*(D5-6), doi:10.1029/2000JD000289, 2002.

Hoor, P., C. Gurk, D. Brunner, M. I. Hegglin, H. Wernli, and H. Fischer, Seasonality and extent of extratropical TST derived from in-situ CO measurements during SPURT, *Atmospheric Chemistry and Physics*, *4*, 1427–1442, 2004.

Hoskins, B. J., Towards a PV-theta view of the general-circulation, *Tellus Series A-Dynamic Meteorology and Oceanography*, *43*(4), 27–35, 1991.

James, P., A. Stohl, C. Forster, S. Eckhardt, P. Seibert, and A. Frank, A 15-year climatology of stratosphere-troposphere exchange with a Lagrangian particle dispersion model: 1. Methodology and validation, *Journal of Geophysical Research-Atmospheres*, *108*(D12), doi:10.1029/2002JD002637, 2003a.

James, P., A. Stohl, C. Forster, S. Eckhardt, P. Seibert, and A. Frank, A 15-year climatology of stratosphere-troposphere exchange with a Lagrangian particle dispersion model - 2. Mean climate and seasonal variability, *Journal of Geophysical Research-Atmospheres*, *108*(D12), doi:10.1029/2002JD002639, 2003b.

Jing, P., D. M. Cunnold, H. J. Wang, and E. S. Yang, Isentropic cross-tropopause ozone transport in the Northern Hemisphere, *Journal of the Atmospheric Sciences*, *61*(9), 1068–1078, 2004.

Kistler, R., et al., The NCEP-NCAR 50-year reanalysis: Monthly means CD-ROM and documentation, *Bulletin of the American Meteorological Society*, *82*(2), 247–267, 2001.

Lamarque, J. F., and P. G. Hess, Cross-tropopause mass exchange and potential vorticity budget in a simulated tropopause folding, *Journal of the Atmospheric Sciences*, *51*(15), 2246–2269, 1994.

Leclair De Bellevue, L., A. Réchou, J. L. Baray, G. Ancellet, and R. D. Diab, Signatures of stratosphere to troposphere transport near deep convective events in the southern subtropics, *Journal of Geophysical Research-Atmospheres*, *111*, D24,107, doi:10.1029/2005JD006947, 2006.

Levy, I., H, J. D. Mahlman, and W. J. Moxim, A stratospheric source of reactive nitrogen in the unpolluted troposphere, *Geophysical Research Letters*, *7*(9), 441–444, 1980.

Luo, M., R. J. Cicerone, and J. M. Russell, Analysis of halogen occultation experiment HF versus CH4 correlation plots - Chemistry and transport implications, *Journal of Geophysical Research-Atmospheres*, *100*(D7), 13,927–13,937, 1995.

Maczek, A., *Statistical Thermodynamics*, *Oxford Chemistry Primers*, vol. 58, Oxford University Press, New York, 1998.

Marshall, G. J., Trends in Antarctic geopotential height and temperature: A comparison between radiosonde and NCEP-NCAR reanalysis data, *Journal of Climate*, *15*(6), 659–673, 2002.

Miloshevich, L., H. Vömel, D. N. Whiteman, B. M. Lesht, F. J. Schmidlin, and F. Russo, Absolute accuracy of water vapor measurements from six operational radiosonde types launched during AWEX-G and implications for AIRS validation, *Journal of Geophysical Research-Atmospheres*, *111*, doi:10.1029/2005JD006083, 2006.

Monahan, K. P., L. L. Pan, A. J. McDonald, G. E. Bodeker, J. Wei, S. E. George, C. D. Barnet, and E. Maddy, Validation of AIRS v4 ozone profiles in the UTLS using ozonesondes from Lauder, NZ and Boulder, USA, *Journal of Geophysical Research-Atmospheres*, *112*, D17,304, doi: 10.1029/2006JD008181, 2007.

Monks, P. S., A review of the observations and origins of the spring ozone maximum, *Atmospheric Environment*, *34*(21), 3545–3561, 2000.

Morcrette, J., Ozone-radiation interactions in the ECMWF forecast system, *Tech. Rep. 375*, European Center for Medium Range Weather Forcasts, 2003.

Newchurch, M. J., M. A. Ayoub, S. Oltmans, B. Johnson, and F. J. Schmidlin, Vertical distribution of ozone at four sites in the United States, *Journal of Geophysical Research-Atmospheres*, *108*(D1), doi:10.1029/2002JD002059, 2003.

Olsen, E. T., E. Fishbein, S. Lee, and E. Manning, AIRS/AMSU/HSB version 4.0 level 2 product levels and layers, Jet Propulsion Laboratory, California Institute of Technology http://disc.gsfc.nasa.gov/AIRS/documentation.shtml, 2005.

Olsen, E. T., et al., AIRS/AMSU/HSB version 5 changes from version 4, Jet Propulsion Laboratory, California Institute of Technology http://disc.gsfc.nasa/AIRS/documentation.shtml, 2007.

Olsen, M. A., A. R. Douglass, and M. R. Schoeberl, Estimating downward cross-tropopause ozone flux using column ozone and potential vorticity, *Journal of Geophysical Research-Atmospheres*, *107*(D22), 2002.

Olsen, M. A., A. R. Douglass, and M. R. Schoeberl, A comparison of Northern and Southern Hemisphere cross-tropopause ozone flux, *Geophysical Research Letters*, *30*(7), doi:10.1029/2002GL016538, 2003.

Olsen, M. A., M. R. Schoeberl, and A. R. Douglass, Stratosphere-troposphere exchange of mass and ozone, *Journal of Geophysical Research-Atmospheres*, *109*(D24), doi:10.1029/2004JD005186, 2004.

Ott, J. B., and J. Boerio-Goates, *Chemical Thermodynamics - Principles and Applications*, Elsevier Academic Press, 2000.

Ovarlez, J., P. van Velthoven, and H. Schlager, Water vapor measurements from the troposphere to the lowermost stratosphere: Some signatures of troposphere to stratosphere exchanges, *Journal of Geophysical Research-Atmospheres*, *104*(D14), 16,973–16,978, doi:10.1029/1999JD900318, 1999.

Pagano, T. S., H. H. Aumann, D. E. Hagan, and K. Overoye, Prelaunch and in-flight radiometric calibration of the Atmospheric Infrared Sounder (AIRS), *IEEE Transactions on Geoscience and Remote Sensing*, *41*(2), 265–273, 2003.

Pan, L. L., W. J. Randel, B. L. Gary, M. J. Mahoney, and E. J. Hintsa, Definitions and sharpness of the extratropical tropopause: A trace gas perspective, *Journal of Geophysical Research-Atmospheres*, *109*(D23), doi:10.1029/2004JD004982, 2004.

Pan, L. L., P. Konopka, and E. V. Browell, Observations and model simulations of mixing near the extratropical tropopause, *Journal of Geophysical Research-Atmospheres*, *111*(D5), D05,106, doi:10.1029/2005JD006480, 2006.

Pan, L. L., J. C. Wei, D. E. Kinnison, R. R. Garcia, D. J. Wuebbles, and G. P. Brasseur, A set of diagnostics for evaluating chemisty-climate models in the extratropical tropopause region, *Journal of Geophysical Research - Atmospheres*, *112*, D09,316, doi:10.1029/2006JD007792, 2007a.

Pan, L. L., et al., Chemical behaviour of the tropopause observed during the stratosphere-troposphere analyses of regional transport START experiment, *Journal of Geophysical Research-Atmospheres*, *112*, D18,110, doi:10.1029/2007JD008645, 2007b.

Patmore, N., Water vapour transport and mixing at the tropopause - chpt 4: An entropy based measure of mixing at the tropopause, Ph.d., Imperial College London, 2006.

Patmore, N., and R. Toumi, An entropy-based measure of mixing at the tropopause, *Quarterly Journal of the Royal Meteorological Society*, *132*(619), 1949–1967, doi:10.1256/qj.05.84, 2006.

Pawson, S., and M. Fiorino, A comparison of reanalyses in the tropical stratosphere. Part 1: Thermal structure and the annual cycle, *Climate Dynamics*, *14*(9), 631–644, 1998.

Plumb, R. A., Stratospheric transport, *Journal of the Meteorological Society of Japan*, *80*(4B), 793–809, 2002.

Plumb, R. A., D. W. Waugh, and M. P. Chipperfield, The effects of mixing on tracer relationships in the polar vortices, *Journal of Geophysical Research-Atmospheres*, *105*(D8), 10,047–10,062, 2000.

Price, G., *Thermodynamics of Chemical Processes*, Oxford University Press, 1998.

Price, J. D., and G. Vaughan, Statistical studies of cut-off-low systems, *Annales Geophysicae-Atmospheres Hydrospheres and Space Sciences*, *10*(1-2), 96–102, 1992.

Price, J. D., and G. Vaughan, The potential for stratosphere troposphere exchange in cut-off-low systems, *Quarterly Journal of the Royal Meteorological Society*, *119*(510), 343–365, 1993.

Proffitt, M. H., J. J. Margitan, K. K. Kelly, M. Loewenstein, J. R. Podolske, and K. R. Chan, Ozone loss in the Arctic polar vortex inferred from high-altitude aircraft measurements, *Nature*, *347*(6288), 31–36, 1990.

Randel, W. J., and M. Park, Deep convective influence on the Asian summer monsoon anticyclone and associated tracer variability observed with Atmospheric Infrared Sounder (AIRS), *Journal of Geophysical Research-Atmospheres*, *111*(D12), 2006.

Randel, W. J., D. J. Siedel, and L. L. Pan, Observational characteristics of double tropopauses, *Journal of Geophysical Research-Atmospheres*, *112*, D07,309, doi:10.1029/2006JD007904, 2007.

Rao, T. N., and S. Kirkwood, Characteristics of tropopause folds over Arctic latitudes, *Journal of Geophysical Research-Atmospheres*, *110*(D18), doi:10.1029/2004JD005374, 2005.

Reichler, T., M. Dameris, and R. Sausen, Determining the tropopause height from gridded data, *Geophysical Research Letters*, *30*(20), doi:10.1029/2003GL018240, 2003.

Rosenlof, K. H., and J. R. Holton, Estimates of the stratospheric residual circulation using the downward control principle, *Journal of Geophysical Research*, *98*(D6), 10,465–10,479, 1993.

Salby, M. L., *Fundamentals of Atmospheric Physics*, Academic Press, 1996.

Savitzky, A., and M. J. E. Golay, Smoothing and differntiation of data by simplified least squares procedures, *Journal of Analytical Chemistry*, *36*(8), 1627–1639, 1964.

Seo, K. H., and K. P. Bowman, A climatology of isentropic cross-tropopause exchange, *Journal of Geophysical Research-Atmospheres*, *106*(D22), 28,159–28,172, 2001.

Seo, K. H., and K. P. Bowman, Lagrangian estimate of global stratosphere-troposphere mass exchange, *Journal of Geophysical Research-Atmospheres*, *107*(D21), doi:10.1029/2002JD002441, 2002.

Shapiro, M. A., Turbulent mixing within tropopause folds as a mechanism for the exchange of chemical-constituents between the stratosphere and troposphere, *Journal of the Atmospheric Sciences*, *37*(5), 994–1004, 1980.

Shepherd, T. G., Large-scale atmospheric dynamics for atmospheric chemists, *Chemical Reviews*, *103*(12), 4509–4531, 2003.

Shepherd, T. G., Transport in the middle atmosphere, *Journal of the Meteorological Society of Japan*, *85B*, 165–191, 2007.

Sprenger, M., M. C. Maspoli, and H. Wernli, Tropopause folds and cross-tropopause exchange: A global investigation based upon ECMWF analyses for the time period March 2000 to February 2001, *Journal of Geophysical Research-Atmospheres*, *108*(D12), doi:10.1029/2002JD002587, 2003.

Stohl, A., et al., Stratosphere-troposphere exchange: A review, and what we have learned from STACCATO, *Journal of Geophysical Research-Atmospheres*, *108*(D12), doi:10.1029/2002JD002490, 2003.

Strow, L. L., S. E. Hannon, S. D. S. Machado, H. E. Motteler, and D. C. Tobin, Validation of the Atmospheric Infrared Sounder radiative transfer algorithm, *Journal of Geophysical Research-Atmospheres*, *111*(D9), 2006.

Stull, R. B., *Meteorology for scientists and engineers*, 2nd ed., Brooks/Cole, 2000.

Sturman, A. P., and N. Tapper, The weather and climate of Australia and New Zealand, Oxford University Press, 1996.

Sudo, K., M. Takahashi, and H. Akimoto, Future changes in stratosphere-troposphere exchange and their impacts on future tropospheric ozone simulations, *Geophysical Research Letters*, *30*(24), 2003.

Susskind, J., C. D. Barnet, and J. M. Blaisdell, Retrieval of atmospheric and surface parameters from AIRS/AMSU/HSB data in the presence of clouds, *IEEE Transactions on Geoscience and Remote Sensing*, *41*(2), 390–409, 2003.

Susskind, J., C. D. Barnet, J. M. Blaisdell, I. L., F. Keita, L. Kouvaris, G. Molnar, and M. T. Chahine, Accuracy of geophysical parameters derived from Atmospheric Infrared Sounder/Advanced Microwave Sounding Unit as a function of fractional cloud cover, *Journal of Geophysical Research-Atmospheres*, *111*, doi:10.1029/2005JD006272, 2006.

Tilmes, S., R. Müller, J. U. Grooβ, R. Spang, T. Sugita, H. Nakajima, and Y. Sasano, Chemical ozone loss and related processes in the Antarctic winter 2003 based on Improved Atmospheric Spectrometer (ILAS)-II observations, *Journal of Geophysical Research*, *111*, D11S12, doi:10.1029/2005JD006260, 2006.

Tobin, D., et al., Atmospheric radiation measurement site atmospheric state best estimates for Atmospheric Infrared Sounder temperature and water vapor retrieval validation, *Journal of Geophysical Research-Atmospheres*, *111*, doi:10.1029/2005JD006103, 2006.

Trigo, I. F., Climatology and interannual variability of storm-tracks in the Euro-Atlantic sector: a comparison between ERA-40 and NCEP/NCAR reanalyses, *Climate Dynamics*, *26*(2-3), 127–143, 2006.

Tsutsumi, Y., Y. Igarashi, Y. Zaizen, and Y. Makino, Case studies of tropospheric ozone events observed at the summit of Mount Fuji, *Journal of Geophysical Research-Atmospheres*, *103*(D14), 16,935–16,951, doi: 98JD01152, 1998.

Van Haver, P., D. De Muer, M. Beekmann, and C. Mancier, Climatology of tropopause folds at midlatitudes, *Geophysical Research Letters*, *23*(9), 1033–1036, 1996.

Vömel, H., D. E. David, and K. Smith, Accuracy of tropospheric and stratospheric water vapor measurements by the cryogenic frost point hygrometer: Instrumental details and observations, *Journal of Geophysical Research-Atmospheres*, *112*(D8), D08,305, doi:10.1029/2006JD007224, 2007.

Wang, P. H., D. M. Cunnold, J. M. Zawodny, R. B. Pierce, J. R. Olson, G. S. Kent, and K. M. Skeens, Seasonal ozone variations in the isentropic layer between 330 and 380 K as observed by SAGE II: Implications of extratropical cross-tropopause transport, *Journal of Geophysical Research-Atmospheres*, *103*(D22), 28,647–28,659, 1998.

Wang, P. H., D. M. Cunnold, C. R. Trepte, H. J. Wang, P. Jing, J. Fishman, V. G. Brackett, J. M. Zawodny, and G. E. Bodeker, Ozone variability in the midlatitude upper troposphere and lower stratosphere diagnosed from a monthly SAGE II climatology relative to the tropopause, *Journal of Geophysical Research-Atmospheres*, *111*, D21,304, doi:10.1029/2005JD006108, 2006.

Waugh, D. W., et al., Mixing of polar vortex air into middle latitudes as revealed by tracer-tracer scatterplots, *Journal of Geophysical Research*, *102*(D11), 13,119–13,134, 1997.

Wernli, H., and M. Bourqui, A Lagrangian "1-year climatology" of (deep) cross-tropopause exchange in the extratropical Northern Hemisphere, *Journal of Geophysical Research-Atmospheres*, *107*(D1-D2), doi:10.1029/2001JD000812, 2002.

Wimmers, A. J., and J. L. Moody, Tropopause folding at satellite-observed spatial gradients: 1. Verification of an empirical relationship, *Journal of Geophysical Research-Atmospheres*, *109*(D19), doi:10.1029/2003JD004145, 2004.

Wimmers, A. J., et al., Signatures of tropopause folding in satellite imagery, *Journal of Geophysical Research-Atmospheres*, *108*(D4), 2003.

Wirth, V., Cyclone-anticyclone asymmetry concerning the height of the thermal and the dynamical tropopause, *Journal of the Atmospheric Sciences*, *58*(1), 26–37, 2001.

Wirth, V., Static stability in the extratropical tropopause region, *Journal of the Atmospheric Sciences*, *60*(11), 1395–1409, 2003.

World Meteorological Organization, Definition of the tropopause, *Tech. rep.*, 1957.

World Meteorological Organization, Atmospheric ozone 1985, *Tech. Rep. WMO Rep. 16*, 1986.

World Meteorological Organization, *Scientific Assessment of Ozone Depletion: 2002*, Global Ozone Research and Monitoring Project - Report No. 47, 498pp., Geneva, Switzerland, 2003.

World Meteorological Organization, *Scientific Assessment of Ozone Depletion: 2006*, Global Ozone Research and Monitoring Project - Report No. 50, 572pp., Geneva, Switzerland, 2007.

Yang, H., and K. K. Tung, Cross-isentropic stratosphere-troposphere exchange of mass and water vapor, *Journal of Geophysical Research-Atmospheres*, *101*(D5), 9413–9423, 1996.

Yang, S., K. M. Lau, and K. M. Kim, Variations of the East Asian jet stream and Asian-Pacific-American winter climate anomalies, *Journal of Climate*, *15*(3), 306–325, 2002.

Zahn, A., and C. A. M. Brenninkmeijer, New directions: A chemical tropopause defined, *Atmospheric Environment*, *37*(3), 439–440, 2003.

Zängl, G., and K. P. Hoinka, The tropopause in the polar regions, *Journal of Climate*, *14*(14), 3117–3139, 2001.